ESTUDIO Y SIMULACIÓN NUMÉRICA DEL TRANSPORTE DE SEDIMENTOS EN FLUJOS CON SUPERFICIE LIBRE

Trabajo realizado
por

PATRICIO BOHÓRQUEZ RODRÍGUEZ DE MEDINA

para la obtención del grado Europeo
Doctor Ingeniero Industrial por la Universidad de Málaga
en el Área de Conocimiento de
Mecánica de Fluidos

E.T.S. Ingenieros Industriales
Departamento de Ingeniería Mecánica y Mecánica de Fluidos
Pza. El Ejido s/n, 29013 Málaga, España

Julio del 2008

STUDY AND NUMERICAL SIMULATION OF SEDIMENT TRANSPORT IN FREE-SURFACE FLOW

A dissertation presented
by
PATRICIO BOHÓRQUEZ RODRÍGUEZ DE MEDINA

Thesis submitted for the degree of
Doctor Europaeus of the University of Málaga
in the subject of
Fluid Mechanics

E.T.S. Ingenieros Industriales
Department of Mechanical Engineering and Fluid Mechanics
Pza. El Ejido s/n, 29013 Málaga, Spain

July 2008

Doctoral Committee:
- Prof. M. A. Losada
- Prof. J. V. Giráldez
- Dr. S. E. Darby
- Dr. I. Villanueva
- Dr. C. del Pino

Substitute Committee:
- Dr. E. Sanmiguel-Rojas
- Dr. J. Ortega-Casanova

Abstract

The flow after the rupture of a dam on an inclined plane of arbitrary slope, and the induced transport of non-cohesive sediment, is analysed using the shallow-water approximation. An asymptotic (analytical) solution is presented for the flow hydrodynamics, and compared with the numerical simulation of the dam-break flood. Differences arise due to the appearance of hydrodynamic instabilities (hereafter called *roll-waves*) in the numerical solution. These roll-waves point out the unstable behaviour of the dam-break wave. It is found that roll-waves enhance the transport of suspended sediment. The limitations of this simple model to predict the transport of sediment in dam-break floods on steep inclines are discussed.

Then, a numerical experiment is designed to analyse the unstable character of the dam-break wave, that constitutes a non-parallel and unsteady base flow. By analysing the linear and non-linear numerical evolution of small perturbations, it is possible to reveal how the nature of the ensuing flow depends not only on the Froude number (as it happens in the classical problem of roll-waves over a uniform and steady flow) but also on the non-parallel and time-varying characteristics of the background flow. Consequently, it is also shown that these effects stabilise turbulent roll-waves and raise the critical Froude number required to achieve an unstable flow. This stability result differs with that obtained with a non-parallel spatial stability analysis, pointing out the strong influence of the base-flow time-dependence in the stability criteria.

A novel Continuum Mechanics model is presented to study the transport of sediment in a laminar/turbulent free-surface flow. The mixture equations for non-cohesive sediment transport in turbulent free-surface flow are derived from the ensemble averaged Navier-Stokes equations of the three-phases (water, sediment and air). This model avoids the limitations of traditional shallow-water models, and is suitable to study, for instance, the transport of sediment in non-hydrostatic shallow-water flows over bed of arbitrary bottom slopes. The model developed in this work reveals a mathematical equivalence between the propagation of the volumetric concentration of the sediment and the phase function used to capture the free surface. We take advantage of this fact to formulate an explicit Finite Volume Method (FVM) with the exact conservation property, that is implemented in the open source software OpenFOAM. Finally, this model is applied to solve the problem of local scour around a pipeline and the transport of sediment after the rupture of a horizontal dam.

It is demonstrated that one-dimensional models based on depth-averaged variables (e.g. generalisations of the one-dimensional Saint-Venant equations to predict morphological changes) are superseded by more sophisticated and accurate procedures valid for hyperconcentrated shallow-water flows over bed of arbitrary bottom slopes (e.g. the model described herein).

Contents

Acknowledgments

I wish to express my gratitude to my office colleagues, for their continued support, guidance and constructive criticism.

Furthermore, I would like to acknowledge the collaboration of Dr. Steve Darby, with whom I shared illusions and work during my stay at the School of Geography (University of Southampton, UK).

I am also indebted to Prof. Norberto Fueyo and Dr. Hrvoje Jasak for organising and delivering, respectively, a week of intensive lectures on Computational Fluid Dynamics and training on the use of OpenFOAM.

The text of this Thesis has benefited from numerous valuable comments from Dr. Carlos del Pino.

Finally, the financial support provided by the Ministerio de Educación y Ciencia of Spain (Grant No. AP-2004-3719) and the European Commission (Grant No. COOP-CT-2005-017725), which made this study possible, is gratefully acknowledged.

Patricio Bohórquez
July 2008

Dedicated to my mother,
María del Carmen Rodríguez de Medina.

A mi madre,
María del Carmen Rodríguez de Medina.

Chapter 1

Introduction

1.1 Background

The subject of two or multiphase flow has become increasingly important in a wide variety of engineering systems for their optimum design and safe operations. Multiphase flow phenomena can be observed in a number of biological systems and natural phenomena which require better understanding. Some of the important applications are: power system (e.g. nuclear reactors, power plants with boilers and evaporators, two-phase propulsors), heat transfer systems (e.g. heat exchangers, spray cooling towers, dryers), process systems (e.g. extraction and distillation units, fluidized beds, chemical reactors), transport systems (e.g. air-lift pump, ejectors, slurries, fibbers), geo-meteorological phenomena (e.g. sedimentation, soil erosion and transport by wind, ocean waves), etc.

All the systems and components listed above are governed by essentially the same physical laws of transport of mass, momentum and energy (Ishii and Hibiki, 2006). It is evident that our rapid advances in engineering technology, the demands for progressively accurate predictions of the systems in interest have increased. The precise understanding of the physics is indispensable for safe as well as economically sound operations.

Although the fundamental way to know the physics of a multiphase system is based on experimental works, its theoretical modelling is a powerful tool to predict

Figure 1.1: View of the break in Sweetwater Dam (Jan 30, 1916). ©San Diego Historical Society (http://www.sandiegohistory.org)

the behaviour of the system. Many times, experiments are really expensive, so it is impossible to reproduce all the situations that one requires to know. There are also multiphase systems that cannot be accessed by measuring instruments, for instance, volcanos, avalanches and glacial outburst floods. The numerical simulation is therefore an economic tool that allow better understanding of these complicated systems. In the context of multiphase flows, this work focus its attention on the modelling of sediment transport in free-surface flows, that represents a problem of great interest in hydraulics, and in environmental flows in general.

Hydraulics is the branch of civil engineering related to the science of water in motion, and the interaction between the fluid and the surrounding. The extreme complexity of hydraulic engineering is closely linked with the geometric scale of water systems, the broad range of relevant time scales, the variability of river flows from zero during droughts to gigantic floods, the complexity of basic fluid mechanics characterised by non-linearity, natural fluid instabilities, interactions between water, solid, air and biological life, and Man's total dependence (Chanson, 2004). The prediction of water floods, the transport of sediment associated to them, as well as the fluid-structure interactions, are needed for the assessment and reduction of risks from extreme flooding caused by natural events, or the failure of dams and flood defence structures. For instance, the Hatfield Flood of San Diego, United States, destroyed the Sweetwater (Figure 1.1) and Lower Otay Dams in 1916. Moreover, it caused 22 deaths and \$4.5 million in damages. In the last decade, several experimental works have been done to better understand the physics of dam-break floods. For instance, figure 1.2 depicts the U.S. Geological Survey (USGS) debris flow flume (Iverson et al., 1992) constructed to conduct controlled experiments on water-sediment floods. The cost of this experiment is however too expensive and just a limited number of runs can be performed, covering only a small portion of all the possible scenarios. Hence, theoretical modelling of water-sediment interaction based on first principles appears as an alternative to experimentation. The decreasing of the computational facility cost and the continuous increase of computational capabilities, allow us to solve complex models based on first principles. To elucidate the observed properties of particles suspensions in experimental works, and to capture these properties in so-called closure relations needed by theroretical models, controlled experiments should be performed. Thus, these closure relations can then be employed to describe the theoretical continuum behaviour of particle suspensions.

The remainder of this Chapter is structured as follows: In the following section, well-known Computational Fluid Dynamics (CFD) methodologies for the prediction of the hydrodynamics and sediment transport in shallow-water flows are introduced, two of which are extensively used and developed further in this study. Then, the objectives of this work are stated in Section 1.3. The objectives are followed by a list of the specific contributions made to the field. Next, Section 1.5 reviews previous and related studies and, finally, an outline of the contents of Chapters 2 to 6 is given in Section 1.6.

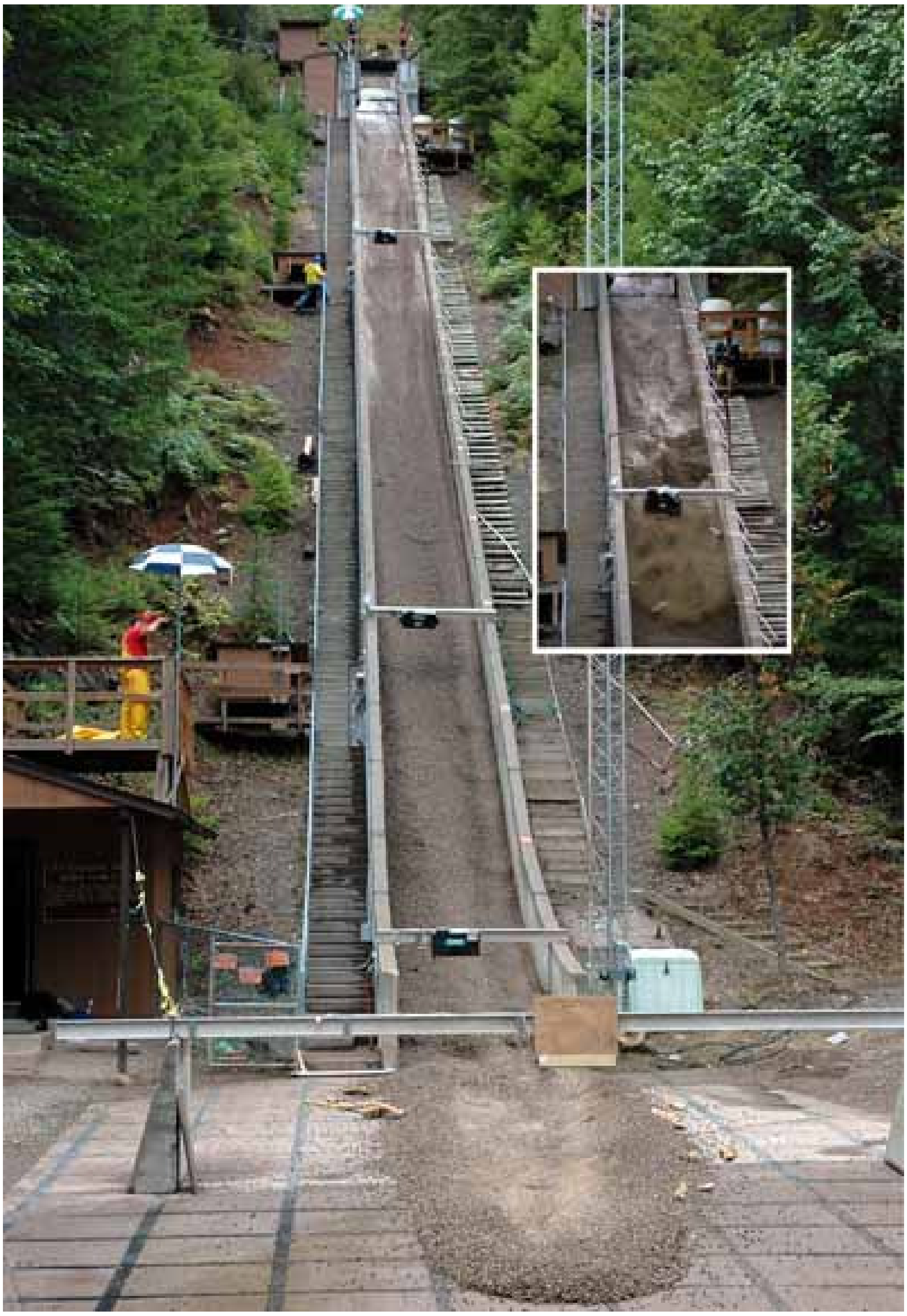

Figure 1.2: Flume constructed in 1991 by the U.S. Geological Survey (USGS), in cooperation with the U.S. Forest Service, to conduct controlled experiments on debris flows (Logan and Iverson, 2007): The flume is a reinforced concrete channel 95 meters long, 2 meters wide, and 1.2 meters deep that slopes 31 degrees (60 percent), an angle typical of terrain where natural debris flows originate.

1.2 CFD methodologies for sediment transport modelling in shallow-water flows

In recent years, the numerical simulation of sediment transport in free-surface flow has focused a wide interest of the hydraulic community (see, for instance, Hutter, 2005; Wright, 2005; Garcia-Navarro and Playan, 2007; Pananicolaou et al., 2008).

Although there are some noticeable exceptions, most of the hydraulic works in sediment transport have been limited to shallow-water flow over bed of small bottom slopes. Consequently, the influence of the vertical velocity (i.e. in the direction of the gravity) on the fluid movement is usually neglected, among many other factors that influence the sediment discharge (see Vanoni, 2006, Section 43: *Criticism of Depth-Discharge Predictors*). Under such conditions, the one- or two-dimensional shallow-water equations can be formulated (Cunge et al., 1980). These equations constitute a system of non-homogeneous hyperbolic laws which can be successfully solved with well-balance numerical techniques, e.g. Riemann solvers, ensuring the conservation of the properties (Toro, 1999, 2001; LeVeque, 2002). In fact, hundreds of papers along the last decade have been devoted to Riemann solvers applied to shallow-water flows (for references, see Toro and Garcia-Navarro, 2007). A natural continuation of this research has been the generalisation of the Saint-Venant equations to predict morphological changes associated with the transport of sediment (see § 1.5.4 for references), but most of these works are still based on depth-averaged magnitudes and continue neglecting the vertical velocity component in the mass continuity and momentum balance equations. Although the ensuing conservation equations can be readily solved with Riemann solvers, because they remain hyperbolic, a noticeable drawback is exhibited: morphological changes associated with the sediment transport usually induce variations of unpredictable magnitude in the bottom slope. When the eroded bed reach high bottom slopes the vertical motion cannot be longer neglected (Dressler, 1978; Bouchut et al., 2003; Keller, 2003).

The extension of the shallow-water equations for bed of arbitrary bottom slopes to include geomorphic processes is a tedious task. In geomorphic flows, the bed may change its shape, break apart, and merge together. Thus, the curvilinear system of coordinates required by the general shallow-water equations may introduces huge algebraical complications in presence of topological changes of the bed. Moreover, the bed of the channel is not sharply defined in flows that transport sediment as bed- and suspended-load. For instance, the boundary between the traction carpet (or bed-load layer) and the intermittently suspended sediment cannot be sharply defined in hyperconcentrated flows (Wan and Wang, 1994; Pierson, 2005). Therefore, the extension of the general shallow-water equations to account for sediment transport may become inappropriate for geomorphic flows.

To avoid discrepancies between the hydrodynamic and sediment transport model predictions and measurements, three-dimensional hydrodynamic and sediment transport models have become much more attractive to use. Recently, Pananicolaou et al. (2008) have reviewed most of the models that are usually employed in hydraulic engineering applications. Three-dimensional approaches are likely to be more appropriate for accurately simulating extreme erosion events, given their ability to characterise the sediment concentration distribution along the vertical coordinate. Most three-dimensional models solve the Reynolds Averaged Navier-Stokes equations (RANS), along with the sediment mass balance equation, using physical models to quantify the sediment transported as bed-load. But few studies have employed the theory of multiphase flows to obtain a Continuum Mechanics formulation for geomorphic flows (in this line, some recent advances have been done by Villaret and Davies, 1995; Ni et al., 1996; Cao et al., 1995; Greimann et al., 1999), i.e. three-dimensional hydraulic models are still based on layers and sediment discharge formulas.

1.3 Objectives of this work

The principle objectives of the study described in this thesis are as follows:

- Revision of previous works on the hydraulics of dam-break flows on inclined planes, paying special attention to the effect of hydraulic resistance and the formulations developed for arbitrary slopes.

- Analysis of the suspended-load in dam-break floods on steep inclines using one-dimensional shallow-water models valid for arbitrary slopes of the bottom. The relative importance of bed-load versus suspended-load is also assessed, as well as the limitations of the model.

- Establishment of the stability criteria, based in the one-dimensional shallow-water equations, for the onset of roll-waves in dam-break floods. The influence of the non-parallel and time-dependent characteristic of the background flow is considered on this study by simulating numerically the linear and non-linear behaviour of the perturbations. It is shown that non-parallel spatial stability analysis alone fails to predict the formation of roll-waves in kinematic waves.

- Development of a research related to the multi-fluid methodology for the transport of non-cohesive sediment in free-surface flows, applicable to fluvial hydraulic. Although the model is formulated for a uniform grain size and non-cohesive sediment, guidelines for the extension to n-grain sizes and cohesive sediment are addressed.

- Development of a numerical solution technique for the multiphase model applicable to the full range of phase fraction.

- Critical evaluation of the methodology.

1.4 Present contributions

This study is concerned with the simulation of non-cohesive sediment transport in shallow-water flows at arbitrary phase fractions, excluding heat and mass transfer as well as phase change. The following specific contributions have been made in this study:

- A review and analysis of the literature with respect to:
    - Theoretical, numerical and experimental studies of dam-break flows on inclines.

  - Theoretical, numerical and experimental studies of turbulent roll-waves.
  - Numerical methodologies for the solution of the mixture model based on the Finite Volume Method (FVM).
  - Test cases suitable for the validation.

- Research related to the hydraulics of dam-break flows on inclines:
  - Revision of analytical solutions available in the literature for small slopes of the bottom.
  - Formulation of a numerical experiment, generalisable to a physical experiment, for the computation of linear and non-linear evolution of perturbations.
  - Determination of the stability criteria for the appearance of roll-waves.
  - Non-parallel spatial stability analysis of roll-waves in kinematic waves.
  - Stability analysis of the linearised shallow-water equations by means of multiple scales.

- Research related to the sediment transport associated with dam-break flows on inclines:
  - One-dimensional numerical study of the transport of suspended sediment after the rupture of a dam.
  - Qualitative comparison of our results with the analytical solution developed by other authors.
  - Analysis of the accuracy of the results, as a function of the hypothesis involved in the model.
  - Discussion of the relative importance between the bed- and suspended-load discharge.

- Research related to the modelling of sediment transport at arbitrary phase fractions in free-surface flows:

  - Formulation of a three-dimensional model for sediment transport based on the ensemble averaged Navier-Stokes equations.
  - Discussion of this approach versus the traditional RANS equations.
  - Reduction of the three-phases model to a mixture model.
  - Incorporation of the k-ϵ turbulence model with buoyant modifications.

- Research related to the mixture methodology:
  - Proposal of a slip velocity incorporating shear-induced particle self-diffusion to account for erosion and the microscopic modelling of yield stress. Fickian and sedimentation fluxes are also incorporated in an algebraical closure law for the slip velocity.
  - Implementation and testing of a numerical algorithm for the mixture methodology which improves stability and convergence in situations where the phase fraction is high, even in regions close to the free-surface.
  - Validation against experimental data: local scour on pipelines and erosional dam-breaks.

1.5 Previous and related studies

1.5.1 General model for turbulent free-surface flow with application to shallow-water flow

One very important class of free-interface problems occurs with two immiscible fluids such as air and water at low Mach numbers. In this section we start describing how to compute the motion of two immiscible fluids using the Level Set Method (LSM) as introduced by Sussman et al. (1994) - the approach that follows was developed in his Ph.D. dissertation. Later, we present other alternatives based on indicator functions and we discuss the advantages and drawbacks of each methodology, with especial attention to fluvial hydraulic applications.

The equations for the conservation of mass and momentum for the gas, at low Mach numbers, and pure water are (e.g. Sethian and Smereka, 2003):

$$\vec{x} \in \text{the gas}: \qquad \nabla \cdot \vec{v}_g = 0\,, \tag{1.1}$$

$$\frac{\partial \rho_g \vec{v}_g}{\partial t} + \nabla \cdot (\rho_g \vec{v}_g \vec{v}_g) = -\nabla p_g + \nabla \cdot (\overline{\overline{\tau}}'_g + \overline{\overline{\tau}}''_g)\,, \tag{1.2}$$

$$\vec{x} \in \text{the liquid}: \qquad \nabla \cdot \vec{v}_f = 0\,, \tag{1.3}$$

$$\frac{\partial \rho_f \vec{v}_f}{\partial t} + \nabla \cdot (\rho_f \vec{v}_f \vec{v}_f) = -\nabla p_f + \nabla \cdot (\overline{\overline{\tau}}'_f + \overline{\overline{\tau}}''_f)\,, \tag{1.4}$$

where the subscript 'g' and 'f' denote the gas and the liquid phase, respectively. In the above equations t is time, $\vec{v}$ is the mean velocity vector, $p = P - \rho \vec{g} \cdot \vec{x}$ is the reduced pressure, P is the absolute pressure, ρ is the density, $\overline{\overline{\tau}}'$ is the viscous stress tensor,

$$\overline{\overline{\tau}}' = \mu_l \left[\nabla \vec{v} + (\nabla \vec{v})^T + \left(\frac{\mu_v}{\mu_l} - \frac{2}{3} \right) (\nabla \cdot \vec{v})\, \overline{\overline{I}} \right]\,, \tag{1.5}$$

μ_l is the dynamic viscosity, μ_v is the bulk viscosity, and $\overline{\overline{\tau}}''$ is the Reynolds stress tensor.

Equations (1.1)-(1.5) are to be solved with appropriated boundary conditions at the interface Γ between the gas and liquid phases. The boundary conditions at the interface between inviscid fluids where the surface tension coefficient is constant are (see, for instance, Batchelor, 1967)

$$\vec{x} \in \Gamma: \quad \vec{v}_f = \vec{v}_g\,, \quad (\overline{\overline{\tau}}_f - \overline{\overline{\tau}}_g) \cdot \vec{n} = (P_f - P_g + \sigma\kappa) \cdot \vec{n}\,, \tag{1.6}$$

where σ is the coefficient of surface tension, $\vec{n}$ is the unit normal vector to the interface drawn outwards from the gas to the liquid, κ is the local surface curvature,

$$\kappa \equiv \nabla \cdot \vec{n}\,, \tag{1.7}$$

and

$$\overline{\overline{\tau}} \equiv \overline{\overline{\tau}}' + \overline{\overline{\tau}}''. \tag{1.8}$$

The system of equations (1.1)-(1.4) and the boundary condition (1.6) can be combined together incorporating the surface tension as a force concentrated on the interface (Peskin, 1977). A derivation of the resulting equations can be found in Chang et al. (1996) and Smereka (1996), although the form below comes from Unverdi and Tryggvason (1992):

$$\rho\frac{\partial\vec{v}}{\partial t}+\rho\nabla\cdot(\vec{v}\vec{v})=-\nabla p+\nabla\cdot\overline{\overline{\tau}}-\sigma\kappa\delta(d)\vec{n}\,,\quad \nabla\cdot\vec{v}=0\,,\quad \vec{x}\in\Omega \tag{1.9}$$

with $\vec{v}$ given by

$$\vec{v}=\begin{cases}\vec{v}_f & \vec{x}\in\text{the water}\\ \vec{v}_f=\vec{v}_g & \vec{x}\in\Gamma\\ \vec{v}_g & \vec{x}\in\text{the gas}\end{cases}\,.$$

The density ρ and viscosity μ are defined in analogous fashion to the velocity $\vec{v}$. On the other hand, Ω is the domain containing both fluids and δ is the Dirac delta function. Besides, d is the signed distance function from the interface, which is defined as follows: at a point $\vec{x}$ in the water, d is the distance to the closest point on the interface; in the gas, d is the negative distance of this quantity.

Then, we introduce the zero-level set $\phi\equiv d$ to parametrise the interface Γ (Osher and Sethian, 1988), that has the property of being a signed-distance function near the interface:

$$\Gamma=\{\vec{x}\,|\,\phi(\vec{x},t)=0\}\,, \tag{1.10}$$

and also takes $\phi>0$ ($\phi<0$) in the liquid (gas) region. Because the interface moves with the fluid volume, the evolution of ϕ is given by

$$\frac{\partial\phi}{\partial t}+\nabla\cdot(\phi\vec{v})=0\,. \tag{1.11}$$

Moreover, the unit normal and curvature on the interface can be easily expressed in terms of $\phi(\vec{x},t)$: $\vec{n}=\nabla\phi/|\nabla\phi|$ and $\kappa=\nabla\cdot(\nabla\phi/|\nabla\phi|)$.

It is clear that we can initialise ϕ as a signed-distance function, but under the evaluation of (1.11), it will not remain so. Therefore, one must reinitialise ϕ so that it remains a distance function near the front as the computation proceeds (see Sussman et al., 1994). Conventional routines for reinitialising a distance function have to explicitly find the contour $\phi = 0$ and reset ϕ at all points close to the front. This takes $O(n)$ operations, where n is the total number of cell points (see Chopp, 1991). Sussman et al. (1994) proposed a reinitialisation algorithm that maintains the signed-distance property by solving to steady state (as fictitious time $\tau \to \infty$) the equation

$$\frac{\partial \phi}{\partial \tau} + \operatorname{sgn}(\phi_0)(|\nabla \phi| - 1) = 0\,, \tag{1.12}$$

where $\operatorname{sgn}(\phi_0)$ is

$$\operatorname{sgn}(\phi_0) = \frac{\phi_0}{\sqrt{\phi_0^2 + (\Delta x)^2}}\,. \tag{1.13}$$

Efficient ways to solve these equations to steady state via fast marching methods are discussed in Sethian (1996, 1999).

The second approach that can be adopted to solve the evolution of the interface is the well known Volume of Fluid method (VOF). The basis of this method is to compute the concentration or volume fraction of one fluid, say γ, which is later used to determine the fluid properties at a particular location. Equations for the VOF method can be derived from the general theory of multiphase flows (Drew, 1983; Ishii and Hibiki, 2006), and provide physical sense to the terms appearing in the equations. In fact, as shown below, this method can be very useful for fluvial regimes that have a not sharply defined interface [i.e., flows with strong turbulence at the free surface, Brocchini and Peregrine (2001)].

The starting point is the conservation equations for mass, momentum and volume fraction (see Chapter 5 for a formal deduction):

$$\frac{\partial \rho}{\partial t} + \nabla \cdot (\rho \vec{v}) = 0\,, \tag{1.14}$$

$$\frac{\partial \rho \vec{v}}{\partial t} + \nabla \cdot (\rho \vec{v}\vec{v}) = -\nabla p + \nabla \cdot \overline{\overline{\tau}} - \sigma \kappa \nabla \gamma - \vec{g} \cdot \vec{x} \nabla \rho\,, \tag{1.15}$$

$$\frac{\partial \gamma}{\partial t} + \nabla \cdot (\gamma \vec{u}) + \nabla \cdot [\gamma(1-\gamma)\vec{u}_{r\gamma}] = 0\,, \tag{1.16}$$

where ρ is the water-air mixture density given by $\rho = \rho_f \gamma + \rho_g (1-\gamma)$, γ is the *volume fraction* occupied by the water in a small control volume centred at $(\vec{x}, t)$, $\vec{v}$ is the *mass velocity* given by

$$\vec{v} = [\gamma \rho_f \vec{v}_f + (1-\gamma)\rho_g \vec{v}_g]/\rho \,, \tag{1.17}$$

$\vec{u}$ is the volumetric flux defined as

$$\vec{u} \equiv \gamma \vec{v}_f + (1-\gamma)\vec{v}_g \quad \text{verifying} \quad \nabla \cdot \vec{u} = 0 \,, \tag{1.18}$$

$\overline{\overline{\tau}} \equiv \overline{\overline{\tau}}' + \overline{\overline{\tau}}'' + \overline{\overline{\tau}}'''$ is the generalised stress tensor that accounts for the viscous stress tensor $\overline{\overline{\tau}}'$, the Reynolds stresses $\overline{\overline{\tau}}''$, and the momentum-diffusion due to the relative motion of the water with respect to the air $\overline{\overline{\tau}}'''$ at the free-surface is

$$\overline{\overline{\tau}}''' \equiv \gamma(1-\gamma)\frac{\rho_f \rho_g}{\rho}\vec{u}_{r\gamma}\vec{u}_{r\gamma} \,, \tag{1.19}$$

where $\vec{u}_{r\gamma} \equiv \vec{v}_f - \vec{v}_g$ is the *relative (slip) velocity* of the water phase with respect to the air phase. The mass velocity $\vec{v}$, required by the continuity (1.14) and momentum balance equation (1.15), and the volumetric flux $\vec{u}$, used in the transport equation (1.16), are linked by the expression

$$\vec{v} = \vec{u} + \gamma(1-\gamma)\frac{\rho_f - \rho_g}{\rho}\vec{u}_{r\gamma} \,. \tag{1.20}$$

For a sharp (or thin) interface, the relative velocity between water and air at the interface vanishes ($\vec{u}_{r\gamma} = 0$), and the most common error in the VOF method appears: the numerical diffusion. In this case, the phase indicator γ changes abruptly from $\gamma = 1$ in the water phase to $\gamma = 0$ in the air phase, and is purely convected at the volumetric velocity $\vec{u}$. For this reason, we find the first difference of the LSM and VOF: while γ is discontinuous at a thin interface, ϕ is a continuous function - therefore, the effects of numerical diffusion are less important for the LSM than for VOF. First-order upwind scheme smears the interface too much and introduces artificial mixing of the two fluids. To avoid the numerical diffusion in the VOF method, one should employ second- and higher-order schemes, which tend to produce over- and undershoots (because of its definition, γ has to stay within bounds $0 \leq \gamma \leq 1$). Thus, the computations to obtain accurate results become a difficult task. Fortunately, it is possible to derive schemes with both keep the interface sharp and produce monotone profiles of γ across it (Ubbink, 1997). On the other hand, the

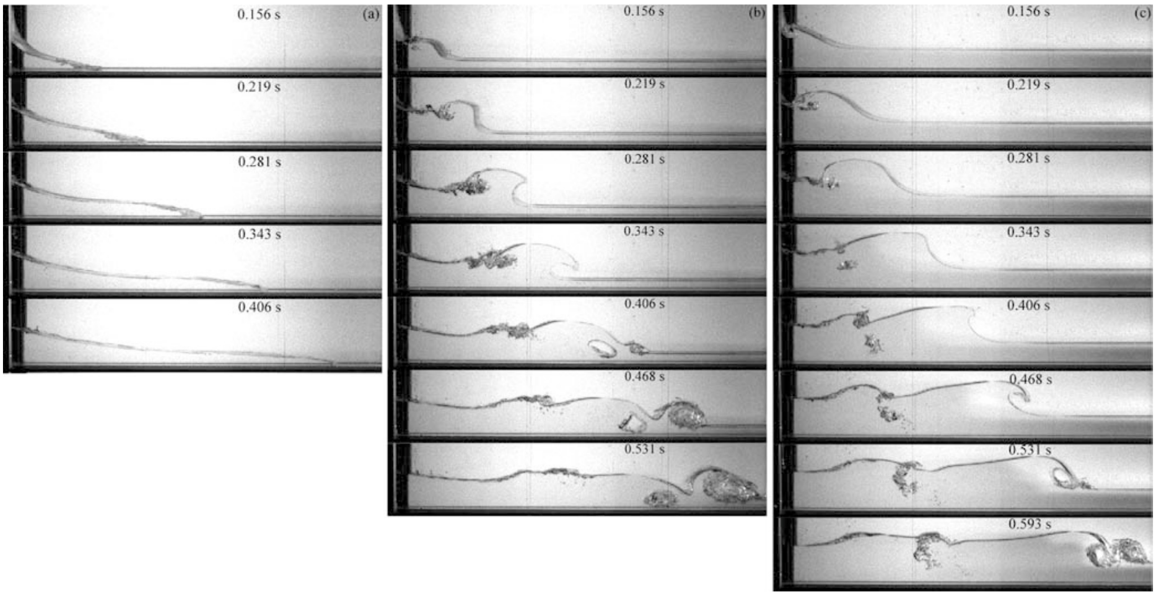

Figure 1.3: Sequences of snapshots ($66 \times 11\,cm^2$) after releasing fresh water from the lock in the dam-break experiment of Jánosi et al. (2004). The initial filling height in the lock is $d_0 = 15\,cm$ and the ambient fluid depth in front of the lock is (a) $d = 0$ (dry bed), (b) $d = 18\,mm$, (c) $d = 38\,mm$.

interface can be defined thin, and formulate an appropriate slip velocity $\vec{u}_{r\gamma}$ with the transition region being as thin as possible. The accuracy and convergence properties of some of these kernels have been discussed by Williams et al. (1998). This approach replaces the drawback previously described with the new difficulty in dealing with changes in interface topology and introducing spurious currents in the near region to the free-surface. Although it is common to neglect the influence of the relative velocity $\vec{u}_{r\gamma}$ in the momentum balance, and identify the volumetric flux $\vec{u}$ with the mixture mass velocity $\vec{v}$, we will retain the original form of the mixture model (1.14)-(1.20), which can be applied to study aeration processes at the free-surface, that usually appear in fluvial processes (i.e. hydraulic jumps). Moreover, as we shall see in § 1.5.3, the equation (1.16) for the propagation of the indicator function is analogous to that of sediment, and the same numerical technique can be employed to solve both equations.

The two numerical approaches described above for the computation of free-surface flows are traditionally known as *interface-capturing* methods because the computa-

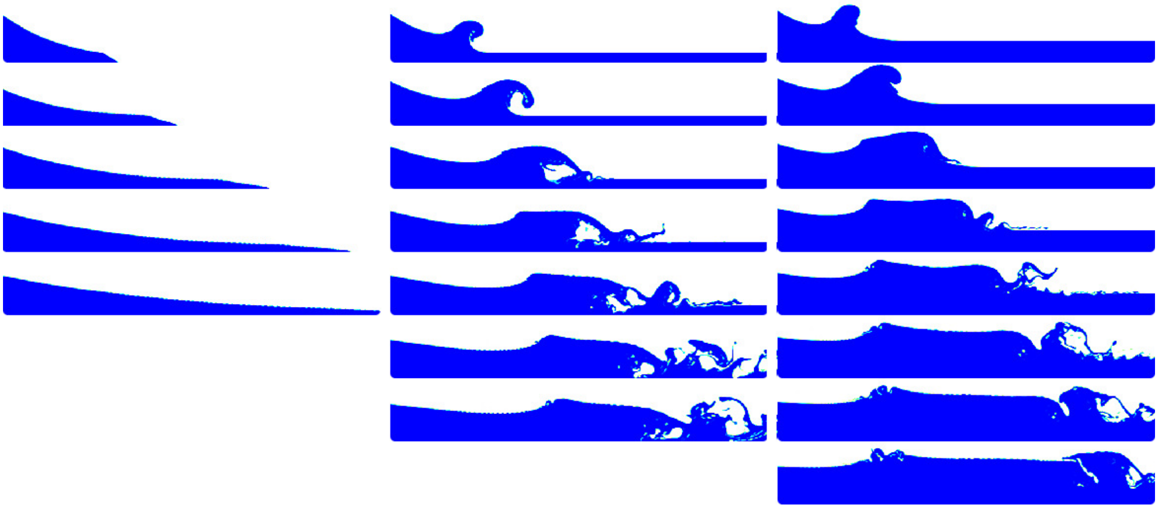

Figure 1.4: RANS numerical simulation of the experiments shown in Figure 1.3. The numerical solver rasInterFoam (OpenCFD Limited, 2007) was employed to compute the solution in a mesh with 1380×200 nodes.

tion is performed in a solution domain which extends over regions occupied by both fluids on a fixed grid. Interface-capturing methods suffer typical accuracy problems in the mass preservation constraint (Losasso et al., 2006). Since ϕ does not explicitly occur in any of the conservation equations, the original level-set method of Osher and Sethian (1988) do not exactly conserve mass. The imposition of a volume preservation constraint in the VOF method does not eliminate these errors, but instead changes their symptoms replacing mass loss with inaccurate mass motion leading to small pieces of fluid non-physically being ejected as jetsam or flotsam (see, for instance, the splashing at the end of the simulations shown in Fig. 1.4). Hybridation between VOF and LSM has been proposed (Sussman and Puckett, 2000) but the drawback is that both Eulerian method have similar difficulties as opposed to *interface-tracking* methods. Interface-tracking methods can follow the evolution of a simple interface very accurately (Muzaferija and Peric, 1998), advancing boundary fitted grids each time the free surface is moved. This lagrangian front tracking methods do not suffer from the typical accuracy problems characteristic of Eulerian methods. The drawback however is that the elements that make up the interface (segments or triangles in 2 or 3 spatial dimensions) can become highly distorted leading to a loss of accuracy. Moreover, if the interface changes topology, some difficult remeshing is required. When the flow conditions are such that there are no breaking or overturning waves, the interface-tracking method is a good approach.

To illustrate the VOF capabilities to simulate shallow-water flows, Figure 1.3 and 1.4 show the dam-break experimental results of Jánosi et al. (2004) and the numerical simulation, respectively. The overall agreement is good, although some discrepancies arise due to the idealisation of the gate release process and the appearance of flotsam. The gate release process in the initial stage of the dam-break problem constitutes a Fluid Structure Interaction (FSI) problem, requiring the addition of computational nodes in the fluid mesh during the numerical simulation. Although the software employed in this work allow us to study problems with topological changes in the mesh, we do not cover this topic. Mesh-free numerical techniques, e.g. Smooth Particle Hydrodynamics (SPH), readily deal with this kind of problems. In fact, Crespo et al. (2007) simulated the gate release process and found a better agreement in their results.

More sophisticated techniques are hybrid methods, that draw their accuracy from the tracked particles at the free-surface. For instance, particle level set method (Enright et al., 2005) derives the particle connectivity from the level set approach combining the best aspect of the LSM and the interface-tracking method. The result is a robust, accurate method that is simple to implement even in the three spatial dimensions (Mokhberi and Faloutsos, 2007). We refer to the reader to the following references for further details in any of these approaches: Losasso et al. (2006); Sethian and Smereka (2003); Ferzinger and Peric (2002); Sethian (2001) and Muzaferija and Peric (1998).

The applicability of the numerical method described above is limited to resolved-scale surface, i.e., a fluid interface with a characteristic length, other than the interface thickness, which is relative large to the computational grid cells. The treatment of multiscale surface phenomena (for instance, breaking waves, splashing and spray atomisation) usually requires the modelling of flow structures smaller than the grid cell. This kind of flows needs a special treatment that is not covered herein. The reader interested in this topic is referred to the recent thesis of Moses (2007) for further details.

1.5.2 Shallow-water equations for arbitrary slopes of the bottom

In the previous section, the conservation equations for a free-surface flow have been presented. In general, these equations are valid for any flow regime (laminar or turbulent) and any physical process (e.g. fluvial or coastal). However, in this work we are specially interested in fluvial hydraulic flows. River flows are usually characterised by turbulence and shallowness (the characteristic streamwise length L is much larger than the characteristic water depth η_0). Turbulent effects tend to uniform the vertical velocity profile, except in the near bottom region where viscous effects are no longer negligible. On the other hand, shallowness implies that the streamwise velocity is much larger than its vertical counterpart. An additional consideration, usually established in fluvial flows, is that the slope of the bottom bed is small. Under such considerations, the previous general formulation (§ 1.5.1) can be simplified given the well-known “non-linear shallow-water equations”.

The basis for most open-channel flow analyses is the non-linear shallow-water equations, and are attributable to de Saint-Venant (1871). They have been in engineering use for more than a century. Usually they are used for analyses of both steady and unsteady flows. The Saint-Venant equations can be derived by applying asymptotic approximations in terms of a shallowness parameter (i.e. the ratio of the typical vertical dimension to the characteristic length in the horizontal dimension, $\epsilon_s \equiv \eta_0/L \ll 1$) to the exact formulation of the flow problem (see Friedrichs, 1948). They represent the lowest order in approximation, and so they cannot retain accuracy when the channel bottom is appreciably curved. To obtain a more accurate solution in presence of high slopes of the bottom bed, Keller (1948) used the systematic method of Friedrichs (1948), obtaining higher-approximation equations for a nonlinear channel bottom in a rigorous manner. Thus, the small bottom slope objection (intrinsic to the traditional Saint-Venant equations) could be partly overcome by employing higher-order correction equations. However, all higher-order correction procedures are complicated, lengthy to solve the various sets of equations successively, and are rarely attempted to solve engineering problems.

Dressler (1978) derived a generalisation of the non-linear unsteady shallow-water equations containing explicitly the curvature of the channel bottom. To that end, a specific set of curvilinear coordinates attached to the bottom bed was employed in the derivation of his equations. Dressler's (1978) equations show that the velocity is no longer constant over any cross-section orthogonal to a curved bottom, and that the pressure expression contains terms, in addition to the hydrostatic term, which describe the effect of the streamline curvatures. Although his equations contain more terms and more complicated coefficients than the Saint-Venant equations, they are identical in structure and, therefore, they are as easy to solve by computer as the Saint-Venant equations. Recently, the guidelines of Friedrichs (1948) were followed by other authors to address again the question of varying topography (Berger and Carey, 1998; Keller, 2003; Rodriguez and Taboada-Vázquez, 2007)

1.5.3 Complex model for sediment transport with application to shallow-water flow

Multiphase theory has been developed and applied in many scientific fields, e.g. slurry flows, cavitating flows, aerosols, debris flows, fluidized beds, and so on. One could classify them according to the state of different phases or components and therefore refer to gas-solid flows or gas-particle flows or bubbly flows and so on. Multiphase flows are also a ubiquitous feature of our environment where one considers rain, avalanches, debris flow, sediment transport, and countless natural phenomena. Water-sediment-air interaction in shallow-water flows can be understood as a particular case of multiphase flow of three incompressible phases (when air is moving at low Mach number). However, few studies on sediment transport in fluvial hydraulic formally apply the multiphase theory (Pananicolaou et al., 2008). Many researchers propose governing equations without citing, or incorrectly citing, a reference for the basis for their equations - Anderson and Jackson (1967) as well as Ishii (1975) derived multiphase flow equations from first principles.

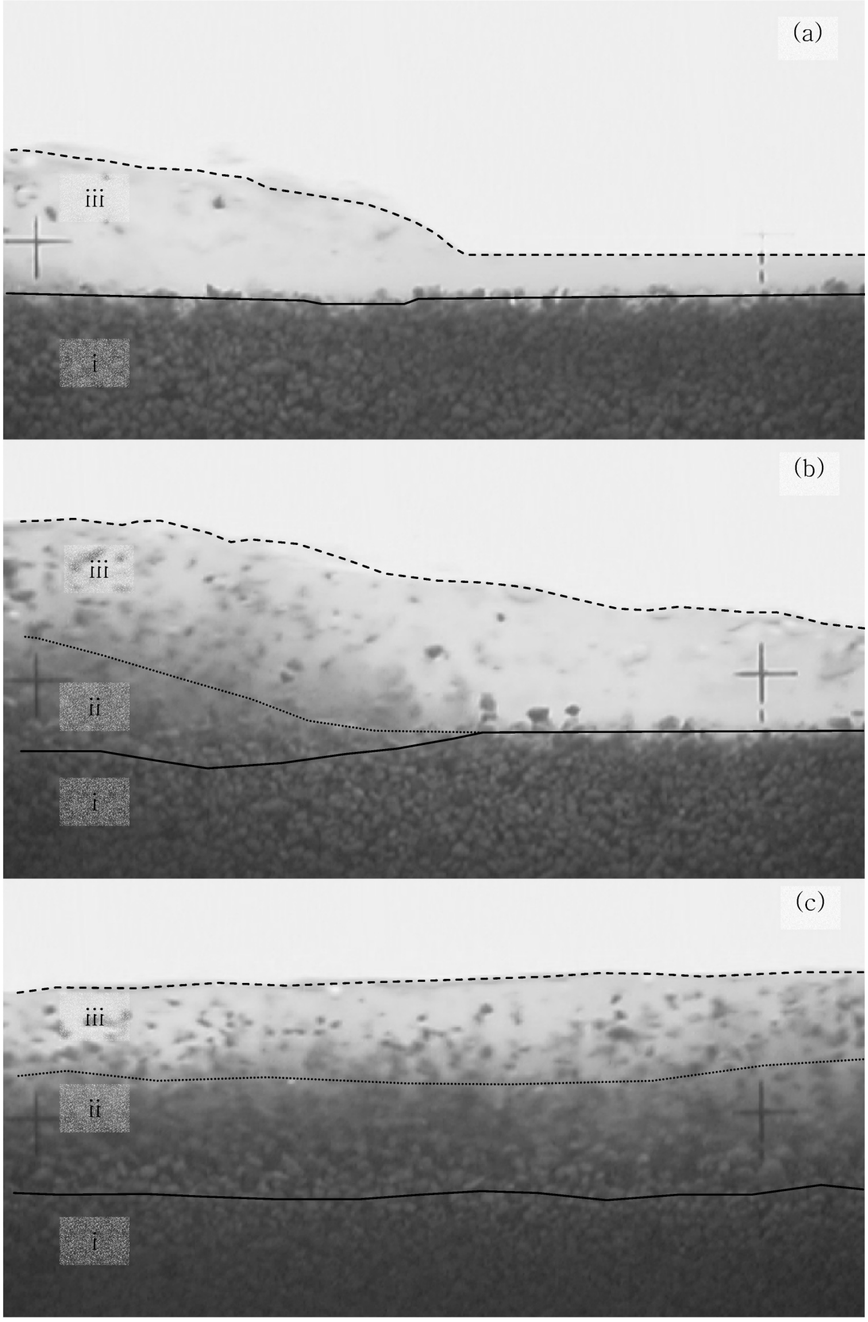

Figure 1.5: Dam-break flow on a horizontal channel from Ferreira (2005, Figure 3.1). Still image from a set of experimental tests performed at Laboratory of Hydraulics of the University of Beira Interior (UBI). Bed composed of pumice with $3\,mm$ of mean diameter and a density of $1500\,kg/m^3$. The initial water depth at the reservoir is $0.25\,m$; the downstream water depth is $0.025\,m$ and the camera is located at $0.5\,m$ from the gate. (a) time $t = 0.2\,s$. (b) time $t = 0.35\,s$. (c) time $t = 1.0\,s$.

Erosional dam-break flows, among many others unsteady fluvial processes, can experience diverse fluvial regimes: beginning with a flow of clear water, continuing with an erosional stage (which starts the 'conversation between the sediment and water'), and finishing with aggradation. So, the dynamic of the flood is affected by the intense transport of sediment. As an example, figure 1.5 shows three snapshoots of the dam-break experiments performed in the Laboratory of Hydraulics of the University of Beira Interior (Ferreira, 2005). This figure clearly depicts three steps: first, the flow of initial clear water and the formation of a hydraulic jump; second, the initiation of aggradation and transport of sediment in a transitory regime; and finally, a quasi-steady and uniform dense flow characterised with a continuum vertical profile in the sediment concentration, without a sharply defined boundary between bed-load and intermittently suspended load (Drake, 1986). Even for highly unsteady hyperconcentrated flows, as shown in Fig. 1.5, the sediment transport is traditionally modelled as the sum of two mechanisms (Pierson, 2005): *bed-load* (or *contact load*), which is the sum of all sliding or rolling particles that stay in more or less continuous contact with the bed, as well as the saltating particles that move close to the bed and are frequently in contact with it; *suspended load*, composed of fines (*wash load*) which form a stable suspension and intermittently suspended load which remain temporarily in dynamic suspension for long periods of time relative to their size during flow. Recent studies suggest that bed-load sediment may be transported in a concentrated zone of intense bed shear, that has been referred as a traction carpet (Hanes and Bowen, 1985; Sohn, 1997). A dense basal underflow layer has also been inferred from field relationships (Pierson, 2005). In water flows, this dense zone of moving bed material has been subdivided into two zones: an upper *saltation* zone and a lower *collisional grain flow* zone (Hanes and Bowen, 1985). A somewhat similar model is used to described motion within dry grain flows (e.g. Larcher, 2004; Armanini et al., 2005): it includes an upper *collisional zone*, which is characterised by large gradients in particle concentration and velocity, active grain collision, high granular temperature, and generation of dispersive pressure; and a lower *frictional* zone, which is a compact layer of slowly moving grains that are entirely in frictional contact with each other.

This example clearly shows the requirements of a general model to correctly predict the behaviour of shallow-water flows on beds composed of uniform and non-cohesive sediment. In the previous section, different approaches were presented for modelling turbulent shallow-water flows of a Newtonian fluid. Trivially, without additional modifications, this model is not able to predict the erosion, transport and sedimentation of solid particles. The eroded particles of sediment interact with the water modifying the properties of the ensuing mixture (i.e. the mixture density and viscosity), they affect the turbulent fluctuations of the velocity and pressure field, and also to the interaction not only with the pure water but with each other, etc. Additional complications arise when the sediment concentration value ranges from zero to its maximum value (the maximum packing factor), because the flow field experience both a turbulent and laminar regime, at the same time; moreover, the water-sediment mixture behaves as a non-Newtonian flow for sediment concentration values close to the maximum packing factor at both low and medium shear rates, due to the existence of yield stress (Huang et al., 2005; Huang and Bonn, 2007) for a dense flow at rest and the development of normal stresses when flowing (Zarraga et al., 2000; Ovarlez et al., 2006), respectively. Although rheological stratification (Armanini et al., 2005) appears in the traction carpet, the transition from a frictional to collisional regime cannot be sharply defined, as well as the border separating the bed and wash load (van Rijn, 1987), and so on. That is, the water-sediment mixture define a Continuum Field. The modelling of turbulence in dense suspensions is also a formidable task since four-way coupling takes place, i.e. turbulence is modified by the presence of solid particle at the same time that the collisions between particles affects its own movement (Muste and Patel, 1997; Muste et al., 2005). A general model for geomorphic processes, should take into account, at least, all these factors. Therefore, a Continuum Mechanics formulation based on first principles seems straightforward to couple all the physical phenomenas described herein.

The theory of multiphase flow is well established if all the species that conform the mixture are fluids (Ishii, 1975; Ishii and Hibiki, 2006). This theory accounts for the existence of the multiple deformable moving interfaces with their motions being unknown, the existence of the fluctuations of variables due to turbulence and to the motion of the interface, and the significant discontinuities of properties at the interface. These effects cause complicated coupling between the field equations of each phase, introduce a statistical characteristic and huge local jumps in various variables in space and time. To deal with these difficulties, the local instant details of the flow field should be filtered. By proper averaging, the multiphase theory is able to obtain the mean values of fluid motions and properties that effectively eliminate local instant fluctuations. The ensemble averaging introduced by Dopazo (1977) is one of the suitable averaging technique that can be employed in the derivation of the multiphase system conservation equations - the equivalence between this technique, the time averaging and Boltzmann statistical averaging can be found in Ishii and Hibiki (2006). The phase fraction α is defined at the number of times a particular phase is present at a certain point in time and space divided by the total number of realisations:

$$\alpha \equiv \frac{1}{N} \sum_{n=1}^{N} \chi_k = \frac{N_k}{N} \,, \tag{1.21}$$

where N is the total number of realisations, χ_k is a phase indicator function which is one when the phase k is present and zero otherwise. N_k is the resulting number of times at which the phase k was present at the particular point in time and space. Thus, the resulting phase fraction can be viewed as the *probability* that a certain phase is present at a certain point in space and time. Then, the Eulerian ensemble average of a general function f is defined by

$$\langle f \rangle(\vec{x}, t) = \frac{1}{N} \sum_{n=1}^{N} f_n(\vec{x}, t) \,.$$

It can be seen that, as such, the phase fraction does not fluctuate in a turbulent regime. That is, the definition of a volume averaging domain suitable for general turbulence multiphase flow cannot help but include contributions from the turbulence in the individual phases.

Being said that, the fact that multiphase and turbulence effects cannot be cleanly separated with valid time or volume averaging domains becomes evident. The essence of the problem is that, in the general case, the volume average and time average domains overlap. This is the reason why, in the more recent past, workers have abandoned double averaging in favour of a single, usually ensemble, average. They argue that the ensemble average is more fundamental than both the time and volume average, without introducing any spatial or temporal restriction into the final equations (Hill, 1998). In the double averaging technique, the *volume fractions* is first defined (as in the previous section) which is subsequently decomposed into mean and fluctuating components and time averaged. As a consequence, phase dispersion terms in the conservation equations appear, being this the main reason argued by proponents of double averaging to adopt it. However, dispersion is adequately predicted without the explicit presence of fluctuating volume fraction terms in the conservation equations but with the fluctuating velocity term (Simonin, 1990).

In presence of a solid phase, Anderson and Jackson (1967) derived the mass continuity and momentum balance equation for the solid phase in a solid-gas mixture from the equation of motion of each discrete particle. On the other hand, Ishii (1975) derive the multi-fluid model time averaging the local instant equations of each phase, and then introducing the unique axiom of his study: **the axiom of continuity**. The equations of Ishii (1975) and Anderson and Jackson (1967) differ in the momentum balance due to the particle shear stresses, being this difference significant near large gradients of sediment volume fraction (Jackson, 1997). Many researchers and commercial codes modify Ishii's (1975) equations to describe fluid-solid and gas-solid flows (e.g. Enwald et al., 1996). However, this fact does not affect the macroscopic flow behaviour, but do modify the predictions of both approaches on a local scale (van Wachem, 2000). In the solid-fluid approach (the Jackson's one), the solid-phase stress tensor is modelled with the kinetic theory. But in dense-suspensions, the fluctuating velocity of the fluid phase and its correlation with the properties of particles are negligible compared to particle-particle interactions (collisions and friction). Particle collisions are no longer instantaneous at very high solids volume fraction, as it was assumed in the kinetic theory (Zhang and Rauenzahn, 1997). Several approaches have been presented in the literature to model the frictional stress for dense packed particles, mostly originating from geological research groups (e.g. Johnson and Jackson, 1987; Johnson et al., 1990), although more recent studies in the field of Rheology show that the frictional shear stresses are purely viscous, that the mixture viscosity depends mainly on the sediment volume fraction (Huang et al., 2005; Ovarlez et al., 2006; Huang and Bonn, 2007), and that the frictional normal stress is proportional to the solid volume fraction and shear stress (Zarraga et al., 2000). It is now evident the complexity associated to a model that includes all the possible physical scenarios in a particulate multiphase system.

The first approach that can be adopted in the multiphase formulation is the multi-fluid model, that considers each phase separately. Thus, the model is expressed in terms of a set of conservation equations governing the balance of mass and momentum in each phase. However, the fields of one phase (i.e. its volumetric concentration, velocity and pressure field) are not independent of the other phase, and there are terms in these balance equations that represent this interaction. The ensemble averaged continuity and momentum balance equation for the k-phase (in our case, with $k = \{p, f, g\}$, where p is the sediment phase, f is the water phase and g is the air phase), in absence of mass transfer between phases, are (Drew, 1983):

$$\frac{\partial \alpha_k \rho_k}{\partial t} + \nabla \cdot (\alpha_k \rho_k \langle \vec{v}_k \rangle) = 0 \,, \tag{1.22}$$

$$\begin{gathered} \frac{\partial \alpha_k \rho_k \langle \vec{v}_k \rangle}{\partial t} + \nabla \cdot (\alpha_k \rho_k \langle \vec{v}_k \rangle \langle \vec{v}_k \rangle) = - \nabla (\alpha_k \langle P_k \rangle) + \nabla \cdot \left[\alpha_k \left(\langle \overline{\overline{\tau}}'_k \rangle + \langle \overline{\overline{\tau}}''_k \rangle \right) \right] + \\ \alpha_k \rho_k \vec{g} + \vec{M}_k \,, \end{gathered} \tag{1.23}$$

where $\overline{\overline{\tau}}''_k$ is the averaged turbulent stresses of the k-phase and the term $\vec{M}_k$ is the interfacial source term, given by

$$\vec{M}_k \equiv - \langle \overline{\overline{\tau}}' \cdot \nabla \chi_k \rangle \,. \tag{1.24}$$

The main contributions in the averaged inter-phase momentum transfer term $\vec{M}_k$ are due to drag, lift, virtual mass forces and Basset force. The expressions for some of these forces are revised, for instance, in Ishii and Hibiki (2006) and Rusche (2002).

As commented on above, the mass-weighted averaging removes the fluctuation term in Eq. (1.22) which describes the turbulent diffusion due to concentration gradients. All turbulent terms appear in the momentum equation (1.23).

The alternative to the model describe above is the *mixture model* (also known as *drift-flux model*) which considers the mixture as a whole, and therefore the field equations should be written for the balance of mixture mass and momentum. These equations are supplemented by a diffusion equation that takes account for the concentration changes of the disperse phase. It is clear that the drift-flux model formulation will be simpler than the multi-fluid model, however it requires some drastic constitutive assumptions causing some of the important characteristics of multi-phase flow to be lost. The mixture model is generally accepted where the dynamics of the components are closely coupled. The usefulness of the drift-flux model in many practical engineering systems comes from the fact that even multi-phase mixtures that are weakly coupled locally can be considered, because the relative large axial dimension of the systems usually gives sufficient interaction time (Ishii and Hibiki, 2006).

The main mixture properties are the mixture density (ρ), the ensemble averaged velocity of the mixture mass centre ($\langle\vec{v}\rangle$), and the ensemble-averaged volumetric flux ($\langle\vec{u}\rangle$), which are given by (see Chapter 5 for a formal deduction)

$$\rho = \rho_m \gamma + \rho_g (1-\gamma)\,, \tag{1.25}$$

$$\langle\vec{v}\rangle = \frac{1}{\rho}\left[\gamma \rho_m \langle\vec{v}_m\rangle + (1-\gamma)\rho_g \langle\vec{v}_g\rangle\right]\,, \tag{1.26}$$

$$\langle\vec{u}\rangle \equiv \gamma \langle\vec{u}_m\rangle + (1-\gamma)\langle\vec{v}_g\rangle\,, \tag{1.27}$$

where the density (ρ_m), the velocity of the centre of mass ($< \vec{v}_m >$) and volume ($< \vec{u}_m >$) in the water-sediment suspension are given by the following expressions:

$$\rho_m = \rho_p \frac{\beta}{\gamma} + \rho_f \left(1 - \frac{\beta}{\gamma}\right)\,, \tag{1.28}$$

$$\langle\vec{v}_m\rangle \equiv \frac{1}{\rho_m}\left[\frac{\beta}{\gamma}\rho_p \langle\vec{v}_p\rangle + \left(1-\frac{\beta}{\gamma}\right)\rho_f \langle\vec{v}_f\rangle\right]\,, \tag{1.29}$$

$$\langle\vec{u}_m\rangle \equiv \frac{\beta}{\gamma}\langle\vec{v}_p\rangle + \left(1-\frac{\beta}{\gamma}\right)\langle\vec{v}_f\rangle\,. \tag{1.30}$$

The definitions established above are functions of the solid particle volumetric concentration ($\alpha_p \equiv \beta$), the air volumetric concentration ($\alpha_g \equiv 1-\gamma$), and the liquid volumetric concentration ($\alpha_f = \gamma - \beta$) in the three-phases mixture. Thus, the equations (1.22)-(1.23) can be reduced to the mixture forms:

$$\frac{\partial \rho}{\partial t} + \nabla \cdot (\rho \langle \vec{v} \rangle) = 0\,, \tag{1.31}$$

$$\frac{\partial \gamma}{\partial t} + \nabla \cdot (\gamma \langle \vec{u} \rangle) + \nabla \cdot [\gamma(1-\gamma)\langle \vec{u}_{r\gamma} \rangle] = 0\,, \tag{1.32}$$

$$\frac{\partial \beta}{\partial t} + \nabla \cdot (\beta \langle \vec{u} \rangle) + \nabla \cdot [\beta(1-\beta)\langle \vec{u}_{r\beta} \rangle] = 0\,, \tag{1.33}$$

$$\frac{\partial \rho \langle \vec{v} \rangle}{\partial t} + \nabla \cdot (\rho \langle \vec{v} \rangle \langle \vec{v} \rangle) = -\nabla \langle p \rangle - \nabla \langle p_s \rangle + \nabla \cdot \langle \overline{\overline{\tau}} \rangle - \sigma \kappa \nabla \gamma - \vec{g} \cdot \vec{x} \nabla \rho\,. \tag{1.34}$$

The first equation (1.31) represents the mass conservation of the mixture, that behaves as a compressible fluid of density ρ. The second equation (1.32) expresses the conservation of the air phase, and captures the evolution of the interface through the phase indicator function γ. Similar to the VOF method introduced in § 1.5.1, the indicator function is convected at the ensemble-averaged volumetric velocity of the three-phase mixture $\langle \vec{u} \rangle$[1]. The relative volumetric flux $\vec{u}_{r\gamma}$ between the water-sediment mixture and the air phase is given by $\vec{u}_{r\gamma} \equiv \vec{u}_m - \vec{v}_g$. The third equation (1.33) establishes the conservation of the sediment particles. The first two terms on the left hand side (LHS) of this equation represent the convection of the sediment phase at the volumetric velocity of the mixture. The last term introduces the relative volumetric flux between the sediment and pure-water phases, denoted by $\vec{u}_{r\beta}$. This term is obviously indispensable to model the erosion and the sedimentation of solid particles, because the sediment particles do not travel attached to the water but move with respect to it at a different velocity. Therefore, in geomorphic processes $\vec{u}_{r\beta}$ cannot be neglected. Finally, the last equation (1.34) shows the momentum balance of the three-phases mixture. It includes analogous terms to that in abscence of sediment (1.15), with the addition of the shear-induced particle-phase pressure p_s that can be

---

[1] As the reader can figure out, the mixture variables defined in § 1.5.1 are ensemble-averaged variables because the multiphase flow occurred at the interface separating the water and air phases. However, when the relative velocity at the interface $\vec{u}_{r\gamma}$ is employed in the VOF method to compress the phase indicator function γ, the air volumetric concentration γ vanishes at the interface. Thus, we can drop (as we made in § 1.5.1) the brackets $\langle \cdot \rangle$ representing the ensemble average, which only has sense at the thin interface $0 < \gamma < 1$.

defined mechanically in terms of the laminar mixture viscosity and the shear rate (Zarraga et al., 2000). The generalised stress tensor $\overline{\overline{\tau}} \equiv \overline{\overline{\tau}}' + \overline{\overline{\tau}}'' + \overline{\overline{\tau}}''' + \overline{\overline{\tau}}''''$ accounts for the viscous stress tensor $\overline{\overline{\tau}}'$ (where the laminar viscosity depends, according to Ovarlez et al. (2006), only on the particle volume fraction and the laminar fluid viscosity), the turbulent stresses $\overline{\overline{\tau}}''$, and both the momentum-diffusion due to the relative motion of the sediment-water mixture with respect to the air $\overline{\overline{\tau}}'''$ and the sediment with respect to the water $\overline{\overline{\tau}}''''$. These two last tensor are defined as

$$\overline{\overline{\tau}}''' \equiv \gamma(1-\gamma)\frac{\rho_m\rho_g}{\rho}\vec{v}_{r\gamma}\vec{v}_{r\gamma} \quad \overline{\overline{\tau}}'''' \equiv \beta\left(1-\frac{\beta}{\gamma}\right)\frac{\rho_f\rho_p}{\rho_m}\vec{v}_r\vec{v}_r\,. \tag{1.35}$$

These tensors establish the first dependence of the rheology of dense suspensions on the mixture microstructure through the relative velocities $\vec{v}_{r\gamma}$ and $\vec{v}_r$ (which are related to $\vec{u}_{r\gamma}$ and $\vec{u}_{r\beta}$, respectively, see § 5.2 for further details). It is evident that the elimination of the air and sediment momentum equations from the formulation requires the kinematic relation between the phases. Therefore, the relative velocity between the phases should be given as a constitutive law.

One of the most noticeable effects of the relative velocity in the particle-fluid mixture is the difference arising between the mass velocities $\vec{v}$ and the volume fluxes $\vec{u}$, associated with the motion of the centre of mass and centre of volume, respectively. In fact, both are related by the slip velocities:

$$\vec{v} = \vec{u} + \gamma(1-\gamma)\frac{\rho_m-\rho_g}{\rho}\vec{u}_{r\gamma} + \beta s\frac{\gamma-\beta}{\gamma+\beta s}\frac{\rho_m}{\rho}\vec{v}_r\,. \tag{1.36}$$

Hence, the fact that the mass transfer is not necessarily accompanied by a similar volume transfer is now evident.

Now, that the multiphase framework has been described and particularised for fluvial hydraulic, the specific characteristics of the models developed by other authors can be discussed and readily understood. Several models for sediment transport in fluvial hydraulic have been formulated based on the theory of multiphase flows (e.g. Cao et al., 1995; Iverson and Denlinger, 2001; Iverson et al., 2001; Greimann and Holly, 2001; Muste, 2002; Jiang et al., 2004; Li and Yu, 2007; Wang et al., 2008).

For suspended sediments with large size or inertia, it was observed that a noticeable lag exists between the transport velocity of the sediments and that of the carrier water (Muste et al., 2005). Traditional sediment diffusion theory, that has become the main approach to quantify suspended-sediment transport, cannot deal with this effect. To take into account the sediment inertia and the sediment-sediment interaction, two-fluid models for solid-liquid flows have been applied to suspensions in open channels. Cao et al. (1995) applied double average technique to construct predictive equations for vertical profiles of sediment concentration and mixture velocity. Their analysis accounted for sediment-turbulence interactions, while sediment-sediment interactions were ignored.

Using a more fundamental averaging, i.e. the ensemble averaging, Greimann et al. (1999) developed analytical expressions for sediment concentration and lag velocity profiles; later, Greimann and Holly (2001) extended this formulation to flows with high concentration of sediments. In these two studies, sediment stresses as well as sediment-fluid velocity covariance were assumed, which resulted in rough prediction of the lag velocity.

A potentially more accurate description of the sediment transport process has been performed by using a kinetic model that has the unique advantage of specifying the constitutive relations for sediments. Closure of the solid-phase momentum equation requires a description for the solid-phase stress. When collisional interactions play an important role in the motion of the particles, concepts from kinetic gas theory (Chapman and Cowling, 1970) can be used to describe the effective stresses in the solid phase resulting from particle streaming (kinetic contribution) and direct collisions (collisional contribution). Constitutive relations for the solid-phase stress based on kinetic theory concepts have been derived by Lun et al. (1984) allowing for the inelastic nature of particle collisions. In this respect, the kinetic models may mitigate the shortcomings of the two-fluid ones in characterising sediment-sediment interactions. For example, Wang and Ni (1990, 1991) analytically reproduced sediment concentration and velocity profiles in a horizontal duct flow, respectively. Later, Ni et al. (2000) extended this formulation to dense flows. In a different way, Jenkins and Hanes (1998) constructed relations for sediment concentration and velocity profiles in highly concentrated sheet flows. Recently, Fu et al. (2005) developed a kinetic model for turbulent sediment laden flows. This model accounts for the effects of sediment-turbulence interactions as well as sediment-sediment collisions and have been adopted to quantify the underlying mechanisms of sediment diffusion, i.e., gravitational settling, turbulent diffusion, effect of lift force, and that of sediment stress gradient. Finally, Wang et al. (2008) presented a comprehensive analysis of suspended sediment transport in open channels under various flow conditions through a kinetic-model-based simulation, accounting for both sediment-turbulence and sediment-sediment interactions. Their model successfully represents experimentally observed diffusion and transport characteristics of suspended sediments with different densities and sizes.

Recently, Zhao and Fernando (2007, 2008) have solved the problem of scour around pipelines by using the two-fluid methodology. Their results show the capabilities of Continuum Mechanics for studying the transport of sediment, avoiding the employment of traditional depth-averaged discharge formulae.

Numerical flow simulation utilising a full multiphase model is impractical for a suspension possesing wide distributions in the particle size or density. Where the secondary phases cannot be ignored due to their influence on the fluid dynamics behaviour of the mixture, and the coupling between the phases is strong, the mixture model is a sufficiently accurate approximation of the multiphase system (Manninen et al., 1996). Due to the requirement of a strong coupling between the phases, the mixture model is more suited for liquid-particles mixtures than for gas-particle mixtures. Iverson (1997) and Iverson and Denlinger (2001) propose a mixture theory framework to describe flowing grain-fluid mixtures, and assume that motion of fluid relative to the solids is negligibly. This assumption is equivalent to neglect the relative velocities $\vec{v}_r$ and $\vec{u}_{r\beta}$ in our mixture model (1.31)-(1.34). Under this hypothesis, neither erosion, deposition, or lag velocities can be modelled. Moreover, the constitutive relations (1.35) for the stress tensor of the mixture are not taken into account. The discrepancy between the depth-averaged numerical predictions and the experimental results in water-saturated debris flows is pretty large (Iverson et al., 2001). Pudasaini et al. (2005) propose a model for debris flows down general channels by using the same simplifying hypothesis of constant mixture density and equality of phase velocities as Iverson and Denlinger, finding better agreement between the numerical simulations and the experimental results for the same experimental scenarios as in

Iverson et al. (2001). In the framework of sediment transport applications, Lalli et al. (2005, 2006) presented a constitutive equation, limited to a laminar regime, that includes the presence of particles in terms of the effective viscosity, which is defined by means of both Newtonian and non-Newtonian (Bingham plastic) models. They proposed a relative velocity equation closure based on particle buoyancy as well as on shear-induced self-diffusion effects (Leighton and Acrivos, 1987). Leighton and Acrivos (1986) shown that the viscous resuspension of a settled layer of particles can be described in terms of the shear-induced diffusion. Furthermore, the change in height of the settled layer when sheared, made dimensionless with the particle radius, was found proportional to an integral involving the shear-induced diffusion coefficient, the settling hindrance function and the shear viscosity. The constant of proportionality is a type of Shields parameter (Shields, 1936), a parameter which often arises in the study of the flow of sediment in rivers and tidal estuaries (e.g. Chanson, 2004). Furthermore, in non-dilute suspensions, the conjunction of shear-induced particle self-diffusion and a Newtonian model for the viscous tensor give rise to the microscopical modelling of a non-Newtonian fluid (Ovarlez et al., 2006), i.e. it is equivalent to a Bingham plastic model. These two facts indicate the proper modelling of the suspension microstructure and the capabilities of the model to account for erosion[2].

Mixture models have been broadly applied in the design of settlers (Ungarish, 1993). Notwithstanding questions of rigour, precision, well-posedness and completeness, the averaging procedures are a powerful tool for engineers and applied mathematicians, capable of explaining and predicting non-trivial phenomena. According to Drew (1983) this "... is the essence, a recommendation for a model that has many known features of two-phase flow dynamics. An enlightened investigator can use the model to make predictions ... It should never be used blindly, but with caution and careful examination of the results and implications". In most published applications of the mixture model, considerations have been restricted to gravitational or/and cen-

---

[2] In most sediment transport problems the flow is highly turbulent and, hence, in such system the viscous resuspension mechanisms play only a minor role except, perhaps, in the viscous sublayer which occurs near the boundaries of the flows.

trifugal forces (e.g. Brennan, 2001; Liu and Garcia, 2007). A more general approach can be developed, first, examining the instantaneous forces acting on a particle in suspension and, then, deriving the slip velocity using the dispersed phase momentum equation (Manninen et al., 1996). With this technique, a constitutive equation is required for the fluctuation terms of the slip velocity. To accomplish this, Manninen and coworkers postulate the following solution for the fluctuation terms (c.f. Ishii, 1975; Simonin, 1990):

$$\frac{D_{c\beta}}{\beta}\nabla\beta\,.$$

Because of its simplicity and applicability to a wide range of two-phase-flow problems of practical interest, the drift-flux model is of considerable importance. Particularly, the one-dimensional drift-flux model obtained by averaging the local drift-flux formulation over the cross-sectional area is useful for complicated engineering problems, since field equations can be reduced to quasi-one-dimensional forms (Ishii, 1977; Hibiki and Ishii, 2003). By area averaging, the information on changes of variables in the direction normal to the main flow within the channel is basically lost. The extensive review of this model is given by Ishii (1977). As commented on in § 1.5.4, this formal approach is uncommon to deduce the one-dimensional conservation equations of the mixture flow in fluvial hydraulic applications.

1.5.4 Extension of the shallow-water equations for sediment transport modelling

One-dimensional shallow-water models that include sediment transport have been used with some success in research and engineering practice. Most of the one-dimensional shallow-water models solve the differential conservation equations of mass and momentum of flow (i.e. the Saint-Venant equations) along with the sediment mass continuity equation (i.e. the Exner equation). Extension of one-dimensional models to two-dimensions is straightforward, and the discussion that follows is, therefore, limited to the simplest case, i.e. one-dimensional formulations.

One-dimensional depth-averaged geomorphic equations should be rigorously derived from the conservation equations of the mixture (1.31)-(1.34). However, it is common to find models in the literature that are deduced, after the establishment of phenomenological assumptions, from integral equation based on the Reynolds transport theorem. The specific formulation for the transport of sediment in one-dimensional shallow-water flows is therefore not unique, and relies on the particular assumptions established by each author. For that reason, and due to the extensive number of works in this matter, it is not possible to review the whole state-of-art. In its place, most significant examples (related with dam-break floods) are then discussed, depending on the coupling between the fluid and sediment phases conservation equations.

It can be said that the simplest, but not for this uncomplete, geomorphic model is such that accounts for the sediment transport just in two different layers, originating the two well-known modes of sediment motion: bed-load and suspended transport. So, three main regions are promptly identified in a longitudinal section of an alluvial channel, as it is shown in figure 1.5: i) the bed, composed of grains with no motion, where the shear stress τ_b acting at a point on the flow boundary is less than a certain "critical" value (τ_c) (corresponding to that point, see Chapter 4 for the definition of τ_b and τ_c); ii) a transport layer over the bed, where the grains are transported by sliding, rolling and saltating, being the *relative tractive force* or *relative flow intensity* $\eta_* \equiv \tau_b/\tau_c$ smaller than a certain value and larger than one; iii) an upper layer where the transported grains diffuse, by turbulence, into the remaining flow region, while some others are still transported in the form of bed-load. The total volume of grains passing through a flow cross-section per unit flow width and per unit time is the sum of the *bed-load rate* q_{sb} and the *suspended-load rate* q_{ss}, and is referred as *total transport rate* $q_s \equiv q_{sb} + q_{ss}$.

The transport continuity equation can be formulated in terms of the bed- and suspended-load rates (e.g. Yalin and Ferreira da Silva, 2001):

$$\alpha_{p,max}\frac{\partial z_b}{\partial t} + \frac{\partial q_{sb}}{\partial x} + \frac{\partial q_{ss}}{\partial x} + \frac{\partial hc}{\partial t} = 0\,, \tag{1.37}$$

where x is the streamwise coordinate, $\alpha_{p,max}$ (< 1) is the maximum packing factor of the sediment phase (the complementary of the granular material porosity), z_b is the bed level, h is the water depth in the direction of the gravity and c is the vertical averaged volumetric concentration in the suspended-load sublayer. This equation provides the evolution of the bed level as a function of each component of the total transport rate, the volumetric concentration of suspended sediment, and the water depth. To compute the bed-load rate q_{sb}, stage-discharge predictors for alluvial channels are usually employed (e.g. Vanoni, 2006). On the other hand, the suspended-load rate should be formulated in terms of the streamwise component of the depth-averaged velocity vector u ($q_{ss} = \alpha_c hcu$, with α_c being a near-to-unity coefficient called as non-equilibrium adaptation coefficient of suspended load). Additionally, the suspended-load transport equation is required to determine the volumetric concentration of suspended load:

$$\frac{\partial hc}{\partial t} + \frac{\partial hcu}{\partial x} = q_e - q_d \tag{1.38}$$

This equation balances for the sediment deposition and entrainment rates at the interface between bed-load and suspended-load layers, denoted by q_d and q_e, respectively. Hence, empirical formulas to determine these rates are also required by one-dimensional models.

To model the interaction of the flow with sediment transport and bed change, one can use the one-dimensional unsteady sediment-laden flow described by the generalised shallow-water equations (e.g. Wu and Wang, 2007):

$$\frac{\partial \rho h}{\partial t} + \frac{\partial \rho hu}{\partial x} + \frac{\partial \rho z_b}{\partial t} = 0\,, \tag{1.39}$$

$$\frac{\partial \rho hu}{\partial t} + \frac{\partial \rho hu^2}{\partial x} + \rho gh\frac{\partial z_s}{\partial x} + \frac{1}{2}gh\frac{\partial \rho}{\partial x} = -\tau_b\,, \tag{1.40}$$

where τ_b is the bed shear stress, that is usually computed with Manning, Chezy or Darcy-Weisbach frictional law. The water surface elevation $z_s \equiv z_b + \epsilon_b + h$ is to be computed as a function of the bed-load depth ϵ_b that depends on the bed-load formula one best to use.

By comparison of the variables involved in the geomorphic equations (1.37)-(1.40) and that of the mixture model (1.25)-(1.35), the following hypotheses intrinsic in the geomorphic model are clearly figured out: both the slip velocity of the sediment particles with respect to the water phase and the sediment particles inertia are neglected; small slope of the bottom bed is assumed, as well as a hydrostatic pressure distribution; erosion and deposition processes are modelled as point sources and sinks of sediment, respectively, and static laws are supposed to be valid in the computation of these volumetric fluxes. The first assumption implies an incorrect modelling of the general stress tensor $\overline{\overline{\tau}}$ of the sediment-water mixture, neglecting the momentum-diffusion stresses $\overline{\overline{\tau}}''''$. Moreover, the momentum interchange between water and sediment when sediment particles are eroded or settled are not accounted for. Therefore, one-dimensional models given by (1.37)-(1.40) do not properly describe the fundamental physics of the water-sediment multiphase flow under consideration. The hydrostatic pressure distribution in presence of sediment stratification is also no longer justified, and the formulation for small bottom slopes limits the applicability of the model when erosion may induce changes in the bottom bed of unpredictable magnitude. Although this kind of models is not universal, they however give good predictions when special care is taken in the calibration of the erosion and deposition fluxes, the bed-load predictor and the coefficients in the friction law, for the specific situation one desires to simulate.

In the particular case that the predominant mode of sediment transport is the bed-load one, the one-dimensional geomorphic equations described above can be simplified neglecting both the suspended-load rate q_{ss} and the suspended-load equation (1.38). An extensive analysis of the mathematical properties of the resulting system of equation, and the appropriate way of solving it was done by Hudson (2001). This option has been adopted by several authors in their studies to analyse, for instance, erosional dam-break problems (Capart and Young, 1998; Rosatti and Fraccarollo, 2006; Murillo et al., 2007), Tsunami originated by landslide (Castro-Díaz et al., 2008), and local scour around object (Liu, 2008). One advantage of this choice is the powerful mathematical tools available to solve non-homogeneous systems of hyperbolic partial differential equations. As commented on in § 1.2, in the last decades special attention has been focussed on the development of conservative numerical schemes for hyperbolic systems of partial differential equations (see Murillo et al., 2007; Castro et al., 2007). Thus, all this machinery can be employed to solve numerically the ensuing problem. Contrarily, if bed-load is expected to vanish with respect to suspended-load, one has to solve the complete system of partial differential equations (1.37)-(1.40) with

$q_{sb} = 0$ in (1.37). In this case, the mathematical problem remains hyperbolic, and the same numerical techniques, as in the previous case, can be employed. Examples of application are erosional dam-break flows (Cao et al., 2004; Wu and Wang, 2008; Bohorquez and Fernandez-Feria, 2008; Murillo et al., 2008) and Tsunami on a coastline (Simpson and Castelltort, 2006), among many others. Finally, more sophisticated approaches consider both bed- and suspended-load on the sediment transport associated with the flow movement (e.g. Fraccarollo and Capart, 2002; Wu and Wang, 2007).

Making a significant step forward with respect to depth-averaged mixture models, Pitman and Le (2005) have recently presented a novel depth-averaged two-phase model for debris flows and avalanches that contains mass and momentum equations for both the solid and fluid component. This implicitly provides equations for the velocities of both phases and for porosity. However, in this work the authors propose a numerical method only for a reduced system that ignores fluid inertial terms. Pelanti et al. (2008) present a mathematical and numerical two-phase granular flow model over variable topography that follows the approach of Pitman and Le. Ferreira (2007) propose a multi-fluid model with closure laws computed by means of the kinetic theory.

1.6 Thesis outline

The remainder of this thesis is organised as follows. Chapter 2 describes the one-dimensional hydraulic modelling of a dam-break flood on a steep incline. The subject has a long history and previous modelling efforts are summarised in a comprehensive literature survey. The discussion covers asymptotic analytical solution as well as numerical simulation. Differences arise due to the development of hydrodynamic instabilities at late time when a kinematic state is reached, which finally give rise to roll waves.

The Chapter 3 presents a linear stability analysis of a kinematic wave on an inclined plane by means of a linear near- and non-parallel spatial stability analysis, multiple scales, and the direct numerical simulation of small perturbations. Both stability analyses are checked against the numerical evolution of non-linear perturbations. The CFD methodologies used in this study, namely FVM and the finite differences methodology, are also presented.

Next, the one-dimensional modelling of the transport of suspended sediment associated with a dam-break flood on an inclined plane is discussed in Chapter 4. The transport of suspended sediment down the inclined bed is obtained and discussed as a function of the slope of the bed for different values of the parameters characterising the sediment and its transport properties. The relative importance of the bed-load (to the suspended load) sediment transport is also discussed as a function of the size of the sediment particles and the slope of the bed for different models on the initiation of sediment suspension from bed-load. We also check the dilute sediment approach and characterise the conditions for its failure.

The objective of Chapter 5 is to contribute to the development of three-dimensional mixture models, based on first principles, for the transport of sediment in free-surface flows. First, the literature related to the modelling of solid-liquid systems is reviewed. For completeness, correlations derived for liquid-liquid systems are also included in this study. A revised model for the mixture viscosity function at high phase fractions is put forward, which is based on recent experimental data. The performance of several models is assessed against experimental data for two test cases. Finally, novel results for a horizontal dam-break are presented.

Each of the Chapters starts by stating the governing equations. Then, the solution procedure is discussed by presenting the discretised equations together with the overall solution procedure. Finally, both methodologies are validated against suitable test cases.

Finally, in Chapter 6, the main findings and conclusions are summarised. Various outstanding issues are identified and suggestions for future research are given.

Chapter 2

One-dimensional dam-break flood on a steep incline

2.1 Introduction

It is well known that the hydraulic resistance, caused by stream bed friction and turbulence, strongly affects the propagation of a dam-break wave of a semi-infinite mass of fluid over a rigid horizontal boundary (Schoklistsch, 1917; Eguiazaroff, 1935; Martin and Moyce, 1952). This frictional effect predominates in the shallow front region of the flow, so called *tip region*, but can be neglected in the bulk of the flow. The experiments of Schoklitsch indicate that actual velocities for the fordward wave may be as slow as 40 percent of the theoretical results given by Ritter's (1892) solution. This behaviour was firstly analysed theoretically by Dressler (1952), and consecutively by Whitham (1955), leading both analytical studies to formulae which are in almost perfect agreement. The overall agreement between their theoretical results and the experiments conducted by Dressler (1954) was also satisfactory - the recent theoretical study by Hogg and Pritchard (2004) confirms this result. The importance of the hydraulic resistance in dam-break flows over a horizontal boundary has motivated further experiments (e.g. Lauber and Hager, 1998a; Jánosi et al., 2004) as well as analytical studies (e.g. Hogg, 2006) that consider the release of a finite mass of fluid. In the case of releasing a finite mass of fluid, it has been noted that hydraulic resistance continues playing an unnegligible role, but the applicability of the results by Dressler (1952), Whitham (1955) and Hogg (2006) reduces to very early times since the bulk flow pattern differs from the Ritter's one (Bohorquez and Fernandez-Feria, 2008).

The influence of the bed slope in dam-break processes is also of great interest, since the slope effect predominates over the resistance for moderately steep slopes (e.g. Lauber and Hager, 1998b; Nsom et al., 2000). The bed slope effect, in the dam-break problem of a finite mass of fluid on an inclined plane, was first analysed by Dressler. After establishing that "One can determine analytically the exact wave-front celerity (neglecting resistance) for the case where the bottom is inclined below the horizontal" (Dressler, 1952), he presented in 1958 an exact solution for ideal dam-break floods on an inclined plane "for slopes which are not excessive" (Dressler, 1958). Later, Hunt (1987) presented a similar solution. Since the earlier work of Dressler other solutions valid for steep slopes were obtained (Fernandez-Feria, 2006; Ancey et al., 2008). However, similarly to the horizontal problem, hydraulic resistance is unnegligible in floods over inclined planes. This fact was originally noted by Lighthill and Whitham (1955), who established that flood waves on inclined planes can be described as kinematic waves (i.e. waves in which a balance is struck between frictional and gravitational forces) for subcritical floods. In this case the hydraulic resistance affects not only the advancing of the fordward wave but also the bulk of the flow, when the flood travels approximately four times its initial extent (Hunt, 1982). Moreover, kinematic waves and dynamic waves are both possible together in supercritical floods (Lighthill and Whitham, 1955). In supercritical streams the kinematic and dynamic waves can play equally important parts, as in the case of *roll-waves* observed in mountain streams (as analysed by Dressler, 1954). This behaviour is radically different to that of an ideal wave, which constitutes a purely dynamic wave. Therefore, it becomes evident the importance of considering frictional effects in floods on inclines, questioning the applicability of ideal solutions to real scenarios. The hydraulic effect in a dam-break flood over an incline of small slope was firstly study analytically by Hunt (1982), and later in floods of a point-source of mass by Weir (1983) and Hunt (1984). Contrary to the ideal dam-break flood, Weir and Hunt's solutions claim that the resulting flow at late time does not depend on its initial configuration. This fact was corroborated by comparison of theoretical solutions with laboratory data. However, in the early stage just after the release of the water the non-linear shallow water equations are to be solved without any simplification. To this end, the use of numerical techniques (e.g. Soulis, 1992; Garcia-Navarro et al., 1999; Tseng and Chu, 2000; Hsu, 2002; Namin et al., 2004) was proven satisfactory by comparison with experimental data (WES 1961, Bellos *et al.* 1992).

This chapter is aimed to review previous analytical solutions for dam-breaks on small slopes, and reformulate them to steep slopes. We focus the analysis on the bulk flow as well as the tip region. These solutions will be then checked against the numerical simulation of the problem, so that their validity is established. As expected from the comment on Lighthill and Whitham (1955), we find roll-waves in our numerical simulations at late time and moderately high Froude numbers (more precisely, for Froude numbers larger than 2). We draw qualitative characteristics of roll-waves in floods on steep slopes based on the numerical results. Finally, some laboratory-based experiments for floods on steep inclines, in which roll-waves were observed, are shown, qualitatively supporting our predictions based on numerical simulations.

Preliminary results concerning this research were presented in Bohorquez (2007b,c).

2.2 Formulation of the problem

We consider here the one-dimensional flow over a constant slope bed. In the shallow-water approximation, the dimensionless equations for the mass conservation and momentum in the direction of the flow can be written as (see Fig. 2.1)

$$\frac{\partial \eta}{\partial t} + \frac{\partial \eta U}{\partial X} = 0\,, \tag{2.1}$$

$$\frac{\partial U}{\partial t} + U\frac{\partial U}{\partial X} + \cos\theta\frac{\partial \eta}{\partial X} = \sin\theta - \frac{s_f}{\eta}\,, \tag{2.2}$$

where θ is the angle between the bed and the horizontal, t is the time, X is the coordinate along the bed, η is the depth of the water measured along the coordinate Y perpendicular to the bed, U is the depth-averaged velocity component along X, and

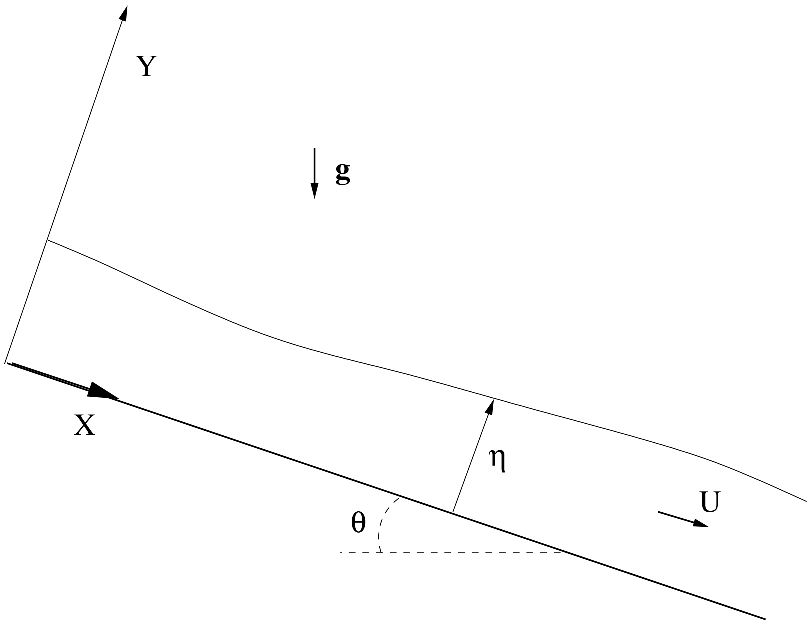

Figure 2.1: Sketch of coordinates and variables.

s_f is a dimensionless bed friction (see below). All the magnitudes in these equations have been non-dimensionalised with respect to a length scale η_0, corresponding to some initial depth, and a velocity scale $U_0 \equiv \sqrt{g\eta_0}$, where g is the acceleration due to gravity. Equations (2.1)-(2.2) are formally the same as the classical Saint-Venant equations for the shallow-water in a channel with small angle of inclination θ (Stoker, 1957). However, it can be shown (Dressler, 1978; Savage and Hutter, 1991; Bouchut et al., 2003; Keller, 2003) that these equations, written in the present coordinates X and Y (see Fig. 2.1), are valid for *any* slope $\tan\theta$ of the *constant-slope* bed, not just for small channel slope, provided that the characteristic length scale of the flow in the direction of the coordinate X is much greater than the characteristic length scale in the Y direction (shallow-water approximation).

To compute the friction term, $s_f \equiv (\tau_b/\rho U_0^2)$, where τ_b is the bed shear stress and ρ the fluid density, we shall use the Darcy-Weisbach friction factor f, so that s_f may be written as (Chanson, 2004)

$$s_f = \frac{f}{8}\,|U|U\,. \tag{2.3}$$

The factor f is a function of the local Reynolds number, based on the velocity U and the hydraulic diameter of the channel, and of the relative height roughness of the bed. To simplify the present analysis we shall assume that the friction factor f is constant to ease the analytical treatment of the problem under consideration.

We are interested here in the wave-front shape, and the advancing of the forward wave, of a point source of mass initially ($t = 0$) located at $X = 0$,

$$U(X, 0) = 0\,, \tag{2.4}$$

$$\eta(X, 0) = A\delta(X)\,, \tag{2.5}$$

where A is the released volume of water and $\delta(X)$ is the Dirac delta function.

We first consider as a test case the dam-break problem, i.e. the flow whose initial condition is given by (see Fig. 2.2)

$$\eta(X,0) = \begin{cases} 0 & \text{for } X < -1/e \\ eX + 1 & \text{for } -1/e \le X \le 0 \\ -X/e + 1 & \text{for } 0 < X \le e \\ 0 & \text{for } X > e \end{cases}\,, \tag{2.6}$$

where $e \equiv \tan\theta$ is the slope of the bed. At $t = 0$, the vertical wall that intersects the bed at $X = e$ is removed instantaneously, causing the fluid to move over the slopping bed under the action of gravity. In this case, we shall use the characteristic length η_0 as the dimensional depth at $X = 0$, $t = 0$, and the volume of water initially at rest is given by

$$A = \frac{1}{2}\left(e + \frac{1}{e}\right). \tag{2.7}$$

2.3 Perturbation solution

In the spirit of Weir (1983) and Hunt (1984), an asymptotic analytical solution can be found in the spreading of a mass of fluid (initially at rest) over an inclined plane at late time. In Hunt's solution, for small slopes of the bottom bed, he showed that the velocity and water depth field can be constructed by an asymptotic expansion in terms of the shallowness parameter ε_{Hunt} ($\equiv \eta_0/l$), which relates the characteristic

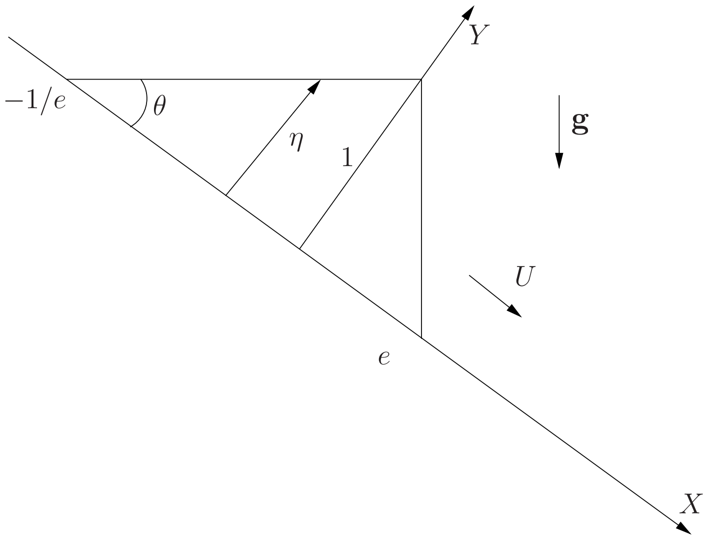

Figure 2.2: Coordinates and sketch of the initial conditions for $\eta(X)$ in the dam-break problem on inclines.

streamwise extent l occupied by the flood and the characteristic water depth η_0. Moreover, the solution does not depend on the initial configuration of the released fluid.

We can also take advantage of this fact to construct the solution for steep inclines, defining a scaling factor ε, and rescaling non-dimensional variables in § 2.2 with the relations that follow:

$$x \equiv X\varepsilon \tan\theta\,, \quad \tau \equiv t\varepsilon \tan\theta \sqrt{\frac{8}{f}\sin\theta}\,, \quad u \equiv U\sqrt{\frac{f}{8\sin\theta}}\,. \tag{2.8}$$

Thus, equations (2.1)-(2.2) now read as

$$\frac{\partial \eta}{\partial \tau} + \frac{\partial \eta u}{\partial x} = 0\,, \tag{2.9}$$

$$\varepsilon\left[Fr_{eq}^2\left(\frac{\partial u}{\partial \tau} + u\frac{\partial u}{\partial x}\right) + \frac{\partial \eta}{\partial x}\right] = 1 - \frac{u^2}{\eta}\,, \tag{2.10}$$

where Fr_{eq} is defined as

$$Fr_{eq} \equiv \sqrt{\frac{8}{f}\tan\theta}\,. \tag{2.11}$$

The *Froude* number, which states the local ratio of the flow velocity U to the wave celerity $c \equiv \sqrt{\eta\cos\theta}$, is given in the new variables (2.8) by

$$Fr \equiv \frac{U}{c} = Fr_{eq}\frac{u}{\sqrt{\eta}}\,, \tag{2.12}$$

and reduces to the constant parameter Fr_{eq} when a balance is struck between the friction of the bottom and the streamwise component of gravity, in other words, when ε can be neglected in the momentum balance (2.10).

To provide ε with physical sense, one can use a characteristic streamwise extent l to make non-dimensional equations, and one obtains the relation that follows between ε and l:

$$\varepsilon \equiv \frac{\eta_0}{l \tan\theta} \, .$$

According to Lighthill & Whitham (1955), kinematic waves are obtained by neglecting ε in (2.10). In view of this, the kinematic regime is attained when $\varepsilon \ll 1$, and it holds for $l \gg \eta_0/\tan\theta$. This means that, with small slopes of the bottom, the wave should travel a long distance downstream to reach the kinematic state, while for very large slopes ($\theta \to \pi/2$) only a very short distance is required.

Here, we are interested in kinematic waves, which are obtained when the parameter ε is small in the momentum balance (2.10), providing u and η, as well as their gradients, of order unity. In this case, the velocity and height can be expanded in powers of ε to find an asymptotic analytical solution:

$$u(x,\tau) = V(x,\tau) + \varepsilon V_1(x,\tau) + O(\varepsilon^2) \, , \tag{2.13}$$

$$\eta(x,\tau) = H(x,\tau) + \varepsilon H_1(x,\tau) + O(\varepsilon^2) \, . \tag{2.14}$$

Substituting this expansion in the momentum balance (2.10), and grouping terms of order $O(1)$, one has $V = H^{1/2}$. Similarly, from (2.9) it follows

$$\frac{\partial H}{\partial \tau} + \frac{3}{2}\sqrt{H}\frac{\partial H}{\partial x} = 0 \, , \tag{2.15}$$

showing that H and V remain constant for waves travelling with velocity $(3/2)H^{1/2}$.

The dam-break problem, whose initial condition for the height (2.6) reads in the present variables

$$\eta(x,0) = \begin{cases} 0 & \text{for } x < -\varepsilon \\ x/\varepsilon + 1 & \text{for } -\varepsilon \le x \le 0 \\ -x/(\varepsilon e^2) + 1 & \text{for } 0 < x \le \varepsilon e^2 \\ 0 & \text{for } x > \varepsilon e^2 \end{cases}$$

can be readily integrated using the kinematic equation (2.15), together with the initial condition shown above. Although the solution obtained by this approach is not valid for the initial stage, at late time the flow losses memory and the asymptotic expansion becomes more and more valid as time increases. Furthermore, after computing this solution, that is valid for *any* slope of the bottom, we will be able to analyse the discrepancy of other theoretical results obtained with the well known Saint-Venant equations, which are just appropriate for small bottom slopes. In order to present the results, and due to the fact that the scaling paremeter ε is arbitrary, we state ε in such a way that $x \equiv X$, i.e. $\varepsilon = 1/e$.

The resulting wave profile for the dam-break problem should be defined in two different regions: the first area (denoted by $\Re_I$) is enclosed by the two real characteristics $C_1 \equiv -1/e$ and $C_2(\tau) \equiv 3\tau/2$, and this region exists for any τ; the second region ($\Re_{II}$) ranges between the characteristic $C_2(\tau)$ and $C_3(\tau) \equiv (16e^2 + 9\tau^2)/(8e)$, and it exists just for $\tau \leq 4e/3$. After defining these two different areas the solution reads

$$H(X,\tau) = \begin{cases} e\xi_I(X,\tau) + 1 & \text{if } X \in \Re_I \\ 1 - \xi_{II}(X,\tau)/e & \text{if } X \in \Re_{II} \end{cases}, \tag{2.16}$$

with

$$\xi_I = \frac{1}{2}\left(e\hat{\tau}^2 + 2X - \hat{\tau}\sqrt{4 + e^2\hat{\tau}^2 + 4eX}\right), \tag{2.17}$$

$$\xi_{II} = \frac{1}{2}\left(2eX - \hat{\tau}^2 - \frac{3}{2}\hat{\tau}\sqrt{4e^2 + \hat{\tau}^2 + 4eX}\right). \tag{2.18}$$

being $\hat{\tau} \equiv 3\tau/2$. As in Hunt's (1982) solution, a shock must be inserted to satisfy the mass conservation requirement,

$$\int_{-1/e}^{X_s(\tau)} \eta(X,\tau)dX = A\,. \tag{2.19}$$

For simplicity, we give the location of the shock $X_s(\tau)$ just for $\tau > 3X_s/2$. In closed-form it is given by

$$\hat{\tau}\left(4 + e^2\hat{\tau}^2 + 4eX_s\right)^{3/2} = e^3\hat{\tau}^4 + 12X_s + 6e^2\hat{\tau}^2X_s + 6e\left(\hat{\tau}^2 + X_s^2 - 1\right). \tag{2.20}$$

Figure 2.3 depicts both the region $\Re_I$ (dashed-dotted line) and the region $\Re_{II}$ (dotted line) in a space-time diagram $\{X,\tau\}$ for $e = 1$. The border between these

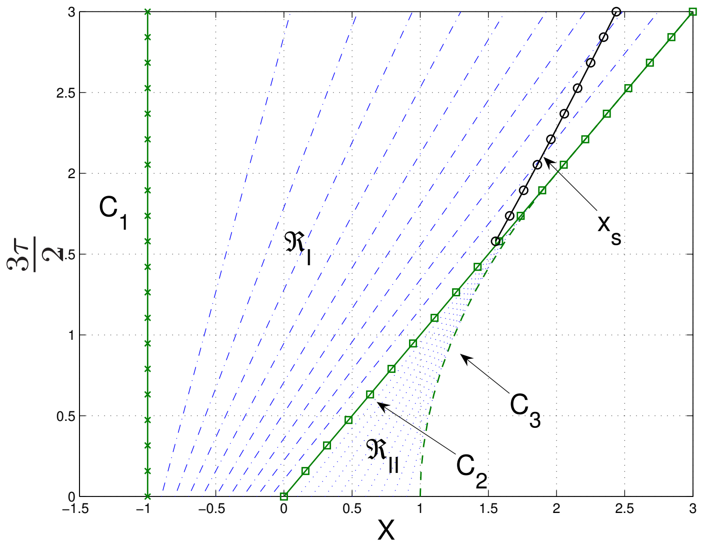

Figure 2.3: Characteristic curves in a space-time diagram for the dam-break problem in § 2.3 with $e = 1$.

two regions is established by the characteristic curve C_2 (solid, squared line). One should note the presence of the shock X_s (solid, circled line), which establishes the validity of the solution (2.16): on the right hand side of the shock the solution is no longer valid, and both the height and the velocity field vanish. The other two characteristics C_1 (solid, crossed line) and C_3 (dashed line) are also shown in the same figure.

A more simple solution can be deduced for the release of a point source of mass initially at rest, as defined in § 2.2 [see equation (2.5) for the initial condition]. As a matter of fact, the set of equations (2.9)-(2.10), together with the initial condition (2.5), is exactly the same as used by Weir (1983) and Hunt (1984), but they come from different dimensional equations. Therefore, the first conclusion to state is that *dimensionless Weir's (1983) and Hunt's (1984) solution is valid also for arbitrary slopes when non-dimensional variables are defined correctly.* Some details of the original study by Hunt (1984) are next reproduced, in order to create a self-contained manuscript.

The height field in the kinematic wave, called first-order *outer* solution, is given by

$$H(X,\tau) = \left(\frac{2X}{3\tau}\right)^2 \quad \text{for} \quad 0 \leq X \leq X_s(\tau)\,, \tag{2.21}$$

being the kinematic shock location X_s,

$$X_s(\tau) = \frac{3}{2}\left(2A\tau^2\right)^{1/3}\,, \tag{2.22}$$

and evaluating (2.21) at the shock (2.22), the shock flow depth holds:

$$H_s(\tau) = \left(\frac{2A}{\tau}\right)^{2/3}\,. \tag{2.23}$$

Next, the solution at the nose region, denoted by *inner* solution, is obtained after rescaling the streamwise coordinate:

$$\chi \equiv \frac{x - x_s}{\varepsilon}\,,$$

in which the continuity equation (2.9) and the momentum balance equation (2.10) read

$$\varepsilon\frac{\partial\eta}{\partial\tau} + \frac{\partial\eta(u - x_s')}{\partial\chi} = 0\,,$$

$$\varepsilon Fr^2\frac{\partial u}{\partial\tau} + (u - x_s')\frac{\partial u}{\partial\chi} + \frac{\partial\eta}{\partial\chi} = 1 - \frac{u^2}{\eta}\,,$$

respectively. Substituting the asymptotic expansion (2.13)-(2.14) in the equations shown above, and grouping terms of order unity, it follows $u = x_s'$ and

$$\frac{\partial H}{\partial\chi} = 1 - \frac{(x_s')^2}{H}\,. \tag{2.24}$$

Therefore, the velocity profile in the tip region is established uniform by the current solution. The above partial differential equation has as implicit solution (Hunt, 1984):

$$\chi_f - \chi = -H_{in} - (x_s')^2 \ln\left[1 - \frac{H_{in}}{(x_s')^2}\right]\,, \tag{2.25}$$

where $\chi_f(\tau)$ is the value of χ at which the nose of the shock intersects the channel bed.

The front location given by (2.22), and the previous result (2.20), has been plotted in Fig. 2.4 for a steep slope, in particular $e = 1$. Both solutions are directly

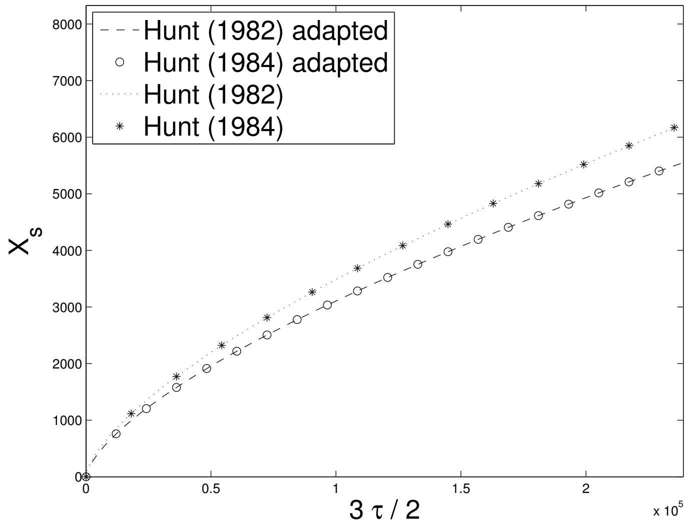

Figure 2.4: Temporal evolution of the water-front given by Eq. (2.20), dashed line, and Eq. (2.22), in circles, compared with the asymptotic result by Hunt (1982, 1984) for $e = 1$.

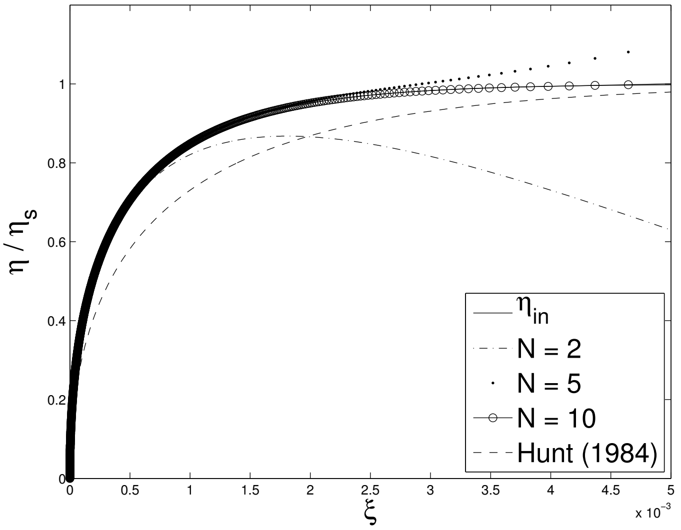

Figure 2.5: Asymptotic solution (2.28) for the height $\eta(\xi)$, made non-dimensional with respect the shock height η_s (2.23), for a given instant of time and several values of N. Also included is the inner solution by Hunt (1984), and the same but rewritten in correct non-dimensional variables (i.e. η_{in} given by Eq. 2.25). We have selected $\tau = 10^5$, $\eta_0 = 1m$, $e = 1$ and $f = 0.0223$.

comparable. We have also plotted the original asymptotic result provided by Hunt (1982, 1984) to quantify the effect of considering the Saint-Venant equations in spite of Eqs. (2.1)-(2.2). The solutions by this author becomes worse as time goes on because the slope e is not small.

2.4 Asymptotic analytical solution for the tip region

Whitham (1955) proposed an asymptotic analytical solution for the tip region of a dam-break flood on a horizontal plane. In the spirit of Whitham, we provide this section with the algebraical expression of the whole expansion for the advancing of a wetting front on an inclined plane.

If we define the variable $\xi = X_f(t) - X$, where X_f is the position of the wetting front, equations (2.1)-(2.2) read (note that $U > 0$)

$$\frac{\partial \eta}{\partial t} + (X_f' - U)\frac{\partial \eta}{\partial \xi} - \eta\frac{\partial U}{\partial \xi} = 0\,, \tag{2.26}$$

$$\frac{\partial U}{\partial t} + (X_f' - U)\frac{\partial U}{\partial \xi} - \cos\theta\frac{\partial \eta}{\partial \xi} = \sin\theta - \frac{f}{8}\frac{U^2}{\eta}\,, \tag{2.27}$$

where primes denote differentiation with respect to t. One can obtain a solution of the resulting equations in powers of ξ using the same expansion as Whitham (1955), which can be written as

$$\eta(\xi,t) = \sum_{j=0}^{N} \eta_j(t)\xi^{\frac{j+1}{2}}\,, \quad U(\xi,t) = \sum_{j=-1}^{N} U_j(t)\xi^{\frac{j+1}{2}}\,. \tag{2.28}$$

The first term in the above expansion for the velocity establishes a uniform velocity profile in the tip region, and taking into account that the particle velocity in the front should be the same as the wave-front velocity, one obtains $U_{-1} = X_f'$. On the other hand, drag forces caused by stream bed friction and turbulence predominate in the shallow tip region of the flow, while away from the front they are often negligible provided the fluid is *sufficiently deep*. Therefore, the effect of hydraulic resistance is to pile up the fluid near the wave-front, the wave has a vertical slope at the tip, and the particle acceleration, $\partial U/\partial t + (X_f' - U)\partial U/\partial \xi$, is expected to be finite there. Thus, to first approximation in the tip region, momentum balance (2.27) reduces to a more simple equation:

$$-\eta \cos\theta \frac{\partial \eta}{\partial \xi} = \eta \sin\theta - \frac{f}{8} U^2. \tag{2.29}$$

This last relationship is exactly the same as (2.24), which was rigorously deduced by asymptotic analysis techniques. Substituting (2.28) into the above equation, and grouping terms of order ξ, one obtains $\eta_0 = X_f'/2(f/\cos\theta)^{1/2}$. The reader should note that for small slopes of the bottom ($\cos\theta \approx 1$) this result is identical to the earlier solution by Whitham (1955), and that the streamwise gradient of the hydrostatic pressure hardly affects the height profile when we are close to the wetting front ($\xi \ll 1$). Analogously, the continuity equation (2.26) supplies the next term for the velocity, $U_0 = 0$. Repeating this process for the next exponents in ξ, first with the momentum equation (2.27), and then with the mass balance (2.26), the coefficients η_i and U_i are obtained explicitly. For instance, grouping terms $O(\xi^{1/2})$ in the mass balance provides $\eta_1 = 2(x_f'' - \sin\theta)/(3\cos\theta)$. All the coefficients can be obtained analytically:

$$U_N = \frac{1}{\eta_0}\left(\frac{2}{N+2}\eta_{N-1}' - \sum_{j=1}^{N-1} U_j \eta_{N-j}\right) \text{ for } N \geq 1\,, \tag{2.30}$$

$$\begin{aligned}\eta_N = &\frac{2}{N+2}\frac{1}{\eta_0 \cos\theta}\left[-\cos\theta \sum_{j=1}^{N-1} \frac{N-j+1}{2}\eta_j \eta_{N-j} - \sin\theta \eta_{N-1} + \frac{f}{8}\sum_{j=-1}^{N-1} U_j U_{N-j-2}\right.\\ &\left. + \sum_{j=0}^{N-1} \eta_j U_{N-2-j}' + \sum_{j=0}^{N-1}\left(-\eta_j \sum_{k=1}^{N+1-j} \frac{N-k-j+1}{2} U_{N-k-j} U_{k-1}\right)\right] \quad \text{for } N \geq 2\,.\end{aligned} \tag{2.31}$$

The asymptotic solution (2.28) was originally found by Whitham (1955) for a horizontal bed ($\theta = 0^o$), but this author only provided explicit expressions for the first few coefficients, just up to $N = 1$. Thus, the first result we must point out is that the velocity field, which actually converges even for $\xi > 1$ (see below), depends on ξ from the third term in the expansion, and therefore the assumption performed by Whitham "that U is nearly uniform in the tip region" (Whitham, 1955) is valid only until $O(\xi)$.

In order to check the asymptotic solution (2.30)-(2.31), and the approximate solution (2.25), we have selected a really large time in such a way that the current is lengthened enough to satisfy the kinematic wave approximation, and the location of the wetting front can therefore be evaluated with (2.22) under the kinematic wave hypothesis. So, we are able to compute the wave front velocity X_f' and next derivatives. As it is shown in Fig. 2.5, where the height η has been plotted as a function of ξ for a given t, the solution converges slowly as N is increased if ξ is not too small. In that figure we also include the original form of the tip region given by Hunt (1984), and the inner solution (2.25) valid for arbitrary bottom slopes. We find that expansion (2.28) is in agreement with the inner solution (plotted in continuous line) for $N \geq 2$. As a consequence, our results are directly comparable to those obtained by Hunt (1984) provided N is sufficiently large. In view of this, it is much easier to evaluate the wave front profile using (2.25) than the full expansion (2.28), and then the first alternative becomes really practical. Moreover, the validity of the present solution allows us to neglect accelerations in the momentum balance, and to establish the velocity profile nearly constant in the tip region. A lack of precision is obtained in the nose region for the height when using the Saint-Venant equations, as it is shown in Figure 2.5, where the height profile obtained by Hunt (1984) has been also plotted for such slope of the bottom. But our solution is actually valid for any constant slope.

2.5 Numerical simulation. Appearance of roll-waves

In previous sections the dependence of the wave-front shape with the wetting front velocity and diverse parameters governing the problem (bed slope e, and friction factor f or Froude number Fr_{eq}) has been established. Moreover, an asymptotic expression for the advancing of the forward wave has been proposed for any mass of fluid that reaches the kinematic regime, in particular the case of dam-break floods has been analysed. However, the non-linear character of the set of equations that governs the fluid movement [i.e, Eqs. (2.1)-(2.2)] allows multiple solutions for the same problem.

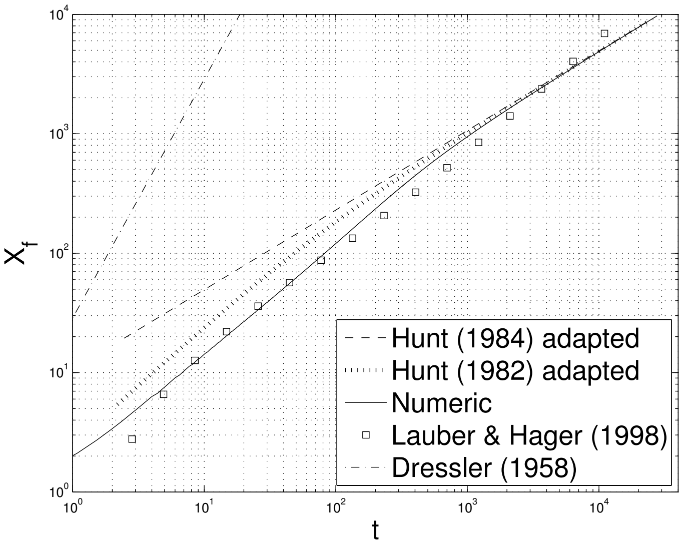

Figure 2.6: Temporal evolution of the wetting front obtained numerically compared with the asymptotic results valid for large time by Hunt (1982, 1984), and semiempirical results by Lauber and Hager (1998). This figure also shows the front location of the ideal flood: "the horizontal acceleration of these boundary ... is ... the true value $g \sin\theta \cos\theta$ for a particle sliding down an inclined plane without friction" (Dressler, 1958). We have selected $\eta_0 = 1m$, $e = 0.0175$ and $f = 0.0223$.

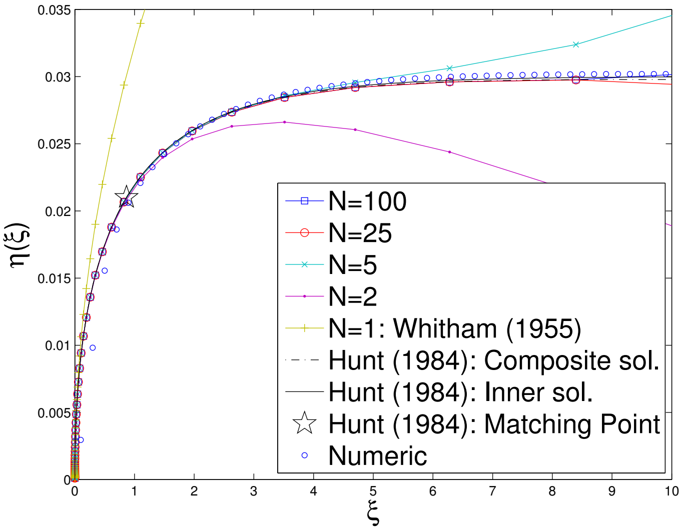

Figure 2.7: Asymptotic solution (2.28) for the height $\eta(\xi)$ for a given instant of time, $t = 4411$, for several values of N. The case $N = 1$ corresponds to the analogous solution given by Whitham (1955). Also included is the asymptotic solution by Hunt (1984) and the numerical one for the same conditions as in Fig. 2.6

The reader should think, for instance, in the development of roll-waves in uniform and steady flows on inclined plane beds (see Lighthill and Whitham, 1955; Brock, 1967, among others). Thus, if roll-waves developed when a quasi-steady and quasi-uniform flow regime is being reached (the kinematic wave), the flow pattern will become significant different, and the location and velocity of the wetting front will be deterministically unknown. Actually, Bohorquez and Fernandez-Feria (2008) have reported this fact for the dam-break problem on inclined plane beds. The main aim of this section is to introduce this new behaviour for the kinematic wave and report some qualitative features of the resulting flow pattern.

To that end, the set of equations (2.1)-(2.2), together with the initial conditions corresponding with the dam-break problem [Eqs. (2.4) and (2.6)], has been solved numerically on a uniform grid using an upwind TVD (total variation diminishing) method, second-order accurate in both space and time, with semi-implicit and upwind treatment of the source terms, as described by Burguete and García-Navarro (2001). The boundary condition used for the wetting front is a cut-off height ($\eta/\eta_{max} < 10^{-4}$), the Courant-Friedrich-Lewy number is $CFL = 0.45$, and the mesh size is $\Delta X = 0.2$.

Figure 2.6 depicts the location of the wetting front as a function of time obtained numerically, the asymptotic results (2.20) and (2.22), and the ideal forward wave (Dressler, 1958). On earlier time, the kinematic regime has not been reached yet, and the kinematic solutions overestimate the wetting front velocity. As time goes by, the agreement between the numerical experiment and the kinematic shock position is better, while the ideal solution diverges more and more. This reveals the reduction of front velocity due to drag effects, according to the semi-empirical results of Lauber and Hager (1998b), also drawn in the same figure. As we stated before, the forward wave corresponding with the ideal or inviscid case is far from the physical one. This fact corroborates the fundamental importance of hydraulic resistance in floods on inclines.

In the tip region, it is found that the asymptotic expansion compares well with the numerical solution (circles plotted in Fig. 2.7). The agreement between (2.25) and (2.28) is better and better as N increases, the expansion (2.28) converges to the inner solution (2.25) for large N. From the matching point (big star) to the right hand side, the inner and the *composite* solution (dashed-dotted line) by Hunt are almost identical, and we need quite a lot terms in the expansion (e.g., $N > 25$) to obtain a similar result. It is also noted the low-precision solution for the case $N = 1$ (the original one by Whitham), which is only applicable in the very proximal distance to the wetting front.

However, the main feature of real flood waves on steep inclines in relation to the predictions of the asymptotic solutions is the appearance of roll-waves. The evolution of the velocity profile at several instants of time for the dam-break problem is addressed in Figure 2.8, corresponding to the same case as in Fig. 2.7. Continuous line shows the numerical solution, while the velocity profiles associated to the water-depth asymptotic solutions (2.16) and (2.21) have been drawn in circles and stars, respectively. As time rises, the kinematic wave approximation becomes more and more valid, but instabilities develop just from numerical noise and the resulting velocity field is rather different. It is found a velocity field composed by the kinematic wave solution and additional roll-waves. The onset of these roll-waves is located in the bulk of the flow (see Fig. 2.9), far from the tip region. As time goes on, their amplitude grows, developing at the end saturated hydraulic-jumps, which travels convected towards the wetting front. This behaviour, termed ‘competition’ between kinematic and dynamic waves, is that figured out by Lighthill and Whitham (1955) half a century ago! The flow changes from a quasi-uniform and quasi-steady state to highly unsteady. We found the occurrence of roll-waves just for supercritical flows - moreover, for $Fr_{eq} > 2$ (the exact value is analysed in the next Chapter). In contrast, when $Fr_{eq} < 2$ we did not find the formation of roll-waves, and thus the kinematic wave describes with accurate precision the flow pattern. This behaviour is analogous to that observed in naturally developed roll-waves on uniform streams in mountain regions and artificial channels (e.g. Cornish, 1934; Brock, 1967; Brauner and Maron, 1982). Finally, it should be pointed out that when roll-waves overtake the wetting front, they disappear but affecting the water-depth profile at the tip region, that is adjusted to the local velocity in the roll-wave velocity profile evaluated at the wetting front (see Fig. 2.10). Thus, the forward wave acquires a pulsating behaviour, which is better appreciated in the simulations shown in Chapter 4 with very large

Froude numbers.

2.6 Roll-waves in field-based experiments in floods on steep slopes

Figure 2.11 depicts three snapshoots of roll-waves observed in clear water dam-break flood over an straight inclined channels of (constant) steep slope. These pictures correspond to the experiments done the dates 08/30/1994, 08/28/2002 and 06/07/2006 (as noted in each photo) at the USGS Debris-Flow Flume. This information was extracted from the Video Documentation of Experiments at the USGS Debris-Flow Flume 1992-2006 (Logan and Iverson, 2007). At the top of the three images, roll-waves are clearly observed along the horizontal prolongation that enlarges the end of the inclined flume. The waves grow on the left-hand side of the picture, maybe denoting some inclination of the bottom channel towards the left bank. This hypothesis is also funded on other dam-breaks experiments performed in the same flume, but employing a mixture of sand, bed and loam instead of clear water (e.g. experiments dated 09/12/2006), in which the mixture flows along this side[1]. In the middle and at the bottom of the three pictures, the plan view of the inclined flume end (without prolongation) shows the evolution of roll-waves when discharging over a horizontal boundary. In absence of data field measures, we are happy to show at least that the phenomenon of roll-waves in floods on inclines has been reported in physical experiments. This is the physical evidence of our numerical predictions previously presented.

2.7 Summary and conclusions

In this chapter we have considered the effects of hydraulic resistance on the dam-break flood over an inclined plane of arbitrary but constant slope of the bottom bed.

---

[1] The reader has open access to the complete version of the films following the link displayed in the bibliography.

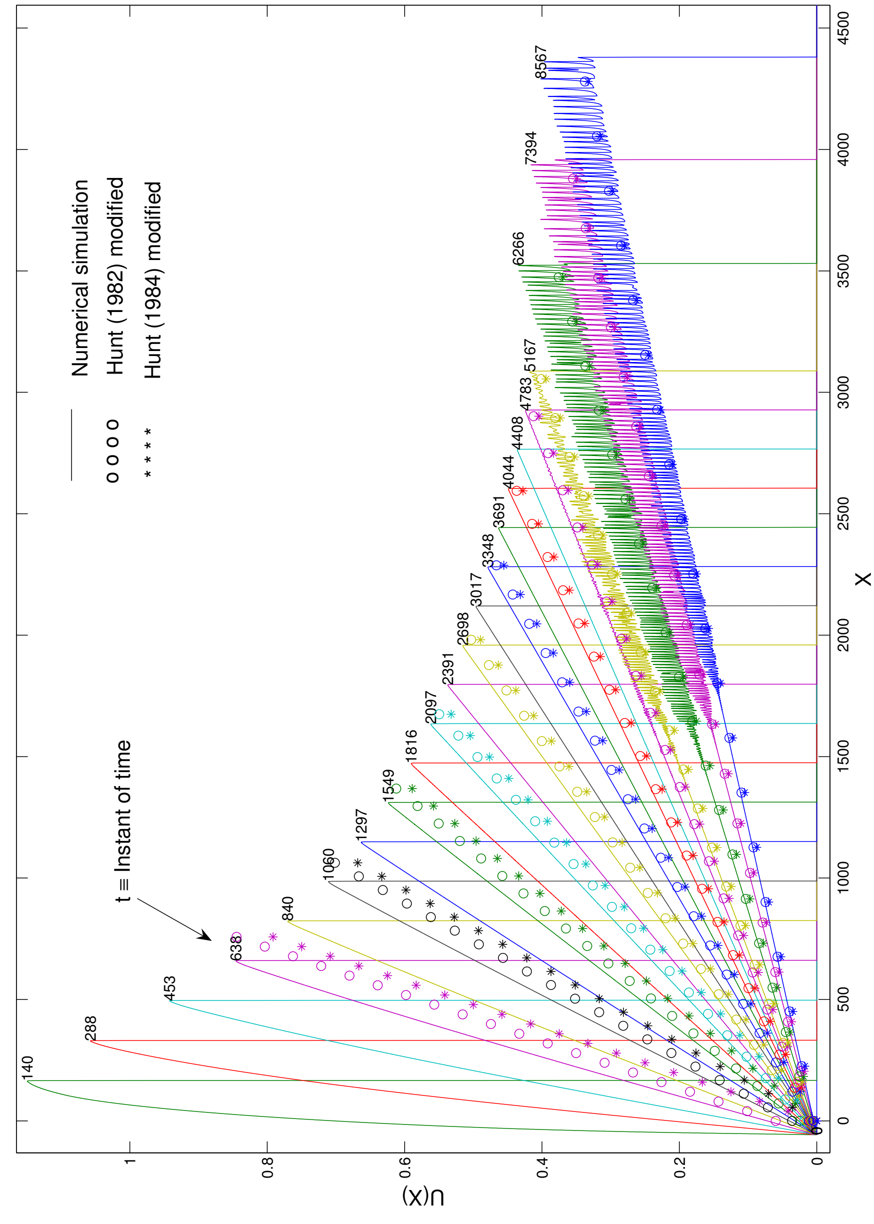

Figure 2.8: Velocity profiles at several instants of time for the same case as in Fig. 2.7. In continuous line is plotted the numerical solution, and in circles and stars the velocity profile corresponding to the asymptotic height given by (2.16) and (2.21), respectively.

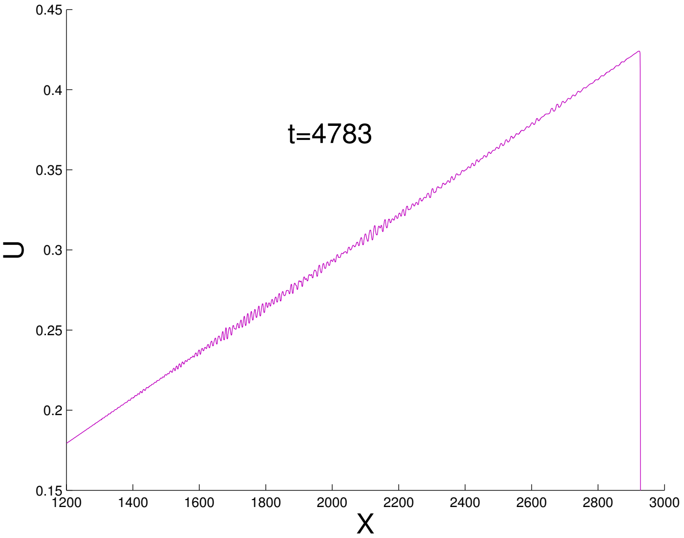

Figure 2.9: Detail of the velocity profile at $t = 4783$ from Fig. 2.8.

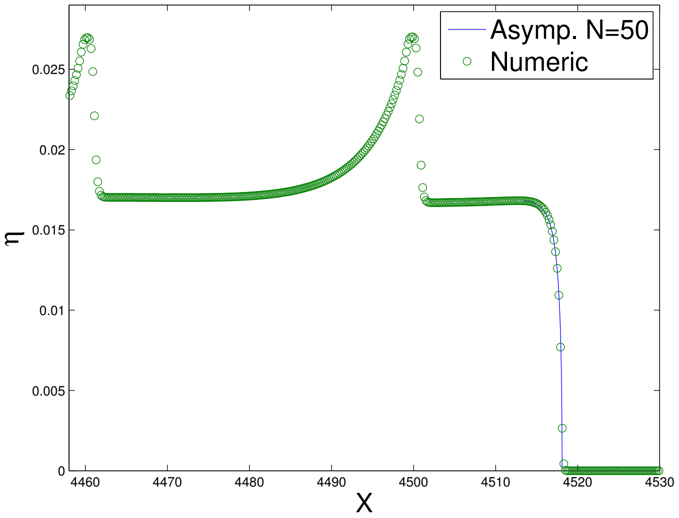

Figure 2.10: Height profile at $t = 8960$ for the same case as in Fig. 2.7. In circles is plotted the numerical solution, and in continuous line the asymptotic expansion in § 2.4.

Figure 2.11: Roll-waves in clear water dam-break flood, observed in the experiments at the USGS Debris-Flow Flume (Logan and Iverson, 2007).

To gain some inroads into this problem, we have considered turbulent flows governed by the one-dimensional shallow-water equations, and we have limited our study to late times, in which the suddenly released, fixed mass of fluid lengthens and reaches a kinematic state.

For a suddenly released mass of fluid and an initial dam-break configuration over an inclined plane, the theoretical location of the wetting front has been supplied in the kinematic wave regime, together with the velocity and water-depth field. One of the most noticeable effects of the results for large slopes of the bottom is the divergence of the previous solution by Hunt (1982, 1984), who provided a similar asymptotic solution using the traditional Saint-Venant equations. This divergence arises mainly because the whole gravity g moves the fluid when the Saint Venant equations are used, instead of its projection along the perpendicular to the plane. The results for *any mass of fluid* that spreads on a plane bed are identical to those reported by Weir (1983) and Hunt (1984) in terms of a specific set of non-dimensional variables.

We have also considered the analysis of the shape of the flood in the tip region. The solution has been obtained as a full expansion in terms of the streamwise coordinate located at the wetting front. Our results are directly comparable to those obtained by Hunt (1984) when we use enough terms in the expansion.

We have also solved the shallow-water equations (with the appropriate initial conditions) using an upwind TVD method, second-order accurate in both space and time, with semi-implicit and upwind treatment of the source terms. We find that the asymptotic analytical solutions and the numerical simulations are in almost perfect agreement, except for Froude numbers larger than two due to the development of roll-waves. The accuracy of the numerical solution has been also checked, and very good results are obtained by just using a cut-off height as boundary condition for the wetting front. The existence of physical instabilities in floods on steep inclines was illustrated.

Finally, we note that the solutions developed could be used to check, for instance, the precision of other numerical schemes or boundary conditions.

Chapter 3

Roll-waves in flood on an inclined plane

3.1 Introduction

‘A thin layer of water-flowing down an inclined surface, may undergo, in some circumstances, a transition to an oscillatory movement where a train of surface waves propagates downstream’. The development of roll-waves happens for large Reynolds numbers, typically above 400 for quasi-2D roll-waves and above $1,200$ for roll-waves for turbulent flow. In this region of large Reynolds numbers the flow can be assumed to be potential except for a viscous boundary layer on the wall. The velocity is therefore assumed to be independent of the cross-stream coordinate leading to the shallow-water or Saint-Venant equations (de Saint-Venant, 1871; Whitham, 1974). The evolution of the surface is governed by a sequence of transitions starting from the primary instability of the plane-parallel flow, filtering mechanism of the linear instability and secondary modulation instability that converts the primary wave field into a roll-wave.

Experiments by Alekseenko et al. (1985) and Brauner and Maron (1982) indicate that waves at inception near the channel entry are indeed well described by the linear theory. However, for conditions far from criticality where the linear growth rate is significant, these waves quickly grow in amplitude and wavelength as they travel downstream (Prokopiou et al., 1991). Beyond an entry length of about 500 times the water-depth, the waves reach a permanent form and travel downstream without discernible changes in speed and shape. These so-called *naturally developed roll-waves* differ from that artificially excited waves (here referred *permanent roll-waves*), which reach their permanent form immediately without an entry region.

The numerical study of Brock (1970) indicates that continuous finite-amplitude waveforms do not exist for Dressler's (1949) shallow-water theory. To remedy this, Needham and Merkin (1984) have added an empirical second-order dissipation term to Dressler's equation in order to model the 'normal shear'. They showed that periodic waveforms were then possible. The solitary waves speed at one and a half time the Nusselt flat-film velocity, comparing favourably to the data of Brock, and Brauner and Maron (Needham and Merkin, 1984; Hwang and Chang, 1987). The normal shear contribution, which Needham and Merkin attempted to model empirically, was derived from first principles by Prokopiou et al. (1991), showing that the non-linear shallow-water equations still do not allow the construction of finite-amplitude periodic waves. This is so because the dissipation term sought by Needham and Merkin remains absent when surface tension is negligible. Prokopiou *et al.* extended Alekseenko *et al.*'s integral boundary-layer theory, and found in their weakly non-linear study a family of periodic waves near the onset. They also shown by comparison to experimental data that the well-developed waves approach the solitary wave limit at large Reynolds number with wave frequencies much smaller than that corresponding to the linear maximum-growing mode. The periodic waves are then sensitive to subharmonic disturbances (which is consistent with Brauner and Maron's experimental observation), and a period-doubling cascade is an important component of the evolution to solitary waves.

It is important to realize the limitations of the non-linear shallow-water equations to quantify the onset of roll-waves. They ignore all disturbances of a small wavelength, such as gravity and capillary waves. The travelling wave solutions analysed by the shallow-water equations are the long ones which appear for $Fr > 2$ (e.g. Jeffreys, 1925). Consequently, thin steady waves which have also been observed at low Froude numbers (and low Reynolds numbers) cannot be described by this analysis (e.g. Usha et al., 2006). However, long waves have been widely studied in fluvial hydraulic by means of the Saint-Venant equations (e.g. Brock, 1967; Foley and Vanoni, 1977; Julien and Hartley, 1986; Chen, 1995; Zanuttigh and Lamberti, 2002; Liu et al., 2005; Di Cristo and Vacca, 2005; Bohorquez and Fernandez-Feria, 2006; Balmforth and Mandre, unpublished).

The effect of bottom topography on linear stability of turbulent flow over uneven surfaces was recently explored by Balmforth and Mandre (2004). Balmforth and Mandre found that low-amplitude topography destabilises turbulent roll-waves and lower the critical value of the Froude number required for instability. In a general case on curved solid walls, roll-waves whose amplitudes remain small at all distances from their origin are possible, and the slope of the wave profile is no longer constant but varies slowly in the streamwise direction (Kluwick, 2006).

The analysis presented herein endeavours to apply the theory of linear stability to the set of equations governing the motion in open channel flow. First, we consider a non-parallel spatial stability analysis of the one-dimensional kinematic waves with turbulent friction down an inclined plane (Bohorquez and Fernandez-Feria, 2006; Bohorquez, 2007a). The main features introduced here that have not been considered before are that non-parallel effects originated from the slow streamwise variations of both the basic flow and the perturbation are taken into account. At this stage, the influence of temporal variations on the basic flow is neglected. We find that a bifurcation occurs in the stability diagram when small non-parallel effects are taken into account, so that the critical parameters at which roll-waves are predicted to occur in a non-uniform flow may be substantially lower than for a uniform flow. This result is then checked against the exact solution of the linear perturbation equations for the Froude number $Fr = 2$. The exact solution is obtained by means of multiple scales and shows that, independent of the wavelength or the wave frequency, perturbations always decrease. The discrepancy between the exact and the nonparallel spatial stability analysis is found pretty large, showing the unnegligible importance of time-varying characteristic of the basic flow in the stability analysis (Bohorquez, 2007c). The non-linear behaviour of the perturbations, obtained with the direct numerical simulation of the non-linear shallow-water equations, corroborates this fact.

3.2 Non-parallel spatial stability analysis

Here we shall analyse the spatial stability of a flow governed by Eqs. (2.1)-(2.2). To that end, if $\eta = H(X,t)$ and $U = V(X,t)$ are solutions to these equations, the perturbed flow is decomposed, as usual, as the sum of the basic flow solution, H and V, plus a small perturbation, $\eta'(X,t)$ and $U'(X,t)$,

$$\eta = H + \eta', \quad U = V + U', \tag{3.1}$$

where the amplitude of the (non-dimensional) perturbations satisfy the conditions

$$|\eta'| \ll H, \quad \text{and} \quad |U'| \ll V\,. \tag{3.2}$$

We also assume that the streamwise variation of the basic flow is small,

$$\left|\frac{\partial H}{\partial X}\right| \ll 1\,, \quad \left|\frac{\partial V}{\partial X}\right| \ll 1\,. \tag{3.3}$$

Substituting (3.1) into (2.1)-(2.2), taking into account that $[H, V]^T$ is a solution to the equations (superscript T denotes transposed vector), and neglecting second order terms in both the small perturbations and the streamwise derivatives of the basic flow, one is left with the following set of linear equations for the perturbations:

$$\frac{\partial \eta'}{\partial t} + \frac{\partial HU'}{\partial X} + \frac{\partial \eta' V}{\partial X} = 0, \tag{3.4}$$

$$\frac{\partial U'}{\partial t} + \frac{\partial VU'}{\partial X} + \cos\theta \frac{\partial \eta'}{\partial X} + \frac{fV^2}{8H}\left(\frac{2U'}{V} - \frac{\eta'}{H}\right) = 0. \tag{3.5}$$

The perturbation $\mathbf{s} \equiv [\eta'(X,t), U'(X,t)]^T$ is decomposed in the standard form

$$\mathbf{s}(X,t) = \mathbf{S}(X)\boldsymbol{\chi}(X,t), \tag{3.6}$$

where the complex amplitude

$$\mathbf{S}(X) \equiv \begin{pmatrix} F(X) \\ G(X) \end{pmatrix} \tag{3.7}$$

depends only on the streamwise coordinate. In accordance with (3.3), we shall assume that $|d\mathbf{S}/dX| \ll 1$. The other part of the perturbation is of exponential form and describes the wave-like nature of the disturbance,

$$\boldsymbol{\chi}(X,t) = \exp\left[\int_{X_i}^{X} a(X')dX' - i\omega t\right], \tag{3.8}$$

where X_i is an initial or reference value of the coordinate X. The non-dimensional, complex wavenumber a is defined as

$$a(X) \equiv \gamma(X) + i\alpha(X)\,. \tag{3.9}$$

The real part $\gamma(X)$ is the local exponential growth rate, and the imaginary part $\alpha(X)$ is the local wavenumber. A non-dimensional frequency ω has also been defined in (3.8).

Substituting (3.6)-(3.9) into (3.4)-(3.5), the resulting set of two linear equations may be written in the matrix form as

$$\mathbf{A}\cdot\mathbf{S} + a\mathbf{B}\cdot\mathbf{S} + \mathbf{B}\cdot\frac{d\mathbf{S}}{dX} = 0, \tag{3.10}$$

where

$$\mathbf{A} = \begin{pmatrix} -i\omega + V_X & H_X \\ -\frac{fV^2}{8H^2} & -i\omega + V_X + \frac{fV}{4H} \end{pmatrix}, \tag{3.11}$$

$$\mathbf{B} = \begin{pmatrix} V & H \\ \cos\theta & V \end{pmatrix}, \tag{3.12}$$

and

$$H_X \equiv \frac{\partial H}{\partial X}\,, \quad V_X \equiv \frac{\partial V}{\partial X}\,. \tag{3.13}$$

The retained terms in (3.10) account for two different non-parallel effects on the stability of the perturbations: the effect of the non-parallelism of the basic flow and of the amplitude of the perturbations, and the effect of the history, or convective evolution, of the perturbations. This last effect is described by the d/dX terms of the stability equation (3.10). All these effects are negligible in the parallel limit of uniform basic flow with uniform perturbations.

As it stands there is some ambiguity in the partition of the perturbations (3.6) into two functions of the coordinate X. To close the problem one has to enforce an additional normalisation condition which puts some restriction on the streamwise variation of the perturbation amplitude (Bertolotti et al., 1992). We perform here a *local* spatial stability analysis (Fernandez-Feria, 2000): given a *real* frequency ω, Eq. (3.10) and its X-derivative will be solved locally for each location $X = X_0$ with the *normalisation* condition $[da/dX]_{X=X_0} = 0$. This condition will restrict, as required, the downstream variation of the perturbation amplitude (eigenfunction), yielding, for each $X = X_0$, the local growth rate and the wavenumber (or the phase speed of the disturbance). To that end, the eigenfunction $\mathbf{S}$ is expanded in a Taylor series about $X = X_0$, where only two terms are retained to be consistent with the approximation made in Eq. (3.10):

$$\begin{aligned} \mathbf{S}(X) &\simeq \mathbf{S}(X_0) + (X - X_0)\frac{d\mathbf{S}}{dX}\Big|_{X=X_0} \\ &\equiv \mathbf{S}_0 + (X - X_0)\mathbf{S}_1. \end{aligned} \tag{3.14}$$

This expansion is now substituted into (3.10) and its X-derivative to obtain two equations for $\mathbf{S}_0$ and $\mathbf{S}_1$ ($|\mathbf{S}_1| \ll |\mathbf{S}_0|$). Using the local normalisation condition $[da(X)/dX]_{X=X_0} = 0$, one has a set of four homogeneous linear equation that may be written in compact form as

$$\mathbf{F} \cdot \boldsymbol{T} = \mathbf{0}, \tag{3.15}$$

where

$$\mathbf{F} = \begin{pmatrix} \mathbf{A} + a\mathbf{B} & \mathbf{B} \\ \mathbf{C} + a\mathbf{D} & \mathbf{E} + a\mathbf{B} \end{pmatrix}, \quad \boldsymbol{T} \equiv \begin{pmatrix} \mathbf{S}_0 \\ \mathbf{S}_1 \end{pmatrix}, \tag{3.16}$$

$$\mathbf{C} = \begin{pmatrix} 0 & 0 \\ -\frac{fV}{4H^3}\left(HV_X - VH_X\right) & \frac{f}{4H^2}\left(HV_X - VH_X\right) \end{pmatrix}, \tag{3.17}$$

$$\mathbf{D} = \begin{pmatrix} V_X & H_X \\ 0 & V_X \end{pmatrix}, \tag{3.18}$$

$$\mathbf{E} = \begin{pmatrix} -i\omega + 2V_X & 2H_X \\ -\frac{fV^2}{8H^2} & -i\omega + 2V_X + \frac{fV}{4H} \end{pmatrix}. \tag{3.19}$$

For a given basic flow, and given ω and $X = X_0$ (for simplicity, in the above expressions, and in what follows, we write X for the local value X_0), the homogeneous equation (3.15) constitutes an eigenvalue problem for the complex eigenvalue a and the complex eigenfunction $\boldsymbol{T}$. That is to say, the homogeneous equation (3.15) has nontrivial solutions only when the determinant of $\mathbf{F}$ vanishes, yielding a dispersion relation of the form

$$\det(\mathbf{F}) \equiv D\left(a, \omega; \theta, f, V, H, V_X, H_X\right) = 0, \tag{3.20}$$

that determines the eigenvalue a.

One is interested in looking for convective instabilities propagating towards $X > 0$, i.e. in the same direction as the basic flow. Thus, for a known positive value of the real frequency ω, one is interested in modes whose eigenvalue a has both its real and imaginary parts positive. According to (3.8)-(3.9), this ensures that the perturbation grows exponentially as it propagates downstream increasing X ($\gamma > 0$), with phase velocity directed downstream (i.e. $c_{ph} \equiv \omega/\alpha > 0$). As a matter of fact, one has to consider the sign of the group velocity,

$$c_g \equiv \frac{\partial \omega}{\partial \alpha}, \tag{3.21}$$

instead of the sign of the phase velocity c_{ph}, in order to determine the propagation direction of the perturbations. But, as we shall see, the sign of c_g always coincide with the sign of c_{ph} in all the cases considered below (all the instabilities found here are convective instabilities, with both c_g and c_{ph} positive). On the other hand, the frequency range of study can be reduced to just non-negative values because the real and imaginary parts of the linear operator $\mathbf{F}$,

$$\mathbf{F}\left(\omega, \alpha, \gamma\right) \equiv \mathbf{F}_{\Re}\left(\gamma\right) + i\mathbf{F}_{\Im}\left(\omega, \alpha\right), \tag{3.22}$$

have the property

$$\mathbf{F}\left(a, \omega\right) = \overline{\mathbf{F}}\left(\overline{a}, -\omega\right), \tag{3.23}$$

where $\overline{(\cdot)}$ denotes the complex conjugate, and both $\mathbf{F}_{\Re}$ and $\mathbf{F}_{\Im}$ are real functions. Thus, if a is the eigenvalue corresponding to the real frequency ω, $\overline{a}$ is also an eigenvalue of the problem, corresponding to the frequency $-\omega$. Therefore, one has to consider only non-negative values of ω to fully analyse the linear spatial stability of the flow.

3.2.1 Results

Parallel flow: Roll-waves

Before undertaking the non-parallel stability analysis of a non-uniform flow down an open inclined channel, it is convenient to consider first the simplest case of a uniform flow, thus reproducing previously known stability results. This analysis will also serve as a reference that will help to understand the results given in the next section.

For a uniform and steady basic flow, $H = constant$ and $V = constant$, one has $d\mathbf{S}/dX \equiv \mathbf{S}_1 = 0$ in (3.15)-(3.16). In fact, the second equation in (3.15) for $\mathbf{S}_1$ becomes unnecessary, and the linear stability equation is just (3.10) with $d\mathbf{S}/dX = 0$. The dispersion relation (3.20) reduces then to

$$\det\left(\mathbf{A}_0 + a\mathbf{B}\right) = 0, \tag{3.24}$$

where $\mathbf{A}_0$ is the matrix (3.11) with $H_X = V_X = 0$.

For a uniform and steady basic flow, the solution to (2.1)-(2.3) relates the constant values of H and V by

$$H = \frac{fV^2}{8\sin\theta}. \tag{3.25}$$

It is convenient to use the Froude number

$$Fr \equiv \frac{V}{c} = \frac{V}{\sqrt{H\cos\theta}} = \sqrt{\frac{8}{f}\tan\theta}, \tag{3.26}$$

instead of the friction factor f, where $c = \sqrt{H\cos\theta}$ is the non-dimensional wave speed for small surface perturbations. Substituting (3.25)-(3.26) into (3.24), one obtains the following dispersion relation for the complex eigenvalue a and the real frequency ω:

$$a^2V^2\left(1 - \frac{1}{Fr^2}\right) + a(3\sin\theta - 2\omega V i) - \omega^2 - \frac{2\sin\theta\omega}{V}i = 0. \tag{3.27}$$

The number of parameters may be reduced to just one, the Froude number, if one makes the following changes of variables, valid for $\sin\theta \neq 0$:

$$e \equiv \frac{aV^2}{\sin\theta}, \quad \varpi \equiv \frac{\omega V}{\sin\theta}, \tag{3.28}$$

so that (3.27) reduces to

$$e^2(1 - \varrho) + e(3 - 2\varpi i) - \varpi^2 - 2\varpi i = 0\,, \tag{3.29}$$

where, for convenience, we use the inverse of the square of the Froude number,

$$\varrho \equiv \frac{1}{Fr^2}\,. \tag{3.30}$$

The new growth rate σ and wavenumber ϵ are defined as [see (3.9)]

$$e \equiv \sigma + i\epsilon\,, \quad \sigma = \frac{\gamma V^2}{\sin\theta}\,, \quad \epsilon = \frac{\alpha V^2}{\sin\theta}\,. \tag{3.31}$$

The neutral curve for instability, corresponding to $\sigma = 0$, is easily obtained by substituting $e = i\epsilon$ into (3.29). The imaginary and real parts of the resulting equation yield, respectively,

$$\epsilon = \frac{2}{3}\varpi \quad \text{and} \quad \varrho = \frac{1}{4}\,. \tag{3.32}$$

The flow is stable ($\sigma < 0$) for $\varrho > \varrho_c = 1/4$, while it is (convectively) unstable ($\sigma > 0$) for any value of the frequency ϖ if $\varrho < 1/4$. This obviously reproduces Jeffreys (1925) instability condition $Fr > 2$: any perturbation is unstable above the critical Froude number 2. In addition, one obtains that the phase velocity of the neutrally stable waves,

$$c_{ph} \equiv \frac{\omega}{\alpha} = \frac{\varpi V}{\epsilon} = \frac{3}{2}V\,, \tag{3.33}$$

is three times larger that the surface wave speed c for the critical $Fr = 2$, $c = V/Fr = V/2$. Incidentally, since ϖ is a linear function of ϵ, the group velocity c_g (3.21) coincides with the phase speed c_{ph}. In all the unstable waves we have computed, both in the uniform flows considered here and in the non-uniform ones of the next section, the signs of c_{ph} and c_g are always positive. That is to say, all the unstable modes correspond to convective instabilities.

Figure 3.1 depicts the neutral curve in the plane (Fr, ϖ), which is just the vertical straight line $Fr = 2$, together with some contour lines for constant growth rate σ. Note that for Fr close to the critical value $Fr_c = 2$ the growth rate is so small that an extremely long channel would be required for the developments of the unstable waves.

To finish this section it is worth to mention that for a horizontal channel ($\sin\theta = 0$), for which the change of variables (3.28) is not valid, Eq. (3.27) does not yield unstable solutions (i.e., solutions with $\sigma > 0$ together with $\epsilon > 0$).

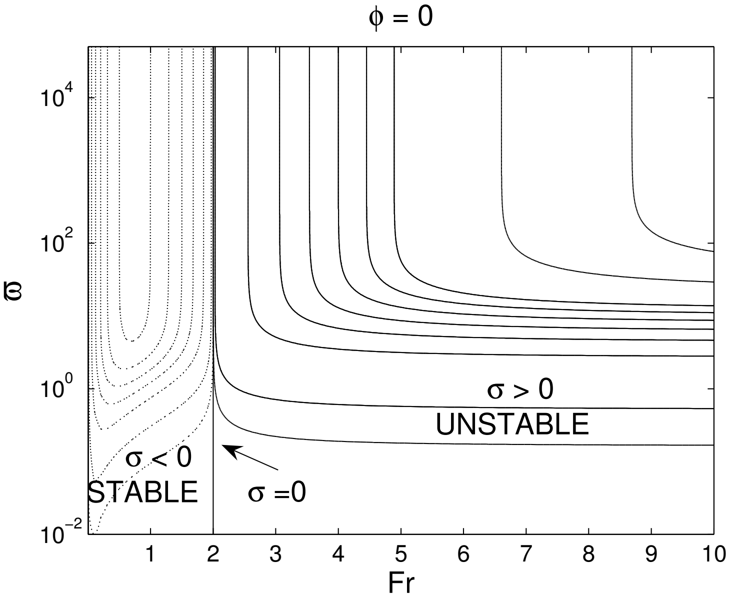

Figure 3.1: Contour lines for constant growth rate σ in the plane (ϖ, Fr) for the parallel-flow case. Continuous lines: $\sigma = 0, .001, .01, .2, .4, .6, .8, 1, 1.2, 2, 3$. Dashed lines: $\sigma = -.001, -.01, -.05, -.1, -.15, -.2, -.25$.

Near-parallel flow: Kinematic wave approximation

In order to obtain some quantitative results, but without recurring to any particular basic flow, we shall consider here the 'kinematic wave approximation' to the shallow-water flow equations (Lighthill and Whitham, 1955; Whitham, 1974), which have proved to be very useful for approximating the long time behaviour of the flow down an open inclined channel (see previous Chapter).

In the kinematic wave approximation, one neglects the left hand side of Eq. (2.2) and, after using the friction law (2.3), obtains the same relation (3.25) between H and V. But now H and V are not constant, they must satisfy the continuity equation (2.1) and the boundary conditions of the particular problem under consideration. Substituting (3.25) into Eq. (2.2) and using (2.1), one obtains the following condition for the validity of this approximation:

$$\left|\frac{\partial H}{\partial X}\right| \ll \left|\frac{\sin\theta}{\cos\theta - \frac{2}{f}\sin\theta}\right| . \tag{3.34}$$

With this approximation, one can eliminate the dependence on H and H_X of the dispersion relation (3.20) by using (3.25) and its derivative with respect to X:

$$H = \frac{fV^2}{8\sin\theta}\,, \quad H_X = \frac{fVV_X}{4\sin\theta}\,. \tag{3.35}$$

In addition, the explicit dependence on the angle θ and on the local flow velocity V can be eliminated from the dispersion relation thanks to the same change of variables (3.28) together with

$$\phi \equiv \frac{V_X V}{\sin\theta} = \frac{4}{f}\,H_X\,. \tag{3.36}$$

In these new variables, the validity condition (3.34) for the kinematic wave approximation reads

$$|\phi| \ll \left|\frac{2}{4\varrho - 1}\right|\,. \tag{3.37}$$

Introducing all these variables into Eqs. (3.15)-(3.19), the dispersion relation (3.20) may be simplified under the near-parallel assumption, which neglects the contribution of the streamwise gradients of complex amplitudes $\mathbf{s}$, resulting

$$D\left(e, \varpi; \varrho, \phi\right) \equiv -e\rho(e + 2\phi) + (e + \phi - i\varpi)^2 + 3e + 4\phi - 2i\varpi = 0, \tag{3.38}$$

Neutral curves are obtained setting $e = i\epsilon$ in Eq. (3.38):

$$\varpi = [3 - 2(\rho - 1)\phi]\left[\frac{\phi(4+\phi)}{1 + 4\rho^2\phi^2 - 4\rho(1 + 3\phi + \phi^2)}\right]^{1/2}\,, \tag{3.39}$$

$$\epsilon = \frac{2(1+\phi)}{3 - 2(\rho - 1)\phi}\varpi\,. \tag{3.40}$$

Figures 3.2(a)-3.2(b) depict neutral curves corresponding to several values of ϕ. It is shown that the flow is stabilised as ϕ grows. Thus, the spatial gradients in the base flow destabilise roll-waves. Defining the critical Froude number such that defines the vertical in the plane Fr, ϖ, one has (see Fig. 3.2(c))

$$Fr_c^2 = \frac{2\phi^2}{1 + 3\phi + \phi^2 - (1+\phi)\sqrt{1 + 4\phi + \phi^2}}\,. \tag{3.41}$$

In the parallel limit case, i.e. $\phi \to 0$, the Jeffreys's (1925) parallel stability criteria is recovered: ‘The flow is stable for Froude numbers lower than 2’. On the other hand, Fig. 3.2(d) shows the σ-isocontours for the particular case $\phi = 10^{-4}$.

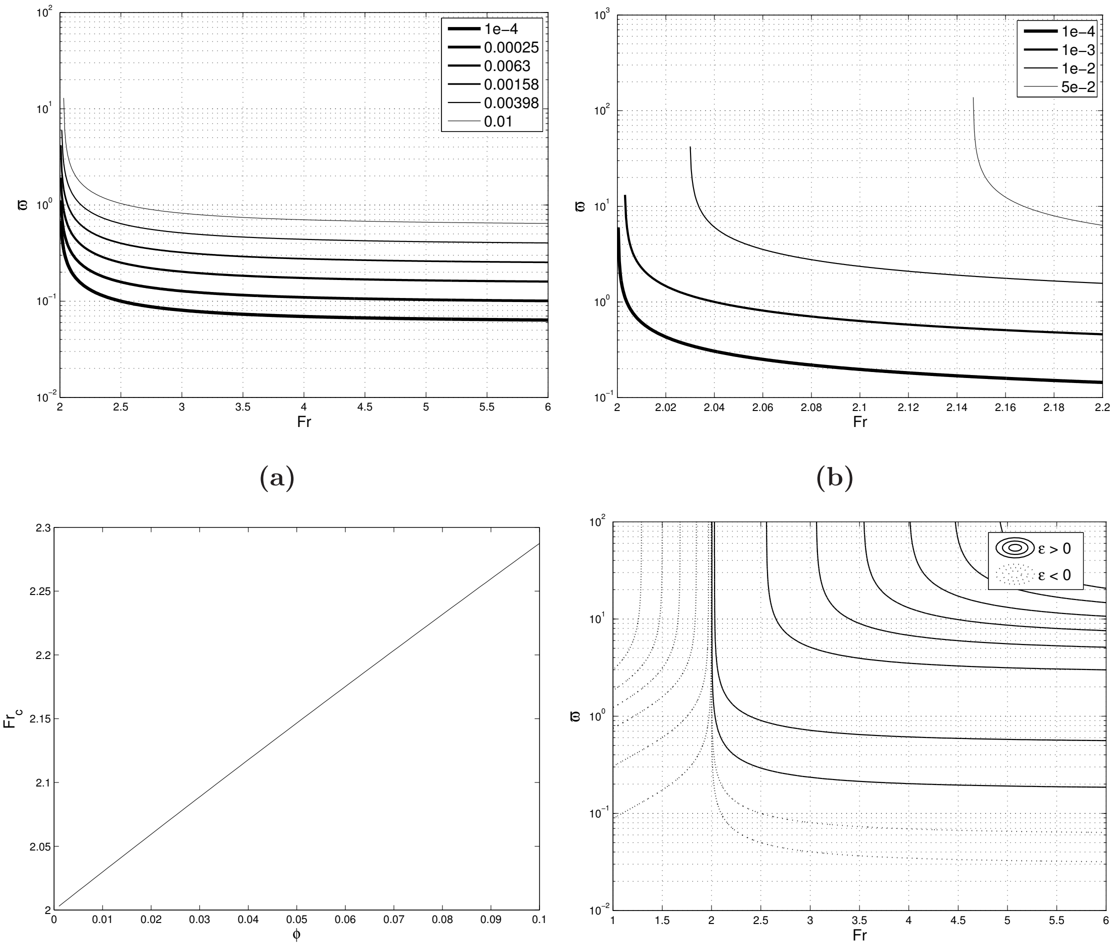

(a) **(b)**

(c) **(d)**

Figure 3.2: (a) Neutral curves for different values of $\phi > 0$; (b) details of the neutral curves near $Fr = 2$ for $\phi = 10^{-4}$, 10^{-3}, 0.01, 0.05; (c) critical Froude number Fr_c as a function of ϕ; (b) contour lines of constant growth rate σ for $\phi = 10^{-4}$ (discontinuous line: $\sigma = -10^{-7}$, -10^{-4}, -10^{-3}, -0.01, -0.05, -0.1, -0.15, -0.2, -0.25; continuous line: $\sigma = 0.001$, 0.01, 0.2, 0.4, 0.6, 0.8, 1, 1.2, 2, 3).

Non-parallel flow

We turn now to the general nonparallel stability formulation (3.15). Introducing all the previous variables (3.34)-(3.36) into Eqs. (3.15)-(3.19), the dispersion relation (3.20) may be written as

$$D\left(e, \varpi; \varrho, \phi\right) \equiv d_0 + d_1\phi + d_2\phi^2 + d_3\phi^3 + d_4\phi^4 = 0, \tag{3.42}$$

where

$$d_0 \equiv \left[e^2\left(\varrho - 1\right) + \varpi^2 + 2ie\varpi + \left(2i\varpi - 3e\right)\right]^2, \tag{3.43}$$

$$\begin{aligned} d_1 \equiv 2 \big[&3i\varpi^3 + 2e^3\left(\varrho - 1\right)^2 + 4e\varpi^2\left(\varrho - 2\right) \\ &+7ie^2\varpi\left(\varrho - 1\right) - 13e^2\left(\varrho - 1\right) - 12\varpi^2 + 2ie\varpi\left(5\varrho - 12\right) + \left(12e - 11i\varpi\right)\big], \end{aligned} \tag{3.44}$$

$$d_2 \equiv -13\varpi^2 + 8e^2\left(\varrho - 1\right)^2 + 4ie\varpi\left(4\varrho - 5\right) + 36 - 2\left[i\varpi\left(27 - 4\varrho\right) + e\left(22\varrho - 25\right)\right], \tag{3.45}$$

$$d_3 \equiv -4\left[3i\varpi + 2e\left(\varrho - 1\right) + 2\left(3\varrho - 5\right)\right], \tag{3.46}$$

$$d_4 \equiv 4, \tag{3.47}$$

and where use has been made of the Froude number (3.26) and (3.30).

The neutral curves for instability, corresponding to vanishing real part of e ($\sigma = 0$) in (3.42), can be written in the form $Fr = Fr(\varpi, \phi)$, together with the wavenumber $\epsilon = \epsilon(\varpi, \phi)$. Actually, one may obtain these expressions in an analytical closed form by taking the real and imaginary parts of that equation, but they are rather involved implicit relations (see Appendix A). Figure 3.3(a) shows these neutral curves in the plane (Fr, ϖ) for several values of $\phi > 0$, while Fig. 3.3(b) shows the corresponding curves in the plane (ϵ, ϖ). As it is observed in Fig. 3.3(a), there are marked differences with the neutral curve for the parallel flow case $\phi = 0$ (i.e., with the vertical line $Fr = 2$). Firstly, the flow is always stable independently of the Froude number for very small frequencies [i.e., for $\varpi < \varpi_\infty(\phi)$]. Secondly, the minimum, or critical, Froude number for instability, $Fr_{c1}(\phi)$, corresponding to the frequency $\varpi_{c1}(\phi)$, is always less that 2 when $\phi > 0$. (All these critical values of Fr and ϖ are marked in Fig. 3.3(a) for $\phi = 0.01$.) This critical Froude number tends to zero as ϕ decreases, though the frequency ϖ_{c1} also vanishes as $\phi \to 0$. As in the parallel case, the flow is

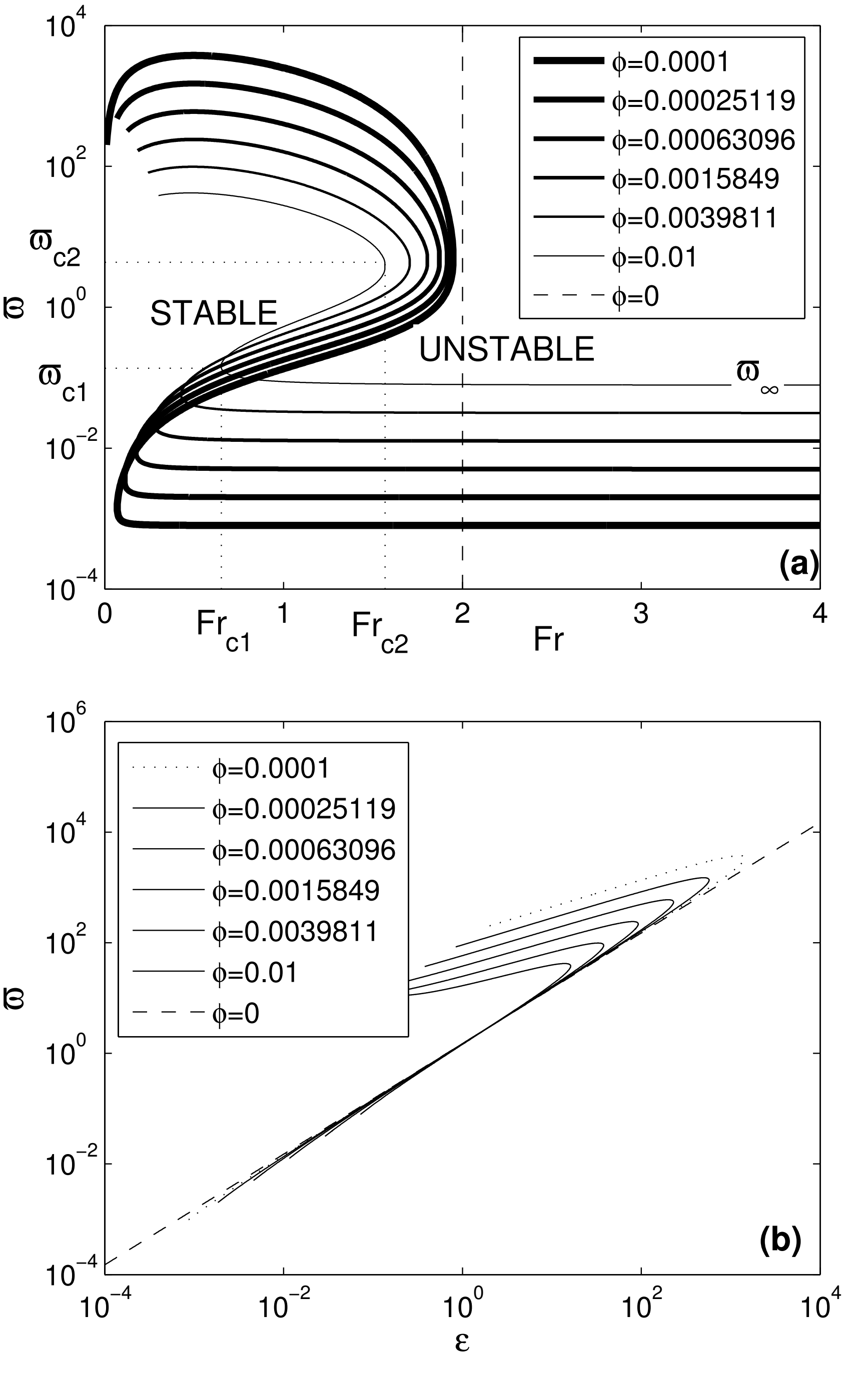

Figure 3.3: (a): Neutral curves ($\sigma = 0$) for different values of $\phi > 0$ (as indicated) in the plane (Fr, ϖ). The critical points (Fr_{c1}, ϖ_{c1}) and (Fr_{c2}, ϖ_{c2}) are shown for one of the curves. (b): Critical wavenumbers in the plane (ϵ, ϖ) corresponding to the neutral curves in (a).

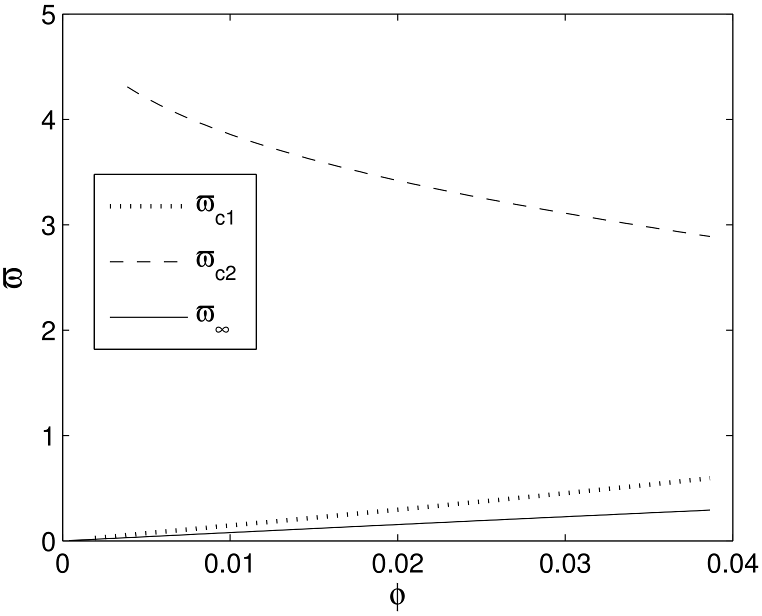

Figure 3.4: ϖ_{c1}, ϖ_{c2}, and ϖ_∞ as functions of $\phi > 0$.

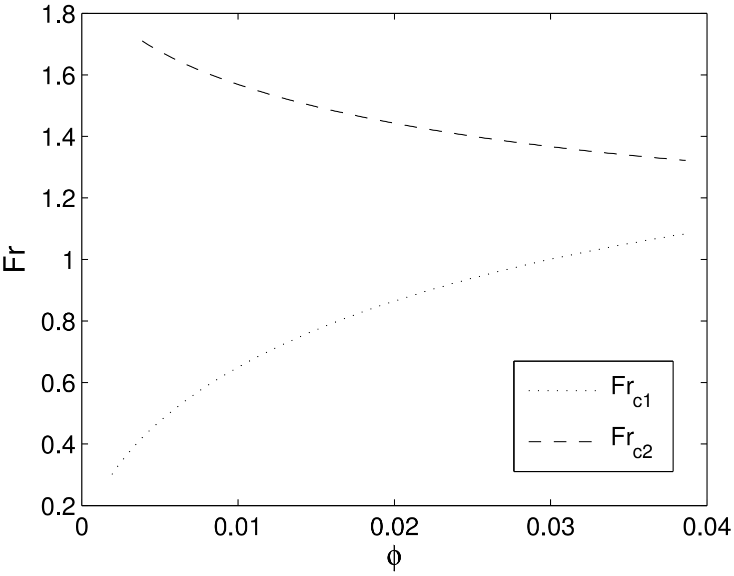

Figure 3.5: Fr_{c1}, and Fr_{c2} as functions of $\phi > 0$.

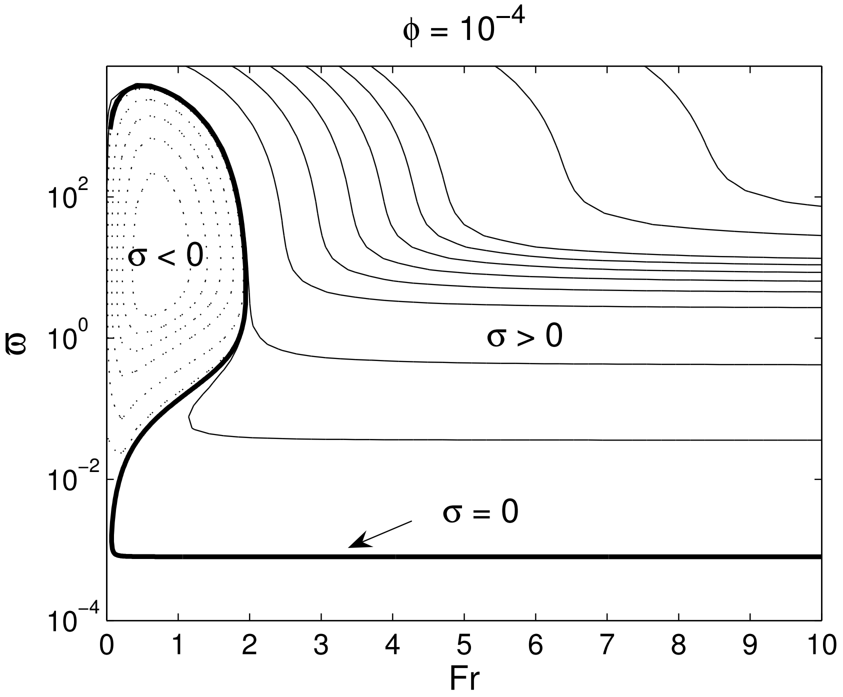

Figure 3.6: Contour lines of constant growth rate σ in the plane (Fr, ϖ) for $\phi = 10^{-4}$. Continuous lines: $\sigma = 0, .001, .01, .2, .4, .6, .8, 1, 1.2, 2, 3$. Dotted lines: $\sigma = -.001, -.01, -.05, -.1, -.15, -.2$.

unstable for almost any frequency when $Fr > 2$ (except for very small frequencies, as commented on above). In fact, there exists another critical value of the Froude number, $Fr_{c2}(\phi) < 2$, corresponding to the frequency $\varpi_{c2}(\phi)$, above which the flow is always unstable, provided that the frequency is not too small. For high frequencies the stability region shrinks to disappear for very high ϖ, the larger the smaller ϕ. But these very high frequencies, like the very small ones $\varpi < \varpi_\infty$, are too extreme to be physically meaningful. Thus, the two pairs of critical values (Fr_{c1}, ϖ_{c1}) and, especially (Fr_{c2}, ϖ_{c2}), are the most significant physical results. Figures 3.4 and 3.5 show these critical values (together with ϖ_∞) as functions of $\phi (> 0)$. For $\varpi_{c1} < \varpi < \varpi_{c2}$ the flow is unstable for Froude numbers less than 2 ($Fr_{c1} < Fr_{c2} < 2$).

To have an idea of the most unstable frequencies, Fig. 3.6 shows contour lines of constant growth rate σ for a particular value of ϕ. It is observed that, though the critical Fr is much smaller than 2 for low frequencies, the growth rate is quite small for $Fr < 2$, thus explaining why it is not easy to see roll-waves for $Fr < 2$. For very high frequencies, the critical Fr may also be much smaller than 2, and with a growth rate not so small. But the frequencies are so high that they are not physically relevant.

Figure 3.7 shows the neutral curves in the planes (Fr, ϖ) and (ϵ, ϖ) for several values of $\phi < 0$, while Fig. 3.8 depicts contour lines of constant growth rate σ for a particular value of $\phi < 0$. As in the cases where $\phi > 0$, the flow may be unstable for $Fr < 2$ and the stability properties are very sensitive to the non-uniformities of the flow: with very small values of $|\phi|$, the region of instability changes dramatically with respect to the parallel flow case. However, the growth rates for $Fr < 2$ are very small, except for very high unrealistic frequencies (Fig. 3.8), as it also occurs for $\phi > 0$. There are, nonetheless, some important differences between the $\phi > 0$ and the $\phi < 0$ cases. First, for $\phi < 0$, no frequency ϖ_∞ exists, and the flow is always unstable as $\varpi \to 0$. In fact, the stable region in the (Fr, ϖ) plane is closed, so that the flow is also unstable for any frequency when Fr is very small (Fig. 3.7). However, for these very small values of the Froude number the kinematic wave approximation is no longer valid because condition (3.37) implies

$$Fr \gg \sqrt{\frac{4|\phi|}{2+|\phi|}} \simeq \sqrt{2|\phi|}\,. \tag{3.48}$$

This condition applies for both $\phi < 0$ and $\phi > 0$.

3.2.2 Asymptotic results for $\phi \ll 1$

Although the dispersion relation of the previous section is given in a closed analytical form, it is convenient to simplify it by making use of the fact that $|\phi|$ is very small. In particular, it is of interest to analyse the bifurcation of the neutral curves shown in Figs. 3.3 and 3.7 when one pass from a uniform ($\phi = 0$) to a non-uniform ($\phi \neq 0$) flow. We will restrict our analysis here to positive velocity gradients ($\phi > 0$), which is the most common situation in physical problems, such as the dam-break problem on a sloping channel (see previous Chapter), for the long time behaviour when the kinematic wave approximation applies. The analysis for $\phi < 0$ is very similar.

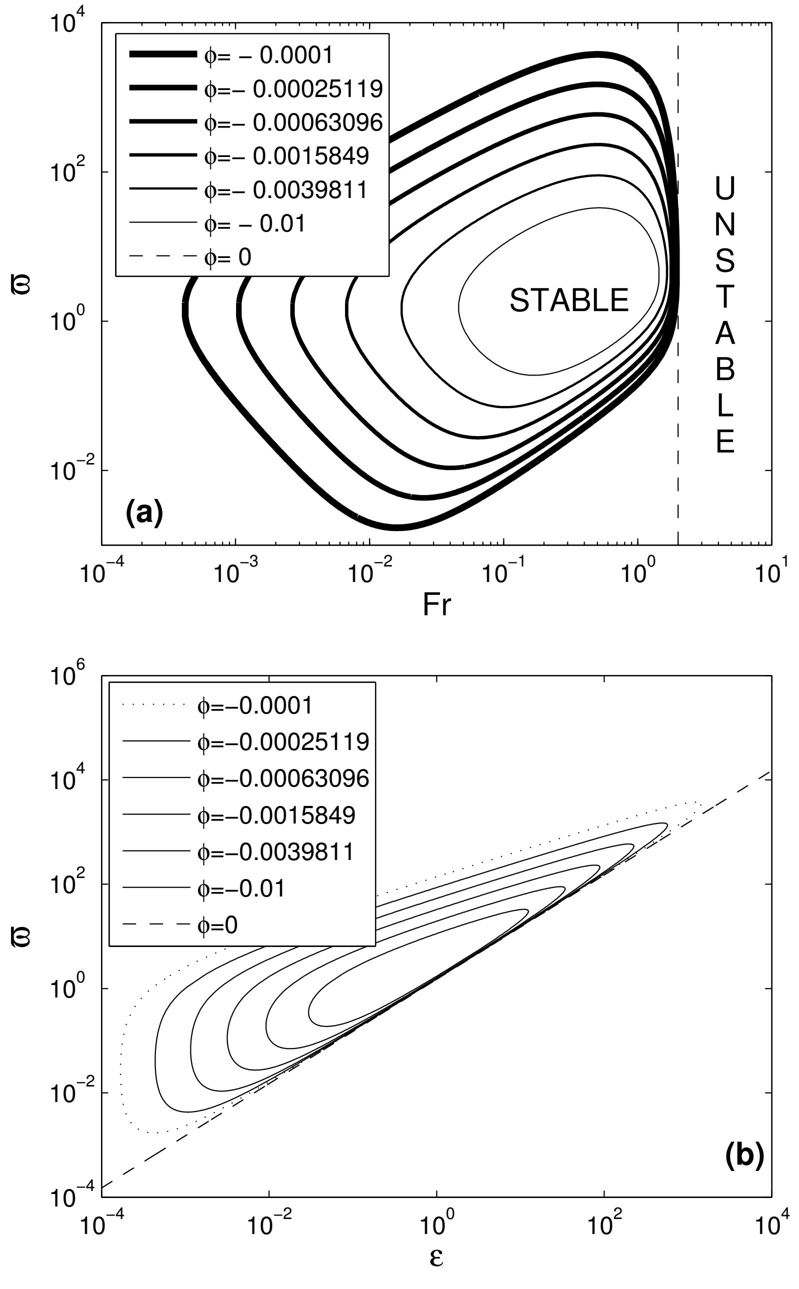

Figure 3.7: As in Fig. 3.3, but for $\phi < 0$.

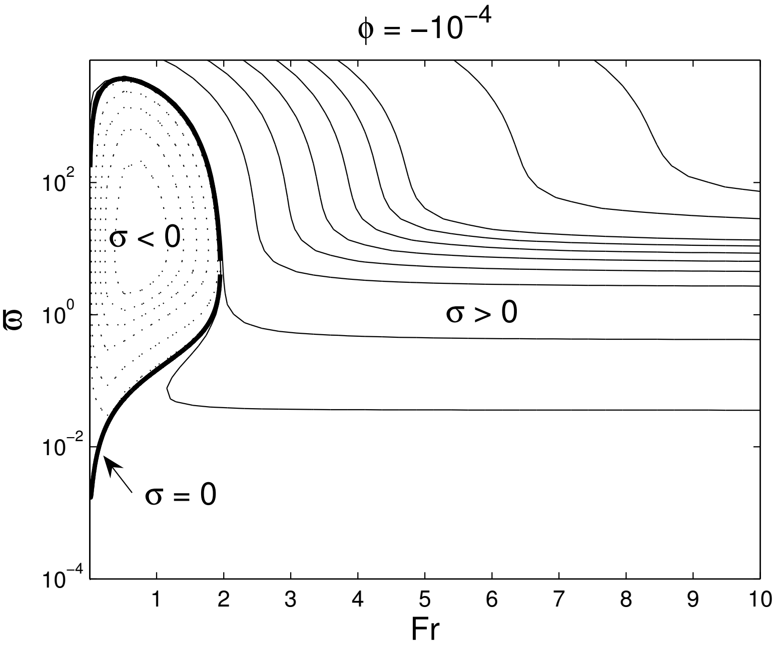

Figure 3.8: As in Fig. 3.6, but for $\phi = -10^{-4}$.

For small $\phi > 0$, the neutral curves $\varrho(\varpi, \phi)$ and $\epsilon(\varpi, \phi)$ behave as

$$\varrho(\varpi, \phi) \sim \varrho_0(\varpi) + \varrho_1(\varpi)\phi^{1/2} + \varrho_2(\varpi)\phi + ... + \varrho_i(\varpi)\phi^{i/2} + ... , \tag{3.49}$$

$$\epsilon(\varpi, \phi) \sim \epsilon_0(\varpi) + \epsilon_1(\varpi)\phi^{1/2} + \epsilon_2(\varpi)\phi + ... + \epsilon_i(\varpi)\phi^{i/2} + ... \tag{3.50}$$

Substituting these expansions into (3.42)-(3.47) with $\sigma = 0$, $e = i\epsilon$ (the expressions (3.42)-(3.47) with $\sigma = 0$ are given analytically in Apendix A), at the lowest order one obtains

$$[\epsilon_0^2(\varrho_0 - 1) - \varpi(2i + \varpi) + \epsilon_0(3i + 2\varpi)]^2 = 0. \tag{3.51}$$

This equation has as unique solution Jeffreys' solution (3.32) for a uniform flow:

$$\epsilon_0 = \frac{2\varpi}{3}, \quad \varrho_0 = \frac{1}{4}\,. \tag{3.52}$$

At the next order, $\phi^{1/2}$, one has

$$2[\epsilon_0^2(\varrho_0 - 1) - \varpi(2i + \varpi) + \epsilon_0(3i + 2\varpi)]\{\epsilon_0^2\varrho_1 + \epsilon_1[3i + 2\epsilon_0(\varrho_0 - 1) + 2\varpi]\} = 0\,, \tag{3.53}$$

which is satisfied identically for any value of ϱ_1 and ϵ_1 if the zeroth order solution (3.52) is substituted. Therefore, one has to go to the next order to obtain ϱ_1 and ϵ_1. Using (3.52), the resulting equation at the order ϕ is

$$-6i\varpi - 4\varpi^2 + \frac{2i\varpi^3}{3} + \frac{16\varrho_1^2\varpi^4}{81} + \frac{8}{9}\epsilon_1\varrho_1\varpi^2(3i+\varpi) + \epsilon_1^2(3i+\varpi)^2 = 0\,, \tag{3.54}$$

which has four possible solutions,

$$\epsilon_1 = \pm\frac{(3-\varpi)\sqrt{\varpi}}{3\sqrt{3}}, \quad \varrho_1 = \pm\frac{\sqrt{3}(9+\varpi^2)}{4\varpi^{3/2}}. \tag{3.55}$$

$$\epsilon_1 = \pm\frac{(3+\varpi)\sqrt{-\varpi}}{3\sqrt{3}}, \quad \varrho_1 = \mp\frac{\sqrt{3}(9+\varpi^2)}{4(-\varpi)^{3/2}}\,. \tag{3.56}$$

The two last solutions (3.56) are complex for positive ϖ and they have no physical meaning (they are the relevant ones for the expansion in the case $\phi < 0$, not considered here). As we show below, the solution that corresponds to the neutral curves depicted in Figs. 3.3 and 3.7 is (3.55) with the plus sign.

At the next order $\phi^{3/2}$, the resulting equations yields

$$\begin{aligned}
\epsilon_2 =& \frac{\varpi[-32\varrho_1^2\varpi^4 + 36\epsilon_1\varrho_1\varpi(\varpi^2-36) + 243\epsilon_1^2(9+\varpi^2)]}{6[72\epsilon_1\varrho_1\varpi^3 + 16\varrho_1^2\varpi^4 + 81\epsilon_1^2(9+\varpi^2)]}, \\
\varrho_2 =& 3\frac{64\varrho_1^2\varpi^4(6+\varpi^2) + 729\epsilon_1^4(9+\varpi^2) - 648\epsilon_1^3\varrho_1\varpi(18+\varpi^2)}{16\varpi^2[72\epsilon_1\varrho_1\varpi^3 + 16\varrho_1^2\varpi^4 + 81\epsilon_1^2(9+\varpi^2)]} \\
& - 3\frac{8\epsilon_1\varrho_1\varpi^3[189 + (9+32\varrho_1^2)\varpi^2] + 18\epsilon_1^2[1944 + 459\varpi^2 + (27+56\varrho_1^2)\varpi^4]}{16\varpi^2[72\epsilon_1\varrho_1\varpi^3 + 16\varrho_1^2\varpi^4 + 81\epsilon_1^2(9+\varpi^2)]}.
\end{aligned} \tag{3.57}$$

After substituting (3.55) into (3.57) and simplifying, the neutral curve (3.49) up to the order ϕ can be written as

$$\varrho = \frac{1}{4} \pm \frac{1}{4}\frac{\sqrt{3}(9+\varpi^2)}{\varpi^{3/2}}\phi^{1/2} + \frac{-72 + 36\varpi - 9\varpi^2 + 5\varpi^3}{8\varpi^2}\phi + O(\phi^{3/2})\,, \tag{3.58}$$

where we have retained the two solutions (3.55). Figure 3.9(a) compares, in the plane (Fr, ϖ), these approximate neutral curves for a particular value of $\phi > 0$ with the exact one (see Fig. 3.3). It is observed that the expression (3.58) with the plus sign agrees quite well with the exact neutral curve. In particular, it catches with a

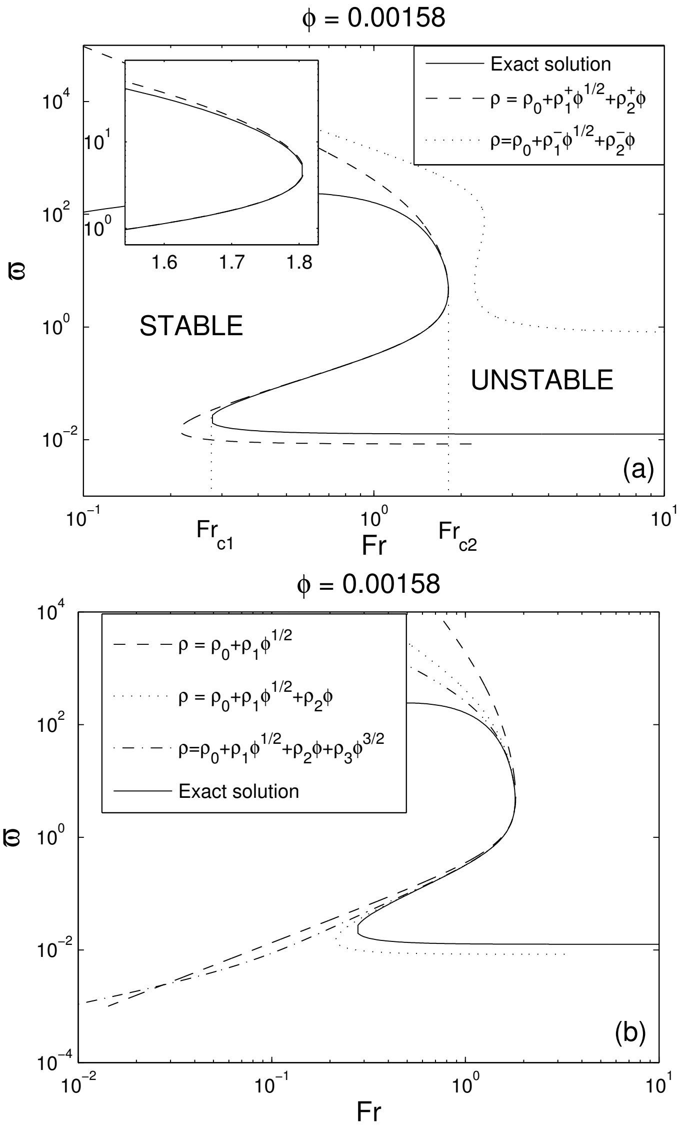

Figure 3.9: (a): Comparison between the exact neutral curve of stability in the plane (Fr, ϖ) and the approximate solutions (3.58) for positive (ρ^+) and negative (ρ^-) signs, for a given value of ϕ. (b): Comparison between exact neutral curves and approximate ones for different orders in the expansion in powers of ϕ.

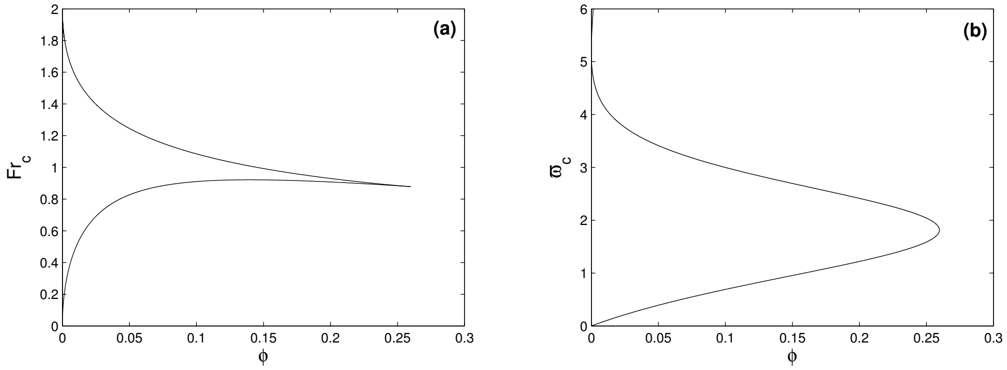

Figure 3.10: Critical Froude numbers (a) and frequencies (b) obtained with the asymptotic expressions (3.58) and (3.59) as functions of ϕ. The upper parts of the curves correspond to Fr_{c2} and ϖ_{c2}, while the lower parts to Fr_{c1} and ϖ_{c1}. Note that the approximation is not valid for the largest values of ϕ plotted.

very good precision the critical point (Fr_{c2}, ϖ_{c2}), and with less precision the other critical point (Fr_{c1}, ϖ_{c1}). In fact, the expansion (3.58) diverges for both $\varpi \to 0$ and $\varpi \to \infty$, but yields a good approximation for the physically relevant (order of unity) frequencies and, in particular, for the most relevant critical point (Fr_{c2}, ϖ_{c2}). Figure 3.9(b) shows that the accuracy near this critical point improves as the next term in the expansion, $(\epsilon_3,\ \varrho_3)$, is taken into account. However, the accuracy does not improve for large and small values of ϖ. In relation to the expression (3.58) when the minus sign is considered, Fig. 3.9(a) shows that the corresponding curve lies in the unstable region, so that it corresponds to a second unstable mode of less physical interest, because it becomes unstable for higher values of the Froude number with a smaller growth rate (the neutral curves for these modes have not been plotted in Fig. 3.3).

The critical points for instability can be obtained as functions of ϕ by making $\partial\varrho(\varpi)/\partial\varpi = 0$. Using the approximation in (3.58), one obtains

$$\phi = \frac{3\varpi_c(-27+\varpi_c^2)^2}{(144-36\varpi_c+5\varpi_c^3)^2}\,, \tag{3.59}$$

which yields, implicitly, $\varpi_c(\phi)$ and, together with (3.58), $\varrho_c(\phi)$ or $Fr_c(\phi)$. These expressions are plotted in figure 3.10. The upper parts of the curves corresponds to

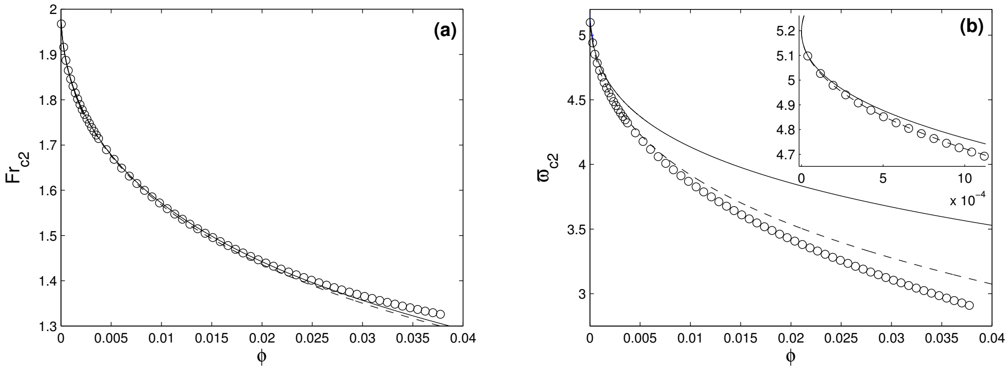

Figure 3.11: Fr_{c2} (a) and ϖ_{c2} (b) as functions of ϕ obtained with the exact solution (circles), with the asymptotic expansion (3.58) (continuous lines), and with an additional term in the expansion (up to order $\phi^{3/2}$; dashed lines).

$Fr_{c2}(\phi)$ and $\varpi_{c2}(\phi)$, and the lower parts to $Fr_{c1}(\phi)$ and $\varpi_{c1}(\phi)$. As discussed above, the most relevant one from a physical point of view is $[Fr_{c2}(\phi), \varpi_{c2}(\phi)]$, which is compared in Fig. 3.11 to the exact solution. Also shown in that figure is the critical point obtained when the next term (ϵ_3, ϱ_3) is taken into account in the expansion (3.49), which obviously improve the accuracy of the approximation. Note that we have plotted in Fig. 3.10 the whole range of ϕ, till Fr_{c1} and Fr_{c2} merge. But the expansion is only valid for very small values of ϕ, for which the lower curve corresponds to very small frequencies and the expansion is not valid (these very small frequencies are also physically irrelevant). Therefore, the most significant asymptotic results given here are the upper curves in Fig. 3.10, plotted in detail for $\phi \ll 1$ in Fig. 3.11.

Finally, the critical frequencies for $\phi = 0$ given by the analytical expression (3.59) are $\varpi_{c1} = 0$ and $\varpi_{c2} = \sqrt{27} \approx 5.2$, corresponding to $Fr_{c1} = 0$ and $Fr_{c2} = 2$. As seen in Figs. 3.4 and 3.5, these are the values to which the exact solution tends as $\phi \to 0$, but they are difficult to compute because the bifurcation of the solution at $\phi = 0$. This bifurcation is evident in Figs. 3.10 and 3.11, where Fr_{c1}, Fr_{c2} and especially ϖ_{c2} have infinite slopes at $\phi = 0$. Whence, another reason why the present asymptotic solution is valuable. Actually, even with an analytic closed solution, it was difficult to see what happened for $\phi = 0^+$ without the present asymptotic solution.

3.3 Linear stability analysis by means of multiple scales

In § 2.3, an asymptotic analytical solution for the background flow resulting from a flood of water at rest on a steep incline was obtained as an asymptotic expansion in terms of the shallowness parameter ε. The rescaling we did, see Eq. (2.8), shows a fundamental characteristic of the *scales* at which the base flow develops: both the temporal and spatial coordinates (x and τ, respectively) characterising the kinematic wave are much smaller than the dynamic wave coordinates (X and t). In this section, we take advantage of this fact to perform a linear stability analysis of the kinematic wave in terms of multiple scales (Kevorkian and Cole, 1996). We shall focus our interest on the particular case $Fr_{eq} = 2$, in order to compare the ensuing stability criteria with that of Jeffreys and the previous ones in § 3.2.

Although the non-dimensional variables X and t in (3.4)-(3.5) are appropriate to analyse the stability, the basic flow moves in a much slower scale:

$$\hat{x} = \delta X \,, \quad \hat{t} = \delta t \quad \text{with} \quad \delta \equiv \frac{\eta_0}{l} \ll 1 \,. \tag{3.60}$$

The basic flow is so supposed to depend just on this scale

$$H \equiv H(\hat{x}, \hat{t}; \delta) \,, \quad V \equiv V(\hat{x}, \hat{t}; \delta) \tag{3.61}$$

whilst the perturbations move at several scales

$$\eta' \equiv \eta'(X, t, \hat{x}, \hat{t}; \delta) \,, \quad U' \equiv U'(X, t, \hat{x}, \hat{t}; \delta) \,. \tag{3.62}$$

The equations for the basic flow (2.1)-(2.2) read in the new variables

$$\frac{\partial H}{\partial \hat{t}} + \frac{\partial HV}{\partial \hat{x}} = 0 \,, \tag{3.63}$$

$$\delta \left[\frac{\partial V}{\partial \hat{t}} + V \frac{\partial V}{\partial \hat{x}} + \cos\theta \frac{\partial H}{\partial \hat{x}} \right] - \sin\theta + \frac{fV^2}{8H} = 0 \,, \tag{3.64}$$

and the linearised equations for the perturbations (3.4)-(3.5) are

$$\frac{\partial \eta'}{\partial t} + H \frac{\partial U'}{\partial X} + V \frac{\partial \eta'}{\partial X} + \delta \left(U' \frac{\partial H}{\partial \hat{x}} + \eta' \frac{\partial V}{\partial \hat{x}} \right) = 0 \,, \tag{3.65}$$

$$\frac{\partial U'}{\partial t} + V\frac{\partial U'}{\partial X} + \cos\theta\frac{\partial \eta'}{\partial X} + \frac{fV^2}{8H}\left(\frac{2U'}{V} - \frac{\eta'}{H}\right) + \delta U'\frac{\partial V}{\partial \hat{x}} = 0\,. \tag{3.66}$$

The coefficients in (3.65)-(3.66) do not depend on (X,t), only on $(\hat{t},\hat{x})$. Therefore, it is possible to write the solution of η' and U' in the rapid scale as an exponential function:

$$\mathbf{s} \equiv \begin{pmatrix} \eta' \\ U' \end{pmatrix} \equiv \mathbf{S}(\hat{x},\hat{t};\delta)e^{i\lambda(X,t;\delta)} \equiv \begin{pmatrix} F(\hat{x},\hat{t};\delta) \\ G(\hat{x},\hat{t};\delta) \end{pmatrix} e^{i\frac{\psi(\hat{x},\hat{t})}{\delta}}\,. \tag{3.67}$$

Taken into account (3.67), equations (3.65)-(3.66) now read

$$i(aV-\omega)F + i\alpha HG = -\delta\left(\frac{\partial F}{\partial \hat{t}} + \frac{\partial HG}{\partial \hat{x}} + \frac{\partial FV}{\partial \hat{x}}\right)\,, \tag{3.68}$$

$$i(aV-\omega)G + ia\cos\theta F + \frac{fV}{4H}G - \frac{fV^2}{8H^2}F = -\delta\left(\frac{\partial G}{\partial \hat{t}} + \frac{\partial HG}{\partial \hat{x}} + \cos\theta\frac{\partial F}{\partial \hat{x}}\right)\,, \tag{3.69}$$

where the complex frequency ω and the complex wave number a are defined as:

$$\omega \equiv -\frac{\partial \psi}{\partial \hat{t}}\,, \quad a \equiv \frac{\partial \psi}{\partial \hat{x}}\,, \tag{3.70}$$

The phase function $\psi(\hat{x},\hat{t})$ can then be written in terms of ω and a:

$$\psi(\hat{x},\hat{t}) = \int_{\hat{x}_0}^{\hat{x}} a(\xi,\hat{t})d\xi - \int_{\hat{t}_0}^{\hat{t}} \omega(\hat{x},\tau)d\tau - \int_{\hat{t}_0}^{\hat{t}}\int_{\hat{x}_0}^{\hat{x}} \frac{\partial a}{\partial \hat{t}}(\xi,\tau)d\xi d\tau\,, \tag{3.71}$$

and the similarity between the present multi-scale stability analysis and the non-parallel spatial stability analysis, presented in the previous section, readily becomes. However, the decomposition (3.70) introduces an additional unknown, which should be closed with the compatibility relation that results from the equality of cross-derivatives:

$$\frac{\partial}{\partial \hat{t}}\left(\frac{\partial \psi}{\partial \hat{x}}\right) = \frac{\partial}{\partial \hat{x}}\left(\frac{\partial \psi}{\partial \hat{t}}\right) \Rightarrow \frac{\partial a}{\partial \hat{t}} + \frac{\partial \omega}{\partial \hat{x}} = 0\,. \tag{3.72}$$

The unknowns are to be expanded in power of δ:

$$\begin{aligned} H &= H_0 + \delta H_1 + O(\delta^2)\,, \qquad & V &= V_0 + \delta V_1 + O(\delta^2)\,, \\ F &= F_0 + \delta F_1 + O(\delta^2)\,, \qquad & G &= G_0 + \delta G_1 + O(\delta^2)\,, \\ a &= a_0 + \delta a_1 + O(\delta^2)\,, \qquad & \omega &= \omega_0 + \delta \omega_1 + O(\delta^2)\,. \end{aligned} \tag{3.73}$$

Substituting the expansion (3.73) into (3.63)-(3.64), and grouping terms of order unity, the first-order background-flow equations are obtained:

$$\frac{\partial V_0}{\partial \hat{t}} + \frac{3V_0}{2}\frac{\partial V_0}{\partial \hat{x}} = 0\,, \quad H_0 = \frac{fV_0^2}{8\sin\theta}\,. \tag{3.74}$$

Following the same procedure but with equations (3.68)-(3.69), it follows

$$\mathbf{L}_0 \cdot \mathbf{S}_0 = \mathbf{0} \tag{3.75}$$

with

$$\mathbf{L}_0 \equiv \begin{pmatrix} i(a_0V_0 - \omega_0) & ia_0H_0 \\ ia_0\cos\theta - \frac{fV_0^2}{8H_0^2} & i(a_0V_0 - \omega_0) + \frac{fV_0}{4H_0} \end{pmatrix}, \quad \mathbf{S}_0 \equiv \begin{pmatrix} F_0 \\ G_0 \end{pmatrix}. \tag{3.76}$$

The system of equations shown above has non-trivial solutions only if the dispersion relation that follows, provided by $\det(\mathbf{L}_0) = 0$, is satisfied:

$$\varpi_0 = e_0 - i \pm (-1 + ie_0 + \rho e_0^2)^{1/2} \tag{3.77}$$

where we have used the same change of variable as in (3.28). In addition, the compatibility relation (3.72) is also to be satisfied at leading-order,

$$\frac{\partial e_0}{\partial \hat{t}} - \frac{2e_0}{V_0}\frac{\partial V_0}{\partial \hat{t}} = -V_0\frac{\partial \varpi_0}{\partial \hat{x}} + \varpi_0\frac{\partial V_0}{\partial \hat{x}}\,. \tag{3.78}$$

To solve the compatibility equation (3.78), it is convenient to rewrite it along the characteristic curve, so that one obtains

$$\frac{de_0}{\partial \hat{t}} = \frac{2e_0}{V_0}\frac{\partial V_0}{\partial \hat{t}} + \varpi_0\frac{\partial V_0}{\partial \hat{x}} \quad \text{with} \quad \frac{d\hat{x}}{d\hat{t}} = V_0\frac{d\varpi_0}{de_0}\,. \tag{3.79}$$

$Fr = 2$ in flood on a steep slope

The first-order partial differential equation (3.74), so-called *kinematic wave equation*, is exactly the same as we solved in § 2.3. Setting an initial condition for the velocity (or the initial water-depth), one can determine the velocity field by integrating (3.74) as in Lighthill and Whitham (1955). In particular, we are interested in the stability criteria of waves occurring in floods on inclines. Thus, we focus the analysis on the solution at late time of a flood which initial conditions are (2.4)-(2.5), which is given by

$$V_0 = \frac{2\hat{x}}{3\hat{t}}\,, \quad H_0 = \frac{fV_0^2}{8\sin\theta}\,. \tag{3.80}$$

In the case that the Froude number value is $Fr = 2$, the corrections to this solution vanish (i.e. $V_i = H_i = 0$ for $i \geq 1$). Furthermore, the dispersion relation (3.77) has the two solutions that follows:

$$\varpi_0 = \tfrac{3}{2}e_0\,, \tag{3.81a}$$

$$\varpi_0 = \tfrac{1}{2}e_0 - 2i\,. \tag{3.81b}$$

The characteristic path for the functions $\varpi_0(e_0)$ shown above are purely real. Thus, the characteristic equation (3.79) easily provides the solution for both cases if the constant complex number a^o is settled as initial condition, resulting

$$\psi_0(\hat{x},\hat{t}) = a^o \tfrac{\hat{t}_0}{\hat{t}}\hat{x}\,. \tag{3.82a}$$

$$\psi_0(\hat{x},\hat{t}) = a^o \left(\tfrac{t_0}{t}\right)^{1/3} x - i\left\{\tfrac{9t^2\sin\theta}{5x}\left[\left(\tfrac{t_0}{t}\right)^{5/3} - 1\right]\right\}\,. \tag{3.82b}$$

The solution (3.82b) is obviously stable [the reader can verify it by substitution into (3.67)], i.e. the amplitude of the perturbation decreases as time proceeds, whilst the stability of the solution (3.82a) is determined from the eigenfuntions F and G. The relation between the eigenfunctions (F, G) is next determined from (3.75)

$$F_0 = \frac{H_0}{V_0}\frac{e_0}{\varpi_0 - e_0}G_0\,, \tag{3.83}$$

which after substitution of (3.81a)-(3.81a) gives

$$F_0 = \tfrac{2H_0}{V_0}G_0\,, \tag{3.84a}$$

$$F_0 = -\tfrac{2H_0}{V_0}\tfrac{e_0}{e_0+2i}G_0\,. \tag{3.84b}$$

Thus, the first-order solution of the linear stability equations, for the Froude number value $Fr = 2$ in a flood on a steep incline, is given by

$$\mathbf{s} = \begin{pmatrix} \eta' \\ U' \end{pmatrix} = G\begin{pmatrix} 2H_0/V_0 \\ 1 \end{pmatrix} e^{ia(\hat{t})\hat{x}} \quad \text{with} \quad a(\hat{t}) \equiv \frac{a^o\hat{t}_0}{\hat{t}}\,. \tag{3.85}$$

This solution should satisfy the leading order of the linear perturbation equations, which provides the function $G(\hat{x},\hat{t})$. This is given by

$$\frac{\partial G}{\partial \hat{t}} + \frac{3}{2} V_0 \frac{\partial G}{\partial \hat{x}} = -\frac{G}{\hat{t}} \,,$$

whose solution is

$$G(\hat{x},\hat{t}) \equiv G^o\left(\frac{\hat{t}_0 \hat{x}}{\hat{t}}\right)\frac{\hat{t}_0}{\hat{t}} \,, \tag{3.86}$$

with $G^o(\xi)$ being the perturbation at the initial time. Curiously, both the basic flow (3.80) and the perturbation solution (3.85)-(3.86) are not only the leading term of the solution but the exact solution to (2.1)-(2.2) and (3.4)-(3.5), respectively! The temporal contribution always decreases the perturbation amplitude. This means that along the ray $x(t) = t$, the perturbation is attenuated as follows

$$\mathbf{s}(\hat{x} = \hat{t}, \hat{t}) = G(\hat{t}_0)\frac{\hat{t}_0}{\hat{t}}\begin{pmatrix} \frac{f}{6\sin\theta} \\ 1 \end{pmatrix} e^{ia^o \hat{t}_0} \,.$$

Therefore, we conclude that the Jeffreys's stability criteria is no longer valid for floods on inclines: the flow is stable for the Froude number $Fr = 2$; furthermore, one eyewitness at rest will observe the modulation of the waves, that increase their wavelengths proportionally to the time.

$Fr = 2$ in a linear velocity profile on a steep slope

We have observed in Fig. (2.8) that the velocity profiles at late times after the rupture of a dam are nearly linear in the streamwise direction, and that roll-waves start to develop under such flow. So, we can analyse the stability of a linear velocity profile instead of considering the asymptotic solution for a flood on a steep slope, as in the previous section.

A linear velocity profile of slope A at the initial instant of time $t = 0$ develops, according to (3.74), the solution that follows:

$$V_0 = \frac{A\hat{x}}{1 + \frac{3}{2}A\hat{t}} \,, \quad H_0 = \frac{f V_0^2}{8\sin\theta} \,. \tag{3.87}$$

For late time, the solution is in fact the same as such analysed in the previous section

$$\lim_{\hat{t}\gg\frac{2}{3A}} V_0 = \frac{2\hat{x}}{3\hat{t}}\frac{1}{1+\frac{2}{3A\hat{t}}} \approx \frac{2\hat{x}}{3\hat{t}}\,.$$

This means that the flow forgets its initial state.

For this basic flow, one can obtain the exact solution of the linear perturbation as in the previous section, which is

$$\mathbf{s} = G^o\left(\frac{x(1+Bt_0)}{1+Bt}\right)\frac{1+Bt_0}{1+Bt}\begin{pmatrix}\frac{fV_0}{4\sin\theta}\\ 1\end{pmatrix}e^{ia(t)x} \quad \text{with} \quad a(t)\equiv a^o\frac{1+Bt_0}{1+Bt}\,, \tag{3.88}$$

where $B\equiv 3A/2$ and the perturbation is introduced in the background flow at the instant of time t_0. It is clear that for the ray $x(t)=1+Bt$, the perturbation amplitude decreases as time goes on at the rate $1/(1+Bt)$. In this case, the initial slope of the background flow affects the growth rate until $t\gg 1/B$.

3.4 Numerical stability analysis

3.4.1 Design of a numerical experiment

The initial configuration (at $t=t_0$) of the perturbation U' to be simulated is depicted in Figure 3.12 on the basic flow V (henceforth, we will use just the first term in the expansion (3.73) to compute the base state), and is given by (Bohorquez, 2007c)

$$U'(X,t_0) = \begin{cases} G^o(l_1)\sin\left(2\pi n\frac{X-l_1}{l_2-l_1}\right) & \text{if } l_1\le X\le l_2 \\ 0 & \text{otherwise}\end{cases}\,, \tag{3.89}$$

where G^o denotes the initial amplitude of the perturbation ($G^o\equiv\delta\,V(l_1,t_0)$, being δ a very small parameter), l_1 and l_2 establish the boundary enclosing the initial waves, and n denotes the number of waves. For the height η', we suppose that the perturbed flow also satisfies the kinematic wave approximation, obtaining the relation that follows:

$$\eta'(X,t_0) = \frac{f}{8\sin\theta}(V+U')^2 - H \approx \frac{f}{4\sin\theta}VU'\,,$$

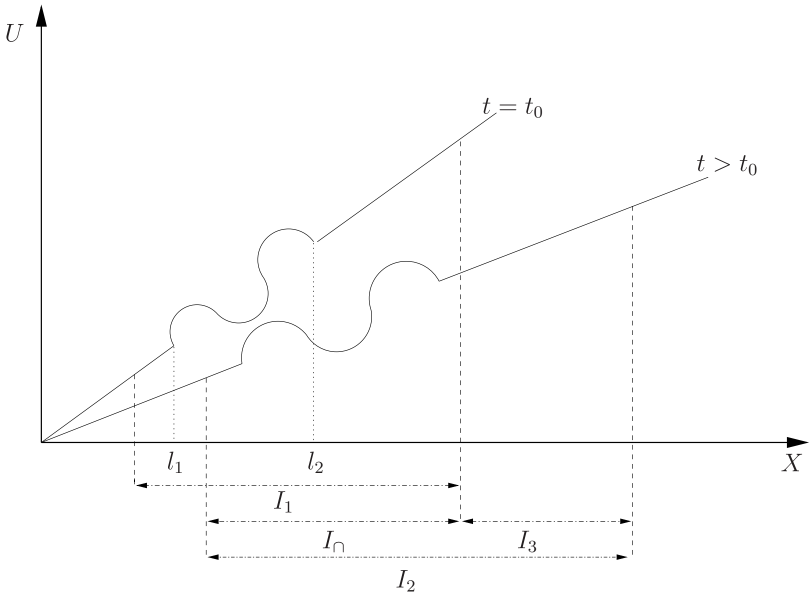

Figure 3.12: Sketch of the initial condition at $t = t_0$ for the velocity field U according to the numerical experiment defined in § 3.4.1.

which is $O(\delta H)$. In fact, the resulting ratio of the perturbation amplitude of the height to the velocity is exactly the same as the ratio between the eigenfunctions F and G in the previous section. So, we are able to compare directly the results in this section with the previous analytical one.

The convective nature of the perturbations is easily established in terms of the Froude number. This is understandable in view of the fact that both the linear (3.4)-(3.5) and non-linear (2.1)-(2.2) system of Partial Differential Equations (PDEs) have two real and distinct characteristic curves, and these are the same for small waves. Hence, perturbations travel along the characteristics $C_\pm : dX/dt = V \pm \sqrt{H \cos\theta}$, and the convective nature comes for supercritical kinematic waves: $dX/dt \approx V(1 \pm 1/Fr_{eq}) > 0$ with $Fr_{eq} > 1$. From now onward, we are interested in supercritical flows.

To compute the linear evolution of the perturbations, we use a finite-difference scheme on a uniform grid with mesh size ΔX. The time integration is performed with a Crank-Nicolson method, and a fourth-order central-differences scheme is applied in space - the truncation error is $O(\Delta t^2, \Delta X^4)$, where Δt is the time step. In order to use the minimal number of nodes, we initially solve the resulting linear system of equations just in a small region I_1 with homogeneous boundary conditions. Before the wave train travelling downwards reaches the end of I_1, a new domain I_2 is defined containing the subregion in which waves live (denoted as $I_\cap$ in Fig. 3.12), and it is enlarged downwards adding new nodes (subdomain I_3). This process is repeated several times during the numerical simulation. Thus, we have to solve in each time step a linear system of equations with just eleven diagonals. Band storage mode is used to minimise memory requirements. To that end, subroutines DGBMV and DLSLRB into the IMSL Numerical Libraries are used.

On the other hand, the full non-linear set of equations (2.1)-(2.2) is solved with the numerical technique described in the next Chapter. In this case, taking into account that the flow is supercritical at both inlet and outlet, two boundary conditions are imposed upstream (given by Eq. 3.74), and the characteristic variable extrapolation (CVE) method is used downstream. For simplicity we apply the first-order version of the CVE method. The first-order extrapolation does not imply a uniform outflow regime, although the physical meaning is similar: the information is travelling from the interior spatial domain and therefore the outflow regime is determined from the solution inside the boundary. Next, we present some results.

3.4.2 Results

First, we will show results corresponding to the parallel case. To that end, we have considered a uniform and steady basic flow with $U = 1$ and $\theta = 1^o$. This flow has been initially disturbed with n small waves ($n = 10$), and its non-linear evolution has been computed following the approach introduced above. Figure 3.13 depicts the maximum amplitude of the wave train as a function of time for several Froude numbers. Initially, the non-linear growth rate is in agreement with theoretical results obtained using the linear theory, but as time goes on, and the wave amplitude is not so small, the wave changes its shape towards hydraulic jumps (see Fig. 3.14) and saturation appears due to non-linear effects. One should note that the main difference of the numerical technique we have used, with respect that applied by Brook et al.

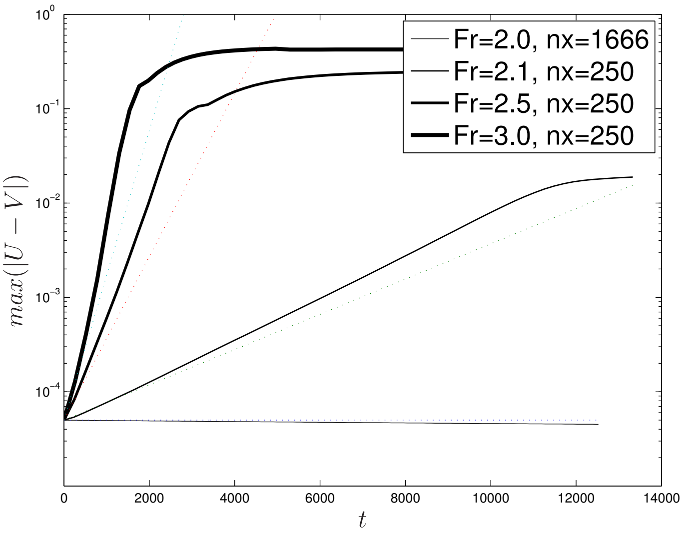

Figure 3.13: Amplitude of the water wave velocity, $U - V$, against non-dimensional time, t, for different steady flow Froude numbers $Fr_{eq} \geq 2$, for a velocity perturbation with an initial amplitude $\delta = 5 \times 10^{-5}$. The solid curves represent the solution obtained from the non-linear numerical code, and the dashed lines indicate the corresponding growth rates obtained from the linear stability analysis (see, e.g., Brook *et al.* 1999). nx represents the number of nodes used by wave.

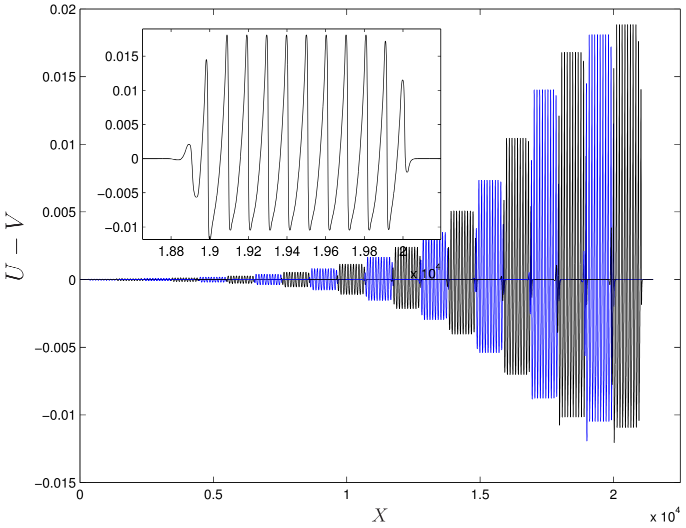

Figure 3.14: Plots of perturbation velocity, $U - V$, against distance along the channel, X, at several instants of time ($t < 1.4 \times 10^4$) corresponding with the case $Fr_{eq} = 2.1$ shown in Fig. 3.13.

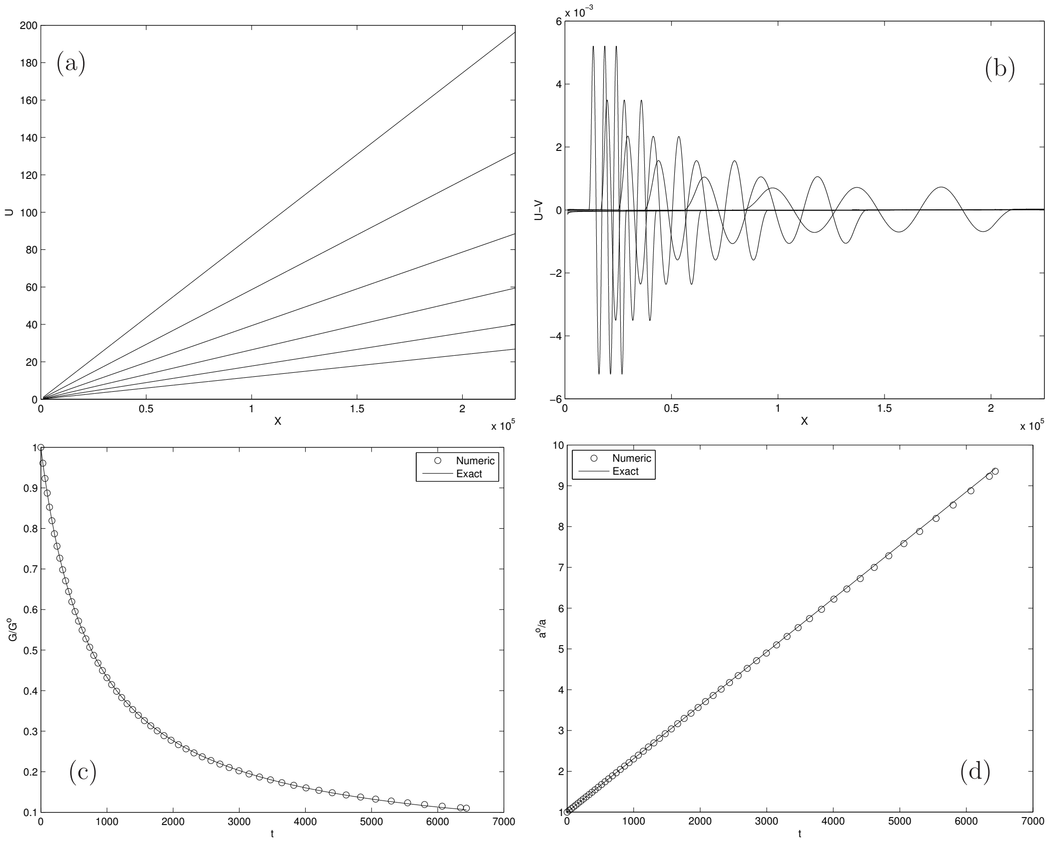

Figure 3.15: Plots of the non-linear flow velocity U (a) and the non-linear perturbation velocity $U - V$ (b) against the distance along the channel X at several instants of time. Figures (c) and (d) depict the evolution in time of both the numerical and the linear [see Eq. (3.88)] amplification factor $G(t)$ and the wavelength $1/a(t)$ along the ray $x(t) = 1 + Bt$. The parameter values are $Fr_{eq} = 2$, $\theta = 1^o$, $B = 0.0013$ and $t_0 = 0$.

(1999), are the boundary conditions. Traditionally, roll-waves are numerically studied by using their periodicity properties, and periodic boundary conditions are usually stated. However, in order to analyse the stability of more general basic flows (see below), which are not periodic, we have followed a different approach.

To check the ability of the non-linear numerical code computing the evolution of small perturbations, and the validity of the linear stability analysis in section 3.3, we start with the analysis of the stability of the unsteady and non-uniform base state given by (3.87). One should focus the interest on the question that follows: how

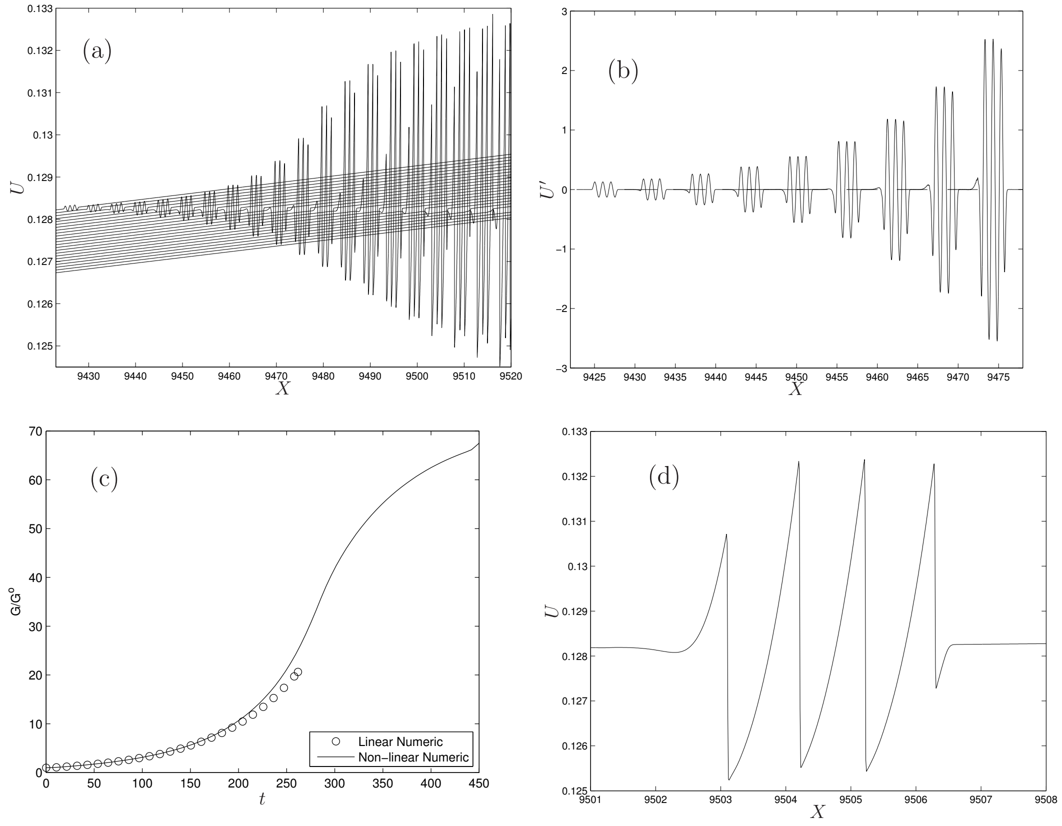

Figure 3.16: Plots of the non-linear flow velocity U (a) and the linear perturbation velocity U' (b) against the distance along the channel X at several instants of time. Figure (c) depicts the evolution in time of the numerical non-linear and linear growth rate, and (d) shows in detail the ensuing roll-waves. The parameter values of the base flow are $Fr_{eq} = 2.2$, $\theta = 1^o$, $B = 2.04 \times 10^{-5}$ and $t_0 = 0$.

temporal and spatial gradients of the basic flow affect the stability criteria. As we expected from the analytical analysis presented in section 3.3, the non-linear velocity profile U, that is linear with X at the initial instant of time $t = 0$, remains being a linear profile in X as the time increases [see subplot 3.15(a)]. The perturbation introduced at the initial instant of time in the basic flow is difficult to be observed in this figure since its amplitude is $\delta = 10^{-5}$ times lower than the basic flow, but is clearly depicted in subfigure 3.15(b). The perturbation was obtained removing the base flow (3.87) from the the non-linear velocity U that was computed numerically. The non-linear perturbation behaviour is in excellent agreement with that inferred in the linear stability analysis by multiple scales (section 3.3). The (exact) linear and (numerical) non-linear amplification factor is indistinguishable, as shown in Fig. 3.15(c), as well as the wavelength modulation [see 3.15(d)]. Therefore, the first novel result we have found, when analysing the particular case $Fr_{eq} = 2$, is that non-parallel and unsteady effects stabilise the flow. Furthermore, the wavelength remains constant in the parallel case as time goes on (e.g. Prokopiou et al., 1991; Brook et al., 1999), whilst disturbances lengthen in the present case.

Second, when increasing the Froude number, the flow may become unstable - as shown in Fig. 3.16(a), which corresponds with the non-linear numerical simulation of a background flow (with Froude number $Fr_{eq} = 2.2$, $\theta = 1^o$, $B = 2.04 \times 10^{-5}$ and $t_0 = 0$) in which a small perturbation, of wavelength unity, is introduced at the initial state. A similar result is obtained with the linear theory as shown in subfigure 3.16(b). The amplitude of the perturbation increases as convected downstream, with a growth rate that is in agreement with the linear theory at early time [see Fig. 3.16(c)]. Similar to the parallel case, the non-linear growth rate is saturated at late time due to the formation of roll-waves, that cannot be studied by using the linear theory. But there are cases with Froude numbers $Fr_{eq} > 2$ that are stable to the presence of small perturbations. For instance, Fig. 3.17 depicts the linear evolution of a stable perturbation in a basic flow with $Fr_{eq} = 2.2$, $\theta = 1^o$, $B = 6.1 \times 10^{-4}$ and $t_0 = 0$ - the wave amplitude decreases while the wave lengthens as time goes on. Hence, even background flows with Froude numbers larger than two are stable for some wave numbers (Bohorquez, 2007c).

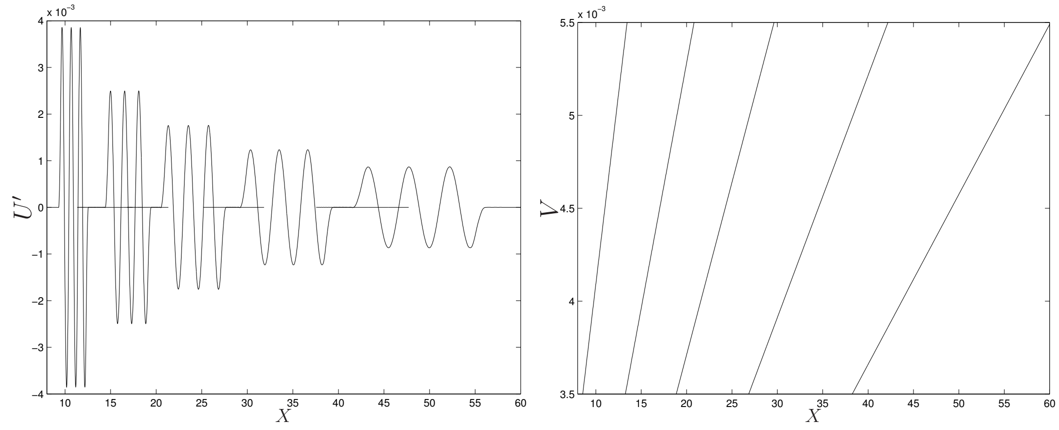

Figure 3.17: (a) Linear numerical simulation of a three-waves train over the base flow shown on the right-hand side (b). We have selected $Fr_{eq} = 2.2$, $\theta = 1^o$, $B = 6.1\times10^{-4}$ and $t_0 = 0$

3.5 Summary and conclusions

In this study we have considered the stability analysis of a suddenly released, fixed mass of fluid that reaches a kinematic regime. In particular, we have considered the influence of near- and non-parallel effects on the linear stability criteria, and found an asymptotic analytical solution for the critical Froude number as a function of both the wave frequency and non-parallel characteristic of the base flow. Then, the exact solution for the linear perturbations with $Fr = 2$ have been obtained by means of multiple scale expansion. This result was compared against the non-linear simulation of the perturbation, showing a perfect matching between both solutions. However, the near- and non-parallel spatial stability analysis fail to predict the linear stability criteria to the unnegligible influence of the base-flow temporal variation. Finally, we have designed a numerical experiment, and a clever numerical method, that allow us to compute the linear and non-linear evolution of small perturbations.

We have found that non-uniform and unsteady effects of the background flow stabilise turbulent roll-waves and raise the critical Froude number required for instability. The well known stability criteria for parallel flows at high Reynolds number (the basic flow is unstable for any wavelength and Froude number larger than 2) differs abruptly of that resulting from kinematic waves. One of the most noticeable effects is stabilisation of disturbances on basic flows with $Fr_{eq} = 2$. In addition to that, for larger Froude numbers, $Fr_{eq} > 2$, the wave amplitude decreases or increases depending on the velocity, and both spatial and temporal gradients of the base flow. Finally, stable waves lengthen as the flow evolutes in time - this behaviour is also different with respect to the parallel one, in which waves remain with constant wavelength even when hydraulic jumps are developed (Bohorquez, 2007c).

Chapter 4

Transport of suspended sediment under the dam-break flow on an inclined plane bed of arbitrary slope

4.1 Introduction

Dam-break hydraulics of natural rivers and its associated erosion and transport of sediments is an important practical problem in civil and environmental engineering. The precise formulation of the equations that govern the problem, with all the fluid mechanics and their transport phenomena is, even in its one-dimensional version and for dilute sediments, a very complex task (see, for instance, Bellos and Hrissanthou, 2003). This panorama becomes much more complex when two- or three-dimensional debris (non-Newtonian fluid) flows are considered (e.g. Spinewine and Zech, 2007; Jakob and Hungr, 2005). In addition, the numerical techniques needed to solve these equations, that must, for instance, capture with precision the advance of water fronts with their induced sediment transport, is a formidable task.

For this reason, to gain some preliminary understanding of these physical and numerical problems, much effort has been dedicated in the recent past to model, in simpler dam-break flows over a horizontal bed, some of the basic ingredients, such as erosion and deposition of sediment particles (Pritchard and Hogg, 2002; Cao et al., 2004) and friction (Hogg and Pritchard, 2004), as well as to the development of powerful and accurate numerical techniques that are able to cope with these problems (e.g. Toro, 2001; LeVeque, 2002; Zoppou and Roberts, 2003).

In this line, we consider here the dam-break flow over a plane inclined bed, which, in relation to its horizontal bed counterpart, is more appropriate to model avalanches after natural dam failures, mainly for two reasons: for the obvious one that the rivers beds are not horizontal, and because it considers the movement of a *finite* mass of water with its associated sediment transport. An important advance was made in this direction by Dressler (1978). This relaxes one of the main limitations of the traditional shallow-water formulation [e.g., Stoker (1957)], which is valid only for small slopes of the bed, and thus inappropriate to model real river flows with large slopes where this kind of avalanches are more frequent to occur. This generalisation obviously makes the shallow-water equations much more involved. However, for a constant, but arbitrary, slope of the bed, the equations are quite similar to the traditional shallow-water equations. We use here these equations to solve the dam-break problem over an inclined bed of arbitrary but constant slope, together with its associated transport of dilute sediments, and taking into account the effect of friction. Thus, our results will shed new light on the problem of transport of sediment due to the release of a finite mass of water after the rupture of a dam on an inclined bed of arbitrary (large) slope. Although these results have the limitations of one-dimensional flow, constant bed slope, and dilute, non-cohesive sediment with depth-averaged concentration, they give general trends about the transport of sediments as a function of the bed slope, and on how the validity of the formulation and the predictions are affected by the several parameters in the erosion, deposition, and friction models. A similar problem was recently considered by Pritchard (2005). However, the asymptotic solutions given by this author do not predict, for instance, the formation of *roll waves* near the advancing water front which we find in our numerical simulations. The effect of these waves on the transport of sediments may be very significant. The results given here will be also valuable to check future numerical codes to solve more complex formulations where arbitrary slopes and slope variations, together with non-dilute sediments with vertical variation of concentration, are taken into account. We also check the accuracy of the different numerical techniques in capturing the advance of water fronts over a dry bed.

Although this chapter is mainly focussed on the computation of the *suspended* transport of dilute sediment down an inclined bed after the rupture of a dam (as the title runs), we shall also consider the *bed-load* transport of sediments. In particular, we shall characterise the relative importance of the bed-load transport to the suspended transport for different slopes of the bed, and different diameters of the sediment particles, by using different conditions for the initiation of sediment suspension from bed-load. This will complete the picture of transport of sediments in the present dam-break problem on an inclined bed, and *characterise the validity* of the dilute suspension approach.

The structure of the chapter is the following. In section 4.2 the mathematical problem is formulated and the numerical method is briefly described. Section 4.3 is devoted to check the numerical method and the friction model by comparison with known analytical solutions and experimental data. In section 4.4 we present the results for the transport of suspended sediments after the breaking of the dam on an inclined bed, which are complemented in section 4.5 with bed-load sediment transport results. Some conclusions are drawn in section 4.6.

4.2 Formulation of the problem and numerical method

We consider here the one-dimensional flow over a constant slope bed. In the shallow-water approximation (see Chapter 2), the dimensionless equations for the mass conservation and momentum in the direction of the flow are given by (2.1)-(2.2). To compute the friction term, s_f, we shall use the Darcy-Weisbach friction factor f (2.3). The factor f is a function of the local Reynolds number, based on the velocity U and the hydraulic diameter of the channel, and the relative height roughness of the bed. In particular, we shall use the Colebrook-White (Colebrook, 1939) expression to approximate f (see below, § 4.2.1). To check the validity of this approximation to model the friction in a dam-break flow, we shall compare in § 4.3 existing experimental data for the dam-break problem on a horizontal bed with the results obtained with this friction model.

The non-dimensional shallow-water equation for the conservation of sediment transported as a dilute, well-mixed suspension can be written as

$$\frac{\partial c}{\partial t} + U \frac{\partial c}{\partial X} = E \, \frac{q_e - q_d}{\eta} \,, \tag{4.1}$$

where c is the dimensionless, depth-average mass concentration of suspended sediment, and q_e and q_d are the dimensionless mass erosion and mass deposition fluxes, respectively. The concentration of sediment is made dimensionless with m_e/w_s, where w_s is the settling velocity of the particles [see Eq. (4.10) in § 4.2.1], and m_e is a characteristic, constant mass flux per unit area that characterises the erosion flux (see, e.g., Sanford and Maa, 2001). This flux m_e is used to non-dimensionalise both the erosion and deposition fluxes. With this choice, the dimensionless parameter

$$E \equiv \frac{w_s}{U_0} \tag{4.2}$$

is a ratio between the settling velocity and the characteristic fluid velocity, and q_e and q_d may be written as (e.g., Dyer and Soulsby, 1988; Sanford and Maa, 2001; Pritchard and Hogg, 2002)

$$q_e = \begin{cases} \left(\frac{U^2}{U_e^2} - 1\right)^p & \text{for } |U| \geq U_e \\ 0 & \text{for } |U| < U_e \end{cases} \,, \tag{4.3}$$

$$q_d = c \,. \tag{4.4}$$

U_e is the non-dimensional velocity above which sediment particles are eroded from the bed and suspended into the flow, and the exponent p is a number often taken to be unity (Sanford and Maa, 2001). According to Bagnold (1966), the threshold velocity U_e for suspension is such that the turbulent friction velocity $v_* \equiv \sqrt{\tau_b/\rho}$ exceeds the settling velocity w_s of the particles by a certain factor (a say). Relating the bed shear stress to the Darcy-Weisbach friction coefficient, one may write the following relation for U_e:

$$U_e = aE\sqrt{8/f}\,, \tag{4.5}$$

where a is a dimensionless constant of order unity to be obtained experimentally. Its value is well defined for small sediment particles, i.e. for d_s/η_0 less than about 10^{-3}, where d_s is the diameter of the sediment particles and η_0 is a characteristic depth (see, e.g., Julien, 1995), but it is not so well defined for larger values of d_s/η_0. In this case of larger particles, the sediment transport does not pass neatly from a bed-load mode to a suspended load mode as v_*/w_s becomes larger than a given constant a, but there exists a mixed mode of sediment transport. Experimental values of a range between 0.2 (for this value, incipient erosion and suspension may occur for large particles) and nearly 5 [for $u_*/w_s > 5$, all the sediment transport is by suspension; e.g Julien (1995)]. In the computations of § 4.4 we shall use a mean value $a = 1.2$ (Chanson, 2004), though several other values will be used in § 4.5 for the comparison between the bed-load, and the suspended, sediment transport mechanisms in the present problem.

Typical values of the remaining parameters p and E are discussed in the next Section, together with some comments on the physical model that underlies the flux (4.3).

We are interested here in solving these equations for the dam-break problem (see Fig. 2.1), i.e., for the flow whose initial condition ($t = 0$) is given by (2.4), (2.6) and

$$c(0, X) = 0\,, \tag{4.6}$$

At $t = 0$, the vertical wall that intersects the bed at $X = e$ is removed instantaneously, causing the fluid to move over the slopping bed under the action of gravity. Note that the characteristic length η_0 is the dimensional depth at $X = 0$, $t = 0$.

Equations (2.1)-(4.1) with initial conditions (2.4)-(4.6) are solved numerically on an uniform grid with mesh size $\Delta X = X_{i+(1/2)} - X_{i-(1/2)}$ using an upwind TVD method (see, e.g., LeVeque, 2002), second-order accurate in both space and time, with a semi-implicit and upwind treatment of the source terms, as described by Burguete and García-Navarro (2001).

A flux limiter function has been used to solve the hyperbolic equations (see, e.g., Sweby, 1984; LeVeque, 2002). In particular we use that termed as 'MinMod' by

Sweby (1984), which works better in the present problem where one has to capture numerically the advance of a water front over a dry bed (see § 4.3.2 below). To avoid numerical discontinuities at the critical points we have used here the entropy correction technique described in Burguete and García-Navarro (2001) whenever they are detected between any two grid points. Finally, the numerical stability condition, based on the Courant-Friedrichs-Lewy number

$$CFL \equiv \frac{\Delta t}{\Delta x}|\lambda_{max}|, \tag{4.7}$$

where Δt is the time step, and $|\lambda_{max}|$ the maximum absolute value of the eigenvalues of the Jacobian of the transformation of the equations to its non-conservative form at the grid points (LeVeque, 2002), can be written as

$$CFL \leq \frac{1}{1+\frac{1}{2}\max(\phi)},$$

being ϕ the flux limiter function.

4.2.1 Friction and sediment models

For the Darcy-Weisbach friction factor f (sometimes also called Darcy, or Fanning, friction factor in the turbulent pipe literature) appearing in Eqs. (2.3) and (4.5), we shall use the Colebrook-White expression (Colebrook, 1939)

$$\frac{1}{\sqrt{f}} = -2.0\log_{10}\left(\frac{k_s}{3.71 D_H} + \frac{2.51}{Re\sqrt{f}}\right), \tag{4.8}$$

where k_s is the average roughness height of the bed [Nikuradse's equivalent sand roughness; see, e.g., Schlichting (1987)], and

$$Re = \frac{U\sqrt{g\eta_0}D_H}{\nu}, \tag{4.9}$$

is the local Reynolds number, where D_H is the hydraulic diameter (note that for one-dimensional flow, $b \gg \eta_0$, where b is the channel width, $D_H \simeq 4\eta_0\eta$), and ν is the kinematic viscosity of the fluid. In the computations reported in Secs. 4.4 and 4.5 we use $\nu = 10^{-6}m^2/s$, and values of η_0 between 1 and $10m$. For the roughness height k_s, several experiments have obtained values between one and ten times the sediment particles mean diameter d_s (e.g. van Rijn, 1987). We shall use a mean value $k_s = 2d_s$ (Chanson, 2004).

The depositional model (4.4), in which all the particles fall at the same settling velocity w_s, is appropriate for fine suspended, non-cohesive sediment, like for example sand (Pritchard and Hogg, 2003). There exists more complex expressions that take into account the formation and break-up of aggregates, or a different near-bed concentration to the average one that controls the deposition of particles (see, e.g., Cao, 1999). However, we will restrict ourselves to the simple model (4.4) in this work. To be coherent with this non-cohesive sediment deposition model, the power p in the erosion model (4.3) must lie in the range $3/2 \leq p \leq 7/2$ (Dyer and Soulsby, 1988). Nonetheless, we have also used the value $p = 1$ in the computations of section 4.3 to compare with previous analytical dam-break results.

For sediment particles with mean diameter in the wide range $d_s < 60\,mm$, one may use the following experimental expression for the settling velocity (Brown and Lawler, 2003):

$$w_s = \sqrt[3]{g\nu(s-1)} \left[\left(\frac{18}{d_*^2} \right)^{0.898\left(\frac{0.936 d_* + 1}{d_* + 1}\right)} + \left(\frac{0.317}{d_*} \right)^{0.449} \right]^{-1.114} . \qquad (4.10)$$

Taking $s = \rho_s/\rho = 2.65$ for quartz particles in water, the settling velocities predicted by this formula lie in the interval $0.003\,m/s < w_s < 0.114\,m/s$. Thus, for a reference depth η_0 between $1m$ and $10m$, the non-dimensional parameter $E = w_s/\sqrt{g\eta_0}$ (4.2) will lie in the range $3 \times 10^{-4} < E < 0.036$, approximately.

4.2.2 Morphological changes in the bed elevation

In the equations (2.1)-(2.2) and (4.1) we have assumed that the suspended sediment particles remains always very dilute, so that we have neglected the effect of the concentration of the particles on the fluid density ρ (we have also neglected its effect in the fluid viscosity to compute the friction factor f). For this reason we have also neglected any morphological change in the bed elevation produced by the deposition and erosion of sediments.

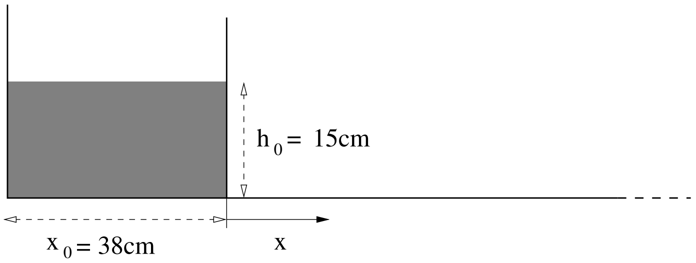

Figure 4.1: Sketch of the experimental setup of Jànosi *et al.* (2004).

To justify this, we re-write below Eq. (2.1) taking into account this effect. But first, the non-dimensional equation for the change of bed elevation due to deposition and erosion of particles may be written as

$$\frac{dz}{dt} = B(q_d - q_e)\,, \tag{4.11}$$

where z is the non-dimensional bed elevation in relation to the initial inclined plane, and the non-dimensional parameter B is defined as

$$B \equiv \frac{m_e}{\rho_s(1-P)U_0}\,, \tag{4.12}$$

where ρ_s is the particles density and P the bed porosity. Then, the non-dimensional mass conservation equation (2.1) that takes into account the variation of the bed elevation may be written, for dilute suspended sediments, as

$$\frac{\partial \eta}{\partial t} + \frac{\partial (u\eta)}{\partial X} = B(q_e - q_d)\,. \tag{4.13}$$

Since m_e usually ranges between 5×10^{-5} and 5×10^{-3} $kg/(m^2 s)$ (Sanford and Maa, 2001), and $\rho_s U_0$ is always larger than $10^3 kg/(m^2 s)$ (for η_0 of the order of $1\,m$, or larger), B is always very small, so that it is justified to neglect the variation of the bed elevation for dilute suspensions, provided that $|q_e - q_d|$ remains order unity.

4.3 Check of the numerical method and frictional model

To check the accuracy of the numerical technique, as well as the validity of the frictional model, in the following two subsections we apply the equations to two

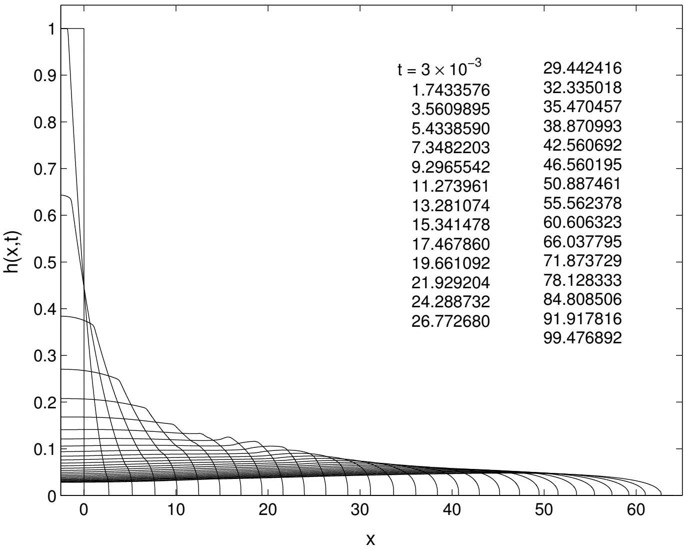

Figure 4.2: Dimensionless height as a function of x for several instants of time (as indicated) after the sudden release of the gate.

different situations described in Jánosi et al. (2004) and Pritchard and Hogg (2002), and compare our numerical results with the experimental data, and with the analytical solution, respectively, given in them. In section 4.3.2 we also compare the results obtained from different numerical schemes.

4.3.1 Comparison with experimental data for the dam-break problem on a horizontal bed (with friction)

Jánosi et al. (2004) have recently reported a series of experimental results for the dam-break problem in a horizontal ($\theta = 0$) glass channel of width $b = 16\,cm$. We compare here our numerical results obtained from different friction models with their experimental data for the dam-break flow of pure water over a dry bed. In particular, the flow is produced when a gate initially at $x = 0$ is suddenly removed, releasing the water filling a lock of length $38 cm$ and height $\eta_0 = h_0 = 15\,cm$ (see sketch in Fig. 4.1). To simulate numerically the vertical wall at the beginning of the channel, $x = -38\,cm/15\,cm \simeq -2.53$, we consider the numerical problem with a symmetry plane there.

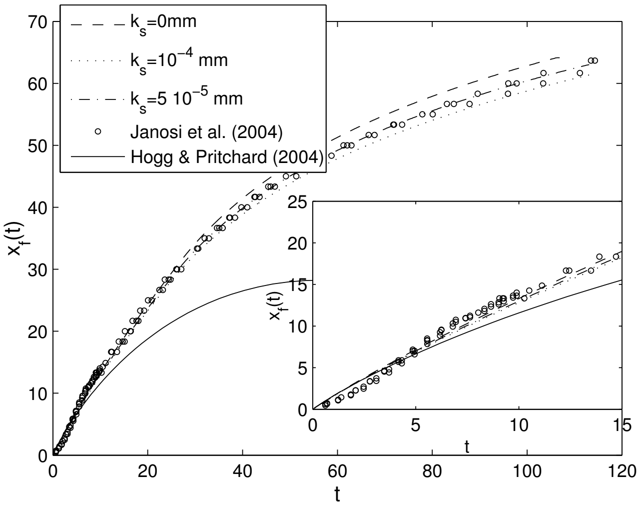

Figure 4.3: Temporal evolution of the water front obtained with Darcy-Weisbach friction factor (4.8) compared to the experimental results from Jànosi *et al.* (2004), and the asymptotic solution by Hogg and Pritchard (2004).

In Figure 4.2 we plot the computed dimensionless height $\eta = h(x,t)$ for several instants of time. In these simulations we have used Darcy's friction factor given by Eq. (4.8), with the hydraulic diameter $D_H = 4bh^*/(2h^* + b)$ (h^* is the dimensional height) and a smooth surface ($k_s = 0$). The computations are performed using a second order TVD-MinMod method with a spatial mesh size $\Delta X = (2/3) \times 10^{-6}$, and a time step given by $CFL = 0.45$. They show that the numerical method simulates correctly the advance of the water front over the dry channel, as well as other qualitative features of the dam-break wave, as compared with the photographs given in Fig.2 of Jánosi et al. (2004). To make a quantitative comparison with the experimental data, we plot in Fig. 4.3 the temporal evolution of the water front $X = x_f$ obtained from these simulations for a smooth surface, together with the experimental data given in Jánosi et al. (2004) (their figure 5). Also shown are the computed values of x_f using several, very small, values of the roughness height k_s. It is seen that the Colebrook-White friction model reproduces very well the experimental results, especially with $k_s = 5\times10^{-5}mm$ (it corresponds to a practically smooth surface). This fact justify the use of the Colebrook-White formula (4.8) to compute the friction term in the results given in sections 4.4 and 4.5. As commented on in § 4.2.1, we shall approximate the equivalent sand roughness with twice the size of the sediment particles, $k_s = 2d_s$. For comparison's sake we also include in Fig. 4.3 the asymptotic results of $x_f(t)$ given by the asymptotic solution in §4 of Hogg and Pritchard (2004). The agreement with our numerical solutions and with the experimental data of Jánosi et al. (2004) is quite good for the initial stages. However, beyond $t = 5$, approximately, the overall flow becomes affected by the rear vertical wall at $x = -x_0$ in the experiments (and in our numerical solution), and this effect is obviously not accounted for in the asymptotic solution by Hogg and Pritchard (2004), valid only near the wetting front.

4.3.2 Comparison with an analytical solution for the sediment transport in the dam-break problem on a horizontal bed without friction

The hydrodynamical part (η, U) of the dam-break problem on a horizontal bed is described by the well known Ritter's (1892) solution:

$$\eta(X,t) = \begin{cases} 1 & \text{for} \quad X < -t \\ \frac{1}{9}\left(2 - \frac{X}{t}\right)^2 & \text{for} \quad -t \le X \le 2t \\ 0 & \text{for} \quad X > 2t \end{cases}, \tag{4.14}$$

$$U(X,t) = \begin{cases} \frac{2}{3}\left(1 + \frac{X}{t}\right) & \text{for} \quad -t \le X \le 2t \\ 0 & \text{otherwise} \end{cases}. \tag{4.15}$$

Introducing these expressions into the suspended sediment transport equation (4.1), Pritchard and Hogg (2002) were able to obtain also an analytical solution for the sediment concentration c in the dam-break problem over a horizontal bed. To this end, these authors used Lagrangian co-ordinates, eliminating first constant E from Eq. (4.1) by re-defining the non-dimensional independent variables as

$$x^+ \equiv EX\,, \quad t^+ \equiv Et\,. \tag{4.16}$$

Figure 4.4 compares the analytical solution of Pritchard and Hogg with our numerical solution when $p = 1$ and $U_e = 1$ in the erosion model (4.3). In particular, this figure shows the sediment charge $Z = c\eta$ as a function of x^+ for $t^+ = 2$. It is

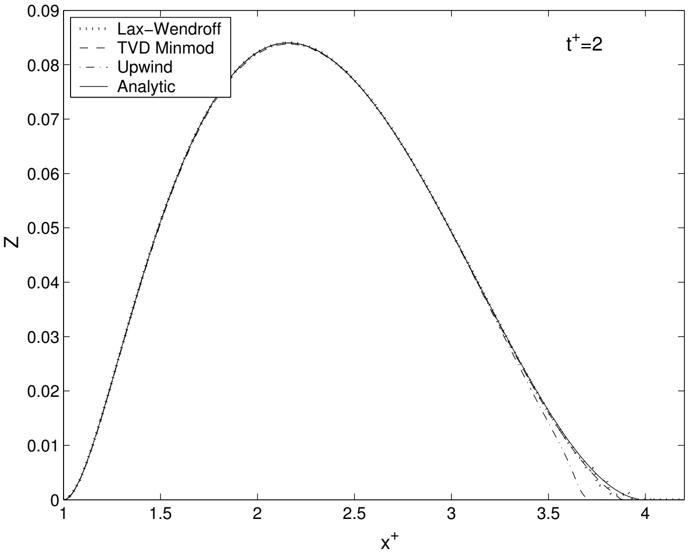

Figure 4.4: Sediment charge as a function of x^+ for $t^+ = 2$ from different numerical schemes, obtained with the same spatial and temporal resolutions ($\Delta x^+ = 10^{-3}$ and $CFL = 0.45$), compared to the analytical solution given in Pritchard and Hogg (2002).

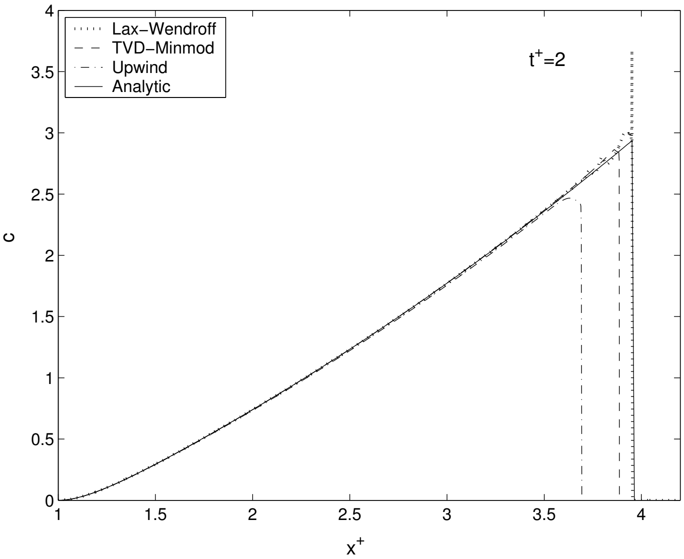

Figure 4.5: Concentration c as a function of x^+ for $t^+ = 2$ from different numerical methods, obtained with the same spatial and temporal resolutions ($\Delta x^+ = 10^{-3}$ and $CFL = 0.45$), compared to the the analytical solution of Pritchard and Hogg (2002).

observed that the agreement between the analytical and the numerical solutions is quite good. The errors are larger in the vicinity of the water front over the dry surface, $x^+ = 2t^+$, where, according to (4.14)-(4.15), the water height η vanishes and the velocity reaches its maximum value $U = 2$. This is due to the fact that the concentration c has a discontinuity at this point, falling abruptly from its maximum value to zero (see Fig. 4.5). This error may be reduced by decreasing the mesh size. In this figure 4.4 we have also compared the accuracy of different numerical techniques [Lax-Wendroff, first-order upwind, and TVD-MinMod; see, e.g., LeVeque (2002)]. It is seen that the TVD-MinMod method reproduces better the analytical solution for all values of x^+, particularly near the right water front: the upwind method has the poorest precision there, while the Lax-Wendroff method undergoes marked oscillation near the water front, where the concentration has a discontinuity. The results from the TVD-MinMod method in Fig. 4.4 are practically indistinguishable from the analytical solution. This comparison between the performance of the different numerical techniques is much better appreciated in Fig. 4.5, where we plot the distribution of the concentration c for the same time $t^+ = 2$.

4.4 Results

In this section we present the numerical results for the suspended sediment transport after the rupture of a dam on an inclined bed of constant, arbitrary slope. All the results are obtained with the second order TVD-MinMod method, $CFL = 0.45$ and 5000 nodes distributed along the spatial coordinate X.

First we present some detailed results for a given bed slope, corresponding to a bed angle $\theta = 20^o$. Figures 4.6-4.7 show some results about the hydrodynamics part of the problem (physical height η, velocity U, and flow rate $Q \equiv U\eta$) for some instants of time just after the rupture of the dam. To compute Darcy's friction factor, we have used a characteristic length $\eta_0 = 10m$ and $k_s = 1mm$. In Fig. 4.6 it is observed that the left ('drying') front remains stationary for the instants of time considered, while the right ('wetting') front advances quickly in time. At the position of this wetting front, where the water height vanishes, the velocity [Fig. 4.7 (a)] has a *fictitious* discontinuity due to the fact that there is no water downstream the front. This discontinuity becomes just a high slope for the flow rate, since we multiply U by η [Fig. 4.7(b)]. Also included as Fig. 4.7 (c) is the distribution of the Froude number $Fr \equiv U/\sqrt{\eta\cos\theta}$, which becomes singular at the wetting front.

The position of the wetting front as a function of time, $L_1(t)$, is plotted in Fig. 4.8 up to $t \approx 90$. For large t one observes some undulations. They are due to the oscillatory behaviour of the flow field near the wetting front at large time, as observed in Figs. 4.9-4.10. This behavior is not numerical, as corroborated by the fact that the same results are obtained with finer numerical resolution, and by the strongly unstable nature of the flow [as proved in the previous chapter]. It corresponds to the formation of roll waves (see, e.g., Brock, 1967; Whitham, 1974) near the wetting front, since the Froude number is significantly larger than 2 there [see Fig. 4.7 (c)]. As shown by Zanuttigh and Lamberti (2002), the shallow-water model, with an accurate numerical method similar to that used in the present work, correctly describes the development of roll waves in rectangular channels and reproduces Brock's (1967) experiments on roll waves. On the other hand, no undulations are observed in the numerical simulations if $Fr \leq 2$.

The corresponding sediment concentration profiles $c(X)$, and sediment charge profiles $Z(X) \equiv c\eta$, are plotted in Fig. 4.11 for the same instants of time considered in Fig. 4.9. They are obtained using $p = 1.5$ in the erosion model (4.3) and a particle size $d_s = k_s/2 = 0.5mm$. As it happens with the velocity, the concentration shows a fictitious discontinuity at the wetting front due to the fact that there is no water downstream it. The sediment charge presents marked local maxima near this front, due to the formation of roll waves, that the present numerical method recovers accurately, as shown by the inset in Fig. 4.11(b).

As an illustration of the physical reality of the roll-waves found in our numerical simulation, Fig. 4.12 depicts a sequence of three snapshoots of a water flood over erodible sediment bed: at the top of the pictures, the spreading of pure water (in pink) over a thin layer of fine sediment initially at rest (in brown) is shown; after travelling approximately half of the channel length, the pure water flood has fluidized and eroded the bed, as shown in the middle of the pictures; then, roll-waves appear

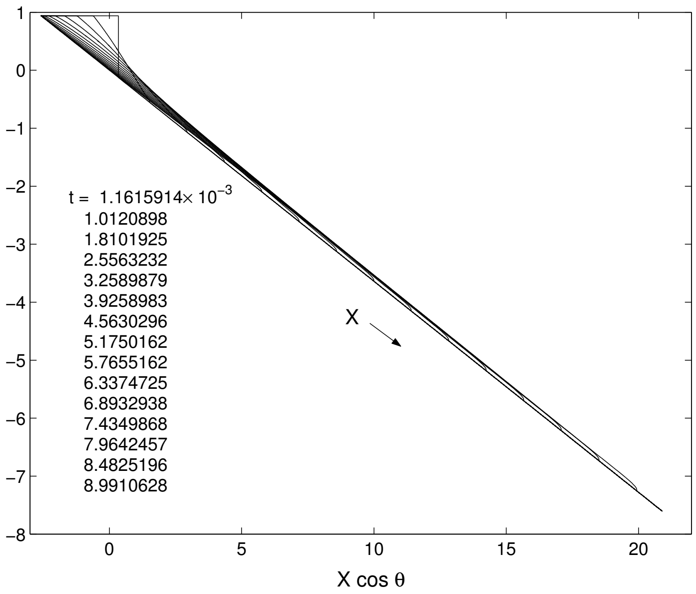

Figure 4.6: Height η for several instants of time (as indicated) just after the rupture of the dam for a bed with inclination $\theta = 20^o$.

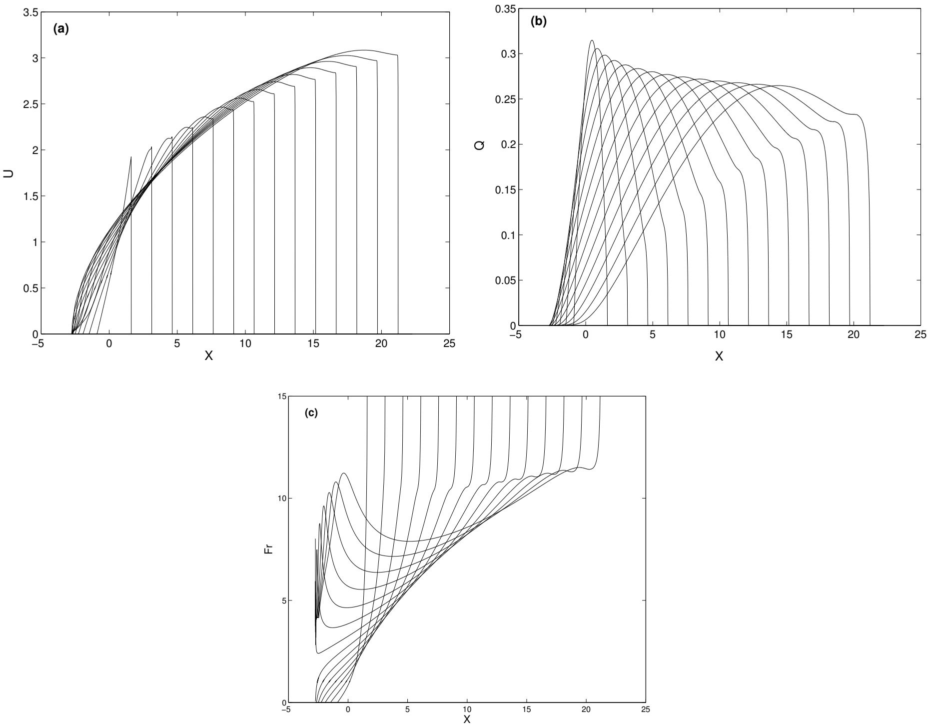

Figure 4.7: Velocity U (a) flow rate $Q = U\eta$ (b) and Froude number $Fr = U/\sqrt{\eta\cos\theta}$ (c) as functions of X for the same instants of time indicated in Fig. 4.6 ($\theta = 20^o$).

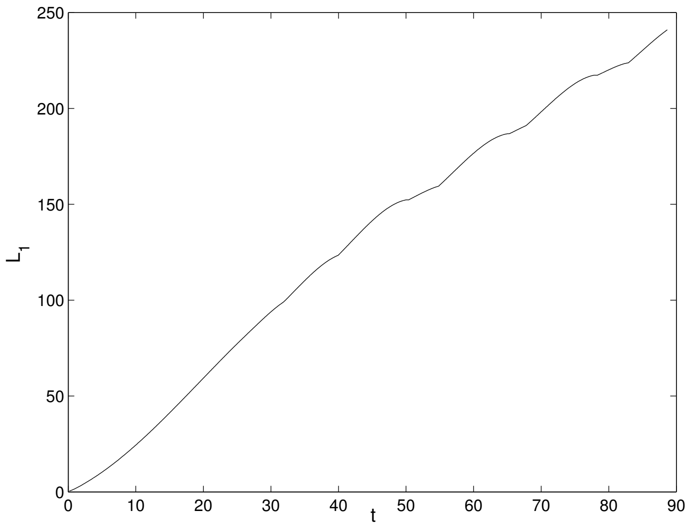

Figure 4.8: Position of the right ('wetting') front as a function of time, $L_1(t)$, for $\theta = 20^o$ ($\eta_0 = 10m$, $k_s = 1mm$).

(see the detail of the sudden expansion at the end of the flume, where the waves are clearly illustrated).

Although the non-dimensional mass concentration c reaches high values near the wetting front for intermediate times, its physical dimensional value depends on the quantity m_e/w_s that is used to non-dimensionalise the sediment concentration. To check the diluted sediment hypothesis, we may compute the maximum value of the sediment volume fraction, given by

$$\upsilon = \frac{cm_e}{w_s\rho_s} \,. \tag{4.17}$$

Using a typical value for the characteristic erosion mass flux, $m_e = 5 \times 10^{-5}\, kgm^{-2}s^{-1}$ (Sanford and Maa, 2001), $\rho_s/\rho = 2.65$ (quartz/water), and the corresponding value of the settling velocity w_s for the present sediment size [see Eq. (4.10)], the maximum value of the sediment volume fraction in the flow is $\upsilon \simeq 8.88 \times 10^{-4}$, reached at the wetting front for $t \simeq 23.58$. Therefore, the diluted sediment hypothesis is well satisfied in the present case.

As time goes on, both the sediment concentration and the sediment charge increase inside the flow, and then decrease (note that c and Z are much smaller for the first instant of time considered in Fig. 4.11). To have an idea of the total amount of

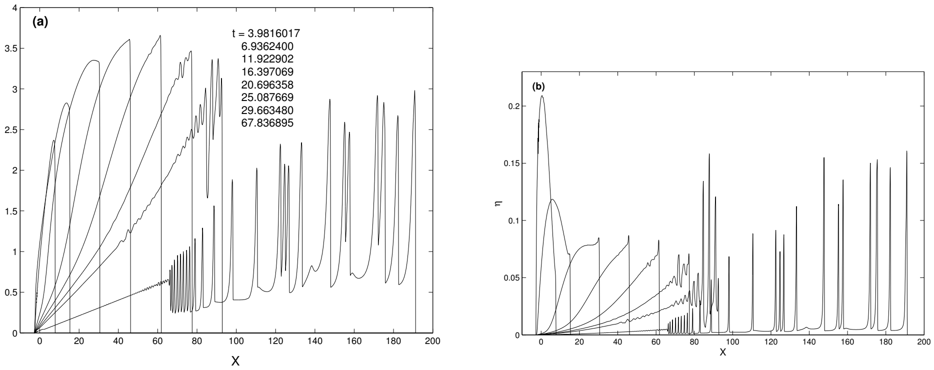

Figure 4.9: Velocity (a) and height (b) as functions of X for several instants of time, as indicated in (a) ($\theta = 20^o$).

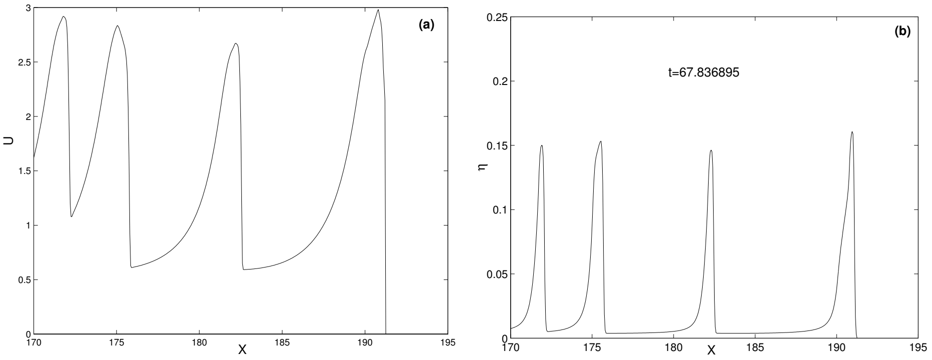

Figure 4.10: Details of the velocity (a) and water height (b) profiles near the wetting front at $t = 67.836895$.

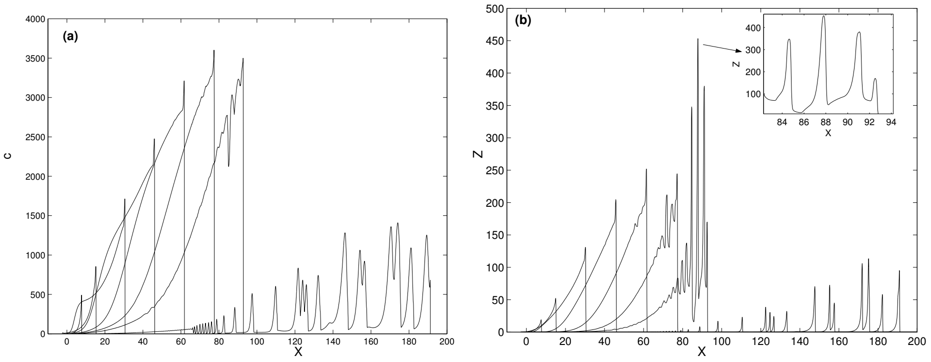

Figure 4.11: Sediment concentration profiles (a) and sediment charge profiles (b) as functions of X for the same instants of time considered in Fig. 4.9. The inset in (b) shows a detail of the largest value of $Z(X)$. $\theta = 20^o$, $\eta_0 = 10m$, $p = 1.5$, $d_s = k_s/2 = 0.5mm$.

Figure 4.12: Roll-waves in water flood over erodible sediment bed, observed in the experiments at the USGS Debris-Flow Flume (Logan and Iverson, 2007).

sediment inside the flow for a given time it is convenient to define the *total suspended sediment load*

$$Q_s(t) \equiv \int_{L_2(t)}^{L_1(t)} Z(X,t)dX \,, \tag{4.18}$$

where L_1 and L_2 are the right and left water fronts, respectively. Figure 4.13 shows $Q_s(t)$ for the present case. Initially it has a rapid growth in time, reaches a maximum $Q_{s,max}$, and then decreases, first as quickly as it increased, and then more slowly, with the oscillatory behavior at large time. At the end, all the eroded particles may become deposited if friction can slow down the flow below the critical value for erosion. This last process may be very slow owing to the oscillatory behavior of the wetting front. This long time behavior of the suspended sediment load is not accounted for by the recent asymptotic solutions by Pritchard (2005), which tend monotonically to zero in the absence of roll waves.

For the present slope ($\theta = 20^o$), we have performed the same computations for other values of the physical parameters. According to the discussion in the § 4.2.1, these parameters are basically reduced to three, η_0, d_s and p. The computations are summarised in Fig. 4.14, where the time evolution of the total suspended sediment charge $Q_s(t)$ is plotted for characteristic (limiting) values of these parameters. The computations are followed in time until Q_s is about ten percent of $Q_{s,max}$. It is observed that $Q_{s,max}$ can be very high (note the logarithmic vertical scale). For this reason, and in order to check the validity of the diluted suspended sediment hypothesis all along the flow, we also give in Fig. 4.14 the highest value of the sediment volume fraction reached along each flow (υ). This maximum value of the volume fraction is reached at the wetting front for some instant close to the time where Q_s reaches its maximum. Obviously, υ increases with η_0 (since more water is put into motion), with decreasing particle size (erosion is enhanced, and deposition reduced, as d_s decreases), and, more markedly, with increasing erosion power p (erosion is much more effective as p increases). All the cases plotted in Fig. 4.14 satisfy the hypothesis $\upsilon \ll 1$ (only for the case with $p = 3.5, \eta_0 = 10m$, and $d_s = 1mm$, υ is not so small). The case with $p = 3.5, \eta_0 = 10m$, and $d_s = 0.5mm$ is not plotted because υ is order unity. For $p = 1.5$, the dilute sediment approach is always valid, even for particle sizes smaller

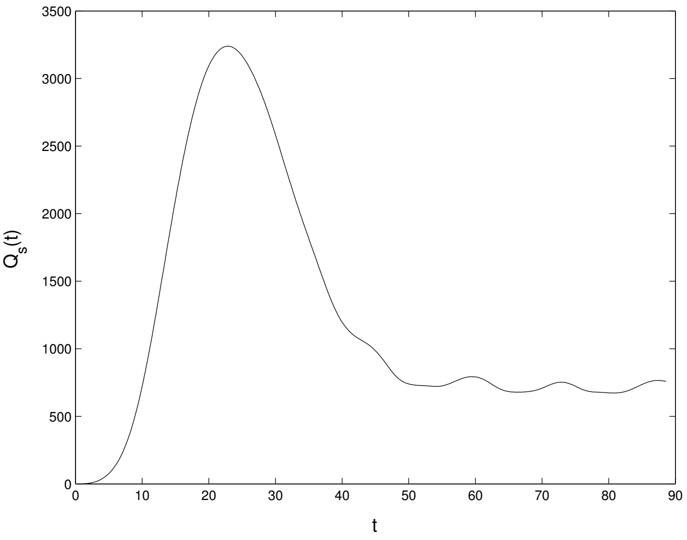

Figure 4.13: Total suspended sediment charge as a function of time for the same case considered in Fig. 4.11.

than those considered in Fig. 4.14.

The computations have been repeated for other values of the angle of the bed θ up to the maximum value given by the angle of repose ϕ_s, which for sand particles with $d_s < 10\,mm$ is between 30^o and 35^o (van Rijn, 1993). To characterise the downhill global transport of sediments after the break of the dam as a function of the bed angle θ we have selected two quantities: the maximum value of the total sediment load, $Q_{s,max}$, and the time at which this maximum is reached, t_{max}. The first quantity gives an idea of the total amount of sediment moved by the flow, and the second one tells us about the distance at which this sediment load is transported downhill the dam (provided one knows the advance of the wetting front). In order that these two dimensionless quantities are always evaluated for the same volume of water (same area in the initial triangle depicted in Fig. 2.1), independently of the bed angle θ, for a given characteristic length η_0, we normalise them by defining $Q^*_{s,max} = Q_{s,max} \sin\theta \cos\theta$ and $t^*_{max} = t_{max}/(\sin\theta\cos\theta)^{1/4}$. These two quantities are plotted in Figs. 4.15-4.16 as functions of the bed angle θ for some values of d_s, for $\eta_0 = 10m$ and $1m$, and for $p = 1.5$. Both $Q^*_{s,max}$ and t^*_{max} increase with decreasing d_s (obviously, as the size of the sediment particles decreases, more sediment load is put

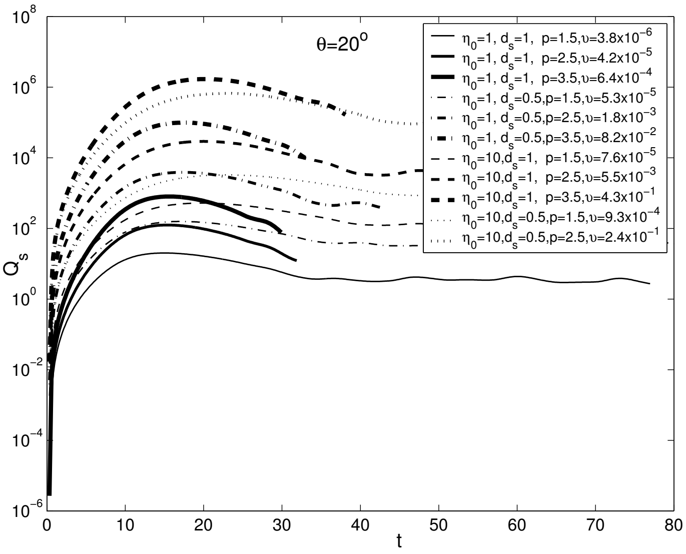

Figure 4.14: Total suspended sediment load as a function of time for $\theta = 20^o$ and several values of η_0 (m), d_s (mm) and p. Also shown is the maximum value reached by the sediment volume fraction inside each flow (υ).

into motion, and it is transported further downstream). Clearly, t^*_{max} decreases with θ, while $Q^*_{s,max}$ increases with θ. On the other hand, $Q^*_{s,max} \to 0$ and $t^*_{max} \to \infty$ as $\theta \to 0$ due to the volume normalisation (the volume of the water tends to infinity as $\theta \to 0$).

4.5 Discussion: Suspended versus bed-load sediment transport

The above results are for suspended sediment transport. As discussed on in section 4.2, sediment particles become eroded from the bed, and get suspended into the flow, when the fluctuation velocity near the bed v_* becomes larger than a times the settling velocity of the particles w_s, where a is an empirical constant that we have taken equal to 1.2 in the above computations. This criterion can be written in terms of a critical velocity U_e, given by Eq. (4.5), in such a way that when $U > U_e$ erosion, and suspended sediment transport, occurs. However, another type of sediment transport takes place along the bed even for velocities smaller than U_e. This bed-load sediment

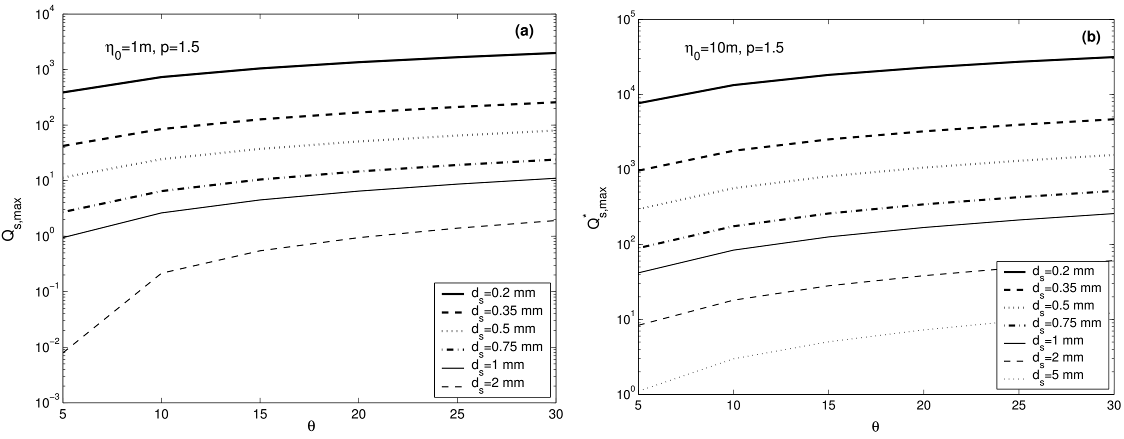

Figure 4.15: Normalised maximum of the suspended sediment load as a function of θ for different values of d_s (as indicated), $p = 1.5$, and for $\eta_0 = 1m$ (a) and $\eta = 10m$ (b).

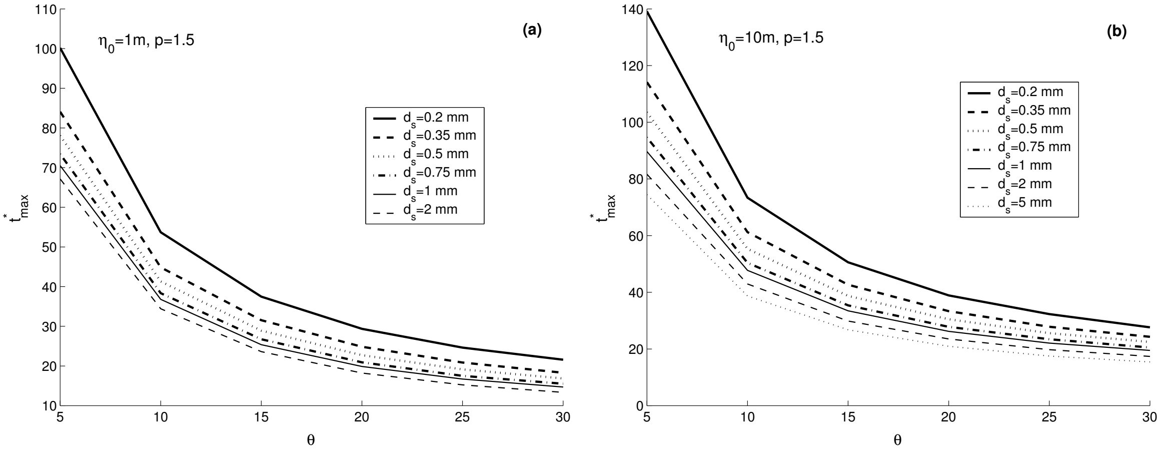

Figure 4.16: Normalised time at which $Q_{s,max}$ is reached as a function of θ for different values of d_s (as indicated), $p = 1.5$ and for $\eta_0 = 1m$ (a) and $\eta = 10m$ (b).

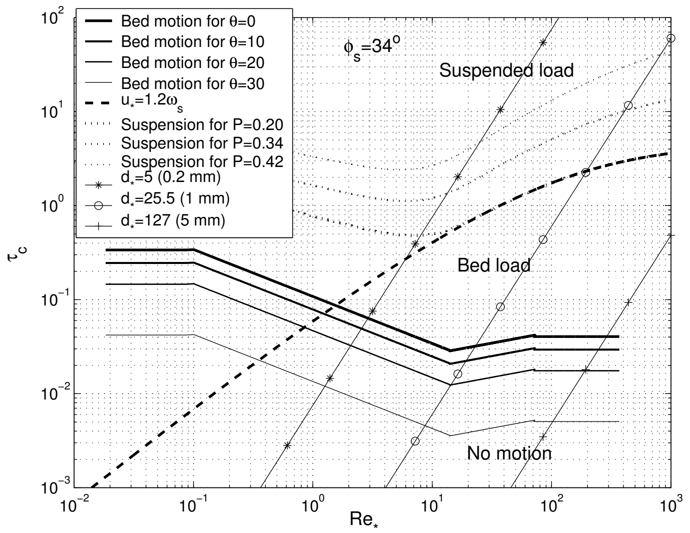

Figure 4.17: Modified critical Shields parameters (τ_c) for inception of bed-load sediment transport and suspended sediment transport as functions of the shear Reynolds number. $\phi_s = 34^o$.

transport occurs when the shear stress at the bed becomes larger than a critical value. Thus, in order to asses what fraction of the total sediment is transported by suspension (the above results), one has to characterise also the bed-load transport. In this section we compute the fraction between bed-load, and suspended load, sediment transport in the present dam-break problem for different sizes of the sediment particles and for different angles of the bed.

Sediment motion along the bed occurs when the so-called Shields parameter, defined as [see, e.g., Chanson (2004)]

$$\tau_* \equiv \frac{\tau_b}{\rho(s-1)gd_s} = \frac{fU_0^2U^2}{8(s-1)gd_s}\,, \qquad s \equiv \frac{\rho_s}{\rho}\,, \tag{4.19}$$

where ρ_s is the density of the sediment particles, is larger than a critical value, that depends only (for horizontal beds) on the shear Reynolds number

$$Re_* \equiv \frac{v_* d_s}{\nu} = \frac{\sqrt{f/8}\,U_0 U d_s}{\nu}\,. \tag{4.20}$$

We have taken $s = 2.65$ in the computations, see section 4.2.1. For inclined beds, this criterion has to be modified to take into account the bed angle θ. According to

Damgaard et al. (1997), if one defines the modified critical Shields parameter

$$\tau_c^\theta \equiv \frac{\sin(\phi_s - \theta)}{\sin\phi_s}\,\tau_c\,, \tag{4.21}$$

where ϕ_s is the angle of repose, sediment bed-load motion occurs when $\tau_* > \tau_c^\theta$, where τ_c is the critical Shields parameter for $\theta = 0$, given by Julien (1995) (see also Chanson, 2004)

$$\tau_c = \begin{cases} 0.5\tan\phi_s & \text{for} \quad d_* < 0.3 \\ 0.25 d_*^{-0.6}\tan\phi_s & \text{for} \quad 0.3 < d_* < 19 \\ 0.013 d_*^{0.4}\tan\phi_s & \text{for} \quad 19 < d_* < 50 \\ 0.06\tan\phi_s & \text{for} \quad 50 < d_* \end{cases} . \tag{4.22}$$

In this expression, the dimensionless particle diameter

$$d_* \equiv d_s \sqrt[3]{\frac{(s-1)g}{\nu^2}} = \sqrt[3]{\frac{Re_*^2}{\tau_*}} \tag{4.23}$$

is used instead of the shear Reynolds number (4.20). The critical Shields parameter for the threshold of sediment bed-load motion is plotted in Fig. 4.17 for different values of the bed angle θ, and for $\phi_s = 34^o$, appropriate for sand particles (e.g. Chanson, 2004). Also plotted in Fig. 4.17 is the threshold for suspension according to Bagnold's criterion (4.5) $v_* = a w_s$, with $a = 1.2$, expressed in the notation $\tau_c = \tau_c(Re_*)$ [note that $\tau_* = v_*^2/((s-1)g d_s)$, and w_s is given by (4.10)]. It is observed that this criterion predicts, for small Re_*, that suspension may occurs for a lower shear stress (a lower flow velocity) than bed-load motion, which cannot be physically correct. As commented on in section 4.2, what happens is that, for larger particles, this suspension criterion is not correct because no sharp boundary between bed-load motion and suspended transport exists; i.e. the suspension process is not characterised by a single constant a in (4.5) (Julien, 1995). For this reason, we also include in Fig. 4.17 curves corresponding to different probabilities P of suspension (Cheng and Chiew, 1999). For a given P, these curves yield the threshold Shield parameter above which the probability of suspension is P, as functions of Re_*. $P = 0.2$ is equivalent to Bagnold's criterion with $a = 1.2$ for large Re_*, $P = 0.34$ to $a = 2.5$, and $P = 0.42$ to $a = 5$ (Cheng and Chiew, 1999). This means that above the curve for $P = 0.42$ all the sediment transport is by suspended load (Julien, 1995), while in between this curve and the Shields' curves one has mixed transport. We have included some straight lines (in the logarithmic plot) corresponding to several values of the particle diameter (note that $d_* = constant$ means that $\tau_* \sim Re_*^2$) in order to have an idea of the behavior of sediment particles of different sizes as Re_* increases.

Taking into account all these considerations, we have evaluated the inception of bed-load and suspended load sediment transport in the present problem. Figure 4.18 compares, for $\eta_0 = 10m$, $d_s = 0.2mm$, and for two values of the bed angle θ, the right wetting front $L_1(t)$ with the front $L_b(t)$ at which bed-load transport begins, and with the different fronts $L_{s,a}(t)$ at which suspended load is initiated for different values of constant a in Bagnold's criterion. This comparison gives us a first idea of the relative importance of both kinds of sediment transport. Figures 4.19-4.20 contain the same information for $d_s = 1mm$ and $d_s = 5mm$. It is observed that L_b becomes first very small and then increases, meaning that the bed motion begins just after the break of the dam and it is present at almost every point of the flow motion since the starting of the flow. Small sediment particles (e.g., $d_s = 0.2mm$, Fig. 4.18) become suspended a little downstream the initiation of the bed motion. Therefore, sediment transport is dominated by suspension in this case [note that the curve $L_{s,5}(t)$, above which all the particles are in suspension, is much closer to $L_b(t)$ than to $L_1(t)$], the more so the larger the bed slope. For $d_s = 1mm$ (Fig. 4.19) the situation is qualitatively similar, but the ratio of suspended transport to bed-load transport is not so large, especially for small bed slopes. Note that although $L_{s,5}$ is closer to L_1 than to L_b ($L_{s,5}$ does not even exist at some intervals of time for small θ), $L_{s,1.2}$ is always closer to L_b, so that an important fraction of the transported sediment particles are in suspension at every instant. However, the situation is inverted for larger particles (Fig. 4.20 for $d_s = 5mm$). In this case, the dominant transport mechanism is bed-load motion for small angles of the bed, though the relative suspended load increases with θ, and for $\theta > 20^o$ suspended load becomes more important than bed-load. Note that in this case, the curve $L_{s,5}(t)$ does not exists for any bed angle. Finally, it is worth to comment that the discontinuities observed in some of these curves are due to the formation of roll waves, which produces intermittencies in the sediment suspension.

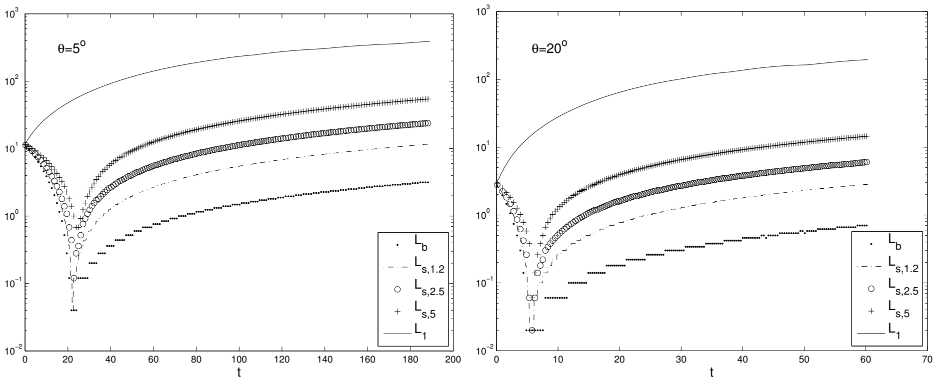

Figure 4.18: Wetting L_1 front as function of time compared to different fronts for bed-load motion (L_b), and for suspension ($L_{s,1.2}$,$L_{s,2.5}$,$L_{s,5}$), for $\eta_0 = 10m$, $d_s = 0.2mm$, and different bed slopes (as indicated in each subfigure).

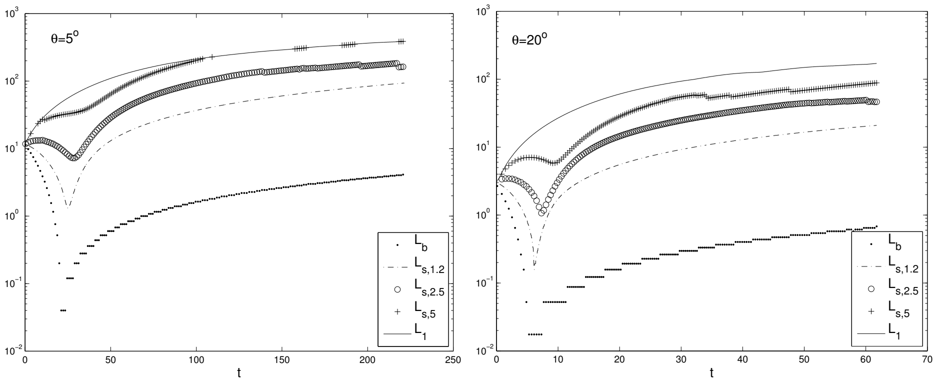

Figure 4.19: As in Fig. 4.18 but for $d_s = 1\,mm$.

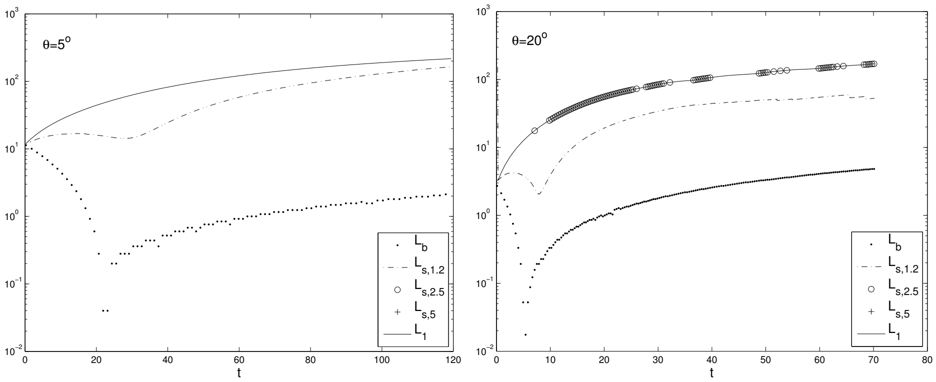

Figure 4.20: As in Fig. 4.18 but for $d_s = 5\,mm$.

Although the above figures give us a qualitative idea of the different sediment transport processes taking place in the flow as time goes on for different values of d_s and θ, to have a more quantitative idea of the relative importance of both sediment transport processes we have computed the quantities

$$\hat{E}_b = \frac{E_b}{E_b + E_s} \quad \text{and} \quad \hat{E}_s = 1 - \hat{E}_b \,, \tag{4.24}$$

where E_b and E_s are the total energies per unit time used for bed-load motion and for suspended transport, respectively (see, e.g., Yalin and Ferreira da Silva, 2001),

$$E_b = \epsilon_b \sum_{i=1}^{N_b} \int_{x_{bi}^{I}}^{x_{bi}^{II}} [\tau_* - (\tau_c)_b] v_* dx \,, \tag{4.25}$$

$$E_s = \epsilon_s \sum_{i=1}^{N_s} \int_{x_{si}^{I}}^{x_{si}^{II}} [\tau_* - (\tau_c)_s] v_* dx \,. \tag{4.26}$$

In these expressions N is the number of intervals $[x^I, x^{II}]$ where a specific erosion process (bed-load or suspension, as the subscript indicates) takes place, and ϵ is the corresponding efficiency of the process [we have used $\epsilon_b = \epsilon_s$ in (4.24)]. $\hat{E}_b$ and $\hat{E}_s$ with $P = 0.2$, corresponding to $a = 1.2$ for large Re_*, are plotted in Figs. 4.21-4.23 for the same cases as in Figs. 4.18-4.20. It is observed that only for large particles ($d_s = 5mm$) and small slopes of the bed ($\theta < 20^o$) $\hat{E}_b > \hat{E}_s$, i.e. bed-load sediment transport is more important than suspended load transport. For $d_s = 1mm$, $\hat{E}_b \ll \hat{E}_s$ for all θ almost from $t = 0$, while for $d_s = 0.2mm$, $\hat{E}_b$ is always negligible.

4.6 Summary and conclusions

We have formulated in this Chapter the problem of transport of dilute suspended sediments after the rupture of a dam on an inclined bed of arbitrary constant slope. The frictional model has been validated against existing experimental data. Several numerical techniques have been tested with available analytical solutions for the transport of sediment in the dam-break problem on a horizontal bed.

We have characterised the transport of suspended sediments as a function of the slope of the bed for different values of the parameters characterising the sediments. To

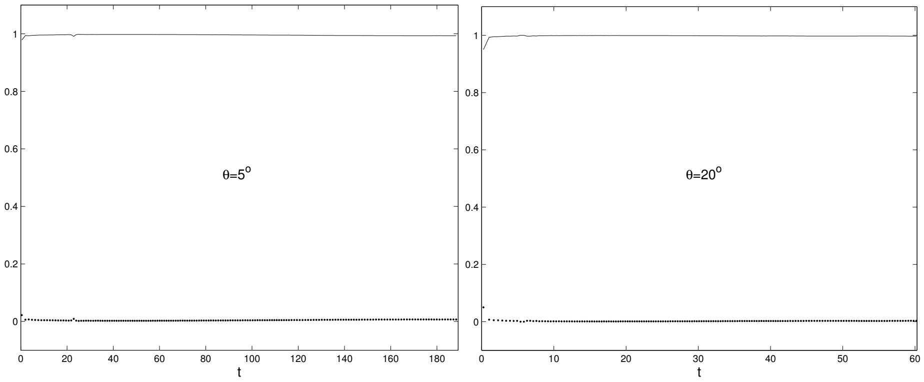

Figure 4.21: $\hat{E}_s$ (continuous lines) and $\hat{E}_b$ (dots) as functions of time for $\eta_0 = 10\,m$, $d_s = 0.2\,mm$, and different bed angles (as indicated). $a = 1.2$ ($P = 0.2$) has been used for the computation of the suspension threshold.

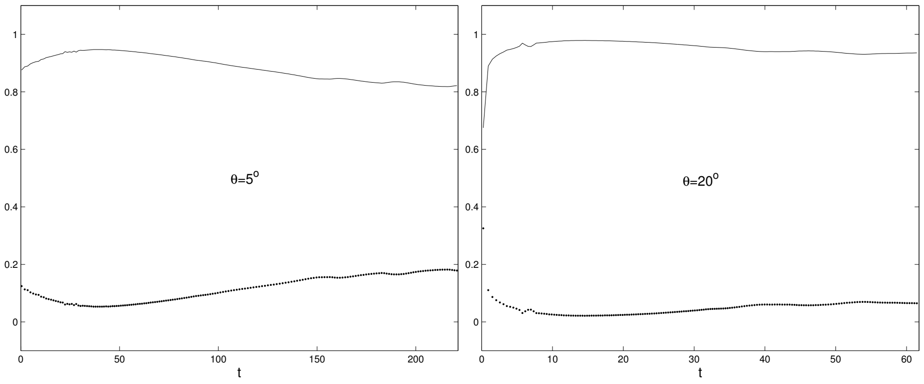

Figure 4.22: As in Fig. 4.21 but for $d_s = 1\,mm$.

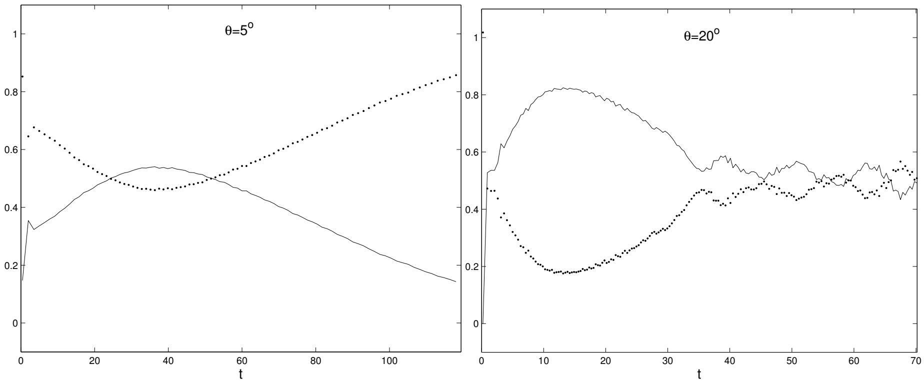

Figure 4.23: As in Fig. 4.21 but for $d_s = 5\,mm$.

that end we have used the maximum value of the normalised sediment load ($Q^*_{s,max}$) and the normalised time at which this maximum is reached after the rupture of the dam (t^*_{max}). Some details on the water height, flow velocity, and sediment concentration profiles are also given. We have observed the formation of roll waves near the advancing water front for large times. They produce spatial oscillations in the sediment concentration near the wetting front, but they do not affect to $Q^*_{s,max}$ since they are produced for $t \gg t_{max}$. However, these oscillations are very relevant in the sediment transport near the wetting front as the dam-break flow evolves downhill because they produce pronounced local maxima of the sediment concentrations, which cannot be predicted from asymptotic solutions of the problem (Pritchard, 2005). We have also characterised the validity of the dilute sediment approach as a function of the bed slope and of the sediment properties. Finally, we have also computed the bed-load transport and discussed its relative importance to the suspended sediment transport in the present problem as a function of the size of the sediment particles and the inclination of the bed. It is concluded that bed-load motion is more important than suspended transport for large sediment particles ($d_s \sim 5mm$), especially for small bed angles. For small particles ($d_s \simeq 1mm$ or smaller), the sediment transport is dominated by suspension, the more so the larger of the bed slope. Of course, all these results have the limitations of a depth-averaged model. For instance, the settling flux is computed with the depth-averaged concentration c and, clearly, basal concentration will be in excess of c, enhancing the bed-load transport. For very small sediment particles this effect is negligible because the sediment concentration profile tend to be uniform, but the concentration of sediment particles becomes increasingly larger near the bed as the sediment size increases (Julien, 1995).

All these limitations, together with the artificial separation between suspended and bed-load sediment transport, are superseded by the much more complex model presented in the next chapter, for which the above numerical results may serve as a check of the models and numerical technique used to solve them.

Chapter 5

Continuum Mechanics model for the transport of non-dilute sediment in river flows

5.1 Introduction

The term *hyperconcentrated flow* is most often applied to river flows transporting large quantity of fine sediments in full dynamic suspension, as well as bed-load. Bed-load (or contact load) is the sum of all sliding or rolling particles that stay in more or less continuous contact with the bed. Suspended load includes fines which form a stable suspension and coarser particles which remains temporarily in dynamic suspension. Hyperconcentrated flow is a process intermediate between normal sediment-laden streamflow, which transport mostly fine sediment in relatively small quantities, and debris or mud flood, in which the sediment plays an integral role in the flow behaviour and mechanics. Field and experimental studies have shown that natural hyperconcentrated flows are turbulent, two-phase, gravity-driven flows of water and sediment (Pierson, 2005).

In recent years, the number of theoretical and numerical models to study open channel and river flows, and related sediment transport, has increased due to the important role that plays in our life. Debris and hyperconcentrated flows are frequently associated with natural hazards, and usually becomes a natural disaster. However, nowadays the behaviour of this kind of flows is not well understood. The simple fact that hyperconcentrated flows are not hydrostatic questions the applicability of up-to-date shallow-water models - which now accounts for morphological changes associated to the sediment transport. Furthermore, most of the actual formulations are based on layers, i.e. one splits the vertical coordinate into layers and select different equations to model the sediment-water mixture depending on the layer regime (frictional, collisional, saltation, etc). Nevertheless, the boundary between the *traction carpet* (or bed-load layer) and intermittently suspended load cannot be sharply defined in hyperconcentrated flows. More sophisticated and rigorous approaches solve the Reynolds-averaged Navier-Stokes equations (see, e.g., Wu et al., 2000; Liu and Garcia, 2006) given generally good results in the suspended-load region and the traction carpet. But, to our knowledge, there are no studies avoiding the use of both layers and empirical formulas to account for the sediment transport mechanism, except the worth work by Lalli et al. (2005) for pipes. That is, there is no Continuum Mechanics formulation for general river flow.

A Continuum Mechanics approach to predict the behaviour of dense suspensions with free-surface implies the analysis of three-phases (i.e., water, sediment and air). Two ways are possible: first, to adopt a diffusion model solving the continuity equation of both phase, and the momentum equation of the three-phase mixture; second, to employ averaged mass and momentum conservation equations of both phases. Many complications are introduced by the dense suspension and the free-surface, which enrich the dynamics of real flows. Thus, the author considers that the study about this multi-phase system is an outstanding issue. We choose the first option to reduce the computation cost of the resulting model.

We start defining the mixture model and the Continuum Surface Force (CSF) formulation in § 5.2, and continue with closure laws in 5.3. Next, in § 5.4, we define the numerical scheme used in following sections. We devote § 5.5 to compare our numerical simulations with some experiments. A summary and some concluding comments are given in § 5.6.

5.2 Turbulent mixture model and CSF formulation

The ensemble averaged continuity equations for the liquid (f), solid (p) and gas (g) phase in a three-phase mixture are respectively given by (e.g. Ishii and Hibiki, 2006):

$$\frac{\partial \alpha_f \rho_f}{\partial t} + \nabla \cdot (\alpha_f \rho_f \langle \vec{v}_f \rangle) = 0\,, \tag{5.1}$$

$$\frac{\partial \alpha_p \rho_p}{\partial t} + \nabla \cdot (\alpha_p \rho_p \langle \vec{v}_p \rangle) = 0\,, \tag{5.2}$$

$$\frac{\partial \alpha_g \rho_g}{\partial t} + \nabla \cdot (\alpha_g \rho_g \langle \vec{v}_g \rangle) = 0\,. \tag{5.3}$$

In particular, we are interested in flows in which the solid phase cannot get in contact with the gas phase. Thus, the phase volumetric concentration α_k should be written in terms of the volume fraction occupied by the solid-liquid mixture in a small control volume, say $\gamma \equiv 1 - \alpha_g$, and the volumetric concentration of solid particles in the three-phase mixture, denoted by $\beta \equiv \alpha_p$. The liquid volumetric concentration is therefore given by $\alpha_f \equiv \gamma - \beta$.Adding the three equations shown above, and defining appropriately the mixture density ρ and mass velocity $\langle \vec{v} \rangle$ (e.g. Manninen et al., 1996):

$$\rho = \rho_p \beta + \rho_f (\gamma - \beta) + \rho_g (1 - \gamma) \tag{5.4}$$

$$\langle \vec{v} \rangle = \frac{1}{\rho} \left\{ \rho_p \beta \langle \vec{v}_p \rangle + \rho_f (\gamma - \beta) \langle \vec{v}_f \rangle + \rho_g (1 - \gamma) \langle \vec{v}_g \rangle \right\} \tag{5.5}$$

the continuity equation of the mixture, given by (1.31), is readily deduced. To simplify the notation it is convenient to introduce dense suspension variables. In general, these variables are denoted with the subscript m, that characterises the particle-liquid suspension. As a matter of fact, in Chapter 1 the dense suspension density ρ_m and mass velocity $\langle \vec{v}_m \rangle$ were introduced [see equations (1.28) and (1.29), respectively].

An alternative formulation of the mixture continuity equation (1.31) is useful to formulate the pressure equation (see section 5.4). This formulation is obtained after dividing the k-phase equation (5.1)-(5.3) by the k-phase density and then adding the three resulting equations, that yields

$$\nabla \cdot (\langle \vec{u} \rangle) = 0\,, \tag{5.6}$$

being the volumetric velocity $\langle \vec{u} \rangle$ known thanks to the equation (1.27). This shows that the volumetric velocity $\langle \vec{u} \rangle$ is a divergence-free vector.

In order to formulate an efficient and conservative numerical scheme, capable to solve the continuity equations, it is convenient to rewrite them in a different way. Dividing equation (5.1) and (5.2) by ρ_f and ρ_p, respectively, and adding the ensuing equations, it yields (1.32) with $\langle \vec{u}_{r\gamma} \rangle \equiv \langle \vec{u}_m \rangle - \langle \vec{v}_g \rangle$. The equation for β, given by Eq. (1.33), however requires some additional algebra. Writing $\langle \vec{v}_p \rangle$ as a function of the relative velocity of the dense suspension with respect to the gas phase, $\langle \vec{u}_{r\gamma} \rangle$, and the relative velocity of the solid particles with respect to the liquid, $\langle \vec{v}_r \rangle \equiv \langle \vec{v}_p \rangle - \langle \vec{v}_f \rangle$, one obtains

$$\langle \vec{v}_p \rangle = \langle \vec{u}_m \rangle + \left(1 - \frac{\beta}{\gamma}\right) \langle \vec{v}_r \rangle = \langle \vec{u} \rangle + (1-\gamma)\langle \vec{u}_{r\gamma} \rangle + \left(1 - \frac{\beta}{\gamma}\right) \langle \vec{v}_r \rangle \,. \tag{5.7}$$

Substituting this relation into (5.2), one deduces (1.33), with

$$\langle \vec{u}_{r\beta} \rangle \equiv \frac{\gamma(1-\gamma)\langle \vec{u}_{r\gamma} \rangle + (\gamma - \beta)\langle \vec{v}_r \rangle}{\gamma(1-\beta)} \,. \tag{5.8}$$

Now, the analogy between the indicator function γ and the volumetric sediment concentration β becomes evident. Moreover, one can apply exactly the same numerical scheme to solve both equations (1.32)-(1.33).

One just rests to obtain the momentum balance equation. We drop the conditional averaged brackets $\langle \cdot \rangle$ along the deduction for sake of simplicity. According to Ungarish (1993), we start with the definition of the resultant (total) momentum flux $\overline{\overline{J}}$ associated to the averaged phase velocities,

$$\overline{\overline{J}} = \beta \rho_p \vec{v}_p \vec{v}_p + (\gamma - \beta)\rho_f \vec{v}_f \vec{v}_f + (1-\gamma)\rho_g \vec{v}_g \vec{v}_g \,, \tag{5.9}$$

which can be rewritten as

$$\overline{\overline{J}} = \rho \vec{v}\vec{v} + \beta \left(1 - \frac{\beta}{\gamma}\right) \frac{\rho_f \rho_p}{\rho_m} \vec{v}_r \vec{v}_r + \gamma(1-\gamma)\frac{\rho_m \rho_g}{\rho} \vec{v}_{r\gamma} \vec{v}_{r\gamma} \,, \tag{5.10}$$

where $\vec{v}_{r\gamma}$ denotes the *slip velocity* between the dense suspension and the air,

$$\vec{v}_{r\gamma} = \vec{v}_m - \vec{v}_g = \vec{u}_{r\gamma} + \frac{\beta}{\gamma} s \frac{\gamma - \beta}{\gamma + \beta s} \vec{v}_r \,.$$

We follow the theoretical development with some algebraical manipulations on the LHS of the momentum equation, denoted by $\vec{C}$, which introduces the material derivatives of each phase [sum of the left-hand side of equation (1.23) for all the species],

$$\vec{C} = \beta\rho_p \frac{D_p\vec{v}_p}{Dt} + (\gamma-\beta)\rho_f \frac{D_f\vec{v}_f}{Dt} + (1-\gamma)\rho_g \frac{D_g\vec{v}_g}{Dt}\,.$$

To rewrite $\vec{C}$ in terms of the mixture mass velocity, we subtract the equation that follows to the previous one, and take into account Eqs. (5.1) and (5.3),

$$\begin{aligned}\frac{\partial\rho\vec{v}}{\partial t} =& \beta\rho_p\frac{\partial\vec{v}_p}{\partial t} + (\gamma-\beta)\rho_f\frac{\partial\vec{v}_f}{\partial t} + (1-\gamma)\rho_g\frac{\partial\vec{v}_g}{\partial t} - \\ & \{\rho_p\vec{v}_p\nabla\cdot(\beta\vec{v}_p) + \rho_f\vec{v}_f\nabla\cdot[(\gamma-\beta)\vec{v}_f)] + \rho_g\vec{v}_g\nabla\cdot[(1-\gamma)\vec{v}_g)]\}\ ,\end{aligned}$$

so that it yields

$$\vec{C} - \frac{\partial\rho\vec{v}}{\partial t} = \nabla\cdot[\beta\rho_p\vec{v}_p\vec{v}_p + (\gamma-\beta)\rho_f\vec{v}_f\vec{v}_f + (1-\gamma)\rho_g\vec{v}_g\vec{v}_g] = \nabla\cdot\overline{\overline{J}}\,.$$

So, substituting Eq. (5.9) into the last expression, the LHS of the momentum balance becomes

$$\vec{C} = \frac{\partial\rho\vec{v}}{\partial t} + \nabla\cdot(\rho\vec{v}\vec{v}) + \nabla\cdot\left[\beta\left(1-\frac{\beta}{\gamma}\right)\frac{\rho_f\rho_p}{\rho_m}\vec{v}_r\vec{v}_r\right] + \nabla\cdot\left[\gamma(1-\gamma)\frac{\rho_m\rho_g}{\rho}\vec{v}_{r\gamma}\vec{v}_{r\gamma}\right]\,. \quad (5.11)$$

The last two terms are called *diffusion stress terms* and represent the momentum convected by the relative motion between the phases [as advanced in equation (1.35)].

Finally, we shall incorporate the surface tension as a force concentrated on the interface in the same way as Unverdi and Tryggvason (1992) and Brackbill et al. (1992). Hence, the jump condition due to surface tension is included in the mathematical model (Drew, 1983). In addition, the solid stress is divided into a compressive normal stress p_s, the so-called solid pressure, and shear stress. The effect of the shear stress is commonly described by the effective viscosity. Sometimes in dense suspensions, the shear stress term has been neglected and only the solid pressure is included (Manninen et al., 1996). So, the momentum balance for the *mixture model* is

$$\vec{C} = -\nabla P - \nabla p_s + \nabla\cdot(\overline{\overline{\tau}}' + \overline{\overline{\tau}}'') - \sigma\kappa\nabla\gamma + \rho\vec{g}\cdot\vec{x}\,.$$

Substituting (5.11) into the expression shown above, and using the definition of the reduced pressure p,

$$p \equiv P - \rho\vec{g}\cdot\vec{x}\,,$$

one has

$$\frac{\partial \rho \langle \vec{v} \rangle}{\partial t} + \nabla \cdot (\rho \langle \vec{v} \rangle \langle \vec{v} \rangle) = -\nabla \langle p \rangle - \nabla \langle p_s \rangle + \nabla \cdot \langle \overline{\overline{\tau}} \rangle - \sigma \kappa \nabla \gamma - \vec{g} \cdot \vec{x} \nabla \rho \,, \qquad (5.12)$$

being $\overline{\overline{\tau}} \equiv \overline{\overline{\tau}}' + \overline{\overline{\tau}}'' + \overline{\overline{\tau}}''' + \overline{\overline{\tau}}''''$ the generalised stress tensor that accounts for the viscous stress tensor $\overline{\overline{\tau}}'$,

$$\langle \overline{\overline{\tau}}' \rangle = \mu_l \left[\nabla \langle \vec{v} \rangle + (\nabla \langle \vec{v} \rangle)^T + \left(\frac{\mu_v}{\mu_l} - \frac{2}{3} \right) (\nabla \cdot \langle \vec{v} \rangle) \,\overline{\overline{I}} \right] , \qquad (5.13)$$

the turbulent stresses $\overline{\overline{\tau}}''$ (see below), and both the momentum-diffusion due to the relative motion of the sediment with respect to the water $\overline{\overline{\tau}}'''$ and the sediment-water mixture with respect to the air $\overline{\overline{\tau}}''''$ [see Eq. (1.35)].

5.3 Constitutive laws and turbulence closure

The physical model presented in the previous section requires some additional ingredients. It should be included a constitutive law for the mixture viscosity, the turbulent stress tensor, the solid pressure and the slip velocities.

It is well known that the rheology of dense or highly concentrated suspensions depends strongly on the microstructure of all the particles and the suspension viscosity (see, for instance, Stickel and Powell, 2005). We deal above with the first dependence through the additional momentum-diffusion tensor of the entire stress tensor. Now we continue establishing the relationship between the laminar viscosity μ_l and the volumetric concentrations β and γ. For a thin interface, the bulk viscosity of the three-phase mixture is given by (Sethian and Smereka, 2003):

$$\mu_l(\vec{x}, t) = \gamma \mu_m + (1 - \gamma) \mu_g \,, \quad \mu_m(\beta) = \mu_f \mu_r(\beta) \qquad (5.14)$$

where the laminar viscosity of the dense suspension μ_m will be formulated as a function of a relative viscosity μ_r. The relative viscosity is, in general, a function of the solid volumetric concentration β, the density parameter s, the Reynolds number $Re_{\dot{\gamma}}$, the Peckllet number $Pe_{\dot{\gamma}}$, and the characteristic time t_r,

$$Re_{\dot{\gamma}} = \frac{\rho_f a^2 \dot{\gamma}}{\mu_f} \,, \quad Pe_{\dot{\gamma}} = \frac{6 \pi \mu_f a^3 \dot{\gamma}}{k_B T} \,, \quad t_r = \frac{t k_B T}{\mu_f a^3} \,,$$

where a is the particle radius, $\dot{\gamma}$ is the effective shear rate proportional to the square root of the second invariant of the rate of deformation tensor $\overline{\overline{\gamma}}$,

$$\dot{\gamma} \equiv \sqrt{2}|\overline{\overline{\gamma}}| \quad \text{with} \quad |\overline{\overline{\gamma}}| := (\overline{\overline{\gamma}} : \overline{\overline{\gamma}})^{1/2}, \quad \overline{\overline{\gamma}} = \frac{1}{2}\left[\nabla\langle\vec{v}\rangle + (\nabla\langle\vec{v}\rangle)^T - \frac{2}{3}(\nabla \cdot \langle\vec{v}\rangle)\overline{\overline{I}}\right],$$

$k_B T$ is the thermal energy, and k_B is Boltzmann's constant $k_B = 1.38 \times 10^{-23}\, J/K$. For simplicity, we consider on this chapter a relative viscosity that depends just on the solid particle volumetric concentration and the effective shear rate. The use of a Krieger (1972) law, see Figure 5.1, for the relative viscosity was proven successful to analyse viscous resuspension and settling processes (e.g., Leighton and Acrivos, 1986; Schaflinger et al., 1990, 1995). However, this first ingredient models the suspension as a pure Newtonian fluid, in which the viscosity is function of the solid volumetric concentration. Non-Newtonian behaviour is generally observed for solids concentrations exceeding 0.4 by volume (Stickel and Powell, 2005): in the zero shear rate limit, the suspension is Newtonian except for the yield stress behaviour of very dense suspensions; all suspensions generally shear-thin at low to intermediate shear rates; with increasing shear rate, there is a Newtonian plateau and finally a steep shear-thickening region; finally, the behaviour beyond the shear-thickening region is not clear. The additional influence of the effective shear rate on the relative viscosity should be introduced in order to model shear-thinning phenomena. In the present work the dynamics of fluids with large amount of suspended solids is described following the work by Lalli et al. (2005), which establishes the constitutive law that follows:

$$\mu_m = \begin{cases} \mu_f \left(1 + \frac{3\beta/2}{1-\beta/\beta_M}\right)^2 & \text{if } \beta < \beta_m \\ \mu_f \left(1 + \frac{3\beta/2}{1-\beta/\beta_M}\right)^2 + \tau_0(\dot{\gamma}+\epsilon)^{-1/2} & \text{if } \beta_m \leq \beta \leq \beta_M \end{cases}. \tag{5.15}$$

Here τ_0 represents the yield stress, β_M is the maximum packing factor and β_m $(=\pi/6)$ is the volumetric concentration at which the flow starts to behave as a Bingham fluid. Finally, ϵ is a small parameter to avoid numerical difficulties. The visco-plastic discontinuous model is approximated by means of a shear-thinning continuous model, whose limit is the visco-plastic one as $\epsilon \to 0$. To compute the yield stress we have

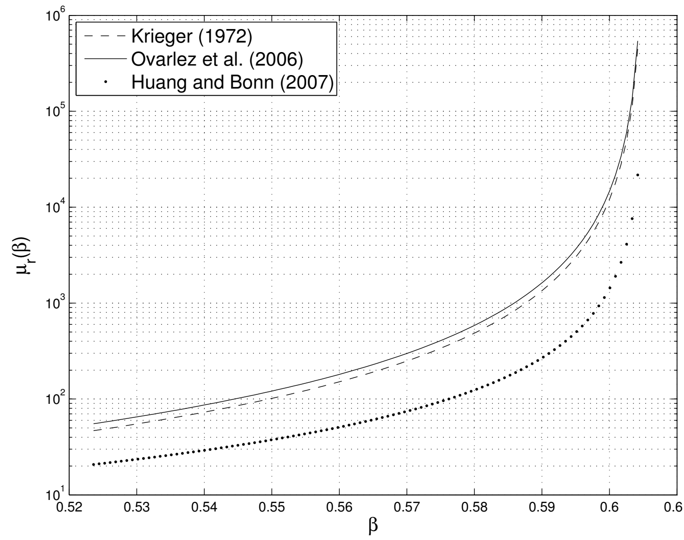

Figure 5.1: Fit to a Krieger-Dougherty law $\mu_r(\beta) = (1-\beta/\beta_M)^{-2}$ of the local viscosity measurements on suspensions of various concentration ranging from 55% to 60% (Ovarlez *et al.*, 2006, continuous line) and Krieger (1972, discontinuous line) law $\mu_r(\beta) = [1 - 1.5\beta/(1 - \beta/\beta_M)]^{-2}$ with $\beta_M = 0.605$. The expression proposed by Huang and Bonn (2007) is also shown.

used the following expression (see Wan and Wang, 1994):

$$\tau_0 = 990 \exp\left\{8.45\left[1.5 + \frac{\beta - \beta_m}{\beta_M}\right]\right\} . \tag{5.16}$$

The modelling of turbulence in dense suspensions is a formidable task since four-way coupling takes place. The turbulence is modified by the presence of solid particle at the same time that the collisions between particles affects its own movement. Hence, the use of a turbulence model that accounts just for the presence of one phase is no longer valid. Most of the studies in multiphase turbulent flows at high phase fractions deal with two-fluid models (see, for a complete review, Rusche, 2002). However, we lost the detailed behaviour of the motion of the phases when an overall mixture momentum equation was considered. We follow in the present study the work by Brennan (2001), so we shall adopt the well known k-ϵ turbulence model of Rodi (1993) with a buoyancy modification term in the k equation to account for density stratification. The k-ϵ eddy-viscosity model [see, e.g., Rodi (1993)] determines the isotropic eddy viscosity μ_t as a function of the turbulent kinetic energy k and its dissipation rate ϵ by

$$\mu_t = C_\mu \rho \frac{k^2}{\epsilon} \,. \tag{5.17}$$

The distributions of k and ϵ are determined from the following model transport equations:

$$\frac{\partial \rho \epsilon}{\partial t} + \nabla \cdot (\rho \vec{v} \epsilon) = \nabla \cdot [(\alpha_\epsilon \mu_t + \mu_l) \nabla \epsilon] + \frac{\epsilon}{k} C_1 \left[P_k + P_B (1 - C_3) - \frac{2}{3} k \rho \nabla \cdot \vec{v} \right] - C_2 \rho \frac{\epsilon^2}{k} \,, \tag{5.18}$$

$$\frac{\partial \rho k}{\partial t} + \nabla \cdot (\rho \vec{v} k) = \nabla \cdot [(\alpha_k \mu_t + \mu_l) \nabla k] + P_k + P_B - \rho \epsilon - \frac{2}{3} k \rho \nabla \cdot \vec{v} \,, \tag{5.19}$$

where

$$P_k = 2 \mu_t (\nabla \cdot \vec{v}) \cdot \mathrm{dev}[\nabla \vec{v} + (\nabla \vec{v})^T] \,, \quad P_B = -\frac{\alpha_k \mu_t}{\rho} \vec{g} \cdot \nabla \rho \,.$$

The constants used in the equations are $C_\mu = 0.09$, $C_1 = 1.44$, $C_2 = 1.92$, $C_3 = 0.85$, $\alpha_k = 1$ and $\alpha_\epsilon = 0.76923$. Certainly, the set of equations (5.18)-(5.19) is not formally valid in presence of a free-surface, and they should be modified taking into account the indicator function γ. However, this task is actually out of the scope of the present study. Because we have adopted the $k - \epsilon$ turbulence model, we can now define the effective viscosity of the continuous phase μ, where

$$\mu \equiv \mu_l + \mu_t \,.$$

At high solid volume fraction, sustained contacts between particles occur, resulting frictional stresses. Several approaches have been presented in the literature to model the frictional stress, mostly originated from geological research groups. At frictional regime, the local constitutive law of the flowing material is that of a purely viscous material (i.e. viscous and not Newtonian as these materials develop normal stresses), as recently observed by Huang et al. (2005) and Ovarlez et al. (2006). Although normal stresses were extensively studied by Zarraga et al. (2000), we use the semi-empirical equation of Johnson and Jackson (1987):

$$p_s = C_p \frac{(\beta - \beta_m)^n}{(\beta_M - \beta)^p} \quad \text{for} \quad \beta > \beta_m \tag{5.20}$$

where C_p, n and p are empirical constants, and β_m being the solid volume fraction when frictional stresses become important. The parameters C_p, n and p depend on the material. The values proposed by Johnson et al. (1990) for the empirical material constants are $C_p = 0.05 N m^{-2}$, $n = 2$ and $p = 5$.

To close the model we need to establish the constitutive laws for the slip velocity $\vec{v}_r$ and $\vec{v}_{r\gamma}$. We now proceed to define the relative movement of the sediment into the sediment-water mixture. To that end we shall use "stationary laws", i.e. we suppose that the response time of the sediment is much smaller than the characteristic time of the flow. We consider that the sediment grain moves with respect to the clear flow due to sedimentation processes ($\vec{v}_s$), diffusion caused by concentration gradients ($\vec{v}_d$), and shear-induced self-diffusion ($\vec{v}_{sh}$). In this case the slip velocity $\vec{v}_r$ is

$$\vec{v}_r = \vec{v}_s + \vec{v}_d + \vec{v}_{sh}\,. \tag{5.21}$$

When analysing the settling of particles in the direction of gravity, the downward flux of particles is given by (see, for instance, Leighton and Acrivos, 1986)

$$\vec{v}_s = \frac{2}{9}\frac{\beta}{\gamma}\left(1 - \frac{\beta}{\gamma}\right)\frac{a^2 g(\rho_p - \rho_f)}{\mu_l}\frac{\vec{g}}{|\vec{g}|}\,. \tag{5.22}$$

In presence of a concentration gradient along the vertical direction, Leighton and Acrivos (1987) shown that the Fickian diffusive flux yields

$$\vec{v}_d = -D_d \nabla\left(\frac{\beta}{\gamma}\right)\,, \tag{5.23}$$

where the dimensionless form of the diffusion coefficient is

$$\widehat{D}_d \equiv \frac{D_d}{a^2\dot{\gamma}} = \frac{1}{3}\left(\frac{\beta}{\gamma}\right)^2\left(1 + \frac{1}{2}e^{8.8\beta/\gamma}\right) + 0.6\left(\frac{\beta}{\gamma}\right)^2\frac{1}{\mu_l}\frac{d\mu_l}{d\beta}\,.$$

Furthermore, when the particle flux due to gradients in the shear stress cannot be neglected a new contribution to the diffusive flux appears, and this is given by (see Zhang and Acrivos, 1994)

$$\vec{v}_{sh} = -D_{sh}\nabla\dot{\gamma} \quad \text{with} \quad \widehat{D}_{sh} \equiv \frac{D_{sh}}{a^2} = 0.6\left(\frac{\beta}{\gamma}\right)^2\,. \tag{5.24}$$

Finally, the compression velocity $\vec{v}_{r\gamma}$ should act perpendicular to the interface (Rusche, 2002):

$$\vec{v}_{r\gamma} = K_c\frac{\nabla\gamma}{|\nabla\gamma|}\,. \tag{5.25}$$

There are many possible formulations for the compression magnitude K_c. In this work we adopt that by default in interFOAM solver (OpenCFD Limited, 2007):

$$K_c = \min(C_\gamma \vec{u} \cdot \vec{n}_f, \max(\vec{u} \cdot \vec{n}_f)) \tag{5.26}$$

where the normal vector at the cell face $\vec{n}_f$ is given by the mesh used to solve numerically the problem under consideration (see below). The compressive constant C_γ is usually fixed to the unity value.

5.4 Computational method

In this work, we adopt the FVM method (see Ferzinger and Peric, 2002) to solve numerically the set of partial differential equations detailed in § 5.2-5.3, together with the appropriate initial and boundary conditions. The FVM has been successfully applied to several, complex physical models involving turbulence modelling, multiphase flows, and fluid-structure interaction problems, among others. Nowadays, the use of advanced data structure and oriented object programing allows one to create high level libraries tailored for Continuum Mechanics problems. In this line, we shall use OpenFOAM (Weller et al., 1998) which actually implements several solvers for multi-phase and free-surface flows.

To make the description of the numerical scheme as easy as possible, we use the finite volume notation by Weller (2002a), that has been previously applied by Rusche (2002). For a detailed description of the discretisation of the convection, diffusion and source terms involved in the equations, as well as the temporal derivative, we refer the reader to Jasak (1996, 2006). Each of these terms are generally found in the *standard transport equation*, and the application of a discretisation practice with second-order accurate in space and time is suitable for second-order continuum mechanics problems.

5.4.1 Compressible pressure-based solver

An implicit scheme has been used for the discretisation of all the terms that are represented in the standard transport equation. However, in our equations there are terms that do not correspond to a term in the standard transport equation, say *extra terms*, which are usually discretised explicitly.

The momentum correction and pressure equation can be readily derived from a semidiscretised form of the momentum equation,

$$\boldsymbol{\mathcal{A}}_D\overline{\mathbf{V}} = \boldsymbol{\mathcal{A}}_H - \nabla p^* - \nabla p_s - \vec{g}\cdot\vec{z}\nabla\rho - \sigma\kappa\nabla\gamma\,, \tag{5.27}$$

where $\boldsymbol{\mathcal{A}}$ denotes a system of linear algebraic equations arising from the discretisation of the momentum equation (5.12) without surface tension and buoyancy terms,

$$\boldsymbol{\mathcal{A}} := \left[\!\!\left[\frac{\partial\rho[\overline{\mathbf{V}}]}{\partial t}\right]\!\!\right] + [\![\nabla\cdot\left(\phi[\overline{\mathbf{V}}]_{f(\phi,S)}\right)]\!] = [\![\nabla\cdot\left(\mu\nabla[\overline{\mathbf{V}}]\right)]\!] + \nabla\cdot\boldsymbol{\mathcal{R}}^{\mathit{eff}\mathcal{C}}\,, \tag{5.28}$$

where the mass flux is $\phi \equiv \rho\overline{\mathbf{V}}\cdot\mathbf{S}$, $\boldsymbol{\mathcal{A}}_D$ is a matrix containing the diagonal coefficients, the "H" operator $\boldsymbol{\mathcal{A}}_H$ (see below) is extensively used in the Jacobi iteration scheme (Ferzinger and Peric, 2002), and the Reynolds stress correction term $\boldsymbol{\mathcal{R}}^{\mathit{eff}\mathcal{C}}$ is useful for the numerical implementation,

$$\boldsymbol{\mathcal{R}}^{\mathit{eff}\mathcal{C}} = \mu\left[(\nabla\overline{\mathbf{V}})^T - \frac{2}{3}(\nabla\cdot\overline{\mathbf{V}})\overline{\overline{I}}\right] - (\overline{\overline{\tau}}''' + \overline{\overline{\tau}}'''')\,. \tag{5.29}$$

The "H" operator is defined as:

$$\boldsymbol{\mathcal{A}}_H \equiv \boldsymbol{\mathcal{A}}_S - \boldsymbol{\mathcal{A}}_N\phi$$

where the special operators $\boldsymbol{\mathcal{A}}_S$ and $\boldsymbol{\mathcal{A}}_N$ are invoked to extract the source vector and the off-diagonal coefficients, respectively. The flux predictor ϕ^* and corrector ϕ are then derived by interpolating the momentum correction equation using central differencing:

$$\phi = \phi^* - \left(\frac{\rho}{\boldsymbol{\mathcal{A}}_D}\right)_f |\mathbf{S}|\nabla_f^\perp p^*\,, \tag{5.30}$$

and the flux prediction ϕ^* is expressed, in the spirit of Rhie and Chow (1983), by

$$\phi^* = \left(\rho\frac{\boldsymbol{\mathcal{A}}_H}{\boldsymbol{\mathcal{A}}_D}\right)_f\cdot\mathbf{S} - \left(\frac{\rho}{\boldsymbol{\mathcal{A}}_D}\right)_f\left[(\vec{g}\cdot\vec{z})_f|\mathbf{S}|\nabla_f^\perp\rho + (\sigma\kappa)_f|\mathbf{S}|\nabla_f^\perp\gamma + \nabla p_s\right]\,. \tag{5.31}$$

The mass flux ϕ is the result of the Pressure-Implicit Split-Operator (PISO) loop. The value of ϕ is not evaluated by taking the scalar product of the face area vector and

1. Solve the continuity equation (5.33).
2. Compute the relative velocities (5.21).
3. Solve the γ-equation (5.34).
4. Calculate the unit normal vector as well as curvature.
5. Construct $\boldsymbol{\mathcal{A}}$, equation (5.28).
6. PISO-Loop:
   (a) Predict fluxes using equation (5.31).
   (b) Construct and solve the pressure equation (5.32).
   (c) Correct fluxes, equation (5.30).
   (d) Solve the continuity equation (5.33).
   (e) Reconstruct velocities.
7. Solve $k - \epsilon$ equations (if required).
8. Solve the β-equation (5.35).

Table 5.1: Implicit three-phase numerical solution procedure.

the face interpolate of the velocity, as this would not obey continuity. The equation for the pressure is then obtained to obey continuity,

$$\left[\!\!\left[\nabla\cdot\left[\left(\frac{\rho}{\boldsymbol{\mathcal{A}}_D}\right)_f \nabla[p^*]\right]\right]\!\!\right] = \nabla\cdot\phi^* + \frac{\partial\rho}{\partial t}\,, \tag{5.32}$$

and the density is updated in the PISO-Loop to satisfy the mass conservation,

$$\left[\!\!\left[\frac{\partial[\rho]}{\partial t}\right]\!\!\right] + \nabla\cdot\phi = 0\,. \tag{5.33}$$

This method gives an oscillation-free velocity in line with Rhie-Chow, even though there is no explicit Rhie-Chow correction (Kärrholm, 2006). This numerical solution procedure is analogous to that currently implemented in *settlingFoam* solver by Brennan (2001).

Special attention should be paid to the γ- and β-equations to obtain a conservative and bounded solution. Several practices for the phase equation has been previously tested (Rusche, 2002) and here we follow the work by Weller (2002b). Therefore, the phase equations (1.32) and (1.33) are discretised as follows:

$$\left[\!\!\left[\frac{\partial[\gamma]}{\partial t}\right]\!\!\right] + \left[\!\left[\nabla\cdot\left(\phi_u[\gamma]_{f(\phi_v,S)}\right)\right]\!\right] + \left[\!\!\left[\nabla\cdot\left(\tilde{\phi}_{r\gamma}[\gamma]_{f(\tilde{\phi}_{r\gamma},S)}\right)\right]\!\!\right] = 0\,. \tag{5.34}$$

$$\left[\!\!\left[\frac{\partial[\beta]}{\partial t} \right]\!\!\right] + [\![\nabla\cdot\left(\phi_u[\beta]_{f(\phi_v,S)}\right)]\!] + \left[\!\!\left[\nabla\cdot\left(\tilde{\phi}_{r\beta}[\beta]_{f(\tilde{\phi}_{r\beta},S)}\right)\right]\!\!\right] = 0\,. \tag{5.35}$$

Taken into account (1.36), the volumetric flux $\phi_u \equiv \overline{\mathbf{U}}_f \cdot \mathbf{S}$ is expressed as a function of the mass flux ϕ:

$$\phi_u = \frac{\phi}{\rho_f} - \left[\gamma(1-\gamma)\frac{\rho_m-\rho_g}{\rho}\right]_f \phi_{r\gamma} - \left[s\beta\frac{\gamma-\beta}{\gamma+\beta s}\frac{\rho_m}{\rho}\right]_f \phi_r \tag{5.36}$$

where

$$\tilde{\phi}_{r\gamma} = (1-\gamma)_{f(-\phi_{r\gamma},S)}\phi_{r\gamma}\,, \quad \tilde{\phi}_{r\beta} = (1-\beta)_{f(-\phi_{r\beta},S)}\phi_{r\beta}\,,$$

$$\phi_{r\gamma} = (\overline{\mathbf{U}}_{r\gamma}\cdot\mathbf{S})_f\,, \quad \phi_{r\beta} = (\overline{\mathbf{U}}_{r\beta}\cdot\mathbf{S})_f, \quad \phi_r = (\overline{\mathbf{V}}_r\cdot\mathbf{S})_f\,.$$

The transport equations for the $k-\epsilon$ turbulence model are discretised treating implicitly the negative source terms, while the positive source terms are incorporated explicitly as in Brennan (2001).

Finally, the sequence of operations for the solution procedure is summarised in Table 5.1.

5.4.2 Segregated pressure-based solver

The compressible pressure-based solver described above deals with the velocity-pressure coupling through a PISO-Loop which employs the continuity equation of the mixture (5.33), based on the mean velocity $\vec{v}$. However, one can adopt a different approach that includes the relation (5.4), in such a way that the density is no longer an unknown to be determined as a function of the volume fraction β and γ. Thus, the PISO algorithm is to be formulated based on the continuity equation (5.6). Rewriting (5.6) in terms of the mean velocity $\vec{v}$, one has

$$\nabla\cdot\vec{v} = \nabla\cdot\left[\gamma(1-\gamma)\frac{\rho_m-\rho_g}{\rho}\vec{u}_{r\gamma}\right] + \nabla\cdot\left[\beta s\frac{\gamma-\beta}{\gamma+\beta s}\frac{\rho_m}{\rho}\vec{v}_r\right]\,. \tag{5.37}$$

This equation should be discretised and then assembled, together with the discretised momentum equation (5.27), into the block system that follows:

$$\begin{bmatrix} \boldsymbol{\mathcal{A}}_D & \nabla \\ \nabla\cdot & 0 \end{bmatrix} \begin{bmatrix} \phi \\ p \end{bmatrix} = \begin{bmatrix} \boldsymbol{\mathcal{A}}_H - \nabla p_s - \vec{g}\cdot\vec{z}\nabla\rho - \sigma\kappa\nabla\gamma \\ \nabla\cdot\left[\gamma(1-\gamma)\frac{\rho_m-\rho_g}{\rho}\vec{u}_{r\gamma}\right] + \nabla\cdot\left[\beta s\frac{\gamma-\beta}{\gamma+\beta s}\frac{\rho_m}{\rho}\vec{v}_r\right] \end{bmatrix}, \tag{5.38}$$

1. Compute the relative velocities (5.21).
2. $\gamma - \beta$-sybcycle:
    (a) Update $\phi_{r\gamma}$ (5.26) and ϕ_γ (5.42).
    (b) MULES::explicitSolve01(γ, ϕ_u, ϕ_γ).
    (c) Update ϕ_r (5.21), ϕ_β (5.43) and $\phi_{u\beta} = \phi_\beta / \beta$.
    (d) MULES::explicitSolve(β, $\phi_{u\beta}$, ϕ_β, β_{min}, β_{max}).
    (e) Calculate the unit normal vector
    as well as curvature of the free-surface.
    (f) Restart 2(a) if the $\gamma - \beta$ subcycle is not ended.
3. Update the mass flux (5.45).
4. Construct $\boldsymbol{\mathcal{A}}$, equation (5.46).
5. PISO-Loop:
    (a) Predict fluxes using equation (5.40).
    (b) Construct and solve the pressure equation (5.39).
    (c) Correct fluxes, equation (5.41).
    (d) Reconstruct velocities.
6. Solve $k - \epsilon$ equations (if required).
7. Update flow properties (density, viscosity, etc)

Table 5.2: Explicit three-phase numerical solution procedure.

where $\phi \equiv \overline{\mathbf{V}} \cdot \mathbf{S}$ is now defined as in the incompressible Navier-Stoke equations. A revised formulation of the pressure equation via a Schur's complement yields:

$$\left[\!\!\left[\nabla \cdot \left[\left(\frac{1}{\boldsymbol{\mathcal{A}}_D} \right)_f \nabla [p^*] \right] \right]\!\!\right] = \nabla \cdot \phi^* - \nabla \cdot \left[\gamma(1-\gamma) \frac{\rho_m - \rho_g}{\rho} \vec{u}_{r\gamma} \right] - \nabla \cdot \left[\beta s \frac{\gamma - \beta}{\gamma + \beta s} \frac{\rho_m}{\rho} \vec{v}_r \right] , \tag{5.39}$$

with

$$\phi^* = \left(\frac{\boldsymbol{\mathcal{A}}_H}{\boldsymbol{\mathcal{A}}_D} \right)_f \cdot \mathbf{S} - \left(\frac{1}{\boldsymbol{\mathcal{A}}_D} \right)_f \left[(\vec{g} \cdot \vec{z})_f |\mathbf{S}| \nabla_f^\perp \rho + (\sigma\kappa)_f |\mathbf{S}| \nabla_f^\perp \gamma + \nabla p_s \right] \tag{5.40}$$

and

$$\phi = \phi^* - \left(\frac{1}{\boldsymbol{\mathcal{A}}_D} \right)_f |\mathbf{S}| \nabla_f^\perp p^* \,. \tag{5.41}$$

The pressure equation (5.39) is a Poisson equation with the diagonal part of the discretised momentum acting as diffusivity and the divergence of the velocity on the RHS. The block $\boldsymbol{\mathcal{A}}_D$ only contains diagonal entries and is easy to invert, preserving the sparseness pattern in the triple product. Therefore, we avoid the inconveniences of the original non-linear system of equations defined by $\boldsymbol{\mathcal{A}}$, which is a sparse matrix whose inverse is likely to be dense and the triple product with $\boldsymbol{\mathcal{A}}^{-1}$ would result in a dense matrix, making it computationally expensive to solve.

Additional difficulties come from the multi-dimensional scalar transport equations (1.32)-(1.33). In the previous section, the standard way of discretising both equations was proposed [see equations (5.34)-(5.35)]. However, the γ function is sharp in the interface and so the numerical solution obtained with standard methods (e.g. Jasak and Weller, 1995) will be strongly diffusive, smearing therefore the interface (Gopala and van Wachem, 2008). Similarly, the β function may exhibit discontinuities (e.g. Ungarish, 1993), introducing the same difficulties as the γ function. Furthermore, special care has to be taken since the solid volumetric concentration cannot cross the free-surface. This implies that the volumetric flux, of both functions γ and β, at the interface should be numerically limited coherently. The best way to guarantee a sharp and bounded solution, and propagate both functions coherently, is to couple both equations and to solve them with a numerical scheme designed for the multi-dimensional advection equation (e.g. LeVeque, 1996). To this end, the explicit Multidimensional Universal Limiter with Explicit Solution (MULES) implemented in OpenFOAM (OpenCFD Limited, 2007) was adapted to our requirements.

MULES employs the following input parameters: the normal convective flux, and the actual explicit flux of the variable which is also used to return limited flux of the bounded-solution. The normal flux of the variables to be solve are given by

$$\phi_\gamma \equiv \left[\gamma\overline{\mathbf{U}} + \gamma(1-\gamma)\overline{\mathbf{U}}_{r\gamma}\right]_f \cdot \mathbf{S} = \gamma[\phi_u + (1-\gamma)\phi_{r\gamma}]\,, \tag{5.42}$$

$$\phi_\beta \equiv \left[\beta\overline{\mathbf{U}} + \beta(1-\beta)\overline{\mathbf{U}}_{r\beta}\right]_f \cdot \mathbf{S} = \beta\left[\frac{\phi_\gamma}{\gamma} + \left(1-\frac{\beta}{\gamma}\right)\phi_r\right]\,, \tag{5.43}$$

being ϕ_u the volumetric flux at the cell face: $\phi_u \equiv \overline{\mathbf{U}}_f \cdot \mathbf{S}$. Consequently, the mass flux at the cell faces can be then determined from the normal flux of γ and β:

$$\rho\phi \equiv \rho\overline{\mathbf{V}} \cdot \mathbf{S} = \rho_g\phi_u + (\rho_p - \rho_f)\phi_\beta + \left[(\rho_m - \rho_g) - \frac{\beta}{\gamma}(\rho_p - \rho_f)\right]\phi_\gamma\,. \tag{5.44}$$

Thus, one should first solve the γ-equation calling "MULES::explicitSolve01(γ, ϕ_u, ϕ_γ)" that returns the limited flux ϕ_γ used in the computation of γ. This normal flux is used to evaluate ϕ_β and then the solution of the β-equation "MULES::explicitSolve(β, $\phi_{u\beta}$, ϕ_β, β_{min}, β_{max});" where $\phi_{u\beta} \equiv \phi_\beta/\beta$. These equations should be iterated inside the so-called γ-β-subcycle. This subcycle consists in solving both equations $N_{\gamma\beta}$-times and then averaging the mass flux:

$$\rho\phi \equiv \rho\overline{\mathbf{V}}\cdot\mathbf{S} = \rho_g\phi_u + \sum_{i=1}^{N_{\gamma\beta}} \frac{\delta t^i}{\Delta t} \left\{ (\rho_p - \rho_f)\phi_\beta^i + \left[(\rho_m - \rho_g) - \frac{\beta^i}{\gamma^i}(\rho_p - \rho_f) \right] \phi_\gamma^i \right\} . \quad (5.45)$$

Then, the mass flux $\rho\phi$ required by the momentum balance should be computed according to (5.45), in such a way that the limited fluxes employed to solve the γ- and β-equation are accounted for in the PISO-Loop. Therefore, the momentum equation has to be formulated explicitly:

$$\boldsymbol{\mathcal{A}} := \frac{\partial\rho[\overline{\mathbf{V}}]}{\partial t} + \nabla\cdot\left(\rho\phi[\overline{\mathbf{V}}]_{f(\rho\phi,S)}\right) = \nabla\cdot\left(\mu\nabla[\overline{\mathbf{V}}]\right) + \nabla\cdot\boldsymbol{\mathcal{R}}^{eff\mathcal{C}} , \qquad (5.46)$$

hence maintaining constant the mass flux $\rho\phi$ in the advection term inside the PISO-Loop. Once the pressure-velocity equations are solved, the volumetric flux ϕ_u is updated from (5.36). The overall numerical procedure is sketched in Table 5.2.

5.5 Test cases

We select the problem of local scour around pipeline (Mao, 1986), and the erosional dam-break wave (Capart and Young, 1998; Spinewine and Zech, 2007) to test the theoretical model and the numerical scheme. The first case is solved with the implicit numerical method (§ 5.4.1), whilst the second one is computed by using the explicit one (§ 5.4.2). According to previous numerical works (e.g. Brors, 1999; Wu et al., 2000; Li and Cheng, 2001; Sumer, 2007), the free-surface is modelled as a symmetric plane in the pipeline scour problem. This assumption is likely to be valid when the curvature of the interface is smooth, and reduces in one the number of partial differential equations to be solved. The main objective at this stage is to take into account the sediment erosion, transport and deposition, and to analyse its dependence on the input parameters of the model. The erosional dam-break wave is highly unsteady, so the capabilities of the model to capture the evolution of the free-surface and the sediment bed are better appreciated herein.

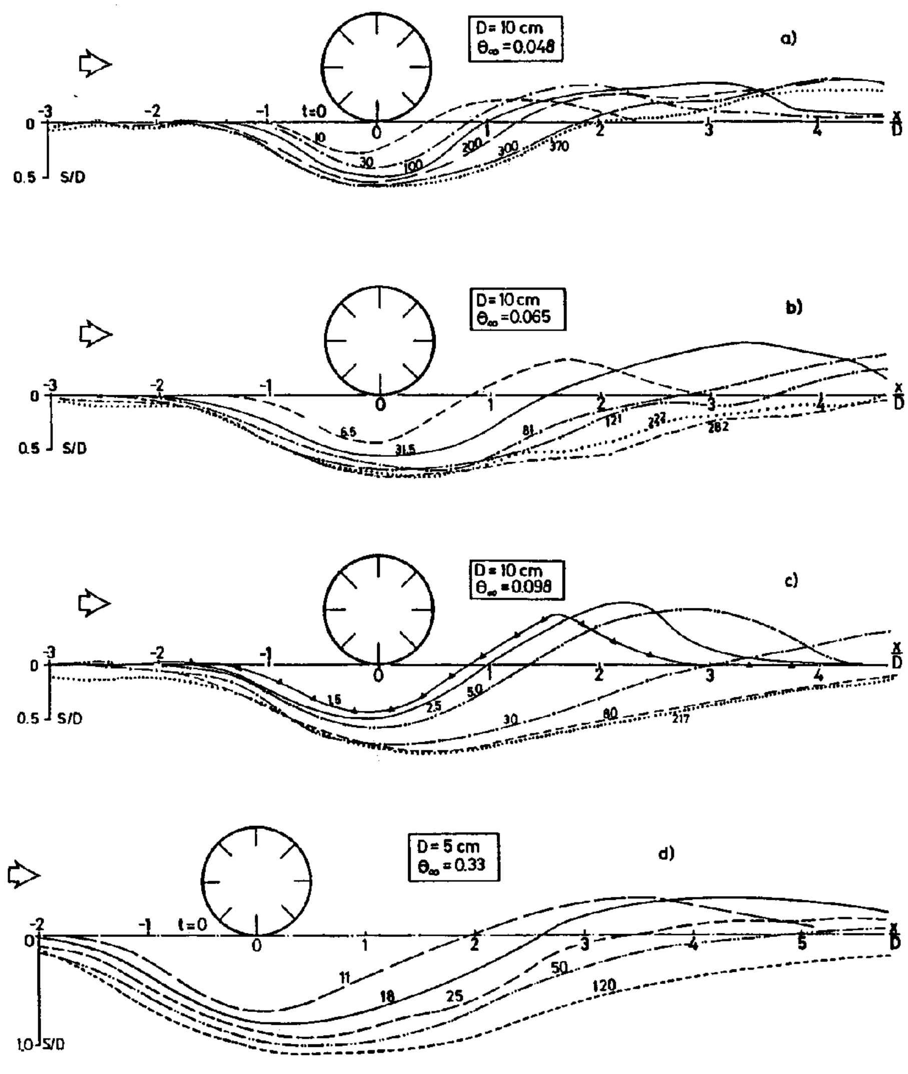

Figure 5.2: Development of bed profile with time (in min). The water-depth in the cases (a,b,c) is $0.35m$ and the cylinder diameter $10cm$, whilst for (d) the water-depth and the cylinder diameter is $0.23m$ and $5cm$, respectively. Figure taken from Mao (1986). The Shields Parameters of 0.048, 0.056, and 0.096 correspond to free stream velocities of 37, 44, and $53cm/s$, respectively.

5.5.1 Local scour

Mao (1986) presented laboratorial experiments for the interaction between a pipeline and an erodible bed. Mao observed the scour around horizontal cylinders in steady current and wave conditions, as well as with different Reynolds numbers, Shields parameters, and pipeline gaps. These experiments investigated such scour features as the shape and size of the scour hole and the time scale of scour hole formation. Scour around the object may cause the structure fail. It is important for engineers to understand the process of scour and to make better designs to prevent or mitigate the damage. This work has motivated further experimental research on scour around solids (e.g. Jensen et al., 1990; Gao et al., 2006; Cataño Lopera and García, 2007), as well as theoretical studies (e.g. Brors, 1999; Li and Cheng, 2001; Lua et al., 2005; Sumer, 2007; Smith, 2004, 2007).

The case considered herein is a clear water case (Shields parameter = 0.048, mean particle diameter = $0.036cm$) where scour and deposition are caused only by the local fluid forcing, with no net transport downstream. The cylinder has a diameter of $10cm$ ($Re = 3.7 \times 10^4$) for these experiments.

The results of the numerical simulation at several instants of time are shown in Figure 5.3, where the water is flowing from left to right. The flow streamlines (pink lines) depict the primary down-stream recirculation zone, that disappears as the bed is eroded. The numerical results were not (quantitatively) compared against the experimental data because of the evident disagreement: the time scale of the erosional process in the numerical results is accelerated with respect to the physical one, and the dune that should be created downstream of the cylinder did not appear in the numerical simulation. This unsatisfactory result may be due to the viscoplastic model employed to describe the shear-thinning behaviour of the dense suspension. It should be noted that viscoplastic models yield *ill-posed problems* - when the bed is fluidized the viscosity changes abruptly from “infinite” to the laminar viscosity, and so the sediment is suddenly ejected from the bed after its fluidization. Lalli et al. (2005) observed the same difficulties when they applied their model to the local scour problem. Therefore, the yield stress plays the main role in our model. In fact,

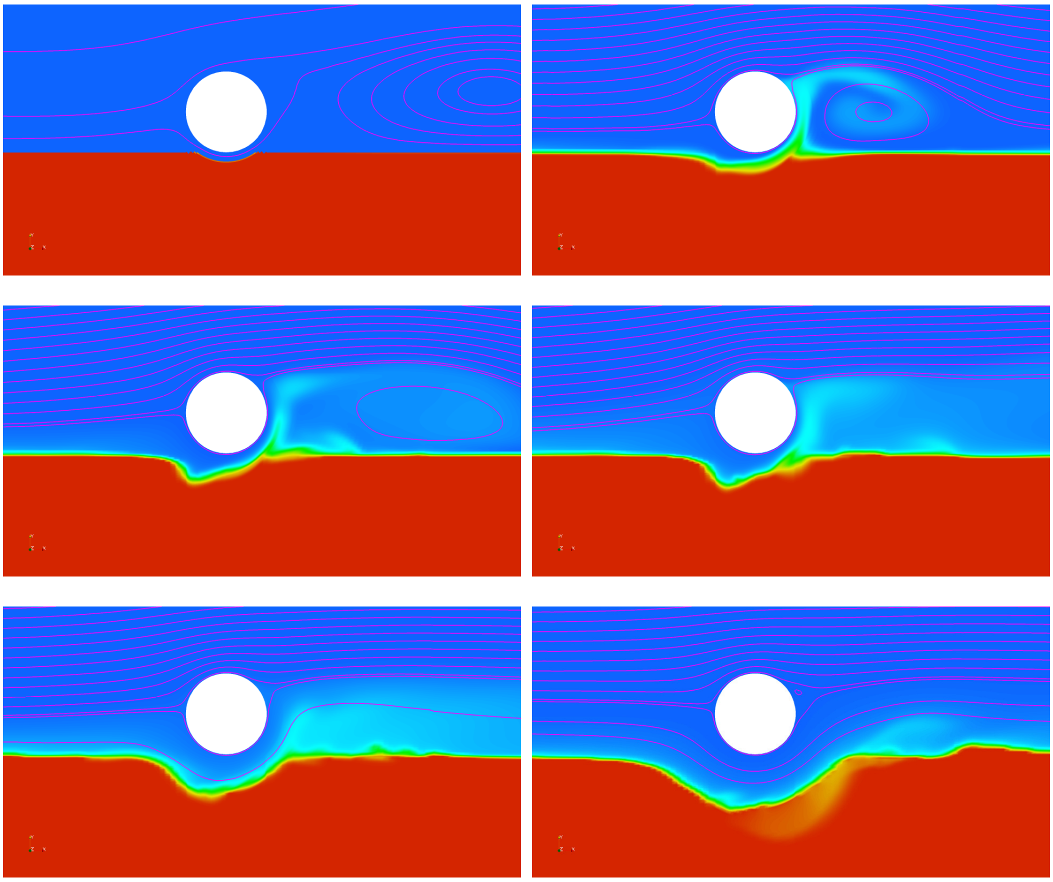

Figure 5.3: Numerical results for the evolution of the bottom bed in the Mao's problem, case a in Figure 5.2, at several instants of time (from left to right, and from top to bottom: $t = 0,\ 35,\ 36,\ 37,\ 40,\ 55s$). The sediment volume fraction scale is the same as that depicted in Figure 5.4.

in absence of yield stress our model is able to give better predictions of the mixture behaviour (see § 5.5.2). However, this fact does not explain the continuous suspension of the eroded sediment, that is convected out of the domain of computation, without predicting the formation of the dune observed experimentally. The source of this error is the turbulent diffusion that was added to the β-equation (1.33), resulting

$$\frac{\partial \beta}{\partial t} + \nabla \cdot (\beta \langle \vec{u} \rangle) + \nabla \cdot [\beta(1-\beta)\langle \vec{u}_{r\beta} \rangle] = \nabla \cdot \left(\frac{\mu_t}{\sigma} \nabla \beta \right) . \tag{5.47}$$

The turbulent diffusion term (on the RHS of the equation shown above) is traditionally considered on hydraulic engineering, but in our case seems to overpredict the transport of suspended sediment. In Mao's experiment the turbulent kinetic energy

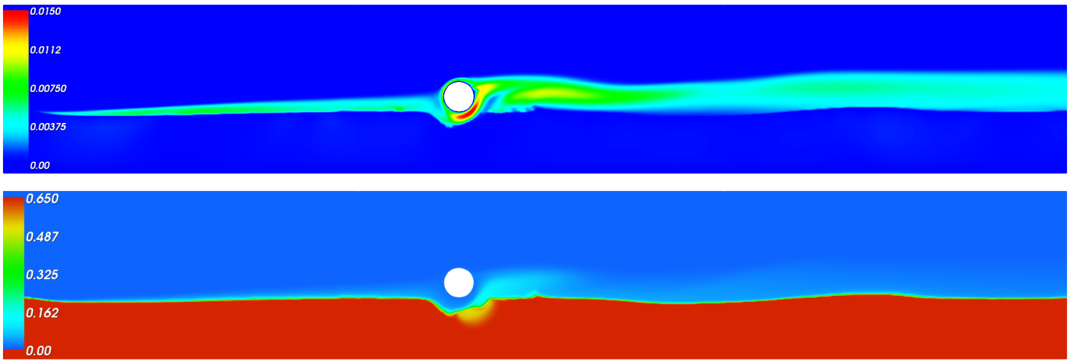

Figure 5.4: Numerical simulation of the turbulent kinetic energy (at the top) in Mao's experiment. At the bottom is shown the sediment volume fraction at the same instant of time.

k is intensively developed over the cylinder and mainly in the turbulent boundary layer growing from the bottom bed, as shown in Figure 5.4.

5.5.2 Erosional dam-break flow

With the Tapei erosional dam-break wave experiments (Capart and Young, 1998) we return to our problem of main interest. Our purpose in this chapter was to avoid the limitations intrinsic to depth-averaged shallow-water models and, to that end, we have presented a formulation valid for non-hydrostatic free-surface flows of non-dilute suspensions. An illustrative problem to show the capabilities of the model, as well as the numerical scheme proposed to solve it, is the erosional dam-break wave. This experiment has been conducted under different initial conditions and with sediment of diverse characteristics (Capart and Young, 1998; Leal et al., 2002; Spinewine and Zech, 2007). To reduce the number of physical parameters that introduce uncertainties in the model, we have selected the case in which the flow does not exhibit yield stress during the flood. The Tapei dam-break experiments was performed into an undisturbed bed with a sediment concentration of 40% in volume, with very light sediment $\rho_s = 1.048\rho_f$. Under these conditions, the rheology of the suspension is expected to depend on the sediment volumetric concentration β.

This test problem was considered on many other studies (e.g. Capart and Young, 1998; Fraccarollo and Capart, 2002; Fraccarollo et al., 2003; Cao et al., 2004; Simpson and Castelltort, 2006; Wu and Wang, 2007), and theoretical predictions were given by using depth-averaged shallow-water models. In general, the overall agreement of the one-dimensional numerical simulations and the experimental results is satisfactory. There are marked differences in some locations between the free-surface location and the bed elevation, but the main behaviour of the dam-break wave is properly captured. The test reach for the Taipei experiments was of length $1.2m$, width $20cm$ and sidewall height $70cm$. The particle diameter was $6.1mm$, the density $1048kg\,m^{-3}$ and fall terminal velocity $7cm\,s^{-1}$. The water level upstream of the gate raised the depth $10cm$ above the top of a granular bed of constant thickness of approximately $5-6cm$. The gate released the water at rest within $50ms$.

The results obtained with our model are shown in Figure 5.5, together with the initial configuration. In order to reproduce the flood in the initial stage, that is pretty affected by the gate release process, it was necessary to set the velocity of the cells bordering with the gate to $0.75ms^{-1}$ along the direction of the gravity. Our numerical simulation does not reproduce exactly the erosional dam-break wave, but is qualitatively very similar to the physical result. It should be pointed out that the relative velocity of the sediment with respect to the water was neglected, i.e. it was supposed that the sediment is purely advected with the dense-suspension. We suggest that the main cause of the discrepancy is that the sediment fall velocity leads vertical stratification that increases substantially the viscosity of the mixture (see Figure 5.1). For this reason, the velocity of the fordward wave is reduced. Another factor that may affect the predictions is the maximum packing factor β_M and the volume fraction threeshold β_m to develop yield stress - the packing limit is a measure of microstructure, and microstructure changes with flow (Stickel and Powell, 2005). Apart from the reality of these results, the numerical scheme implemented is able to propagate the free-surface as well as the sediment volume fraction with success, and conserves the mass (as the volume-averaged phase-fraction of each specie remains constant during the numerical simulation).

On the other hand, the useful configurations of erosional dam-break waves, recently presented by Spinewine and Zech (2007), can be used to check the capability

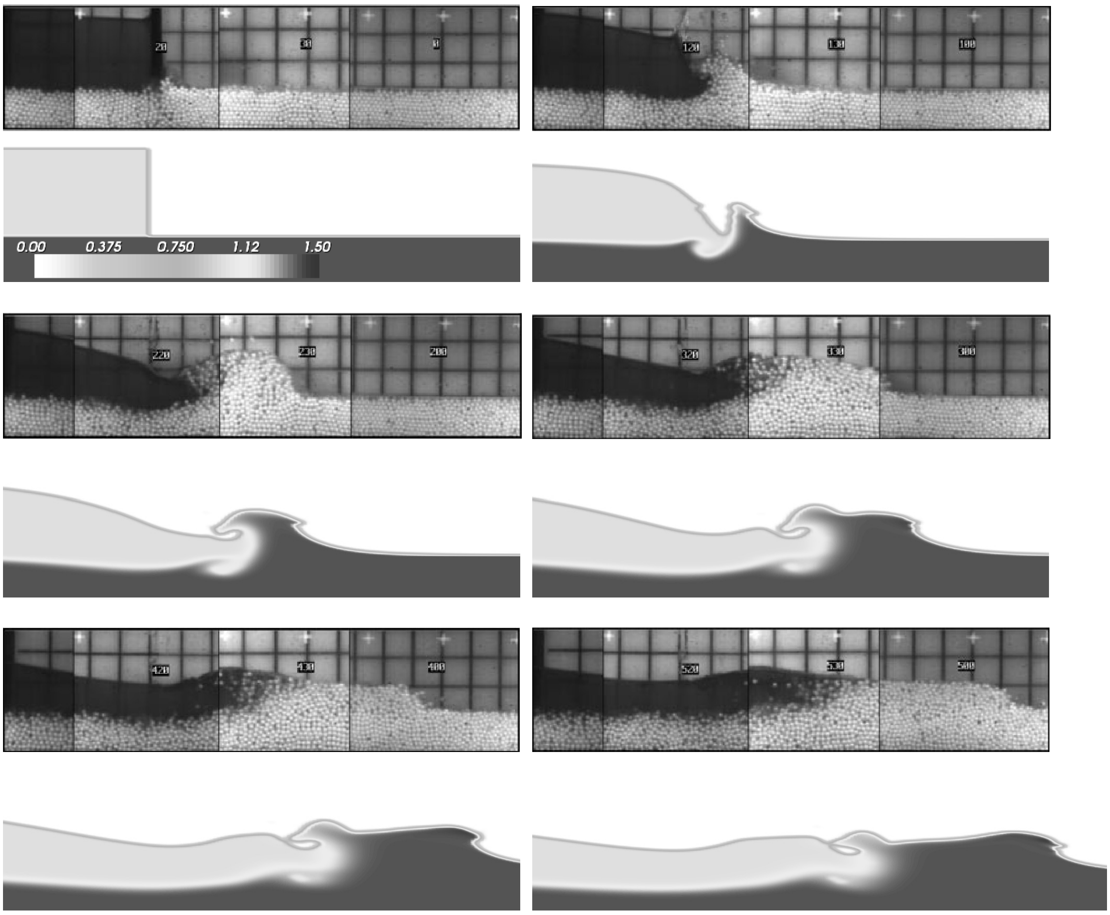

Figure 5.5: Image mosaics for the Tapei erosional dam-break wave experiments, conducted with light granular material ($\rho_s = 1.048\rho_f$), and the numerical simulation using the numerical scheme in § 5.4.2, where the scalar field $\gamma + \beta$ is drawn. The instants selected are: $t = 0\,s$, $0.1\,s$, $0.2\,s$, $0.3\,s$, $0.4\,s$, $0.5\,s$. Digital footpage from the experiments of Capart and Young (1998) in Fraccarolo and Capart (2002).

of the mixture model presented in this work to predict the transport of sediment. They provide six scenarios, each of them for two kinds of sediment, sand and PVC sediment. These scenarios differ each other in the initial configuration of the sediment and water at rest. Thus, the input parameters of the model can be calibrated, simulating one of the six experiments, and then the goodness of the model should be checked against the other five experiments. We now present the calibration result for the configuration f (see Fig. 5.6) with PVC pellets. The PVC pellets are slightly cylindrical in shape, with an equivalent spherical diameter of $3.9mm$, a specific density $\rho_p = 1580\, kg\, m^{-3}$, a frictional angle of 38^o and no cohesion. This PVC sediment is set in place at the random close packing 58%. With this sediment volume fraction, we expect the dense suspension to develop yield stress. We have corroborated this fact by simulating the configuration f with different values of β_m, fixing the other input parameters to the values $\beta_M = 0.608$, $C_p = 0.5$ and $n = p = 2$. However, as was discussed in the previous section, the shear stress law (5.16) is not appropriate, and we adopt now the proposal of Wildemuth and Williams (1984):

$$\tau_0 = \left[A_{WW} \frac{\beta_M}{\beta_m} \left(\frac{\beta - \beta_m}{\beta_M - \beta_m} \right) \right]^{1/m_{WW}} , \tag{5.48}$$

being A_{WW} and m_{WW} constants that depend on the sediment under consideration - we use the values $A_{WW} = 33\, kg\, m\, s^{-2}$ and $m_{WW} = 1$.

Figure 5.6 depicts the numerical simulation at three instants of time (as indicated in the figure caption) with $\beta_m = 0.4$. This value of the Newtonian limit β_m is lower than we could expect from the rheological analysis of the sediment particles but gives good predictions of the bed deformation. This disparity should be caused by the uncertainty of the other input parameters, which were given default values. The present test shows the capability of the Bingham model to capture the bed-load mechanism of sediment transport. We are still working in the other five configurations that exhibit the difficulty of capturing the advance of a wetting front responsable of the bed fluidization.

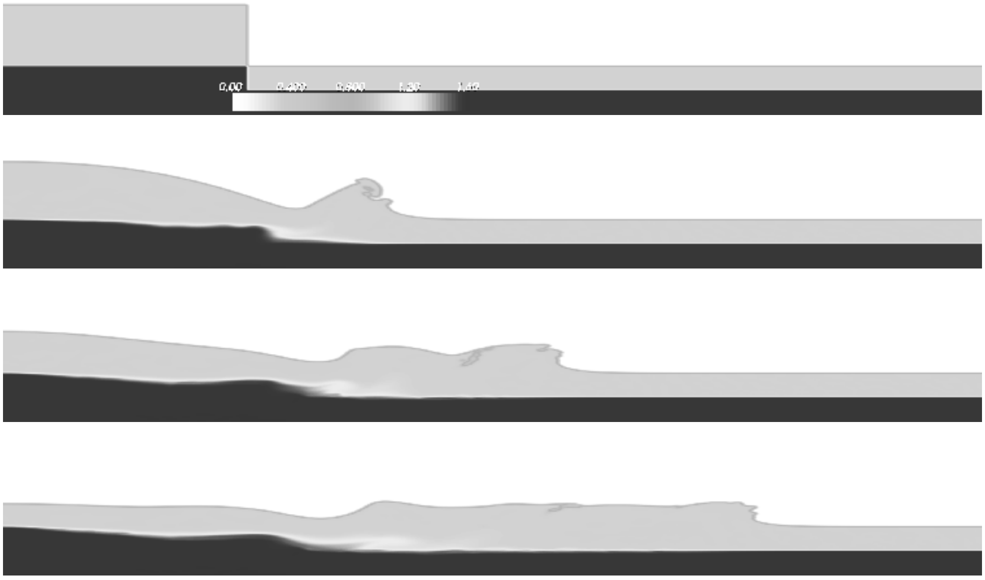

Figure 5.6: Image mosaics ($400 \times 50\, cm^2$) for the numerical simulation of the Louivain erosional dam-break wave experiments, conducted with PVC (configuration f). The instants selected are: $t = 0$, 0.4, 0.8 and $1.25\, s$; the color scale corresponds to $\beta + \gamma$.

5.6 Summary and conclusions

A Continuum Mechanics formulation for the transport of sediment in free-surface flows was formulated from the ensemble-averaged Navier-Stokes equations. The multi-fluid equations were simplified to the mixture equations. The terms in the equations were formulated, when possible, as in the standard scalar transport equation, in such a way that they admit Computational Continuum Mechanics solvers that ease their implementation and solution. In particular, the sediment transport equation was rewritten in terms of the relative velocities, resulting a similar equation to that of the free-surface. Two numerical schemes were proposed to solve the mixture model: a segregated implicit FVM, and a segregated explicit FVM. Both numerical schemes were implemented in the OpenFOAM package and were applied to the problem of local scour and erosional dam-break, respectively.

The implicit method was applied to the local scour problem around pipelines in order to show the capabilities of the model to account for sediment erosion, transport and deposition, and check the constitutive laws proposed in § 5.3. Although the numerical results described the structure of the flow field, the transport of sediment exceeded the physical one. The main cause of the divergence seemed to be the expression employed for the yield stress and the introduction of turbulent diffusion in the sediment transport equations.

The Tapei dam-break wave was analysed numerically, showing the capabilities of the explicit numerical scheme to capture the propagation of the free-surface and sediment volume fraction. The yield stress was neglected at this stage. The numerical results were quite promising, although the matching between the numerical solution and the physical experiment could be improved by considering a shear-thinning mechanism. Then, one of the configurations of the Louivain dam-break wave experiment was solved. This experiment, which shows high yield stress, pointed out again the importance of the appropriate modelling of the shear-thinning mechanisms in the transport of sediment.

Chapter 6

Closure

This last Chapter concludes the thesis and is divided in two Sections. The first Section summarises the conclusions acquired from this work and the second one makes suggestions for future work.

6.1 Conclusions

The results of the present study have been extensively assessed and discussed in the previous Chapters. In the following, the most important conclusions are summarised.

- For a suddenly released mass of fluid over an inclined plane, the theoretical location of the wetting front has been supplied in the kinematic wave regime, together with the velocity and water-depth field, based on depth-averaged equations. One of the most noticeable effects of the results for large slopes of the bottom is the divergence of the previous solution by Hunt (1982, 1984) obtained by using the traditional Saint-Venant equations. The results for *any mass of fluid* that spreads on a plane bed are identical to those reported by Weir (1983) and Hunt (1984) in terms of a specific set of non-dimensional variables. We paid special attention to the shape of the flood in the tip region, where the solution has been obtained as a full expansion in terms of the streamwise coordinate located at the wetting front. The present results are directly comparable to those obtained by Hunt (1984) when we use enough terms in the expansion.

- The shallow-water equations (with the appropriate initial conditions for a dam-break over an inclined surface) have been solved using an upwind TVD method, second-order accurate in both space and time, with semi-implicit and upwind treatment of the source terms. We found that the asymptotic analytical solutions and the numerical simulations are in almost perfect agreement, except for Froude numbers larger than two due to the development of roll-waves. The accuracy of the numerical solution has been also checked, and very good results have been obtained by just using a cut-off height as boundary condition for the wetting front.

- The existence of physical instabilities in floods on steep inclines was illustrated.

- The theory of linear stability has been applied to the set of equations governing the depth-averaged motion in open channel flow.

    - First, we considered a non-parallel spatial stability analysis of the one-dimensional kinematic waves with turbulent friction down an inclined plane, and we found an asymptotic analytical solution for the critical Froude number as a function of both the wave frequency and non-parallel characteristic of the base flow.

    - The exact solution for the linear perturbations with $Fr = 2$ have been obtained by means of multiple scale expansion. This result has been compared against the non-linear simulation of the perturbation, showing a perfect matching between both solutions.

    - However, the non-parallel spatial stability analysis fails to predict the linear stability criteria due to the unnegligible influence of the base-flow temporal variation.

    - We designed a numerical experiment, and a clever numerical method, that allows to compute the linear and non-linear evolution of small perturbations.

    - We have found that non-uniform and unsteady effects of the background flow stabilise turbulent roll-waves and raise the critical Froude number required for instability.

- The well known stability criteria for parallel flows at high Reynolds number (the basic flow is unstable for any wave length and Froude number larger than 2) differs abruptly of that resulting from kinematic waves. One of the most noticeable effects is the stabilisation of disturbances on basic flows with $Fr_{eq} = 2$. In addition to that, for larger Froude numbers, $Fr_{eq} > 2$, the wave amplitude decreases or increases depending on the velocity, and both spatial and temporal gradients of the base flow. Furthermore, stable waves lengthen as time goes on - this behaviour is also different with respect to the parallel one, in which waves remain with constant wave length even when hydraulic jumps are developed.

- In this work, the one-dimensional problem of transport of dilute suspended sediments after the rupture of a dam on an inclined bed of arbitrary constant slope is formulated. The frictional model has been validated against existing experimental data. Several numerical techniques have been tested with available analytical solutions for the transport of sediment in the dam-break problem on a horizontal bed.
  - The transport of suspended sediments has been characterised as a function of the slope of the bed for different values of the parameters characterising the sediments. To that end, we use the maximum value of the normalised sediment load ($Q^*_{s,max}$) and the normalised time at which this maximum is reached after the rupture of the dam (t^*_{max}).
  - Some details on the water height, flow velocity, and sediment concentration profiles are also given.
  - We observe the formation of roll waves near the advancing water front for large times. They produce spatial oscillations in the sediment concentration near the wetting front, but they do not affect to $Q^*_{s,max}$ since they are produced for $t \gg t_{max}$.

  - We have also characterised the validity of the dilute sediment approach as a function of the bed slope and the sediment properties.
  - We have also computed the bed-load transport and discussed its relative importance to the suspended sediment transport in the present problem as a function of the size of the sediment particles and the inclination of the bed.
  - It is concluded that bed-load motion is more important than suspended transport for large sediment particles ($d_s \sim 5mm$), especially for small bed angles. For small particles ($d_s \simeq 1mm$ or smaller), the sediment transport is dominated by suspension, the more so the larger of the bed slope.

- A Continuum Mechanics formulation for the transport of sediment in free-surface flows was formulated. Starting from the ensemble averaged Navier-Stokes equations, the multi-fluid equations were simplified to the mixture equations. The derivative operators in the equations were formulated, when possible, as in the standard scalar transport equation, that ease their implementation and solution with OpenFOAM.

- The k-ϵ turbulent model with a buoyancy modification term in the k equation to account for density stratification is considered on the closure laws. To account for the transport of sediment in the laminar regime, a Bingham model is adopted in the determination of the laminar viscosity.

- Two Finite Volume Methods were provided: first, an implicit segregated approach, useful for problems in which the free-surface remains nearly flat; then, an explicit segregated scheme, able to capture with high precision the free-surface advection, breaking apart and merge together, as well as the evolution of the sediment volume fraction. The last numerical scheme was able to maintain constant the mass of water and sediment during the numerical simulation.

- The numerical simulation of Mao's (1986), Capart and Young (1998) and Spinewine and Zech (2007) dam-break experiments reported a strong dependence of the results with the yield stress. The agreement between the numerical solution and the physical experiments was better when the yield stress can be neglected, as it happens in the Taipei dam-break experiments.

6.2 Suggestions for future works

Obviously, all the suggestions on future works are related to the more ambitious model for three-dimensional, hyper-concentrated flows described in the last chapter. Before we proceed with recommendations for the future work, the important role of measurements has to be emphasised. The mixture model rely on the availability and accuracy of measurements. Therefore, only more extensive experimental data will reduce the uncertainty inherent in some of the models and/or will give evidence of phenomena currently unaccounted for.

Due to the fact that this work does not focus on experimental methods, the suggestions will be mainly directed towards researchers in the field of modelling and numerics. Tasks which are, arguably, of the most priority are as follows:

- Comparison of the depth-averaged results presented in Chapters 2-4 with that obtained using the mixture model.
- Derivation of accurate and reliable correlations for the solid phase pressure and stress tensor, that could be incorporated into the mixture model.
- Inclusion of the k-ϵ turbulence model in the interface-capturing calculations. Improvements in the turbulence modelling for the mixture methodology must be developed. Although the influence of turbulence modelling has not been investigated extensively, it is very likely that some of the discrepancies discovered in this study are due to deficiencies in the models used. For example, it is very difficult to incorporate the effects of large scale eddies, so-called coherent structures, on the slip velocity.
- Improvement of the wall functions used by the k-ϵ turbulence model to account for the bed roughness.

- Inclusion of Large Eddy Simulation (LES) turbulence models and comparison against RANS. The main idea of LES is to filter the small scales out of the Navier-Stokes equations and resolve the larger ones. The smaller scales are represented using a so-called sub-grid model by relating the sub-grid Reynolds stress tensor to the sub-grid fluctuations.
- Validation of the current mixture methodology against a more complete set of experimental data. In particular, a comparison between the sediment and pressure distribution along the vertical direction against physical measures could be valuable.

The present study should be regarded as a further step towards the accurate simulation of sediment transport in free-surface flows. The mixture model presented in here has not addressed many important phenomena, such as heat- and mass transfer, size distribution effects as well as phase change. The inclusion of these into the framework of the mixture model is by no means uncharted territory and many researchers have made contributions towards it. However, it is unlikely that a single model will emerge eventually because of the many ways these phenomena interact with each other. More likely, several multi-fluid methodologies will co-exist, each specialising in the aspects most relevant to the particular application in mind. In this respect, it is the hope of the author that this study might serve as a tool-box to other modellers and engineers in industry who attempt the prediction of sediment transport in environmental flows.

Appendix A

Neutral curves

Taking $e = i\epsilon$ (i.e., $\sigma = 0$) in Eq. (3.42), dividing its imaginary part by ϖ, and solving it for ϖ, one obtains

$$\varpi^2 = \frac{\phi\,\{(11-12\beta)+\phi\,[27-25\beta+\varrho(22\beta-4)]+2\phi^2\,[3+2\beta(\varrho-1)]\}}{(3\beta-2)\,[-1+2\beta+(\varrho-1)\beta^2]+\phi\,[3+4(\varrho-2)\beta-7(\varrho-1)\beta^2-2(\varrho-1)^2\beta^3]}\,, \tag{A.1}$$

where $\beta = \epsilon/\varpi$. Substituting into the real part of (3.42), the following expression is obtained

$$\sum_{i=0}^{6} r_i(\varrho,\phi)\,\beta^i = 0\,, \tag{A.2}$$

where

$$\begin{aligned} r_0 \equiv\ & -88+(32\varrho-661)\phi+8(7\varrho-195)\phi^2+2(-877-56\varrho+8\varrho^2)\phi^3 \\ & -9(101+12\varrho)\phi^4-162\phi^5, \end{aligned} \tag{A.3}$$

$$\begin{aligned} r_1 \equiv\ & 668+(4220-1000\varrho)\phi+(9763-4080\varrho+224\varrho^2)\phi^2+(9737-5156\varrho+128\varrho^2)\phi^3 \\ & +(4569-2854\varrho-208\varrho^2)\phi^4+(756-612\varrho)\phi^5, \end{aligned} \tag{A.4}$$

$$\begin{aligned} r_2 \equiv\ & 88\varrho-2098+(-12101+5514\varrho-32\varrho^2)\phi+(-25479+20836\varrho-3184\varrho^2)\phi^2 \\ & +(-22537+25417\varrho-6396\varrho^2+352\varrho^3)\phi^3+(-9533+13277\varrho-3708\varrho^2-32\varrho^3)\phi^4 \\ & +(-1458+2418\varrho-848\varrho^2)\phi^5, \end{aligned} \tag{A.5}$$

$$\begin{aligned} r_3 \equiv\ & 3489 - 492\varrho + (18453 - 13250\varrho + 848\varrho^2)\phi + (35492 - 44365\varrho + 12860\varrho^2 \\ & - 192\varrho^3)\phi^2 + (27825 - 48629\varrho + 24150\varrho^2 - 2992\varrho^3)\phi^3 + (10567 - 23359\varrho \\ & + 15072\varrho^2 - 2552\varrho^3 + 128\varrho^4)\phi^4 - 8(-186 + 481\varrho - 363\varrho^2 + 68\varrho^3)\phi^5 , \end{aligned} \tag{A.6}$$

$$\begin{aligned} r_4 \equiv\ & 54(-60 + 19\varrho) + (-15787 + 16379\varrho - 2815\varrho^2)\phi + (-27827 + 48083\varrho - 22648\varrho^2 \\ & + 2032\varrho^3)\phi^2 + (-19312 + 46379\varrho - 35759\varrho^2 + 9008\varrho^3 - 208\varrho^4)\phi^3 + (-6562 \\ & + 20292\varrho - 21150\varrho^2 + 8092\varrho^3 - 672\varrho^4)\phi^4 - 8(-1 + \varrho)^2(106 - 171\varrho + 16\varrho^2)\phi^5 , \end{aligned} \tag{A.7}$$

$$\begin{aligned} r_5 \equiv\ & 1593 - 945\varrho + (7185 - 10311\varrho + 3288\varrho^2)\phi + (11639 - 26439\varrho + 18528\varrho^2 \\ & - 3728\varrho^3)\phi^2 + 4(1784 - 5547\varrho + 6042\varrho^2 - 2615\varrho^3 + 336\varrho^4)\phi^3 - 4(-1 + \varrho)^2 \\ & (-541 + 1110\varrho - 504\varrho^2 + 16\varrho^3)\phi^4 + 64(-1 + \varrho)^3(-4 + 7\varrho)\phi^5 , \end{aligned} \tag{A.8}$$

$$\begin{aligned} r_6 \equiv\ & 324(-1 + \varrho) - 9(151 - 293\varrho + 142\varrho^2)\phi + 12(-1 + \varrho)^2(-169 + 154\varrho)\phi^2 \\ & - 3(-1 + \varrho)^2(365 - 696\varrho + 316\varrho^2)\phi^3 + 8(-1 + \varrho)^3(37 - 78\varrho + 32\varrho^2)\phi^4 \\ & + 32(-1 + \varrho)^4(-1 + 2\varrho)\phi^5 . \end{aligned} \tag{A.9}$$

These rather involved algebraic expressions have been obtained with the help of *Mathematica*.

Appendix B

Resumen extendido

B.1 Introducción

El flujo unidimensional que se produce tras la rotura de una presa sobre un plano inclinado de pendiente arbitraria, así como el transporte suspendido de sedimento no cohesivo, se analiza haciendo uso de la aproximación de aguas someras. En condiciones diluidas, en la cual el sedimento trasportado por el agua no modifica las propiedades reológicas de la mezcla sedimento-agua, la hidrodinámica de dicho flujo puede ser estudiada analíticamente en los instantes tardíos. Para tiempos suficientemente grandes tras la rotura de la presa, la solución analítica es presentada bajo la hipótesis de onda cinemática, y comparada con la solución numérica. Entre la solución numérica y la analítica se observan discrepancias debido a la aparición de inestabilidades hidrodinámicas (de ahora en adelante denominadas *ondas rodantes*). La solución numérica, obtenida con un método numérico de volúmenes finitos anti-oscilatorio (de segundo orden en espacio y tiempo, y con tratamiento semi-implícito de los términos fuente), pone de manifiesto el carácter inestable del flujo resultante tras la rotura de una presa en un plano inclinado. Se observa que las inestabilidades hidrodinámicas degeneran en resaltos hidráulicos, que incrementan el transporte de sedimento suspendido. Las limitaciones del modelo, originadas por las hipótesis reológicas, son discutidas con detalle.

Posteriormente, el carácter inestable de dicho flujo, caracterizado por variar tanto a lo largo de la coordenada longitudinal como con el tiempo, es analizado mediante diversos procedimientos. En primer lugar, se considera un estudio analítico de estabilidad lineal siguiendo tres métodos: primero, un estudio *casi paralelo*, el cual retiene la influencia de las variaciones espaciales del flujo base; segundo, un estudio *no paralelo* que considera, además de las variaciones espaciales del flujo base, las variaciones espaciales de las perturbaciones; tercero, un análisis de *múltiples escalas* que retiene la dependencia espacial y temporal del flujo base, así como de las perturbaciones. El análisis de múltiples escalas permite obtener la solución exacta de las perturbaciones lineales cuando el número de Froude Fr toma el valor 2. Así, la bondad de los resultados obtenidos con el método casi paralelo y no paralelo puede ser objetivamente cuantificada. Por otro lado, también se realiza el análisis de estabilidad lineal y no lineal mediante la simulación numérica directa de la evolución de las perturbaciones lineales y no lineales. El estudio numérico es validado con la solución analítica para el caso particular $Fr = 2$. Para casos en el que el número de Froude es distinto a 2, la simulación numérica permite establecer el carácter estable o inestable de las perturbaciones.

Posteriormente, se abandonan todas las hipótesis inherentes a los modelos de transporte de sedimento en flujos unidimensionales de aguas someras, formulando un modelo novedoso basado en la Mecánica del Continuo. El modelo de mezcla para el transporte de sedimento no cohesivo en flujos laminares/turbulentos es derivado a partir de las ecuaciones de Navier-Stokes de la mezcla trifásica agua, sedimento y aire. Este modelo genérico es aplicable, por ejemplo, a problemas no hidrostáticos de flujos de aguas someras sobre terrenos de pendiente arbitraria. Este modelo revela una equivalencia matemática entre la ecuación de propagación de la superficie libre y la del sedimento. Este hecho se aprovecha para formular un método numérico explícito, que usa una discretización de volúmenes finitos, y es implementado en el programa de código abierto OpenFOAM. Los resultados muestran que el método numérico conserva la masa. En particular, se aplica el modelo al problema de erosión de sedimento debajo de un cilindro y al problema de la rotura de una presa horizontal en distintas condiciones.

A la vista de los resultados presentados en el presente documento, se observa que los modelos unidimensionales basado en variables promediadas en altura (es decir, ecuaciones de Saint-Venant generalizadas para estudiar el transporte de sedimento) son superados por modelos más sofisticados y precisos, válidos para regímenes hiperconcentrados y flujos sobre terrenos de pendiente arbitraria.

B.2 Conclusiones

Los resultados del presente estudio se encuentran detallados al final de cada uno de los capítulos previos. A continuación, se resumen las conclusiones más importantes.

- La localización del frente de avance de un lquido inicialmente en reposo, que fluye sobre un plano inclinado, ha sido obtenida analíticamente, junto con el campo de velocidad y la elevación de la superficie libre, haciendo uso de la hipótesis de aguas someras y onda cinemática. Para pendientes del terreno elevadas, los resultados presentados divergen de la solución obtenida con las ecuaciones tradicionales de Saint-Venant, obtenida por Hunt (1982, 1984). Sin embargo, se ha proporcionado un reescalado de variables que permite aplicar los resultados asintóticos de Weir (1983) y Hunt (1984). Se ha prestado especial atención al análisis del campo de velocidad y altura en la región más próxima al frente de avance, donde la solución analítica ha sido obtenida como una serie de potencias. Los resultados obtenidos concuerdan a la perfección con los de Hunt (1984) cuando se consideran suficientes sumandos en la serie de potencias.

- Se ha implementado numéricamente un método numérico de volúmenes finitos, que permiten las resolución de las ecuaciones de aguas someras unidimensionales. Dicho método emplea una discretización semi-implícita "upwind" de los términos fuente, e incluye un limitador TVD que garantiza el filtro de soluciones espúreas. En particular, se ha aplicado dicho esquema numérico al problema de la rotura de una presa sobre un plano inclinado, sirviendo la solución numérica como test de la solución analítica (basada en la hipótesis de onda cinemática). Para tiempos suficientemente grandes, la solución analítica y numérica son prácticamente indistinguibles. Sin embargo, en la solución numérica se observa el desarrollo de inestabilidades hidrodinámicas para números de Froude mayores que 2. La multiplicidad de soluciones es debida al carácter no lineal de las ecuaciones de aguas someras. Por otra parte, la solución analítica en la proximidad del frente de avance ha sido validada con la solución numérica, siendo los resultados altamente satisfactorios.

- Se ha ilustrado la existencia física de inestabilidades en inundaciones sobre planos inclinados.
- Con el objeto de caracterizar las condiciones en las que aparecen ondas rodantes en roturas de presas, se ha aplicado la teoría de estabilidad lineal a las ecuaciones de aguas someras.
  - En primer lugar, se consideró un análisis de estabilidad lineal casi paralelo y no paralelo de ondas cinemáticas con fricción turbulenta sobre planos inclinados, encontrándose resultados muy dispares. El número de Froude crítico (es decir, aquél requerido para que crezcan las perturbaciones) fue expresado analíticamente mediante desarrollos asintóticos.
  - La solución de las perturbaciones lineales, en el caso particular en el que el número de Froude toma el valor $Fr = 2$, fue obtenida mediante la técnica de múltiples escalas. Este resultado sirvió para establecer la incorrección de los resultados previos, así como de test para el código numérico lineal y no lineal presentado para estudiar la evolución temporal de las perturbaciones. La incorrección de los resultados casi paralelo y no paralelo son debidos a la influencia de las variaciones temporales del flujo base en el comportamiento de las perturbaciones. Los códigos numéricos propuestos son capaces de reproducir con precisión los factores de crecimiento y la fase de las perturbaciones en el caso $Fr = 2$.
  - Se ha encontrado que los efectos no paralelos y transitorios de la onda cinemática estabilizan las ondas rodantes turbulentas e incrementan el número de Froude crítico requerido para la aparición de ondas rodantes.
- El archiconocido criterio de estabilidad para ondas rodantes turbulentas en flujos uniformes y estacionarios sobre planos inclinados (es decir, el flujo base

es inestable para cualquier longitud de onda cuando su número de Froude es mayor que 2) difiere considerablemente del obtenido para ondas cinemáticas. El efecto más destacable es la estabilización de perturbaciones para flujos base con $Fr = 2$. Adicionalmente, para números de Froude mayores, $Fr > 2$, la amplitud de las ondas crece o decrece dependiendo tanto de la velocidad del flujo base como de sus gradientes espaciales y temporales. Además, las ondas estables se modulan a medida que son convectadas aguas abajo. Este resultado es también diferente respecto del caso paralelo, en el que las ondas mantienen constante su longitud de onda incluso cuando se transforman en resaltos hidráulicos.

- En este trabajo, se ha formulado el problema unidimensional de transporte de sedimento suspendido y diluido tras la rotura de una presa inclinada. El modelo de fricción ha sido validado con datos experimentales. Diversos limitadores numéricos han sido testeados con soluciones analíticas para el transporte de sedimento suspendido en terrenos horizontales.
  - El transporte de sedimento suspendido ha sido caracterizado en función de la pendiente del terreno para diversos valores de los parámetros que caracterizan el sedimento. Para ello se consideró el valor máximo que alcanza la carga de sedimento suspendido ($Q^*_{s,max}$) y el tiempo en el que se alcanza dicho valor (t^*_{max}).
  - Los detalles de la elevación de la superficie libre, la velocidad del flujo y los perfiles de concentración de sedimento se han mostrado.
  - Se observó la formación de ondas rodantes en las proximidades del frente de avance para tiempos suficientemente grandes. Las ondas rodantes producen oscilaciones en la concentración de sedimento cerca del frente de avance, pero no afectan los valores de $Q^*_{s,max}$ debido a que las ondas ocurren para $t \gg t_{max}$.
  - También se caracterizó la validez de la hipótesis diluida en función del ángulo del terreno y de las propiedades del sedimento.
  - Se determinó la carga de fondo, estableciéndose la importancia relativa

  respecto de la carga suspendida en función del tamaño y la inclinación del terreno.
  - Se concluye que la carga de fondo es más importante que la suspendida para sedimentos de gran diámetro ($d_s \sim 5mm$), especialmente cuando la pendiente del terreno es suave. Para partículas de menor diámetro ($d_s \simeq 1mm$ o inferiores), el transporte de sedimento es dominado por suspensión, tanto más cuanto mayor es la pendiente del terreno.

- Se ha presentado una formulación para el transporte de sedimento en flujos con superficie libre, tanto laminares como turbulentos, basada en la Mecánica del Continuo. Partiendo de las ecuaciones de Navier-Stokes, las ecuaciones de un sistema multifase han sido simplificadas a su versión de mezcla. Los operadores diferenciales de las ecuaciones fueron formulados de manera análoga a la ecuación de transporte escalar, que facilita su implementación y resolución con las librerías numéricas OpenFOAM.

- El modelo turbulento k-ϵ se ha modificado en los términos de flotabilidad de la ecuación de la energía turbulenta k. Para modelar el transporte de sedimento en régimen laminar, se ha considerado un modelo Bingham, que determina la viscosidad laminar en función del esfuerzo tangencial denominado "yield stress" (τ_0).

- Dos métodos de volúmenes finitos han sido formulados para resolver el modelo de mezcla: primero, un modelo segregado e implícito, útil en problemas en los que la superficie libre permanece casi plana; posteriormente, un esquema segregado y explícito, capaz de capturar con precisión la superficie libre y la evolución de la concentración de sedimento. El esquema numérico explícito mostró que conserva la masa durante la simulación numérica.

- La simulación numérica de los experimentos de Mao (1986), y de la rotura de presa con transporte de sedimento (Capart and Young, 1998; Spinewine and Zech, 2007) mostró una excesiva dependencia de los resultados con el esfuerzo tangencial τ_0. En ausencia de τ_0, la simulación numérica y los experimentos físicos son muy similares, tanto mejores cuando menor es τ_0, tal y como muestran las simulaciones de los experimentos Taipei.

B.3 Sugerencias para trabajos futuros

Obviamente, todas las sugerencias para trabajos futuros están relacionadas con el modelo más ambicioso, el modelo tridimensional para flujos hiperconcentrados descrito en el último capítulo. Antes de proceder con las recomendaciones para trabajos futuros, se debe destacar la importancia de las medidas experimentales de las características reológicas del sedimento, que cierran el modelo teórico de mezcla.

Las tareas de mayor prioridad son las siguientes:

- Comparación de los resultados promediados presentados en los Capítulos 2-4 con aquellos obtenidos usando el modelo de mezcla.

- Derivación de leyes constitutivas para la presión de la fase sólida y el tensor de esfuerzos viscoso sólido que pueda ser incorporado en el modelo de mezcla.

- Inclusión de los efectos de la turbulencia en los cálculos de la evolución de la superficie libre, así como el perfeccionamiento de los modelos de turbulencia de mezcla. Aunque la influencia del modelo de turbulencia no ha sido investigada intensivamente, algunas de las discrepancias entre las predicciones teóricas y los resultados experimentales pueden ser debidos al modelo de turbulencia. Sería interesante incorporar los efectos de las estructuras turbulentas coherentes en la determinación de la velocidad de deslizamiento del sedimento respecto del agua.

- Mejora de las funciones “pared” del modelo turbulento, para incluir los efectos de la rugosidad del sedimento en el modelo k-ϵ.

- Inclusión de un modelo de turbulencia “Large Eddy Simulation” (LES) y comparación de los resultados con aquellos obtenidos con RANS.

- Validación del modelo de mezcla con un conjunto más completo de datos experimentales. En particular, el análisis de la distribución vertical de la concentración de sedimento y presión es de especial interés.

El trabajo actual debe ser considerado como un paso adelante hacia el modelado preciso del transporte de sedimento en flujos con superficie libre. El modelo de mezcla presentado en el documento no incluye fenómenos tan importantes como transferencia de masa, calor y distribución de tamaños, así como cambio de fase. La inclusión de estos efectos da lugar a un entorno teórico en el que actualmente se están realizando contribuciones de gran interés. Sin embargo, es difícil unificar todos los modelos actualmente disponibles o incorporar los avances de unos en otros.

Bibliography

Alekseenko, S. V., Nakoryakov, V. Y., Pokusaev, B. G., 1985. Wave formation on a vertical falling liquid film. AIChE J. 31, 1446–1460.

Ancey, C., Iverson, R. M., Renschler, M., Denlinger, R. P., 2008. An exact solution for ideal dam-break floods on steep slopes. Water Resour. Res. 44, W01430.

Anderson, T., Jackson, R., 1967. A fluid mechanical description of fluidized beds. Ind. Engng. Chem. Fundam. 6 (4), 527–539.

Armanini, A., Capart, H., Fraccarollo, L., Larcher, M., 2005. Rheological stratification in experimental free-surface flows of granular–liquid mixtures. J. Fluid. Mech. 532, 269–319.

Bagnold, R. A., 1966. An approach to the sediment transport problem for general physics. Tech. Rep. Professional Paper: 422-I, US Geological Survey, Washington, DC.

Balmforth, N. J., Mandre, S., 2004. Dynamics of roll waves. J. Fluid Mech. 514, 1–33.

Balmforth, N. J., Mandre, S., unpublished. Roll waves, hydraulic jumps and cyclic steps.

Batchelor, G. K., 1967. An Introduction to Fluid Dynamics. Cambrige, UK: Cambridge Univ. Press.

Bellos, C., Hrissanthou, V., 2003. Numerical simulation of morphological changes in rivers and reservoirs. Comput. Math. Appl. 45, 453–467.

Bellos, C. V., Soulis, J. V., Sakkas, J. G., 1992. Experimental investigation of two-dimensional dam-break induced flow. J. Hydraul. Res. 30, 47–63.

Berger, R. C., Carey, G. F., 1998. Free-surface flow over curved surfaces, Part I: Perturbation analysis. Int. J. Num. Meth. Fluids 28 (2), 191–200.

Bertolotti, F. P., Herbert, T., Spalart, P. R., 1992. Linear and nonlinear stability of the Blasius boundary layer. J. Fluid Mech. 242, 441–474.

Bohorquez, P., 2007a. Estabilidad espacial no paralela de corrientes poco profundas sobre un plano inclinado de pendiente arbitraria. Tech. Rep. ISBN: 84-690-3171-6, Dept. Legal: 149/2007, Universidad de Málaga.

Bohorquez, P., 2007b. On the wave-front shape and the advancing of the wetting front of a dam-break flood over an inclined plane of arbitrary bottom slope. In: Garcia-Navarro, P., Playan, E. (Eds.), Numerical Modelling of Hydrodynamics for Water Resources. Taylor and Francis, London, pp. 355–360.

Bohorquez, P., 2007c. Roll waves in floods on inclines. In: Garcia-Navarro, P., Playan, E. (Eds.), Numerical Modelling of Hydrodynamics for Water Resources. Taylor and Francis, London, pp. 361–366.

Bohorquez, P., Fernandez-Feria, R., 2006. Nonparallel spatial stability of shallow water flow down an inclined plane of arbitrary slope. In: Ferreira, R., Alves, E., Leal, J., Cardoso, A. (Eds.), River Flow 2006. Vol. 1. Taylor and Francis, London, pp. 503–512.

Bohorquez, P., Fernandez-Feria, R., 2008. Transport of suspended sediment under the dam-break flow on an inclined plane bed of arbitrary slope. Hydrol. Process. (*in press*, doi: 10.1002/hyp.6858).

Bouchut, F., Mangeney-Castelnau, A., Perthame, B., Vilotte, J., 2003. A new model of Saint-Venant and Savage-Hutter type for gravity driven shallow water flows. C. R. Acad Sci Paris, Ser. I 336, 531–536.

Brackbill, J. U., Kothe, D. B., Zemach, C., Jun. 1992. A continuum method for modeling surface-tension. J. Comput. Phys. 100 (2), 335–354.

Brauner, N., Maron, . M., 1982. Characteristics of inclined thin films, waviness and the associated mass transfer. Int. J. Heat Mass Transfer 25 (1), 99–110.

Brennan, D., 2001. The numerical simulation of two-phase flows in settling tanks. Ph.D. thesis, Imperial College, University of London.

Brocchini, M., Peregrine, D. H., 2001. The dynamics of strong turbulence at free surfaces. Part 1. Description. J. Fluid Mech. 449, 225–254.

Brock, R., 1967. Development of roll waves in open channels. Tech. Rep. KH-R-16, W.M. Keck Lab. of Hydr. and Water Resources, California Inst. of Tech.

Brock, R. R., 1970. Periodic permanent roll waves. J. Hydraul. Div. 12, 2565–2580.

Brook, B. S., Falle, S. A. E. G., Pedley, T. J., 1999. Numerical solutions for unsteady gravity-driven flows in collapsible tubes: evolution and roll-wave instability of a steady state. J. Fluid Mech. 396, 223–256.

Brors, B., 1999. Numerical modeling of flow and scour at pipelines. J. Hydr. Engrg. 125, 511–523.

Brown, P. P., Lawler, D. F., 2003. Sphere drag and settling velocity revisited. J. Environ. Engrg. 129, 222–231.

Burguete, J., García-Navarro, P., 2001. Efficient construction of high-resolution TVD conservative schemes for equations with source terms: application to shallow water flows. Int. J. Num. Meth. Fluids 37(2), 209–248.

Cao, X., Pender, G., Wallis, S., Carling, P. A., 2004. Computational dam-break hydraulics over erodible sediment bed. J. Hydr. Engrg. 130 (7), 689–703.

Cao, Z., 1999. Equilibrium near-bed concentration of suspended sediment. J. Hydr. Engrg. 125, 1270–1278.

Cao, Z. X., Wei, L. Y., Xie, J. H., 1995. Sediment-laden flow in open channels from two-phase flow viewpoint. J. Hydr. Engrg. 121 (10), 725–735.

Capart, H., Young, D. L., 1998. Formation of a jump by the dam-break wave over a granular bed. J. Fluid Mech. 372, 165–187.

Castro, M. J., Fernández-Nieto, E. D., Ferreiro, A., Parés, C., 2007. Numerical approach of sediment transport problems by high order finite volume methods. In: Garcia-Navarro, P., Playan, E. (Eds.), Numerical Modelling of Hydrodynamics for Water Resources. Taylor and Francis, London, pp. 211–232.

Castro-Díaz, M., Fernández-Nieto, E., Ferreiro, A., 2008. Sediment transport models in Shallow Water equations and numerical approach by high order finite volume methods. Comput. & Fluids 37, 299–316.

Cataño Lopera, Y. A., García, M. H., 2007. Geometry of scour hole around, and the influence of the angle of attack on the burial of finite cylinders under combined flows. Ocean Engineering 34, 856–869.

Chang, Y. C., Hou, T. Y., Merriman, B., Osher, S., Mar. 1996. A level set formulation of eulerian interface capturing methods for incompressible fluid flows. J. Comput. Phys. 124 (2), 449–464.

Chanson, H., 2004. The hydraulics of open channel flow: An introduction. Elsevier, Amsterdam.

Chapman, S., Cowling, T., 1970. The mathematical theory of non-uniform gases. Cambridge University Press, Cambridge.

Chen, C., 1995. Free-surface stability criterion as affected by velocity distribution. J. Hydr. Engrg. 121 (10), 736–743.

Cheng, N.-S., Chiew, Y.-M., 1999. Analysis of initiation of sediment suspension from bed load. J. Hydr. Engrg. 125, 855–861.

Chopp, 1991. Computation of minimal surfaces via mean-curvature flow. Ph.D. thesis, University of California, Berkeley.

Colebrook, C. F., 1939. Turbulent flow in pipes with particular reference to the transition region between the smooth- and rough-pipe laws. J. Inst. Civil Eng., 133–156.

Cornish, V., 1934. Ocean waves. Cambridge University Press.

Crespo, A. J. C., Gómez-Gesteira, M., Dalrymple, R. A., 2007. 3D SPH simulation of large waves mitigation with a dike. J. Hydraul. Res. 45 (5), 631–642.

Cunge, J. A., Holly, F. M., Verwey, A., 1980. Practical aspects of computational river hydraulics. Pitman: London, UK.

Damgaard, J. S., Whitehouse, R. J. S., Soulsby, R. L., 1997. Bed-load sediment transport on steep longitudinal slopes. J. Hydr. Engrg. 123, 1130–1138.

de Saint-Venant, A. J. C., 1871. Théorie du mouvement non-permanent des eaux, avec application aux crues des rivìere at à l'introduction des marées dans leur lit. C. R. Acad. Sci. Paris 73, 147–154.

Di Cristo, C., Vacca, A., 2005. On the convective nature of roll waves instability. J. Appl. Math. 3, 259–271.

Dopazo, C., 1977. On conditioned averages for intermittent turbulent flows. J. Fluid Mech. 81, 433–438.

Drake, T. G., 1986. High-speed motion pictures of nearly steady, uniform, two-dimensional, inertial flows of granular material. J. Rheol. 30 (5), 981–993.

Dressler, R. F., 1949. Mathematical solution of the problem of roll-waves in inclined open channels. Comm. Pure Appl. Math. 2, 149–194.

Dressler, R. F., 1952. Hydraulic resistance effect upon the dam-break functions. J. Res. Nat. Bur. Stand. 49, 217–225.

Dressler, R. F., 1954. Comparison of theories and experiments for the hydraulic dam-break wave. Publication 38 de l'Association Internationale d'Hydrologie Scientifique, 319–328.

Dressler, R. F., 1958. Unsteady non-linear waves in sloping channels. Proc. Roy. Soc. Ser. A 247, 186–198.

Dressler, R. F., 1978. New nonlinear shallow-flow equations with curvature. J. Hydraul. Res. 16, 205–222.

Drew, D. A., 1983. Mathematical modeling of two-phase flow. Annu. Rev. Fluid Mech. 15, 261–91.

Dyer, K., Soulsby, R. L., 1988. Sand transport on the continental shelf. Annu. Rev. Fluid Mech. 20, 295–324.

Eguiazaroff, I. B., 1935. Regulation of the water level in the reaches of canalized rivers. In: XVI International Congress of Navigation. Brussels.

Enright, D., Losasso, F., Fedkiw, R., Feb. 2005. A fast and accurate semi-lagrangian particle level set method. Computers & Structures 83 (6-7), 479–490.

Enwald, H., Peirano, E., Almstedt, A., 1996. Eulerian two-phase flow theory applied to fluidization. Int. J. Multiphase Flow 22 (1), 21–66.

Fernandez-Feria, R., 2000. Axisymmetric instabilities of bödewadt flow. Phys. Fluids 12 (7), 1730–1739.

Fernandez-Feria, R., 2006. Dam-break flow for arbitrary slopes of the bottom. J. Engrg Math. 54 (7), 319–331.

Ferreira, R., 2007. Fundamentals of mathematical modelling of morphodynamic processes. Application to geomorphic flows. In: Garcia-Navarro, P., Playan, E. (Eds.), Numerical Modelling of Hydrodynamics for Water Resources. Taylor and Francis, London, pp. 69–93.

Ferreira, R. M. F., 2005. River morphodynamics and sediment transport. Conceptual models and solutions. Ph.D. thesis, Instituto Superior Técnico, Technical University of Lisbon.

Ferzinger, J. H., Peric, M., 2002. Computational Methods for Fluid Mechanics. Springer.

Foley, M. G., Vanoni, V. A., 1977. Pulsing flow in steep alluvial streams. J. Hydr. Div. 103 (8), 843–850.

Fraccarollo, L., Capart, H., 2002. Riemann wave description of erosional dam-break flows. J. Fluid. Mech. 461, 183–228.

Fraccarollo, L., Capart, H., Zech, Y., 2003. A godunov method for the computation of erosional shallow water transients. Int. J. Num. Meth. Fluids 41, 951–976.

Friedrichs, K. O., 1948. On the derivation of the shallow water theory. Comm. Pure Appl. Math. 1 (1), 82–85.

Fu, X. D., Wang, G. Q., Shao, X. J., 2005. Vertical dispersion of fine and coarse sediments in turbulent open-channel flows. J. Hydr. Engrg. 131 (10), 877–888.

Gao, F.-P., Yang, B., Wu, Y.-X., Yan, S.-M., 2006. Steady current induced seabed scour around a vibrating pipeline. Applied Ocean Research 28, 291–298.

Garcia-Navarro, P., Fras, A., Villanueva, I., 1999. Dam-break flow simulation: some results for one-dimensional models of real cases. Journal of Hydrology 216, 227–247.

Garcia-Navarro, P., Playan, E. (Eds.), 2007. Numerical Modelling of Hydrodynamics for Water Resources. Taylor and Francis, London.

Gopala, V. R., van Wachem, B. G. M., 2008. Volume of fluid methods for inmiscible-fluid and free-surface flows. Chem. Eng. J.

Greimann, B., Holly, F., 2001. Two-phase flow analysis of concentration profiles. J. Hydr. Engrg. 127 (9), 753–762.

Greimann, B. P., Muste, M., Holly, F. M., 1999. Two-phase formulation of suspended sediment transport. J. Hydraul. Res. 37 (4), 479–500.

Hanes, D. M., Bowen, A. J., 1985. A granular-fluid model for steady intense bed-load transport. J. Geophys. Res 90, 9149–9158.

Hibiki, T., Ishii, M., 2003. One-dimensional drift-flux model and constitutive equations for relative motion between phases in various two-phase flow regimes. Int. J. Heat and Mass Transfer 46, 4935–4948.

Hill, D. P., 1998. The computer simulation of dispersed two-phase flows. Ph.D. thesis, Imperial College, University of London.

Hogg, A., 2006. Lock-release gravity currents and dam-break flows. J. Fluid Mech. 569, 61–87.

Hogg, A. J., Pritchard, D., 2004. The effects of hydraulic resistance on dam-break and other shallow inertial flows. J. Fluid Mech. 501, 179–212.

Hsu, C-T, Y. K.-C., 2002. Iterative explicit simulation of 1D surges and dam-break flows. Int. J. Meth. Fluids 38, 647–675.

Huang, G., Bonn, D., 2007. Viscosity of a dense suspension in Couette flow. J. Fluid Mech. 590, 497–507.

Huang, N., Ovarlez, G., Bertrand, F., Rodts, S., Coussot, P., Bonn, D., 2005. Flow of wet granular materials. Phys. Rev. Lett. 94 (2), 028301.1–028301.4.

Hudson, J., 2001. Numerical techniques for morphodynamic modelling. Ph.D. thesis, The University of Reading.

Hunt, B., 1982. Asymptotic solution for dam-break problem. J. Hydr. Div. 108 (1), 115–126.

Hunt, B., 1984. Perturbation solution for dam-break floods. J. Hydr. Engrg. 110 (8), 1058–1071.

Hunt, B., 1987. An inviscid dam-break solution. J. Hydraul. Res. 25 (3), 313–327.

Hutter, K., 2005. Geophysical granular and particle-laden flows:review of the field. Phil. Trans. R. Soc. Ser. A 363, 1497–1505.

Hwang, S., Chang, H., 1987. Turbulent and inertial roll waves in inclined film flow. Phys. Fluids 30 (5), 1259–1268.

Ishii, M., 1975. Thermo-fluid dynamic theory of two-phase flow. Direction des Etudes et Reserches d'Electricité de France, Eyrolles, Paris, France.

Ishii, M., 1977. One-dimensional drift-flux model and constitutive equations for relative motion between phases in various two-phase flow regimes. Tech. Rep. ANL-77-47, Argonne National Lab., Ill. (USA).

Ishii, M., Hibiki, T., 2006. Thermo-fluid dynamics of two-phase flow. Springer.

Iverson, R. M., , Denlinger, R. P., 2001. Flow of variably fluidized granular masses across three-dimensional terrain 2. Numerical predictions and experimental tests. J. Geoph. Res. 106, 553–566.

Iverson, R. M., 1997. The physics of debris flows. Reviews of Geophysics 35 (3), 245–296.

Iverson, R. M., Costa, J. E., LaHusen, R. G., 1992. Debris-flow flume at H. J. Andrews Experimental Forest, Oregon. Open-File Report 92-483, U.S. Geological Survey.

Iverson, R. M., Denlinger, R. P., 2001. Flow of variably fluidized granular masses across three-dimensional terrain 1. Coulomb mixture theory. J. Geoph. Res. 106, 537–552.

Jackson, R., 1997. Locally averaged equations of motion for a mixture of identical spherical particles and a Newtonian fluid. Chem. Engrg. Sci. 52 (1), 2457–2469.

Jakob, M., Hungr, O., 2005. Debris-Flows Hazards and Related Phenomena. Springer.

Jánosi, I. M., D., J., Szabó, K. G., T., T., 2004. Turbulent drag reduction in dambreak flows. Exp. Fluids 37, 219–229.

Jasak, H., 1996. Error analysis and estimation in the Finite Volume method with applications to fluid flows. Ph.D. thesis, Imperial College, University of London.

Jasak, H., 2006. Numerical solution algorithms for compressible flows: Lecture Notes. Tech. rep., University of Zagreb, Croatia.

Jasak, H., Weller, H., 1995. Interface-tracking capabilities of the intergamma differencing scheme. Tech. rep., CFD research group, Imperial College, London.

Jeffreys, H., 1925. The flow of water in an inclined channel of rectangular section. Philos. Mag. 49, 793–807.

Jenkins, J. T., Hanes, D. M., 1998. Collisional sheet flow of sediment driven by a turbulent fluid. J. Fluid Mech. 370, 29–52.

Jensen, B. L., Sumer, B. M., Jensen, H. R., Fredse, J., 1990. Flow around and forces on a pipeline near a scoured bed in steady current. J. Offshore Mech. Arct 112, 206–213.

Jiang, J., Law, A.-K., Cheng, N.-S., 2004. Two-phase modeling of suspended sediment distribution in open channel flows. J. Hydraul. Res. 42 (3), 273–281.

Johnson, P. C., Jackson, R., 1987. Frictional-collisional constitutive relations for granular materials, with application to plane shearing. J. Fluid Mech. 176, 67–93.

Johnson, P. C., Nott, P., Jackson, R., 1990. Frictional-collisional equations of motion for particulate flows and their application to chutes. J. Fluid Mech. 210, 501–535.

Julien, P. Y., 1995. Erosion and Sedimentation. Cambridge University Press: Cambridge.

Julien, P. Y., Hartley, D. M., 1986. Formation of roll waves in laminar sheet flow. J. Hydraul. Res. 24 (1), 5–17.

Kärrholm, F. P., 2006. Rhie-Chow interpolation in OpenFOAM. Tech. rep., Department of Applied Mechanics, Chalmers Univesity of Technology.

Keller, J., 1948. The solitary wave and periodic waves in shallow water. Comm. Pure Appl. Math. 1 (3), 323–339.

Keller, J., 2003. Shallow-water theory for arbitrary slopes of the bottom. J. Fluid Mech. 489, 345–348.

Kevorkian, J., Cole, J. D., 1996. Multiple Scale and Singular Perturbation Methods. Springer.

Kluwick, A., 2006. The effect of surface topography on weakly nonlinear roll waves. Proc. Appl. Math. Mech. 6, 607–608.

Krieger, I., 1972. Rheology of monodisperse lattices. Adv. Colloid Interface Sci. 3, 111–136.

Lalli, F., Esposito, P., Verzicco, R., 2006. A constitutive equation for fluid-particle flow simulation. Int. J. Offshore and Polar Engrg. 16 (1), 18–24.

Lalli, F., Esposito, P. G., Piscopia, R., Verzicco, R., 2005. Fuid-particle flow simulation by averaged continuous model. Comput. & Fluids 34, 1040–1061.

Larcher, M., 2004. Vertical structure of high-concentration liquid-granular flows. Ph.D. thesis, Università degli Studi di Trento, Italia.

Lauber, G., Hager, W. H., 1998a. Experiments to dambreak wave: Horizontal channel. J. Hydraul. Res. 36 (3), 291–307.

Lauber, G., Hager, W. H., 1998b. Experiments to dambreak wave: Sloping channel. J. Hydraul. Res. 36, 761–773.

Leal, J. G. A. B., Ferreira, R. M. L., Cardoso, A. H., 2002. Dam-break waves on movable bed. In: Bousmar, D., Zech, Y. (Eds.), River Flow 2002. Balkema, IAHR Monograph, Rotterdam, The Netherlands, pp. 981–990.

Leighton, D., Acrivos, A., 1986. Viscous resuspension. Chem. Eng. Sci. 41 (6), 1377–1384.

Leighton, D., Acrivos, A., 1987. The shear-induced migration of particles in concentrated suspensions. J. Fluid Mech. 181, 415–439.

LeVeque, R., 2002. Finite Volume Methods for Hyperbolic Problems. Cambridge University Press.

LeVeque, R. J., 1996. High-resolution conservative algorithms for advection in incompressible flow. SIAM J. Numer. Anal. 33 (2), 627–665.

Li, F., Cheng, L., 2001. Prediction of lee-wake scouring of pipelines in currents. Journal of Waterway, Port, Coastal, and Ocean Engineering 127, 106–112.

Li, Y., Yu, X., 2007. Two-phase turbulent flow model for suspended sediment motion. Qinghua Daxue Xuebao/Journal of Tsinghua University 47 (6), 805–808.

Lighthill, M., Whitham, G., 1955. On kinematic waves: I. Flood movemement in long rivers; II. Theory of traffic flow on long crowded roads. Proc. Roy. Soc. Ser. A 229, 281–345.

Liu, Q., Chen, L., Li, J., Singh, V., 2005. Roll waves in overland flow. J. Hydr. Engrg. 10 (2), 110–117.

Liu, X., 2008. Numerical models for scour and liquefaction around object under currents and waves. Ph.D. thesis, University of Illinois.

Liu, X., Garcia, M. H., 2006. Numerical simulation of local scour with free surface and automatic mesh deformation. In: Randall Graham, P. (Ed.), World Environmental and Water Resources Congress 2006.

Liu, X., Garcia, M. H., 2007. Numerical modeling for the Calumet Water Reclamation Plant (CWRP) primary settling tank. Tech. rep., University of Illinois.

Logan, M., Iverson, R. M., 2007. Video documentation of experiments at the usgs debris-flow flume 1992-2006. Tech. Rep. Open-File Report 2007-1315, U.S. Geological Survey, `http://pubs.usgs.gov/of/2007/1315/`.

Losasso, F., Fedkiw, R., Osher, S., Dec. 2006. Spatially adaptive techniques for level set methods and incompressible flow. Comput. & Fluids 35 (10), 995–1010.

Lua, L., Lia, Y., Qin, J., 2005. Numerical simulation of the equilibrium profile of local scour around submarine pipelines based on renormalized group turbulence model. Ocean Engineering 32, 2007–2019.

Lun, C. K. K., Savage, S. B., Jeffrey, D. J., Chepurniy, N., 1984. Kinetic theories for granular flow: inelastic particles in couette flow and slightly inelastic particles in a general flowfield. J. Fluid Mech. 140, 223–256.

Manninen, M., Taivassalo, V., Kallio, S., 1996. On the mixture model for multiphase flow. Tech. Rep. VTT Publications 288., Centre of Finland.

Mao, Y., 1986. The interaction between a pipeline and an erodible bed. Ser. Paper, Inst. of Hydrodynamics and Hydr. Engrg., Technical University of Denmark, Copenhagen.

Martin, J. C., Moyce, W. J., 1952. Part IV. An experimental study of the collapse of liquid columns on a rigid horizontal plane. Phil. Trans. R. Soc. Ser. A 224 (88), 312–324.

Mokhberi, E., Faloutsos, P., 2007. A particle level set library. http://www.magix.ucla.edu/software/levelSetLibrary.

Moses, B., 2007. Simulation of multiphase fluid flows using a spatial filtering process. Ph.D. thesis, Standford University.

Murillo, J., García-Navarro, P., Brufau, P., Burguete, J., 2007. The influence of source terms on stability and conservation in 1D hyperbolic equations: Application to shallow water on fixed and movable beds. In: Garcia-Navarro, P., Playan, E. (Eds.), Numerical Modelling of Hydrodynamics for Water Resources. Taylor and Francis, London, pp. 47–66.

Murillo, J., Garcia-Navarro, P., Brufau, P., Burguete, J., 2008. 2D modelling of erosion/deposition processes with suspended load using upwind finite volumes. J. Hydraul. Res. 46 (1), 99–112.

Muste, M., 2002. Sources of bias errors in flume experiments on suspended-sediment transport. J. Hydraul. Res. 40 (6), 695–708.

Muste, M., Patel, V. C., 1997. Velocity profiles for particles and liquid in open-channel flow with suspended sediment. J. Hydr. Engrg. 123 (9), 742–751.

Muste, M., Yu, K., Fujita, I., Ettema, R., 2005. Two-phase versus mixed-flow perspective on suspended sediment transport in turbulent channel flows. Water Resour. Res. 41 (10), 1–22.

Muzaferija, S., Peric, M., 1998. Computation of free surface flows using interface-tracking and interface-capturing methods. In: Mahrenholtz, O., Markiewicz, M. (Eds.), Nonlinear water waves interaction. Computational Mechanics Publications, Southampton, Ch. 2.

Namin, M., Lin, B., Falconer, R. A., 2004. Modelling estuarine and coastal flow using an unstructured triangular finite volume algorithm. Advances in Water Resources 27, 1179–1197.

Needham, D. J., Merkin, J. H., 1984. On roll waves down an open inclined channel. Proc. Roy. Soc. Ser. A 394 (1807), 259–278.

Ni, H. Q., Huang, Z. C., Zhou, L. X., Zhou, J. Y., 1996. Flow modeling and turbulence measurements vi. In: Chen, Hih, Lienau, Kundn (Eds.), Fundamentals of Mathematical Modelling of Morphodynamic Processes. Application to Geomorphic Flows. Balkema, Rotterdam, pp. 781–788.

Ni, J. R., Wang, G. Q., Borthwick, A. G. L., 2000. Kinetic theory for particles in dilute and dense solid-liquid flows. J. Hydr. Engrg. 126 (12), 893–903.

Nsom, B., Debiane, K., Piau, J., 2000. Bed slope effect on the dam-break problem. J. Hydr. Engrg. 38 (6), 459–464.

OpenCFD Limited, 2007. OpenFOAM 1.4.1: User guide. Tech. rep., http://www.opencfd.co.uk/openfoam.

Osher, S., Sethian, J. A., Nov. 1988. Fronts propagating with curvature-dependent speed - algorithms based on Hamilton-Jacobi formulations. J. Comput. Phys. 79 (1), 12–49.

Ovarlez, G., Bertrand, F., Rodts, S., 2006. Local determintation of the constitutive law of a dense suspension of noncolloidal part through magnetic resonance imaging. J. Rheol. 50 (3), 259–292.

Pananicolaou, A. N., Elhakeem, M., Krallis, G., Prakash, S., 2008. Sediment transport modeling reviewcurrent and future developments. J. Hydr. Engrg. 134 (1), 1–14.

Pelanti, M., Bouchut, F., Mangeney, A., 2008. A Roe-type scheme for two-phase shallow granular flows over variable topography. Hydrol. Process.(submitted).

Peskin, C. S., 1977. Numerical-analysis of blood-flow in heart. J. Comput. Phys. 25 (3), 220–252.

Pierson, T. C., 2005. Hyperconcentrated flow - transitional process between water flow and debris flow. In: Jakob, M., Hungr, O. (Eds.), Debris-flow hazards and related phenomena. Springer-Verlag, pp. 159–203.

Pitman, B., Le, L., 2005. A two-fluid model for avalanche and debris flows. Phil. Trans. R. Soc. Ser. A 363, 1573–1601.

Pritchard, D., 2005. On fine sediment transport by a flood surge. J. Fluid Mech. 543, 239–248.

Pritchard, D., Hogg, A. J., 2002. On sediment transport under dam-break flow. J. Fluid Mech. 473, 265–274.

Pritchard, D., Hogg, A. J., 2003. On fine sediment transport by long waves in the swash zone of a plane beach. J. Fluid Mech. 493, 255–275.

Prokopiou, T., Cheng, M., Chang, H., 1991. Long waves on inclined films at high reynolds number. J. Fluid Mech. 222, 665–691.

Pudasaini, S. P., Wang, Y., Hutter, K., 2005. Modelling debris flows down general channels. Natural Hazards and Earth System Sciences 5, 799–819.

Rhie, C. M., Chow, W. L., 1983. Numerical study of the turbulent flow past an airfoil with trailing edge separation. AIAA journal 21 (11), 1525–1532.

Ritter, A., 1892. Die fortpflanzung der wasserwellen. Z. Verein. Deutch. Ing. 36, 947–954.

Rodi, W., 1993. Turbulence Models and Their Applications in Hydraulics. Balkema, Rotterdam, The Netherlands.

Rodriguez, J. M., Taboada-Vázquez, R., 2007. From Euler and Navier–Stokes equations to shallow waters by asymptotic analysis. Adv. Engrg. Soft. 38 (6), 399–409.

Rosatti, G., Fraccarollo, L., 2006. A well-balanced approach for flows over mobile-bed with high sediment-transport. J. Comput. Phys. 220, 312–338.

Rusche, H., 2002. Computational fluid dynamics of dispersed two-phase flows at high phase fractions. Ph.D. thesis, Imperial College, University of London.

Sanford, L. P., Maa, J. P. Y., 2001. A unified erosion formulation for fine sediments. Marine Geology 179, 9–23.

Savage, S., Hutter, K., 1991. The dynamics of avalanches of granular materials from initiation to run-out. Acta Mech. 86, 201–223.

Schaflinger, U., Acrivos, A., Stivi, H., Aug. 1995. An experimental-study of viscous resuspension in a pressure-driven plane channel flow. Int. J. Multiphase Flow 21 (4), 693–704.

Schaflinger, U., Acrivos, A., Zhang, K., Jul. 1990. Viscous resuspension of a sediment within a laminar and stratified flow. Int. J. Multiphase Flow 16 (4), 567–578.

Schlichting, H., 1987. Boundary Layer Theory, 7th Edition. McGraw-Hill.

Schoklistsch, A., 1917. über dambruchwellen. Sitzber Akad. Wiss. Wien. 126.

Sethian, J. A., Feb. 1996. A fast marching level set method for monotonically advancing fronts. Proceedings Of The National Academy Of Sciences Of The United States Of America 93 (4), 1591–1595.

Sethian, J. A., 1999. Fast marching methods. SIAM Review 41 (2), 199–235.

Sethian, J. A., 2001. Evolution, implementation, and application of level set and fast marching methods for advancing fronts. J. Comput. Phys. 169, 503–555.

Sethian, J. A., Smereka, P., 2003. Level set methods for fluid interfaces. Annu. Rev. Fluid Mech. 35, 341–372.

Shields, A., 1936. Anwendung der aehnlichkeitsmechanik und fer turnulenzfroschung auf die geschiebebewegung. Ph.D. thesis, Preuischen Versuchsanstalt fr Wasserbau und Schiffbau.

Simonin, O., 1990. Eulerian formulation for particle dispersion in turbulent two-phase flows. In: Proc. 5th Workshop on two-phase flow predictions. March 19-22, Erlangen, FRG Jülich kornforschungsanalge Jülich. pp. 156–166.

Simpson, G., Castelltort, S., 2006. Coupled model of surface water flow, sediment transport and morphological evolution. Computers & Geosciences 32, 1600–1614.

Smereka, P., 1996. Level set method for two-fluid flows, 1996.

Smith, H. D., 2004. Modelling the flow and scour around an immovable cylinder. Master's thesis, The Ohio State University.

Smith, H. D., 2007. Flow and sediment dynamics around three-dimensional structures in coastal environments. Ph.D. thesis, The Ohio State University.

Sohn, Y. K., 1997. On traction-carpet sedimentation. J. Sed. Res. 67, 502–509.

Soulis, J. V., 1992. Computation of two-dimensional dam-break flod flows. Int. J. Num. Meth. Fluids 14, 631–664.

Spinewine, B., Zech, Y., 2007. Small-scale laboratory dam-break waves on movable beds. J. Hydraul. Res. 45 (Extra Issue), 73–86.

Stickel, J. J., Powell, R. L., 2005. Fluid mechanics and rheology of dense suspensions. Annu. Rev. Fluid Mech. 37, 129–149.

Stoker, J., 1957. Water waves, the mathematical theory with applications. Interscience: London.

Sumer, B. M., 2007. Mathematical modelling of scour: A review. J. Hydraul. Res. 45 (6), 723–735.

Sussman, M., Puckett, E. G., 2000. A coupled level set and volume-of-fluid method for computing 3D and axisymmetric incompressible two-phase flows. J. Comput. Phys. 162 (2), 301–337.

Sussman, M., Smereka, P., Osher, S., Sep. 1994. A level set approach for computing solutions to incompressible two-phase flow. J. Comput. Phys. 114 (1), 146–159.

Sweby, P. K., 1984. High resolution schemes using flux limiters for hyperbolic conservation laws. SIAM J. Numer. Anal. 21, 995–1011.

Toro, E. F., 1999. Riemann Solvers and Numerical Methods for Fluid Dynamics: A Practical Introduction. Springer.

Toro, E. F., 2001. Shock-Capturing Methods for Free-Surface Shallow Flows. Wiley.

Toro, E. F., Garcia-Navarro, P., 2007. Godunov-type methods for free-surface shallow flows: A review. J. Hydraul. Res. 45 (6), 736–751.

Tseng, M. H., Chu, C. R., 2000. The simulation of dam-break flows by an improved predictor-corrector TVD scheme. Advances in Water Resources 23, 637–643.

Ubbink, O., 1997. Numerical prediction of two fluid systems with sharp interfaces. Ph.D. thesis, Imperial College, University of London.

Ungarish, M., 1993. Hydrodynamics of Suspensions. Fundamentals of centrigugal and gravity separation. Springer-Verlag.

Unverdi, S. O., Tryggvason, G., May 1992. A front-tracking method for viscous, incompressible, multi-fluid flows. J. Comput. Phys. 100 (1), 25–37.

Usha, R., Sharma, A., Dandapat, B. S. (Eds.), 2006. Wave Dynamics and stability of thin film flow systems. Narosa.

van Rijn, L., 1987. Mathematical modelling of morphological processes in the case of suspended sediment transport. Ph.D. thesis, Civil Engineering and Geosciences, Waterloopkundig Laboratorium Delft.

van Rijn, L. C., 1993. Principles of Sediment Transport in Rivers, Estuaries and Coastal Seas. Aqua: Amsterdam.

van Wachem, B. G. M., 2000. Derivation, implementation, and validation of computer simulation models for gas-solid fluidized beds. Ph.D. thesis, Delft University of Thechnology.

Vanoni, V. A. (Ed.), 2006. Sedimentation Engineering. No. 54 in ASCE Manuals and Reports on Engineering Practice. ASCE, Ch. Sediment Transportation Mechanics, pp. 11–191.

Villaret, C., Davies, A. C., 1995. Modeling sediment-turbulent flow interactions. Appl. Mech. Rev. 48 (9), 601–609.

Wan, Z., Wang, Z., 1994. Hyperconcentrated Flow. Balkema, IAHR Monograph, Rotterdam, The Netherlands.

Wang, G., Fu, X., Huang, Y., Huang, G., 2008. Analysis of suspended sediment transport in open-channel flows: Kinetic-model-based simulation. J. Hydr. Engrg. 134 (3), 328–339.

Wang, G. Q., Ni, J. R., 1990. Kinetic theory for particle concentration distribution in two-phase flow. J. Eng. Mech. 116 (12), 2738–2748.

Wang, G. Q., Ni, J. R., 1991. The kinetic theory for dilute solid/liquid two-phase flow. Int. J. Multiphase Flow 17 (2), 273–281.

Weir, G. J., 1983. The asymptotic behaviour of simple kinematic waves of finite volume. Proc. Roy. Soc. Ser. A 387, 459–467.

Weller, H. G., 2002a. Derivation, modelling and solution of the conditionally averaged two-phase flow equations. Tech. Rep. TR/HGW/02, Nabla Ltd.

Weller, H. G., 2002b. Derivation, modelling and solution of the conditionally averaged two-phase flow equations. Tech. Rep. TR/HGW/02, Nabla Ltd.

Weller, H. G., Tabor, G., Jasak, H., Fureby, C., 1998. A tensorial approach to computational continuum mechanics using object-oriented techniques. Comput. Phys. 12 (6), 620–631.

WES (Waterways Experiment Station), 1961. Floods resulting from suddenly breached dams: Report 1, Conditions of minimum resistance; Report 2: Conditions of high resistance. Tech. rep., U.S. Army Corps of Engineers, Vicksburg, Miss.

Whitham, G., 1955. The effects of hydraulic resistance in the dam-break problem. Proc. Roy. Soc. Ser. A 227, 399–407.

Whitham, G. B., 1974. Linear and nonlinear waves. Wiley, New York.

Wildemuth, C. R., Williams, M. C., 1984. Viscosity of suspensions modeled with a shear-dependent maximum packing fraction. Rheol. Acta 23, 627–635.

Williams, M. W., Kothe, D. B., Puckett, E. G., 1998. Accuracy and convergence of continuum surface tension models. Tech. Rep. LA-UR-98-2268, Los Alamos National Laboratory, http://citeseer.ist.psu.edu/327505.html.

Wright, N. G., 2005. Introduction to numerical methods for fluid flow. In: Bates, P., Lane, S., Ferguson, R. (Eds.), Computational Fluid Dynamics: Applications in Environmental Hydraulics. Wiley, pp. 147–168.

Wu, W., Rodi, W., Wenka, T., 2000. 3D numerical modeling of flow and sediment transport in open channels. J. Hydr. Engrg. 126 (1), 4–15.

Wu, W., Wang, S. S. Y., 2007. One-dimensional modeling of dam-break flow over movable beds. J. Hydr. Engrg. 133 (1), 48–58.

Wu, W., Wang, S. S. Y., 2008. One-dimensional explicit finite-volume model for sediment transport with transient flows over movable beds. J. Hydraul. Res. 46 (1), 87–98.

Yalin, M. S., Ferreira da Silva, A. M., 2001. Fluvial processes. IAHR.

Zanuttigh, B., Lamberti, A., 2002. Roll waves simulation using shallow water equations and weighted average flux method. J. Hydraul. Res. 40 (5), 610–622.

Zarraga, I. E., Hil, D. A., Leighton, D. T., 2000. The characterization of the local stress of concentrated suspensions of noncolloidal spheres in newtonian fluids. J. Rheol. 44, 185–220.

Zhang, D., Rauenzahn, R., 1997. A viscoelastic model for dense granular flow. J. Rheol. 41, 1275–1298.

Zhang, K., Acrivos, A., 1994. Viscous resuspension in fully-developed laminar pipe flows. Int. J. Multiphase Flow 20 (3), 579–591.

Zhao, Z., Fernando, H., 2007. Numerical simulation of scour around pipelines using and Euler–Euler coupled two-phase model. Environ Fluid Mech. 7, 121–142.

Zhao, Z., Fernando, H., 2008. Numerical modeling of a sagging pipeline using an Eulerian two-phase model. J. Turbulence 9, 1–20.

Zoppou, C., Roberts, S., 2003. Explicit schemes for dam-break simulations. J. Hydr. Engrg. 129, 11–34.